Transport properties of critically disordered TiN films

Dissertation
zur Erlangung des Doktorgrades der Naturwissenschaften
(Dr. rer. nat.)
Fakultät für Physik
Universität Regensburg
vorgelegt von
Klaus Kronfeldner
aus Bogen

Durchgeführt am
Institut für Experimentelle und Angewandte Physik
der Universität Regensburg
unter Anleitung von
Prof. Dr. Christoph Strunk

November 2016

Das Promotionsgesuch wurde am 7.7.2016 eingereicht.
Die Arbeit wurde von Prof. Dr. Christoph Strunk angeleitet.
Das Promotionskolloquium fand statt am:

Prüfungsausschuss:	Vorsitzender:	Prof. Dr. Vladimir Braun
	Erstgutachter:	Prof. Dr. Christoph Strunk
	Zweitgutachter:	Prof. Dr. Ferdinand Evers
	Weiterer Prüfer:	Prof. Dr. Christian Back

Contents

1 Introduction

It is well known that the resistance of many bulk-metals sharply drops to zero below the critical temperature T_c. In the case of disordered thin films, T_c is lowered compared to the bulk critical temperature and additionally the decrease of the resistance below T_c is broadened to a certain temperature range. The temperature at which the resistance vanishes completely is known as the Berezinskii-Kosterlitz-Thouless (BKT) transition. This years Nobel price goes to Kosterlitz and Thouless particularly for the finding of the vortex-antivortex binding-unbinding transition [1, 2] based on the preceding publications of Berezinskii [3, 4]. This award demonstrates the importance of the physics in two dimensional superconductors for today's science.

However, disordered metallic thin films that can form a superconducting phase at low temperatures are by no means fully described by the physics of the BKT transition. At high temperatures the conductivity σ can be described by the Drude expression

$$\sigma = ne^2\tau/m, \tag{1.1}$$

where m is the mass of the electrons, n is the charge carrier density, $-e$ is the electron charge and τ is the scattering time. Upon lowering temperature localization effects occur. The electrons get more and more localized due to coherent backscattering and disorder-enhanced electron-electron interactions [5]. Above $T \gtrsim T_c$, superconducting fluctuations lower the resistance R. Within the mean-field theory of superconducting fluctuations the resistance would drop to zero at T_c. But in the BKT phase, where unbound vortex-antivortex pairs can freely move across the superconducting thin film, the resistance stays finite. Finally at T_{BKT}, the BKT transition temperature, the resistance vanishes completely and the vortex-antivortex pairs are bound together. Between the temperature regions where either electron localization or superconducting fluctuations or BKT physics dominate the temperature dependence of the resistance, continous descripitions of the $R(T)$ dependence under the influence of multiple effects are necessary. It is a tough challenge to identify the regions in the temperature dependence of the resistance that are dominated by different effects.

In some materials, such as titanium nitride (TiN) or indium oxide, a highly insulating state occurs upon increasing disorder or magnetic field B. Instead of a decrease of the resistance at low temperatures, an increase is observed. This transition is called superconductor-insulator transition (SIT). This increase of the resistance is supposed to be caused by a localization of Cooper pairs instead of a localization of electrons. Measurements of the local density of states near the disorder driven SIT (D-SIT) lead to this conclusion [6].

The SIT is considered to be a second order quantum phase transition which is also called a continuous quantum phase transition. Continuous quantum phase transitions are driven by the change of a single parameter in the Hamiltonian of the system. The superconducting ground state is formed by a condensate of Cooper pairs and excitations in form of vortices. The insulating state is can be visualised by a condensate of vortices and the excitations are hopping Cooper pairs [7]. Either disorder or magnetic field is the parameter that induces the phase transition. The change from a Cooper pair condensate to a vortex condensate is suggested by a duality transformation where conductivity is replaced by resistivity. Based on general properties of continous quantum phase transitions at finite temperatures, the theory of finite size scaling was adapted to the SIT [7, 8]. A signature of a superconductor-insulator quantum phase transition are critical values for disorder and magnetic field, at which the resistance is temperature independent. Such a plateau in the $R(T)$ dependence is accompanied by a crossing point in the magnetoresistance isotherms. Crossing points in the $R(B)$ isotherms are extensively discussed in the context of a quantum phase transition. Though, the found apparent intersection points are not an unambiguous evidence for a quantum phase transition. Superconducting fluctuations can cause approximate crossing points in the magnetoresistance isotherms [9]. Multiple crossing points are already found in Refs. [10, 11]. There a finite size scaling analysis was pursued and to each crossing point in the $R(B)$ isotherms a different type of the quantum phase transition was attributed.

Artificial Josephson junction arrays consist of superconducting islands coupled by Josephson weak links. Two competing energy scales deterimine the conductivity of the array. On the one side the Josephson energy E_J favours charge transport, on the other side the charging energy E_c forms an energy barrier the Cooper pairs have to overcome to move. The increase of the ratio E_c/E_J induces a SIT. As both energy scales are tunable by the geometry and E_J can be tuned by an applied magnetic field, Josephson junction arrays offer a more controllable access to the SIT than disordered thin films. From the measured fluctuation of the local superconducting energy gap across a TiN film [6], the formation of superconducting islands that are embedded in a normalconducting matrix is likely to lead to the SIT in TiN. The similarity of such a natural array to artificial Josephson junction arrays, motivated the explanation of the SIT in TiN in terms of a competing E_c and E_J.

Dual to the vortex BKT on the superconducting side of the SIT, the charge BKT was postulated in the insulating state of Josephson junction arrays. An Arrhenius law which describes a temperature activated $R(T)$ dependence was found to be to weak for the $R(T)$ curves presented in Refs. [12, 13]. The convex shape of the $R(T)$ dependence in the Arrhenius plot was attributed to the charge BKT. In TiN thin films a similar behaviour was found which was called “hyperactivated” [14] and the new highly insulating phase was called “superinsulator” [15].

In this thesis differently disordered samples of different lateral sizes were measured at low temperatures and magnetic fields ranging from zero up to $B = 17\,\mathrm{T}$. A thorough investigation of the disorder-driven as well as the magnetic field induced SIT was pursued on the basis more than 700000 measurement files where most of these files contain recorded current-voltage characteristics.

In chapter 2 the fundamental ideas of superconductivity and the SIT are presented. The sample properties and the measurement setups are explained in chapter 3. The main results of this work are splitted into five chapters. Chapter 4 contains the three found crossing points in the magnetoresistance isotherms and phenomenological descriptions of the $R(T, B)$ dependences in the three corresponding temperature regimes. A finite size scaling analyis is included. In chapter 5 superconducting fluctuations according to the theory of Galitski and Larkin [16] are found to well describe the magnetoresistance isotherms at high magnetic fields. Tests for a electrostatic screening effect due to a metallic top-gate are discussed in chapter 6. In chapter 7 heating phenomena in the IV characteristics, the evolution of the critical temperature T_c and the evolution of the BKT transition temperature T_{BKT} are investigated in the vicinity of the D-SIT. The application of a special measurement technique enabled to find a dual shape of the IV characteristics in the insulating state with interchanged current and voltage axes with respect to the superconducting IV characteristics. In chapter 8 the size dependence and the disorder dependence of both T_{BKT} in the superconducting state and the activation energy in the field-driven insulating state are revealed. In the discussion in chapter 9 the results of chapters 4, 5, 6, 7, 8 are dicussed in a comprehensive way. The results are discussed in the light of to recent publications. Chapter 10 summarizes the obtained results and gives an outlook.

2 Fundamental ideas about the superconductor-insulator transition (SIT)

2.1 Superconductivity

In 1911 Heike Kamerlingh Onnes discovered superconductivity while he studied the resistivity of pure metals at low temperatures [17]. When he and his coworker van Holst measured the resistivity of a mercury sample, they noticed a sharp drop in resistance below 4.2 K. They found that below a characteristic critical temperature T_c many materials became perfectly conducting. These superconducting samples were not only perfect conductors, they were perfect diamagnets as well, which was found by Meissner and Ochsenfeld in 1933 [18]. In the observed Meissner phase a magnetic field is expelled completely from the inside of a superconducting bulk of a Type I superconductor. Within a penetration depth λ the magnetic field is screened exponentially from the interior of the superconductor. The penetration depth λ_L can be derived from the London equations for electrical field $\mathbf{E}$, magnetic field $\mathbf{B}$ and the density $\mathbf{J}_s$ of the supercurrent

$$\mathbf{E} = \mu_0 \lambda_L^2 \frac{\partial}{\partial t}(\mathbf{j}_s) \tag{2.1}$$

$$\mathbf{B} = -\mu_0 \lambda_L^2 \ \mathrm{curl}(\mathbf{j}_s) \tag{2.2}$$

where n_s is the number density of superconducting electrons. The Maxwell equation curl $\mathbf{H} = \mathbf{j}$, where $\mathbf{B} = \mu\mu_0\mathbf{H}$ with $\mu \approx 1$, combined with the second London equation 2.2 leads to

$$\nabla^2 \mathbf{B} = \frac{\mathbf{B}}{\lambda_L^2} \tag{2.3}$$

where the London penetration depth λ_L is given by

$$\lambda_L = \sqrt{\frac{m}{(2e)^2 \mu_0 n_s}}. \tag{2.4}$$

The Meissner phase vanishes at a critical field B_c above which the sample is nor-

mal conducting. The critical field is thermodynamically connected to the free energy difference between the normal and superconducting states:

$$f_n(B=0,T) - f_s(B=0,T) = \frac{B_c^2}{2\mu_0} \tag{2.5}$$

The following introduction to the basics of superconductivity is taken from [19, 20].

2.1.1 Ginzburg-Landau equation

Based on Landau's theory of second order phase transitions, Ginzburg and Landau expanded the free energy with respect to a complex order parameter $\psi = |\psi|e^{i\phi}$ with the local density of superconducting electrons

$$n_s = |\psi(x)|^2 \tag{2.6}$$

The free energy is then given by

$$f = f_0 + \alpha|\psi|^2 + \frac{\beta}{2}|\psi|^4 + \frac{1}{2m}|(-i\hbar\nabla + 2e\mathbf{A})\,\psi|^2 + \frac{1}{2\mu_0}\mathbf{B}^2 \tag{2.7}$$

with $\alpha(t) = \alpha'(t-1)$ around T_c where $t = T/T_c$ and with the positive constants α' and β. If α is positive, the minimum free energy occurs at $|\psi|^2$, which corresponds to the normal state. For $\alpha < 0$ the minimum occurs at

$$|\psi|^2 = |\psi_\infty| \equiv -\frac{\alpha}{\beta} \tag{2.8}$$

where ψ_∞ is used because ψ reaches this value infinitely deep in the interior of the superconductor, where all surface currents and fields are screened. The Ginzburg-Landau differential equations are found by minimizing the free energy with respect to ψ and $\mathbf{A}$:

$$\alpha\psi + \beta|\psi|^2\psi + \frac{1}{2m}\left(-i\hbar\nabla + 2e\mathbf{A}\right)^2\psi = 0 \tag{2.9}$$

$$\mathbf{j}_\mathrm{s} = \frac{ie\hbar}{m}(\psi^*\nabla\psi - \psi\nabla\psi^*) - \frac{4e^2}{m}|\psi|^2\mathbf{A} \tag{2.10}$$

Inserting $|\psi|^2 = -\alpha/\beta$ in Eq. 2.10, the second London equation 2.2 is obtained and the Ginzburg-Landau expression for the penetration depth λ is

$$\lambda_L = \sqrt{\frac{m\beta}{4\mu_0 e^2|\alpha|}} \tag{2.11}$$

The Ginzburg-Landau coherence length ξ_{GL} is introduced as a the characteristic dis-

tance over which spatial changes in ψ occur:

$$\xi_{GL} = \frac{\hbar}{\sqrt{2m|\alpha|}} \tag{2.12}$$

From the first Ginzburg-Landau equation 2.9, without a magnetic field, the spatial variation of ψ and accordingly n_s on the boundary of a superconductor is:

$$\frac{\psi(x)}{\psi_\infty} = \tanh \frac{x}{\sqrt{2}\xi_{GL}} \tag{2.13}$$

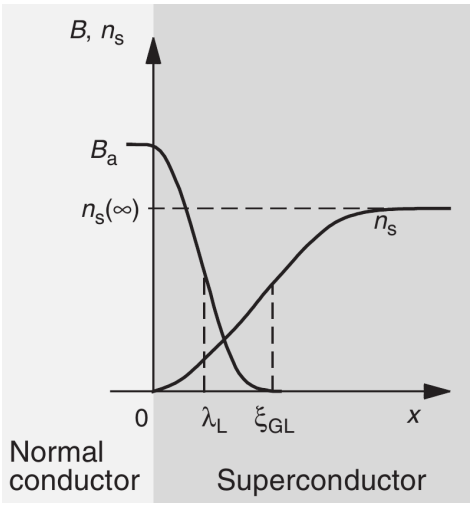

Fig. 2.1: At the boundary between a normal metal and a superconductor the magnetic field B and the superconducting wave function spatially varies according to the Ginzburg-Landau theory (from [20]).

It is useful to introduce the dimensionless Ginzburg-Landau parameter $\kappa = \lambda/\xi_{GL}$. For $\kappa < 1/\sqrt{2}$ the material is a type I superconductor, for $\kappa > 1/\sqrt{2}$ it is a type II superconductor. In a type I superconductor no vortices can exist in the interior, the superconducting state is a Meissner state and the sample becomes normal conducting above B_c (Eq. 2.5). In a type II there are two critical fields. Above B_{c1} superconducting vortices penetrate the Meissner phase with a flux quantum $\phi_0 = h/2e$. The so called Shubnikov phase holds up to a critical field B_{c2} which is determined by the maximum density of vortices. At B_{c2} the area per flux quantum is $2\pi\xi_{GL}^2$, therefore the critical field above which superconductivity vanishes is

$$B_{c2} = \frac{\phi_0}{2\pi\xi_{GL}^2} \tag{2.14}$$

2.1.2 Bardeen-Cooper-Schrieffer theory

The superconducting state could be explained microscopically for the first time by Bardeen Cooper and Schrieffer [21] in 1957. Here just the basic concepts and the main results are given. A weak attractive interaction between electrons mediated by electron-phonon interaction leads to the formation of bound pairs of electrons. Within these pairs the electrons occupy states with equal but opposite momentum and spin. These bosonic pairs are called Cooper pairs and they condense to a superconducting ground state in which the pair energy is lowered by the energy gap Δ compared to the Fermi energy of the normal Fermi sea without electron-phonon interaction. The superconducting ground state quantum-mechanically forms a macroscopic wave function. From this quantum-mechanical interpretation of superconductivity many features of superconducting materials could be explained and also predicted. The Cooper pair size ξ_0 could be estimated to be

$$\xi_0 = \frac{\hbar v_F}{\pi |\Delta|} \tag{2.15}$$

with v_F the Fermi velocity. The minimum energy required to break a pair, creating two quasiparticle excitations is for $T \ll T_c$

$$E_g(T=0) = 2\Delta(T=0) = 3.528 k_B T_c \tag{2.16}$$

with $E_g = 2\Delta$ the energy gap which tends to zero for $T \to T_c$:

$$\frac{\Delta(T)}{\Delta(0)} \approx 1.74 \left(1 - \frac{T}{T_c}\right)^{1/2} \qquad T \approx T_c \tag{2.17}$$

From the BCS theory the behaviour of the penetration depth λ can be deduced for a number of important cases, such as thin films. In parallel magnetic field the supercurrent response of a nonlocal (BCS) thin-film ($d \ll \lambda$) superconductor is equivalent to that of a local (London) superconductor with an effective penetration depth

$$\lambda_{eff} = \lambda_L (\xi_0'/d)^{1/2} \qquad (\text{for} \quad d \ll \xi') \tag{2.18}$$

with film thickness d, the London penetration depth (Eq. 2.4) and ξ_0' is the modified Pippard coherene length. When a magnetic field is applied perpendicular to a thin film the penetration depth is modified to

$$\lambda_\perp = \lambda_{eff}^2 / d \tag{2.19}$$

which is also known as the Pearl penetration depth. Werthamer, Helfand, and Hohenberg [22] evaluated the temperature dependence of the upper critical field H_{c2} of type II superconductors based on a BCS model where Pauli spin paramagnetism and

spin-orbit impuritiy scattering is included.

$$\begin{aligned}\ln\frac{1}{t} = &\left(\frac{1}{2}+\frac{i\lambda_{SO}}{4\gamma_{WHH}}\right)\cdot\psi\left(\frac{1}{2}+\frac{\bar{h}+\frac{1}{2}\lambda_{SO}+i\gamma_{WHH}}{2t}\right)\\ &+\left(\frac{1}{2}-\frac{i\lambda_{SO}}{4\gamma_{WHH}}\right)\cdot\psi\left(\frac{1}{2}+\frac{\bar{h}+\frac{1}{2}\lambda_{SO}-i\gamma_{WHH}}{2t}\right)-\psi\left(\frac{1}{2}\right)\end{aligned} \tag{2.20}$$

where ψ is the digamma function, $\gamma_{WHH} \equiv [(\alpha\bar{h})^2 - (\frac{1}{2}\lambda_{SO})^2]^{1/2}$, $t = T/T_c$, $\bar{h} = 2eH(v_F^2\tau/6\pi T_c)$, $\alpha = 3/2mv_F^2\tau$ and $\lambda_{SO} = 1/3\pi T_c\tau_2$. With $\tau^{-1} = \tau_1^{-1}+\tau_2^{-1}$ and (τ_1, τ_2) are the scattering times for spin-independent and spin-orbit scattering respectively. H is the magnetic field and v_F is the Fermi velocity. α includes the effect of Pauli spin paramagnetism and λ_{SO} includes spin orbit effects. T_c is the highest temperature for which the Usadel-equations [23] have non-trivial solutions. The diffusion-like Usadel-equations are only valid for a superconductor of type II in the dirty limit.

With Eq. 2.20 it is possible to calculate $t = T/T_c$ at a known magnetic field H. Since this field H is the critical field H_{c2} at the given t, $H_{c2}(T)$ can be obtained. For our TiN thin films $H_{c2}(T)$ can be approximated within 1% by (Tatyana Baturina, personal communication):

$$H_{c2}(T) = H_{c2}(0)\cdot\cos\left(\frac{\pi}{2}\cdot\left(\frac{T}{T_c}\right)^{0.87}\right) \tag{2.21}$$

2.1.3 Josephson effect

A weak link connecting two superconducting electrodes is called a Josephson junction. The weak link can be a thin insulating layer, a thin normal metal layer or a short narrow constriction of in otherwise continuous superconducting material. In such geometries the ac- and dc-Josephson effects occur. In a Josephson junction a supercurrent I_s flows which is driven by the phase difference $\Delta\phi$ of the Ginzburg-Landau wave function in the two superconducting electrodes:

$$I_s = I_c\sin\Delta\phi \tag{2.22}$$

with I_c the Josephson critical current, the maximum supercurrent through the junction. Eq. 2.22 is the first Josephson equation. For an externally applied voltage V across the junction the ac-Josephson effect with an alternating current of amplitude I_c and frequency $\nu = 2eV/h$ across the junction appears. The ac-Josephson effect is desribed by the second Josephson equation

$$d(\Delta\phi)/dt = 2eV/\hbar. \tag{2.23}$$

2.2 Superconductivity in thin films

2.2.1 Berezinskii-Kosterlitz-Thouless transition

In two dimensional superconducting films ($d \ll \xi$) even at zero magnetic field vortices spontaneously can be generated below the mean-field critical temperature T_{c0}. The energy cost of the creation of a single pancake vortex (field axis perpendicular to the film-plane) of volume $\sim \pi\xi^2 d$ is $E_v = (H_c^2/2\mu_0)4\pi\xi^2 d \ln\kappa$. With $\xi(T) = \phi_0/2\sqrt{2}H_c(T)\lambda_{eff}(T)$ from the Ginzburg-Landau theory and with Eq. 2.19 we obtain:

$$E_v = \left(\frac{\phi_0^2}{4\pi\lambda_\perp\mu_0}\right)\ln\left(\frac{\lambda_\perp}{\xi}\right) \tag{2.24}$$

If the sample size with radius R in a simplified model is smaller than $\lambda_\perp$, the logarithm in Eq. 2.24 is substituted by $\ln(R/\xi)$. In the Berezinskii-Kosterlitz-Thouless (BKT) phase vortex-antivortex pairs with opposite circulation sense are generated by thermal activation. For an intervortex separation of $\sim R_{12}$, the creation energy of such a pair of vortices is not double the value of E_v, instead of the sample size R the length R_{12} sets the total energy of the vortex-pair:

$$E_{v-pair} = 2\cdot\left(\frac{\phi_0^2}{4\pi\lambda_\perp\mu_0}\right)\ln\left(\frac{R_{12}}{\xi}\right) \tag{2.25}$$

The energy hence increases with increasing distance of the vortices with $\sim \ln(R_{12}/\xi)$ which results in an attractive force between the vortex-antivortex pair. For $R_{12} \sim \xi$ the vortex cores are touching and the vortices annihilate each other. In thermal equilibrium for temperatures $T_{v-BKT} < T < T_{c0}$ the annihilation and creation processes occur with the same frequency. Below $T = T_{v-BKT}$, the vortex BKT transition temperature, no thermally activated unbinding of vortex-antivortex pairs appears. T_{v-BKT} is determined by the balance of entropy gain that results from the two rather independently moving vortices for $T > T_{v-BKT}$ compared to pair-like bound vortices for $T < T_{v-BKT}$ and the energy cost for creation of the vortex pair:

$$k_B T_{v-BKT} \approx \frac{\phi_0^2}{8\pi\lambda_\perp\mu_0} \tag{2.26}$$

A current flow through the sample in the BKT phase leads to flux-flow resistance due to the movement of the unbound vortex-antivortex pairs, followed by a motion of the vortices in opposite directions until they disappear at opposite edges of the sample. According to Halperin and Nelson the temperature dependence of the resistance in the BKT regime reads [24, 25]

$$R(T) \propto \exp\left(-\frac{b}{(T/T_{v-BKT}-1)^{-1/2}}\right) \tag{2.27}$$

where b is a constant of the order of unity. In the vortex BKT regime the resistance is linear as there is an equilibrium population of unbound vortices. Below T_{v-BKT} there are no free vortices for zero driving current. The number of vortices that are created by a finite current I increases as I^2 just below T_{v-BKT}. Therefore there is no linear resistance below T_{v-BKT}, the voltage V rises with a powerlaw $V \sim I^{\alpha(T)}$ with $\alpha(T_{v-BKT}) \approx 3$ at T_{v-BKT}. Beasley, Mooij and Orlando found a relationship between the BKT transition temperature and the sheet resistance in the normal state R_N [26]:

$$\frac{T_{v-BKT}}{T_c} \cdot \left(f\left(\frac{T_{v-BKT}}{T_c}\right)\right)^{-1} = 0.561 \frac{\pi^3}{8}\left(\frac{\hbar}{e^2}\right)\frac{1}{R_N} \tag{2.28}$$

$$\text{where} \quad f\left(\frac{T}{T_c}\right) = \frac{\Delta(T)}{\Delta(0)} \tanh\left[\frac{\beta\Delta(T)T_c}{2\Delta(0)T}\right] \tag{2.29}$$

However it is not always clear how to determine the resistance R_N. A plot of R_N vs. T_{v-BKT}/T_c that is calculated with Eqs. 2.28 2.29 is shown in Fig. 9.3b. In [27] the sheet resistance at room temperature and the maximum resistance in the temperature dependence of the resistance at zero magnetic field are discussed to be taken for R_N. In Ref. [28] the extrapolated zero-temperature value of the normal state resistance R_N is argued to be a useful approximation for R_N in Eq. 2.28. The extrapolated value of R_N was obtained under usage of the phenomenological description of $\sigma \propto T^{1/4}$ for $T \gg T_c$ [29].

2.2.2 Superconducting fluctuations

In the BCS model right at the mean field critical temperature T_{c0} a finite amplitude of the order parameter forms. In contrast, the resistivity of thin films does not vanish until it is cooled below the vortex BKT transition temperature T_{v-BKT} which can be estimated according to Eq. 2.26 (see chapter 2.2.1). For temperatures exceeding $T_c(B)$ with $B > B_{c2}(T)$, superconducting fluctuations contribute to the conductivity of 2D films.

Additionally, above T_c, electron localization effects have to be considered, such as weak localization and disorder enhanced interelectron interference due to the Aronov-Altshuler effect [5]. The weak localization effect concerns the diffusive motion of single electrons. An electron that is at time $t = 0$ at the place $r = 0$ takes part in the diffusion motion with Fermi velocity v_F and mean free path $l = v_F\tau$, where $1/\tau$ is the frequency of the elastic scattering events. The probability for the electron to be found at a position $\mathbf{r}$ after a time $t \gg \tau$ is given by the classical expression

$$p(\mathbf{r},t) = (4\pi Dt)^{-d/2} e^{-r^2/4Dt}, \quad r^2 = \sum_1^d x_i^2, \quad \int p(\mathbf{r},t)d\mathbf{r} = 1 \tag{2.30}$$

where d is the dimension of the system and $D = lv_F/d$ is the diffusion coefficient. The classical return probability for an electron in a 2D system to come back to the place $r = 0$, within the characteristic time τ_ϕ for loosing the phase memory due to inelastic

scattering, is $p(0,\tau_\phi) = (4\pi D\tau_\phi)^{-1}$. For $t < \tau_\phi$ an electron that passes the same place twice, interferes with itself. Since this interference is of a quantum mechanical nature, the probability for finding the electron at this place is double of that for a classical diffusive description. As a result of the interference, the conductivity is lowered. With growing disorder the mean free path $l = v_F\tau_\phi$ shrinks due to a smaller mean time τ between the elastic scattering events. In consequence the diffusion coefficient decreases and with that the classical return probability $p(0,\tau_\phi)$ increases. The enhanced $p(0,\tau_\phi)$ due to increasing disorder leads to a higher correction to conductivity originated from weak localization.

The Aronov-Altshuler effect in contrast, results from the interelectron interference of two different electrons that meet twice. The requirement for the constructive interference of two electrons is the same phase of the wave functions for both electrons at a time $t = 0$. The characteristic time τ_{ee} within phase coherence of the two electrons which have the same phases at $t = 0$ is conserved, depends on the energy difference $\Delta\epsilon$ of the two electrons. Only electrons with energies ϵ around the fermi level E_F take part in the diffusion motion with

$$E_F - k_BT \lesssim \epsilon \lesssim E_F + k_BT. \tag{2.31}$$

Under this condition the characteristic dephasing time is $\tau_{ee} \simeq \hbar/k_BT$. As a consequence the interelectron interference effect becomes stronger at lower temperatures. The size of the interference region can be estimated to

$$L_{ee} \simeq l\left(\frac{\tau_{ee}}{\tau}\right)^{1/2} \simeq v_F\left(\frac{\hbar\tau}{T}\right)^{1/2} \simeq \sqrt{\frac{\hbar D}{T}}. \tag{2.32}$$

The collision frequency of two electrons with diffusive motion is described as

$$\frac{\hbar}{\tau_e} \sim \frac{1}{g_d L_{ee}^d} \tag{2.33}$$

where $g_d \sim E_F^{d/2-1}m^{1/2}$ is the density of states at the fermi level, d is the dimension of the system and m is the electron mass. Since for a disordered system $\tau_e \gg \tau$, the collision of electrons does not directly make a noticeable contribution to conductivity. However, the interelectron interaction in the diffusion channel reduces the density of states for ϵ around the fermi level to

$$\Delta g(T = 0,\epsilon) \sim (\hbar D)^{-1} \cdot \ln\left(\frac{\epsilon\tau}{\hbar}\right) \tag{2.34}$$

for a two-dimensional system at zero temperature T. With increasing disorder, τ and D decrease and in consequence the reduction of the density of states Δg is stronger.

For both weak localization and interelectron interference effects, the temperature

dependence of the correction to conductivity is logarithmic with

$$\Delta G^{AA} = \Delta G^{WL} + \Delta G^{ID} = G_{00}(\alpha p + B) \ln\left(\frac{k_B T\tau}{\hbar}\right) = G_{00} A \ln\left(\frac{k_B T\tau}{\hbar}\right) \quad (2.35)$$

where $A = \alpha p + B$ and $G_{00} = e^2/(2\pi^2\hbar) \simeq (81\,\mathrm{k\Omega})^{-1}$. The term with αp originates from the weak localization effect and the term with B from the interelectron interaction (see Eq. 2.41). B is of order unity. The parameter p is given by $1/\tau_\phi \propto T^p$ and the parameter α is given by $\alpha = 1, -1/2, 0$ for the potential, spin-orbit and spin scattering, respectively.

term	expression
WL + AA	$\Delta G^{AA} = G_{00} A \ln\left(\frac{k_B T\tau}{\hbar}\right)$
AL	$\Delta G^{AL} = \frac{e^2}{16\hbar}\frac{T}{T - T_c}$
DOS	$\Delta G^{DOS} = G_{00} \ln\left(\frac{\ln(T_c/T)}{\ln(k_B T_c \tau/\hbar)}\right)$
MT	$\Delta G^{MT} = G_{00}\beta(T) \ln\left(\frac{T\tau_\phi}{\hbar}\right)$
DCR	$\Delta G^{DCR} = \frac{4}{3} G_{00}\left(\ln\ln\frac{1}{T_c\tau} - \ln\ln\frac{1}{T_c}\right)$

Table 2.1: Corrections to conductivity for the diffusion channel (WL + AA) and for the Cooper channel. For the Cooper channel the Aslamazov-Larkin term (AL), the correction to the conductivity due to the depression of the density of states (DOS), the Maki-Thompson contribution (MT) and the correction to the conductivity originated from the renormalization of the single particle diffusion coefficient (DCR) are listed. The calculated temperature dependences for the seperate corrections to conductivity as well as the total conductivity, where all the corrections are summed, are shown in Fig. 2.2a. The prefactor $G_{00} = e^2/(2\pi^2\hbar) \simeq (81\,\mathrm{k\Omega})^{-1}$ is usually taken to be the maximum correction to conductivity due to fluctuations. It is connected to $k_F l = 1$ which is a lower limit (and hence an upper limit for disorder) for the applicability of perturbative corrections to conductivity.

A differentiation of weak localization and the Aronov Altshuler effect is only possible under an applied magnetic field, where the correction to conductivity due to weak localization vanishes but the Aronov Altshuler contributions are not affected.

Superconducting fluctuations arise due to the interaction of electrons with nearly opposite momenta, called Cooper channel. Terms of the following four types describe the fluctuation conductivity [27]: 1) Aslamazov-Larkin (AL) term which is connected

with the direct conductivity of the fluctuating Cooper pairs. The AL contribution to conductivity is positive; 2) Due to the AL-type of fluctuations above T_c, the number of normal electrons decreases. The density of states term (DOS) describes the decrease of the conductivity of the electrons according to the Drude expression Eq. 1.1; 3) The presence of fluctuations, the renormalization of the single-particle diffusion coefficient leads to another correction to conductivity (DCR); 4) The Maki-Thompson term (MT) is connected with coherent scattering of electrons on impurities. The resulting contribution to conductivity can either be positive or negative, depending on the conventional pair breaking parameter $\delta = \pi\hbar/(8k_BT\tau_\phi)$.

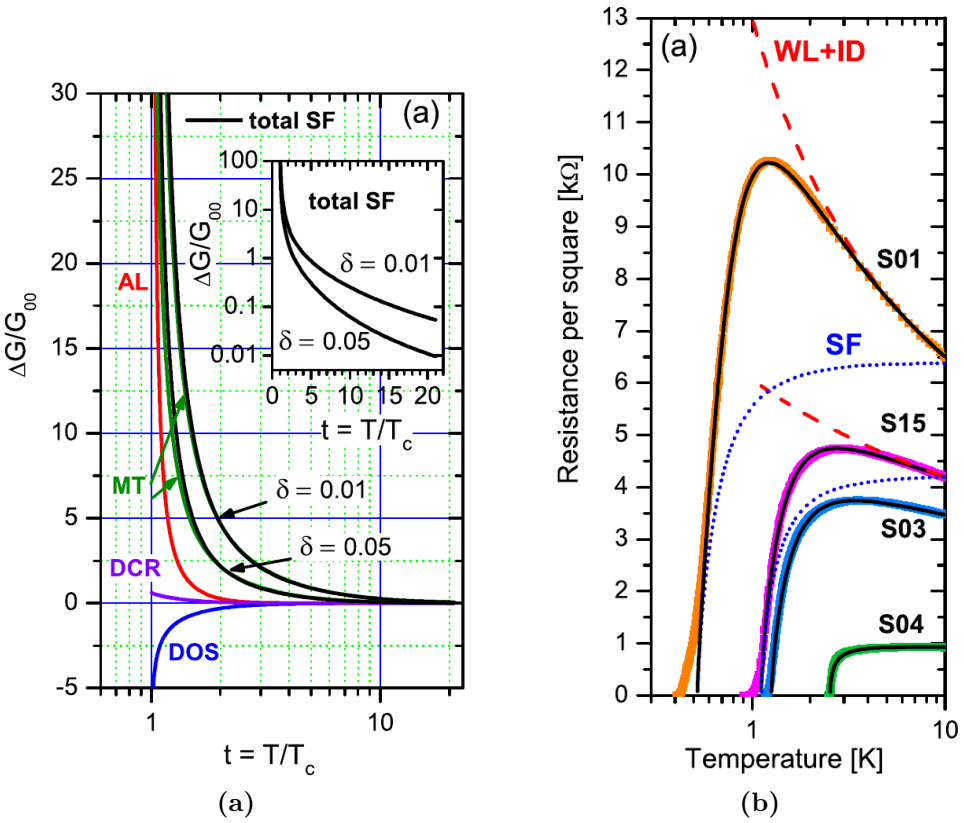

Fig. 2.2: (a) Calculated temperature dependence of superconducting fluctuation contributions to conductivity (in units of $G_{00} = e^2/(2\pi^2\hbar)$) (image from [27] with theoretical expressions taken from [30]). The derived curves for AL, DOS, and DCR are universal functions of reduced temperature $t = T/T_c$, the MT correction is presented for the convential pair breaking parameters $\delta = 0.01$ and $\delta = 0.05$. The black solid lines are the sum of all contributions to superconducting fluctuations on a logarithmic temperature scale. The inset shows the same total sum on a logarithmic conductivity scale. (b) Measured resistance per square vs. temperature for four differently disordered TiN film samples. Solid black lines correspond to fits accounting for all the quantum contributions. The red dashed lines, marked as WL+ID, are the separate contributions of the sum of weak localization and interparticle interaction to the resistances of the samples S01 and S15. The blue dotted lines show the sum of corrections due to superconducting fluctuations [27]).

In table 2.1 the contributions to conductivity from the diffusion channel as well as from the Cooper channel are listed. The Larkin factor $\beta(T)$ has the form [31]

$$\beta(T) = \frac{\pi^2}{4} \sum_m (-1)^m \Gamma_{MT}(|m|) - \sum_{m \geq 0} \Gamma''_{MT}(2m+1) \tag{2.36}$$

where m is an integer $m = 0, \pm 1, \pm 2, ...$, and

$$\Gamma_{MT}(|m|) = \left[\ln \frac{T}{T_c} + \psi\left(\frac{1}{2} + \frac{|m|}{2}\right) - \psi\left(\frac{1}{2}\right) - \psi'\left(\frac{1}{2} + \frac{|m|}{2}\right) \frac{1}{4\pi k_B T \tau_\phi} \right]^{-1} \tag{2.37}$$

with the digamma function ψ. For low temperatures $\ln(T/T_c) \ll 1$ the expression for $\beta(T, \tau_\phi)$ reduces to

$$\beta(T, \tau_\phi) = \frac{\pi^2}{4} \frac{1}{\ln(T/T_c) - \delta} \tag{2.38}$$

where $\delta = \pi/(8 k_B T \tau_\phi$ is the Maki-Thompson pair breaking parameter.

In Fig. 2.2a the different contributions to conductivity for the four latter fluctuation types are calculated for given parameters. In Ref. [27] all the quantum contributions to conductivity mentioned in table 2.1 were taken into account for an anaysis of superconducting fluctuations at zero magnetic field for a number of differently disordered TiN films. The theoretical expressions taken from Ref. [30] served as a comprehensive formula. The fit to measured $R(T)$ data is shown in Fig. 2.2b for the differently disordered TiN films.

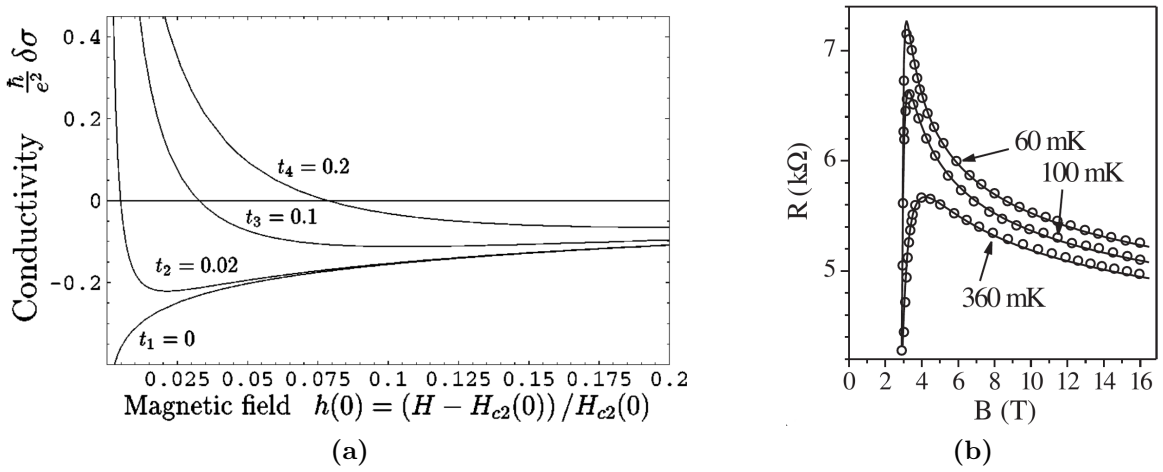

Fig. 2.3: (a) Fluctuating conductivity according to Eq. 2.39 as a function of magnetic field is plotted for four different temperatures (from [16]). Resistance per square (open symbols) vs. perpendicular magnetic field for a TiN sample deeply in the superconducting regime at various temperatures. Solid lines are plotted functions calculated on basis of Eq. 2.40 with $B_{c2}(0) = 2.8\,\mathrm{T}$ and $T_c = 2\,\mathrm{K}$ (from [32]).

We now turn to the superconducting fluctuations at low temperatures $T < T_c$ above

the critical magnetic field B_{c2}. Galitski and Larkin evaluated the total correction to conductivity $\delta\sigma$ for superconducting fluctuations above B_{c2} for $T \ll T_{c0}$ [16]. T_{c0} is the temperature at which an equilibrium concentration of Cooper pairs appears (the BCS transition temperature). Aslamazov-Larkin, Maki-Thompson and density of states contributions for the dirty case with $T_{c0}\tau \ll 1$ (where τ ist the scattering time) are concerned in the first (one-loop) approximation:

$$\Delta G^{SF} = \frac{2e^2}{3\pi^2\hbar}\left[-\ln\frac{r}{h} - \frac{3}{2r} + \psi(r) + 4[r\psi'(r) - 1]\right] \tag{2.39}$$

where $r = (1/2\gamma)h/t$, $\gamma = 1.781$ is Euler's constant, $h = (B - B_{c2}(T))/B_{c2}(0)$ and $t = T/T_{c0}$. $B_{c2}(T) = B_{c2}(0) \cdot \cos(\pi(T/T_{c0})^{0.87}/2)$ is an approximation of the Werthamer-Helfand $B_{c2}(T)$ [22] for TiN (Eq. 2.20). ψ is the digamma function with $\psi(x) = \frac{d}{dx}\ln(\Gamma(x)) = \frac{\Gamma'(x)}{\Gamma(x)}$, where Γ is the gamma function. ψ' is the trigamma function with $\psi'(z) = \frac{d^2}{dz^2}\ln(\Gamma(z))$. The total conductivity is calculated with

$$G(T, B) = G_0 + \Delta G^{ID} + \Delta G^{SF}. \tag{2.40}$$

with G_0 the normal state conductivity. ΔG^{ID} the correction to conductivity due to Aronov Altshuler type of interelectron interference [5]:

$$\Delta G^{ID} = G_{00} B \ln\left(\frac{k_B T\tau}{\hbar}\right) \tag{2.41}$$

where B is a constant which depends on the Coulomb screening and it remains of the order of unity. In Fig. 2.3a the calculated magnetic field dependence of $\delta\sigma$ for several values of t is depicted.

In Ref. [32] the magnetoresistance isotherms of TiN samples deeply in the superconducting regime could be well described by the theory of superconducting fluctuations according to Eq. 2.40 (see Fig. 2.3b).

In subsequent works the result for the correction to conductivity of Eq. 2.39 was reproduced by Tikhonov, Schwiete and Finkelstein [33], based on the Usadel equation in the real-time formulation, and by Glatz, Varlamov and Vinokur [30], based on the perturbative first order fluctuation theory. Burmistrov, Gornyi and Mirlin [34] evaluated a magnetoresistance behaviour that resembles Eq. 2.39. Their analysis is based on the renormalization group for a nonlinear sigma model. This approach is not restricted to the case of perturbative superconducting fluctuations that are small compared to the Drude conductivity. Though the latter three works reproduce the magnetoresistance above B_{c2} for low temperatures according to Eq. 2.39, the contributions to conductivity due to fluctuations in Ref. [34] differs from that in Refs. [33, 30]. Tarasinski and Schwiete [35] generalized the results of Ref. [33] under usage of a quasiclassical kinetic equation approach. They obtained an expression for the correction to conductivity above B_{c2} similar to Eq. 2.39. Summarizing, Eq. 2.39 was reproduced already several times [33, 30, 34, 35] with just slight modifications.

2.2.3 Vortex-based resistive mechanisms

Under an applied magnetic field which is perpendicular to the plane of the film, a superconducting disordered thin film with $\kappa < 1/\sqrt{2}$ is penetrated by vortices with a distance $a_0 = (\phi_0/B)^{1/2}$. For an applied current through the superconducting film, the vortices move according to the Lorentz force, perpendicular to the current to the edges of the film. This movement induces an electric field which is parallel to the applied current and therefore acts like a resistive voltage. Pinning of the vortices to certain sites on the superconducting film can slow down the motion of the vortices. For strong pinning any substantial vortex motion is prevented and a supercurrent can flow up to a certain critical current, above which the Lorentz force overcomes the pinning forces. For less strong pinning a variety of resistive mechanims due to vortex motion can be observed.

In a very simplified model Bardeen and Stephen estimated the *flux-flow resistance*, phenomenologically assuming a viscous drag coefficient η. The viscous force on a vortex with velocity $\mathbf{v}_L$ is then $\eta\mathbf{v}_L$. They found that η is related to the upper critical field H_{c2} and the normal state resistivity ρ_n in the following way:

$$\eta \approx \frac{\phi_0 H_{c2}}{\rho_n c^2} \tag{2.42}$$

where c is the velocity of light in vaccum. For the flux-flow resistance ρ_f they found

$$\frac{\rho_f}{\rho_n} \approx \frac{B}{H_{c2}} \tag{2.43}$$

Experimental data follows this linear dependence quite well, at least for small magnetic fields and low temperatures. Kim, Hempstead and Strnad [36] refined the theory of flux-flow resistance to explain the deviations from the linear dependence of Eq. 2.43 (see Fig. 2.4)

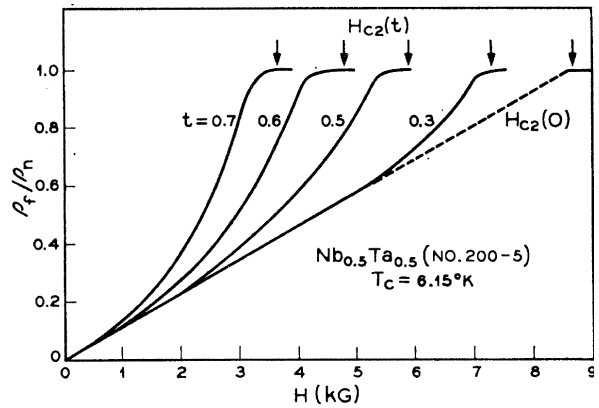

Fig. 2.4: ρ_f/ρ_n of a Nb-Ta specimen is shown as a function of magnetic field H at given values of $t = T/T_c$. $H_{c2}(T)$ is indicated by vertical arrows. The dashed line corresponds to the Bardeen-Stephen flux-flow resistance (Eq. 2.43). For low temperatures and low magnetic fields the linear dependence of Eq. 2.43 resembles the measured data. (from [36]).

Inui, Littlewood and Coppersmith [37] used a model of *single vortex depinning* to explain the experimentally observed temperature activated motion of vortices from homogeneous and densely distributed pinning centers. They treat the vortices independent of each other, with interaction included in the single-vortex dynamics. They justify this approach with the unusual softness of the flux lattice for localized deformations, which occurs for large screening lengths and anisotropy. Inui et al. explicitly do not consider the possibility of collective pinning. For low temperatures they derived the barrier height for the temperature activated motion of vortices for two different types of field dependence:

$$V_{barrier} \approx \begin{cases} V_0 + \sigma \ln(H_0/H), & H \ll H_1, \quad (2.44) \\ V_0 - \pi^2\gamma/K^2, & H \gg H_1 \quad (2.45) \end{cases}$$

With a crossover field H_1. H_0 and σ are some constants. $\gamma \approx d\phi_0 H/128\pi^3\lambda^2$ where d is the coherence length perpendicular to the film. The logarithmic dependence in Eq. 2.44 results in a powerlaw of the magnetoresistance for a Arrhenius-like temperature activated resistance. This $R \propto B^{T/T_0}$ behaviour has been seen many times [38, 39, 40, 41, 42, 43, 44, 45].

In [39, 40] a different explanation by the *collective creep model* is given for the logarithmic dependence of the activation energy from the magnetic field. In this model the motion of dislocations in a 2D flux line lattice of pinned vortices determines the temperature and field dependence of the resistance. In [39, 40] the authors refer to [46]. According to this paper, the size of a dislocation is $R_0 \simeq a_0^2/\xi$ with the intervortex spacing $a_0 = \phi_0/B$ and the coherence lenght ξ. Over this distance R_0 around the dislocations, the vortices of the flux line lattice are displaced by more than ξ and the vortices are shifted to some other minima of the random pinning potential. Outside this circle with radius R_0 the vortices are just slightly displaced within the same potential minima. The interaction of two dislocations with distance ρ is also logarithmic:

$$\epsilon_d(\rho) = \epsilon_d \ln \frac{\rho}{a_0} \qquad \text{with} \quad \epsilon_d = \frac{\phi_0^2 d}{64\pi^3\lambda^2} \tag{2.46}$$

The characteristic scale R_c of flux line lattice regions, which are pinned independently from each other, is given by:

$$R_c = \frac{\epsilon_0 \xi^2}{U_p a_0} \tag{2.47}$$

where $\epsilon_0 = d\phi_0^2/16\pi^2\lambda^2$ and U_p is the characteristic energy of vortex interaction with disorder also called pinning energy. The displacements of vortices with a distance bigger than $R_1 \simeq R_0 + R_c$ decrease exponentially with increasing distance, so the logarithmic interaction between two dislocations is cut off at R_1 and the energy of one dislocation becomes finite:

$$\tilde{\epsilon}_d \simeq \frac{\epsilon_d}{2} \ln \frac{R_1}{a_0} = \frac{\epsilon_d}{2} \ln \left(\frac{R_c}{a_0} + \frac{a_0}{\xi} \right) \tag{2.48}$$

The authors in [39, 40] apply this model to samples with high disorder where they expect a very small $R_c \approx (1-2) \cdot a_0$. For such a small R_c, which is much smaller than the size of a dislocation R_0, vortices outside of a radius R_0 from the dislocation stay in the same minima of the disorder potential. Thus, beyond the the size of the dislocation R_0, the intrinsic disorder dominates the configuration of the flux lines. The longe-range logarithmic interaction between dislocations is cut off at a distance of R_0 from the center of each dislocation. For $R_c/a_0 < a_0/\xi$ (collective pinning) the energy to create a single dislocation $\tilde{\epsilon}_d$ in Eq. 2.48 then takes the form

$$\tilde{\epsilon}_d \simeq \frac{\epsilon_d}{2} \ln \frac{R_0}{a_0} = \frac{\epsilon_d}{2} \ln \frac{a_0}{\xi} = \frac{\epsilon_d}{4} \ln \frac{B_{c2}}{B}. \tag{2.49}$$

In the here described collective pinning regime, the pinning barriers that must be overcome to move free dislocations $U_p(a_0/\xi)^{1/2} \ll \epsilon_d$ is much less than the free energy barrier to create the dislocations. The activation energy is then determined by the energy barrier $\tilde{\epsilon}_d$. When we put Eq. 2.49 into an Arrhenius law, a powerlaw in the $R(B)$ dependence appears:

$$R(T,B) = R_0 \left(\frac{B}{B_{c2}} \right)^{T_0/T} \tag{2.50}$$

with some R_0 and $T_0 = \epsilon_d/4$.
For an extensive review about vortices in high-temperature superconductors as well as 2D films, see [47].

2.2.4 Phase slip centers and heating in superconducting thin films

In 1974 Scocpol, Beasley and Tinkham succeded with an explanation of the low-bias [48] as well as the high-bias [49] behaviour of IV characteristics of superconducting thin-film microbridges. When the bias current applied to a long superconducting filament is increased above a critical current I_c, the voltage increases not continuously but in a series of quite regular steps (see Fig. 2.5). This low-bias behaviour is interpreted by the model of phase-slip centers, called SBT model after the autors of Ref. [48]. For each voltage step in the IV characteristics an additial resistive center appears. These centers are called phase-slip centers (PSC). A superconducting microbridge is typically not perfectly homogeneous, which implies a spatial variation of I_c. When the minimum critical current I_c is exceeded, the superconducting order parameter collapses and the entire current must be carried as a normal current. This appearence of resistivity slows down the current flow below I_c and allows superconductivity to reappear. The phase difference slips in the PSC at each cycle, when the order parameter goes to zero, by 2π. The resulting current through the filament is an ac-supercurrent with an time average $\bar{I}_s = \beta I_c$ and $\beta \sim 1/2$. The rest of the applied current has to be carried as normal current which results in a voltage difference across the PSC:

$$V = \frac{2\Lambda_{Q^*}\rho}{A}(I - \beta I_c) \tag{2.51}$$

with $\beta \sim 1/2$, the charge relaxation distance Λ_{Q^*}, ρ the normal state resistivity and A the cross-sectional area of the filament.

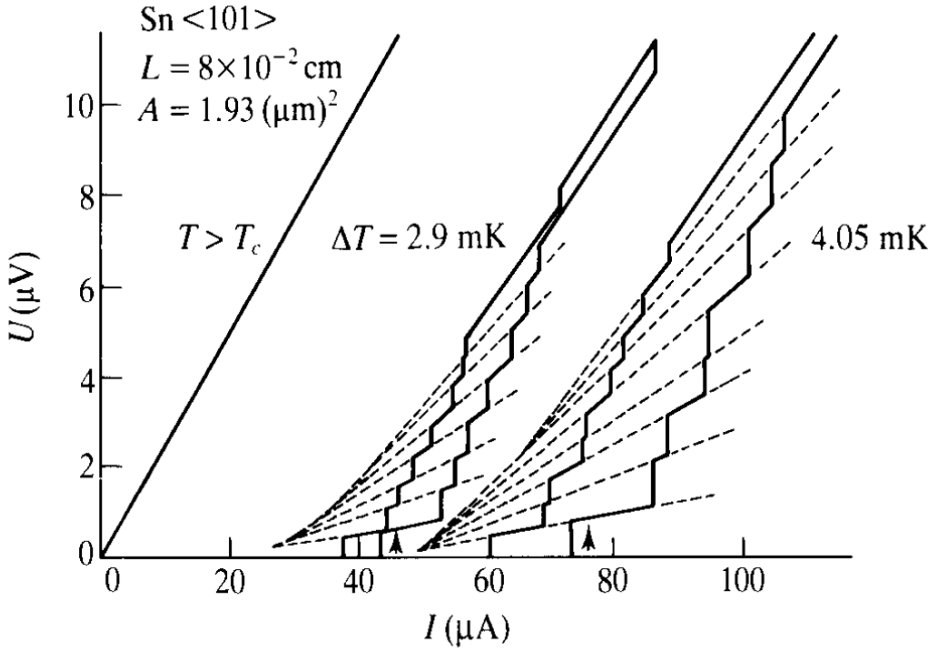

Fig. 2.5: Current-voltage characteristics for tin whisker crystals. Regular step structures are due to successive establishment of phase-slip centers. $\Delta T = T_c - T$ (from [19])

In 2D films the resistive regions do not consist of phase slip centers, they consist of phase slip lines (PSL), where vortices flow in so called vortex rivers traversing the microbridge vertical to the applied current [50, 51, 52]. The IV characteristics for 2D films behave like for PSCs.

As each PSC makes the filament more resistive, for higher bias-currents dissipation heats up the sample significantly. In Ref. [49] a simple model for self-heating in superconducting microbridges is presented. Two ways of heat conduction from disipative regions in the microbridge are concerned: Thermal heat conduction within the film to the leads which are at a bath-temperature T_b and surface heat transfer from the film to the substrate in which the phonons have a temperature of T_b, too. Obviously, due to the longest possible distance to the leads and the most inefficient heat transfer to those, the normal region ("hotspot") starts to develop from the middle of the bridge. The model makes several drastic assumptions for simplification. The bridge has a length L, width w and thickness d with a normal region of length $2x_0$ and resistivity ρ placed in the center of the bridge. $K_{N,S}$ is the thermal conductivity in the normal-conducting and superconducting regions, respectively, and is taken to be temperature independent. α is the total heat-transfer coefficient per unit area of film for the heat-transfer between superconducting film and substrate and is taken to be temperature independent, too. The combination of heat conduction within the film to the leads and from the film to the substrate leads to a characteristic thermal healing length $\eta_{N,S}$, for

the normalconducting/superconducting regions respectively, given by

$$\eta_{N,S} = \left(\frac{K_{N,S}d}{\alpha}\right)^{\frac{1}{2}} \tag{2.52}$$

Typical thermal healing length were found to be around 5 μm.

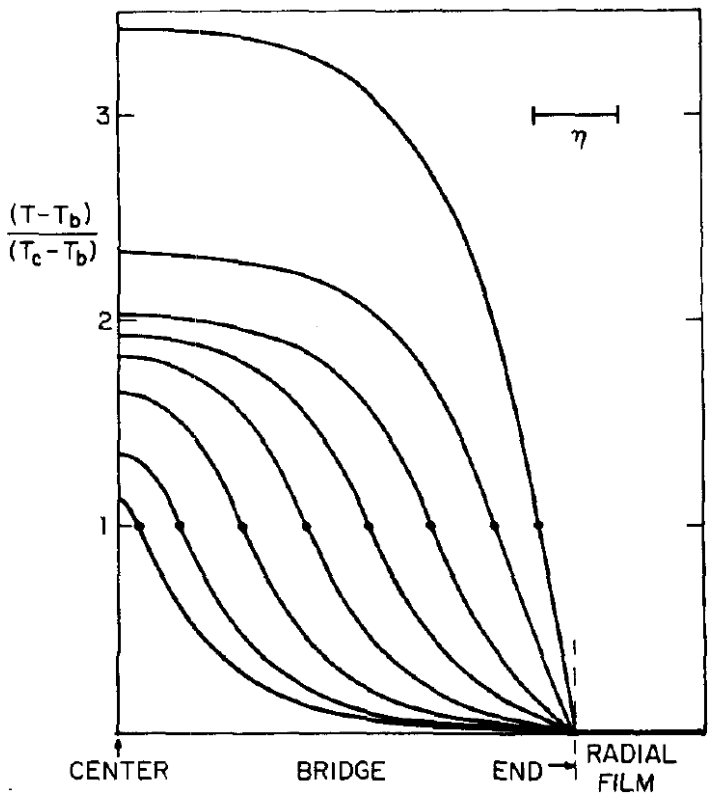

Fig. 2.6: Temperature distributions for a series of hotspot sizes in one-half of a long microbridge ($L/\eta_{N,S} = 11$) with the assumption $T = T_b$ at the end of the film. The temperature distributions in the other half are axis-symmetrically to the center the same. The dots indicate the normalconducting/superconducting interface with $T(\pm x_0) = T_c$. (from [49])

For long bridges where the length of the bridges is much longer than the healing length η, the temperature distribution $T(x)$ must satisfy the heat-flow equations

$$-K_N\frac{d^2T}{dx^2} + \frac{\alpha}{d}(T - T_b) = \left(\frac{I}{Wd}\right)^2\rho \qquad (|x| < x_0) \tag{2.53}$$

$$-K_S\frac{d^2T}{dx^2} + \frac{\alpha}{d}(T - T_b) = 0 \qquad (|x| < x_0) \tag{2.54}$$

with I the current through the bridge and $x = 0$ at the middle of the bridge. The boundary condition at the leads is $T(\pm\frac{1}{2}L) = T_b$ which includes the assumption that the leads cool the boundary to the film perfectly to the bath temperature T_b. At the normalconducting/superconducting interface x_0, T and $K(dT/dc)$ have to match with

the boundary condition $T(\pm x_0) = T_c$. The temperature distribution is then given by

$$\begin{aligned} T_n(x) =& T_c + (T_c - T_b)\left(\frac{K_S}{K_N}\right)^{1/2} \coth\left(\frac{x_0}{\eta_N}\right) \\ & \times \coth\left(\frac{\frac{1}{2}L}{\eta_S} - \frac{x_0}{\eta_S}\right)\left\{1 - \cosh\left(\frac{x}{\eta_N}\right)\left[\cosh\left(\frac{x_0}{\eta_N}\right)\right]^{-1}\right\} \qquad (|x| < x_0) \end{aligned} \tag{2.55}$$

$$T_s(x) = T_b + (T_c - T_b)\left[\sinh\left(\frac{\frac{1}{2}L}{\eta_S} - \frac{x}{\eta_S}\right)\right]\left[\sinh\left(\frac{\frac{1}{2}L}{\eta_S} - \frac{x_0}{\eta_S}\right)\right] \qquad (|x| > x_0) \tag{2.56}$$

This self-consistent solution requires a current depending on the position of the superconducting/normalconducting interface

$$I(x_0) = \left(\frac{\alpha W^2 d(T_c - T_b)}{\rho}\right)^{1/2}\left[1 + \left(\frac{K_S}{K_N}\right)^{1/2}\coth\left(\frac{x_0}{\eta_N}\right)\coth\left(\frac{\frac{1}{2}}{\eta_S} - \frac{x_0}{\eta_S}\right)\right]^{1/2} \tag{2.57}$$

and by Ohm's law the sample dimensions and the normal state resistivity give the voltage

$$V(x_0) = \frac{2x_0\rho}{Wd} \cdot I(x_0) \tag{2.58}$$

The temperature distributions for a series of hotspot sizes for a sample with $L/\eta = 11$ with the assumption $\eta_N = \eta_S$ is displayed in Fig. 2.6. IV characteristics for several values of L/η, again with $\eta_N = \eta_S$, are shown in Fig. 2.7. $R_B = \rho L/Wd$ is the normal state resistance of the bridge. The model contains a characteristic current scale

$$I_1 = \left(\frac{\alpha W^2 d(T_c - T_b)}{\rho}\right)^{1/2} \tag{2.59}$$

which is the minimum current to generate a normalconducting hot-spot beglecting the heat conduction within the film.

As can be seen in Fig. 2.7, for long microbridges with $L \gg x_0 \gg \eta$ the IV approaches a constant minimum current at $I = (1 + K_S/K_N)^{1/2} I_1$. A scheme of a long superconducting microstrip with a normalconducting hotspot placed in the center of the strip is displayed as an inset of Fig. 2.7. Experimental data of IV characteristics for a 42 μm long and 3 μm wide microstrip is shown in Fig. 2.8. The dotted line, which corresponds to the hotspot theory for long microbridges, resembles the measured data (solid and dashed lines) quite well. The theoretical parameters L, W, d, T_c and T_b are independently measured, ρ was estimated from the normal resistance of the bridge, K_N is estimated by the Wiedemann-Franz law for thermal conductivity with $K_N = \frac{1}{3}\pi^2(k_B/e)^2 T\rho^{-1}$ and K_S is taken to be a bit less than K_N. Despite the surface heat-transfer coefficient α is assumed to be constant within the hotspot theory, it is the only fitting parameter which is varied for various bath temperatures. The coefficient α in the hotspot theory can be regarded as a mean heat-transfer coefficient

across the bridge for a set bath temperature T_b. It is found that current and voltage scaling parameters are proportional to $(T_c - T_b)^{1/2}$, as expected from the theory.

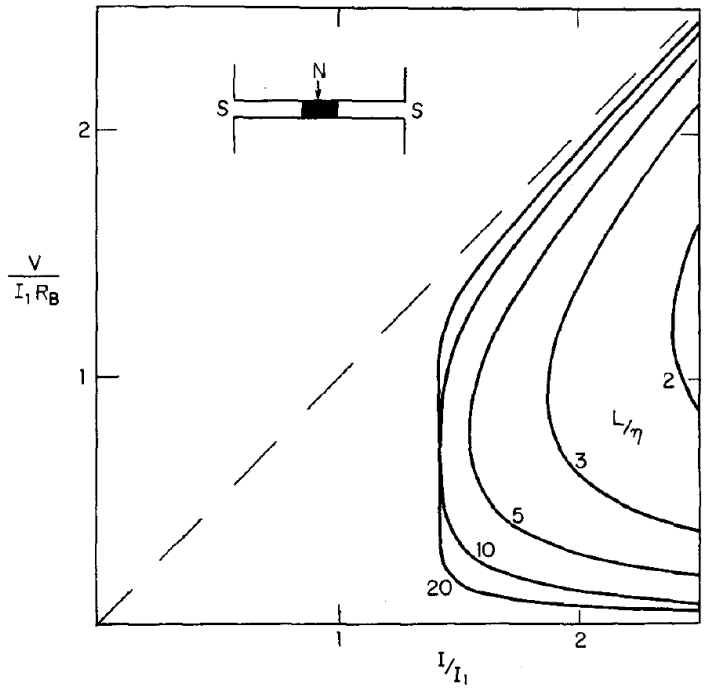

Fig. 2.7: Theoretical IV characteristics for differently long microbridges. Current and voltage are calculated with Eqs. 2.57 and 2.58 respectively. (from [49])

A guidline for fitting is given: ρ adjusts the voltage scale, α/ρ adjusts the minimum current. K_S/α and K_N/α (and consequently η_S and η_N) adjust the curvature above and below the region of minimum current, respectively. For all the measured curves in [49] α was in the range $1.0 - 3.5\,\mathrm{W/cm^2K}$ for glass and saphire substrates and samples which were in vaccum or immersed in a normal helium bath. Though α was taken to be a average coefficient across the bridge within the theory of the hotspot-model, it increases rapidly with increasing bath temperature T_b.

A close look at the low-bias regime of the IV characteristics in Fig. 2.8 reveals a behaviour that is not expected from the hotspot theory. Most distinct this feature can be seen for 3.4 K. When the current exceeds the critical current I_c, it does not switch immediately along the load line to the current predicted by the hotspot theory. Instead, circuit-controlled relaxation oscillations occur.
Vernon and Pedersen [53] observed these relaxation oscillations while investigating Josephson junctions. They gave a simple explanation considering a Josephson junction embedded in an external circuit consisting of a dc source with voltage V_0 in series with a resistor and an inductor. For a small bias-voltage ($V_0 \ll \Delta/(2e)$, with Δ the superconducting energy gap) across the junction, a supercurrent gets accelerated with a time constant that is determined by the external circuit. When the current which is defined by the series resistor exceeds I_c, the voltage across the junction jumps to $\Delta/(2e)$. The current hence is reduced below I_c according to circuit-dependent time

scales. The repetition frequency raises with increasing bias-voltage with a maximum at a voltage of $\Delta/(2e)$.
Experimentally, a switching from a plateau-shaped relaxation oscillation region to a zero current region in the IV characteristics was observed, as expected for a small Josephson junction without quasiparticle tunneling below the gap energy of the junction. For superconducting microbridges this switching occurs along the load line resistance to the current predicted by the hotspot theory. The waveform of the oscillating voltage and current due to relaxation oscillations is shown in the inset of Fig. 2.8.

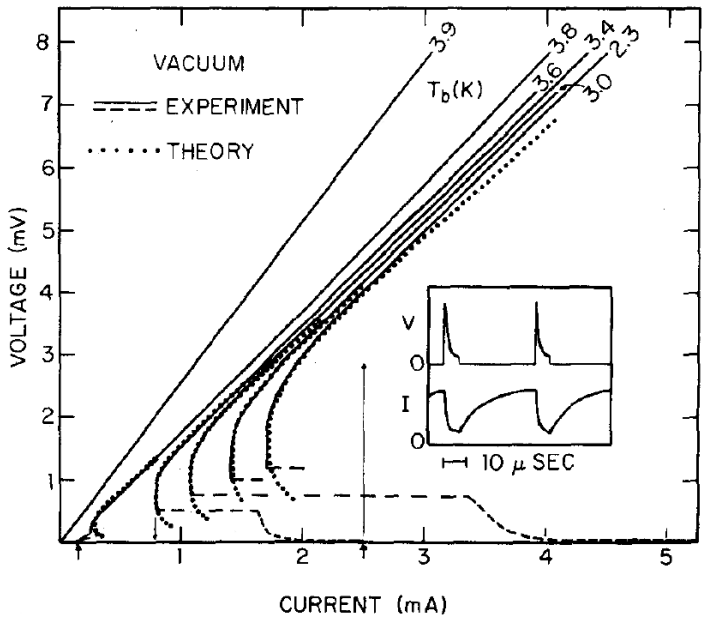

Fig. 2.8: Experimentally obtained voltage-biased IV characteristics of a long tin microbridge measured at different bath temperatures T_b. The solid and dashed curves are measured data, the dotted curves are based on the hotspot theory for long microbridges. The inset shows the time-evolution of voltage and current across the bridge which correspond to curcuit-controlled relaxation oscillations. (from [49])

The load line in the IV characteristics represents the response of the linear circuit, that is combined with a non-linear system. In the case here, the linear circuit is comprised by the series resistor and the superconducting bridge is the non-linear system. A IV curve for a superconducting niobium nitride film is shown in Fig. 2.9 from Ref. [54]. The measurement is voltage-biased with a series resistor of $R_B = 10\,\Omega$. The corresponding load line is indicated by the dashed red line with a slope of $\dot{V}/\dot{I} = -R_B = -10\,\Omega$. When the critical current I_c is exceeded according to a dc bias voltage $V = R_B \cdot I_c$, the current not immediately drops to the relaxation oscillation plateau, the maximum negative slope in the IV characteristics is determined by the slope of $\dot{V}/\dot{I} = -R_B = -10\,\Omega$. The dashed blue line indicates a load line originating from a series resistor of $R_B = 100\,\Omega$. When the critical current is exceeded under the $R_B = 100\,\Omega$ configuration, the IV curve switches across the load line with a slope of $\dot{V}/\dot{I} = -R_B = -100\,\Omega$ to the hotspot plateau. The relaxation oscillation

plateau is not visible in this configuration.

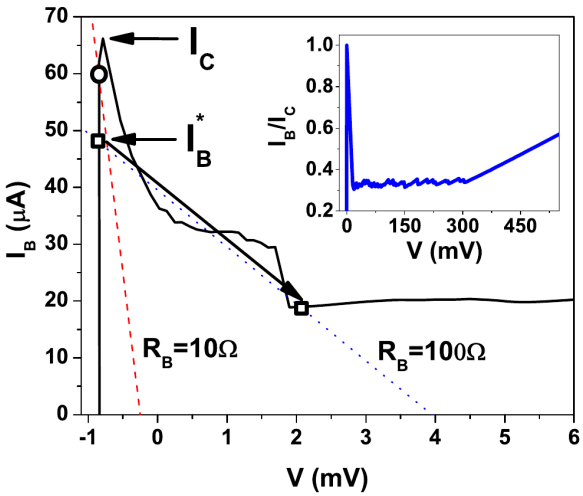

Fig. 2.9: Experimentally obtained voltage-biased IV characteristics of a long microbridge measured at different bath temperatures T_b. The solid and dashed curves are measured data, the dotted curves are based on the hotspot theory for long microbridges. The inset shows the time-evolution of voltage and current across the bridge which correspond to curcuit-controlled relaxation oscillations. (from [49])

In niobium nitride (NbN) extensive studies of phase slippages and the evolution of a normalconducting hotspot were pursued (see e.g. [55]), also because the formation of the hotspot in NbN can be used for single-photon detection in so called hot electron bolometers [56, 57]

2.3 Superconductor-insulator transition

For a review about the superconductor-insulator transition read Refs. [58, 59, 60].

2.3.1 Two-dimensional superconducting systems under the influence of disorder

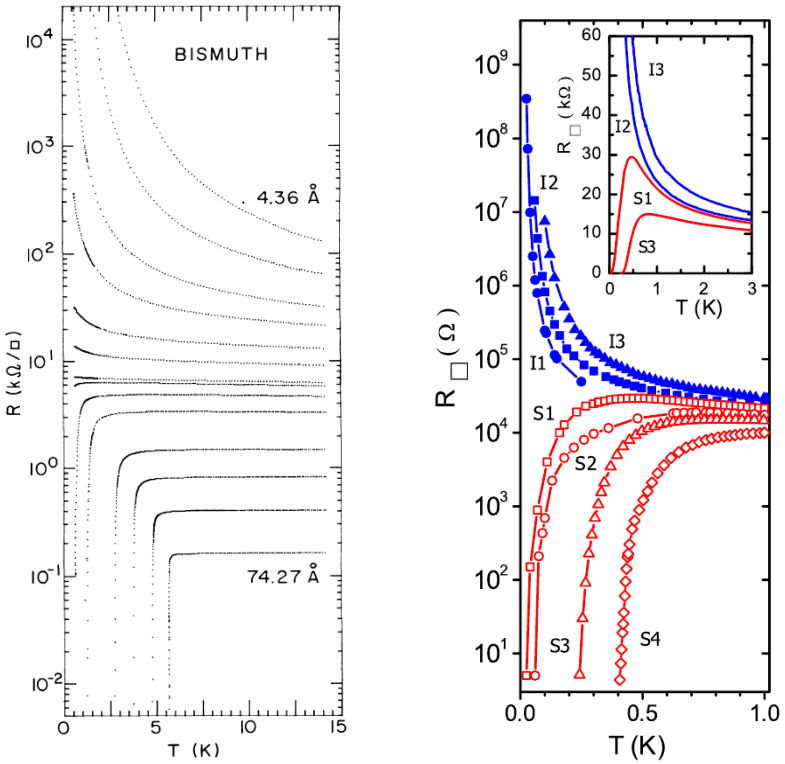

Fig. 2.10: (a) Evolution of the temperature dependence of the resistance of amorphous Bismuth films deposited onto a Germanium layer. The $R(T)$ curves shown correspond to film thicknesses ranging from 4.36 to 74.27 nm (from [61]) (b) SIT for a series of TiN films with different resistances at room temperature, which was tuned by soft plasma etching. (from [62])

The preceding sections of this work shed light on the theory of superconductivity and resistive mechanisms in superconductors. These resistive mechanisms raise the resistivity of superconducting samples maximally to about $G_{00}^{-1} = 81\,\mathrm{k\Omega}$ which is connected to $k_F l = 1$. But for sufficiently disordered 2D films, the resistance increases with decreasing temperature, contrary to what is expected for a superconducting sample. This phenomenon in called the disorder-driven superconductor insulator transition (D-SIT). In 1989, Haviland et al. [61] first noticed that Bismuth films grown on Germanium undergo a disorder-driven SIT (Fig. 2.10a). Since then, the D-SIT has been observed

in amorphous (e.g. indium oxide [63]), polycristalline (TiN) (Fig. 2.10b [62]), granular (lead grains [64]) and also high-T_c superconductors [65, 66].

The question how the drop of resistance at low temperatures disappears with increasing disorder is still strongly discussed. Anderson showed that nonmagnetic impurities do not affect the superconducting transition temperature [67], but for strong enough disorder Anderson localization of electrons develops, forming a rather than a metal insulating state. Then a superconducting state can not be established, even in the presence of an attractive electron-electron interaction [68].

Finkel'stein [69] estimated the suppression of the superconducting order parameter by disorder, based on a perturbative microscopic description of homogeneously disordered systems under consideration of the competition between attractive and repulsive electron-electron interactions in the presence of disorder. The repulsive Coulomb interaction increases as disorder increases due to a reduced electron mobility caused by impurity scattering. Finkel'stein calculated the suppression of the critical temperature T_c relative to the superconducting transition temperature in the bulk T_{c0} with the sheet resistance at room temperature $R_\square$ taken as a measure for disorder in thin films:

$$\frac{T_c}{T_{c0}} = \exp\left(-\frac{1}{\gamma_\tau}\right)\left[\left(1+\frac{(t_{00}/2)^{1/2}}{\gamma_\tau - t_{00}/4}\right)\cdot\left(1-\frac{(t_{00}/2)^{1/2}}{\gamma_\tau - t_{00}/4}\right)^{-1}\right]^{1/\sqrt{2t_{00}}} \tag{2.60}$$

where $\gamma_\tau = 1/\ln(k_B T_{c0}\tau/\hbar) < 0$ and $t_{00} = (e^2/2\pi^2\hbar)R_\square = G_{00}R_\square$. For TiN it has been found that in the vicinity of the SIT Eq. 2.60 holds perfectly [70, 6] despite the predicted strong mesoscopic fluctuations which may develop in the critical region and lead to deviations from Eq. 2.60 [71]. For sufficiently high disorder the Coulomb repulsion between electrons is strong enough to break down Cooper pairing and destroy superconductivity.

In such a fermionic scenario the arising Anderson localization of electrons leads to an insulating state. This at first sight offers a plausible explanation of the SIT, but the degree of disorder to balance Coulomb repulsion and Cooper pairing ($T_c \to 0$), is not sufficient to localize normal carriers. This would result in a SIT with an intermediate metallic state between the superconducting and insulating states. As can be seen in Fig. 2.10b this obviously is not always the case, a sharp transition between the superconducting and insulating regimes is observed.

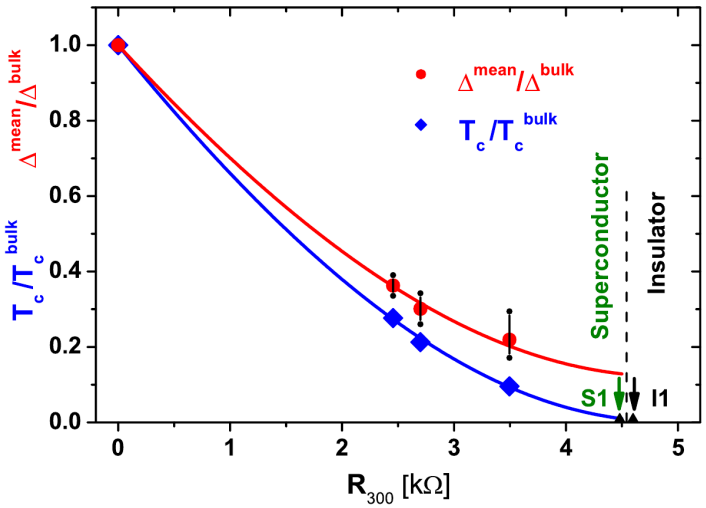

(a)

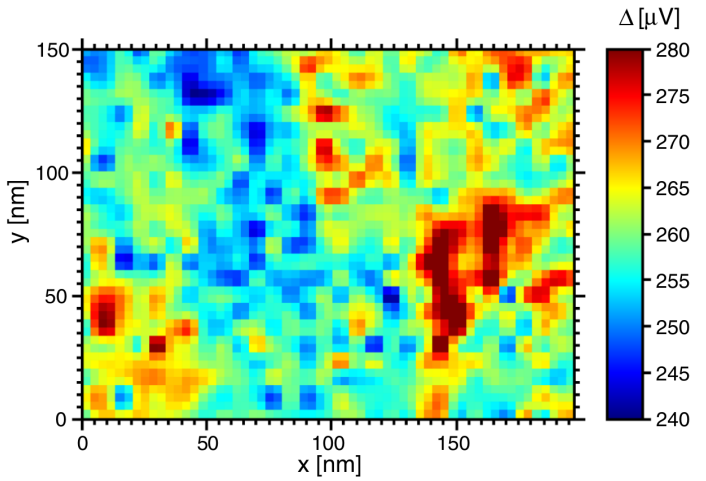

(b)

Fig. 2.11: (a) Critical temperature estimated from $R(T)$ normalized by its bulk value of $T_c^{bulk} = 4.7\,\mathrm{K}$ and mean spectral gap $\bar{\Delta}$ at $T = 50\,\mathrm{mK}$ normalized by Δ^{bulk}, which is the BCS value of the energy gap corresponding to T_c, versus room temperature sheet resistance. The blue line is a fit to Finkel'stein's Eq. 2.60 with $\gamma = 6.2$. The red line is a guide to the eye. S1 and I1 mark the room temperature resistances for the last superconducting and the first insulating sample with respect to the vicinity to the D-SIT (from [6]). (b) The colour map of spatial fluctuations of the superconducting energy gap of a TiN film from the wafer D03 (the same like measured in this thesis). Inhomogeneities of the superconducting properties appear on a length scale of a few ten nanometers (from [6])

But what happens if Cooper pairs rather than electrons are localized? Generally, since the phase ϕ and particle number N of the superconducting state are conjugate variables, there is an uncertainty relation

$$\Delta N \Delta\phi \gtrsim 1 \tag{2.61}$$

In a superconductor the phase of the macroscopic wave function is well defined, but the particle number of the many-particle condensate are unknown. This well defined phase corresponds to perfect conductivity ((following from Eq. 2.10). The other extreme, when the phase is fluctuating and the particle number is fixed, leads us to a bosonic scenario of the SIT where the insulating state is obtained by localized Cooper pairs.

Indeed, the SIT can not be sufficiently described by the uncertainty principle. A model for the localization of Cooper pairs requires a more sophisticated approch. Anderson [72] was the first who considered small superconducting regions coupled by Josephson weak links where Cooper pairs eventually can be localized at the superconducting islands. Indeed, in artificial Josephson junction arrays, even if superconductivity is locally maintained, a globally insulating state can be observed for certain geometries and material parameters. The physics of Josephson junction arrays will be introduced in section 2.3.4. For granular superconductors, where superconducting granules are separated by interlayers of nomal metal or an insulator, the model of Josephson junction arrays is well applicable.

In homogeneously disordered TiN, disorder not just reduces the critical temperature according to Eq. 2.60 (see Fig. 2.11a), it also leads to strong spatial inhomogeneities in the superconducting order parameter as can be seen in Fig. 2.11b [6]. The superconducting gap strongly varies over a length scale of a few ten nanometers. The red curve in Fig. 2.11a displays $\Delta^{mean}/\Delta^{bulk}$ where Δ^{mean} is the average energy gap measured by scanning tunneling microscopy (STM) (like in Fig. 2.11b) and Δ^{bulk} is the BCS energy gap $2\Delta = 3.528 k_B T_{c0}$ for the critical temperatures which are estimated from the $R(T)$ curves. Since the ratio $\Delta^{mean}/\Delta^{bulk}$ remains finite at the extrapolated point of the SIT at about $R_\square(T = 300\,\mathrm{K}) = 4.5\,\mathrm{k\Omega}$, the local density of states is likely to remain gapped in the insulating phase. Dubi, Meir and Avishai [73] pursued numerical simulations of homogeneously disordered thin films on the basis of the microscopic two-dimensional disordered negative-U Hubbard model including thermal phase fluctuations. For low disorder they obtained the superconducting ground state with global phase coherence. They found that sufficiently high disorder leads to the formation of superconducting islands in which the superconducting order parameter is higher than between them. In the regime of high disorder, on the insulating side of the SIT, they found superconducting islands embedded in an insulating sea. This result, obtained from a theoretical approach, is consistent with the experimental observations of Ref. [6].

In Fig. 2.12 the evolution of the peaks beside the gap in the local density of states, the coherence peaks, are mapped under the influence of disorder. In both materials shown, it is visible that the coherence peak vanishes for increasing disorder. The suppression of the low-energy density of states was called pseudo-gap. But the TiN samples studied in [6] and the indium oxide samples studied in [74] still were on the superconducting side of the SIT. The density of states of the insulating side of the SIT for the first time was observed in [75], where the existence of an energy gap in the insulating state of homogeneously amorphous indium oxide was presented.

An additional aspect to explain the SIT involves percolation. In [76] granular super-

conductors were modelled by two-dimensional random resistor percolation networks. The resistance between neighbouring grains is governed either by Cooper pair tunneling through a Josephson junction or by quasiparticle tunneling. The random resistors in the latter model include inhomogeneities to the Josephson junction network. On the superconducting side of the SIT in the inhomogenious Josephson junction network, the paths in the superconducting network between the leads have different critical currents. On the insulating side, the corresponding percolation paths are insulating up to different threshold voltages. On the transition from the superconducting to the insulating state, the number of superconducting paths goes to zero and the system is determined by the weakest insulating paths in the percolation network. But percolation may play a role even in homogeneously disordered systems, since slight inhomogeneities in the samples are unavoidable in the real world [60].

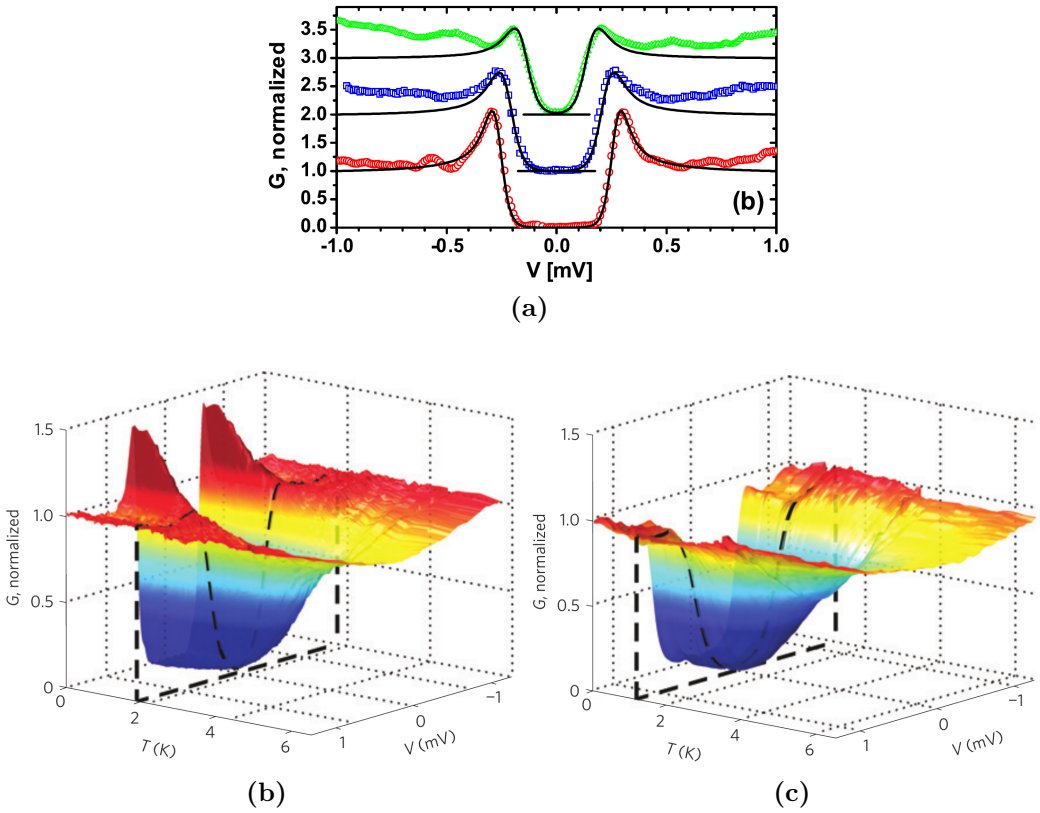

Fig. 2.12: (a) Normalized differential tunneling conductance measured at $T = 50\,\mathrm{mK}$ for three differently disordered TiN samples. Disorder raises from bottom to top curve (from [6]). (b) Temperature evolution of the local density of states for a low-disorder InOx sample and (b) for a high-disorder InOx sample (from [74]).

2.3.2 Phenomenology of the disorder- and field-driven SIT

Next, we focus on the temperature dependence of the resistance on both sides of the SIT, while we restrict to titanium nitride (TiN) and indium oxide (InOx). On the superconducting side of the SIT the vortex-BKT physics plays an important role.

In Fig. 2.13a the temperature dependence of the resistance at zero magnetic field of different TiN films is analyzed according Eq. 2.27 [25]. The onset of resistivity starting from the BKT transition temperature up to a resistance, which strongly depends on the maximum resistance in the $R(T)$ and accordingly to the sheet resistance at room temperature, can be explained by the physics of the vortex BKT transition. In a later chapter (chapter 2.2.2) the evolution of the $R(T)$ at higher temperatures and thus higher resistances will be revealed in the framework of superconducting fluctuations.

For critically disordered samples in the vicinity of the D-SIT, but still on the superconducting side, a small magnetic field causes a highly insulating regime. This is called the magnetic field driven SIT (B-SIT). If a sample is already on the insulating side of the D-SIT but still near to it, a small magnetic field can increase the resistance even more. For both cases a magnetoresistance peak appears which is followed by a decrease of resistance with magnetic field. In high fields the sample obtains a metallic behaviour. Fig. 2.13b displays the typical shape of magnetoresistance isotherms for a superconducting sample at zero magnetic field which undergoes the B-SIT for applied magnetic field.

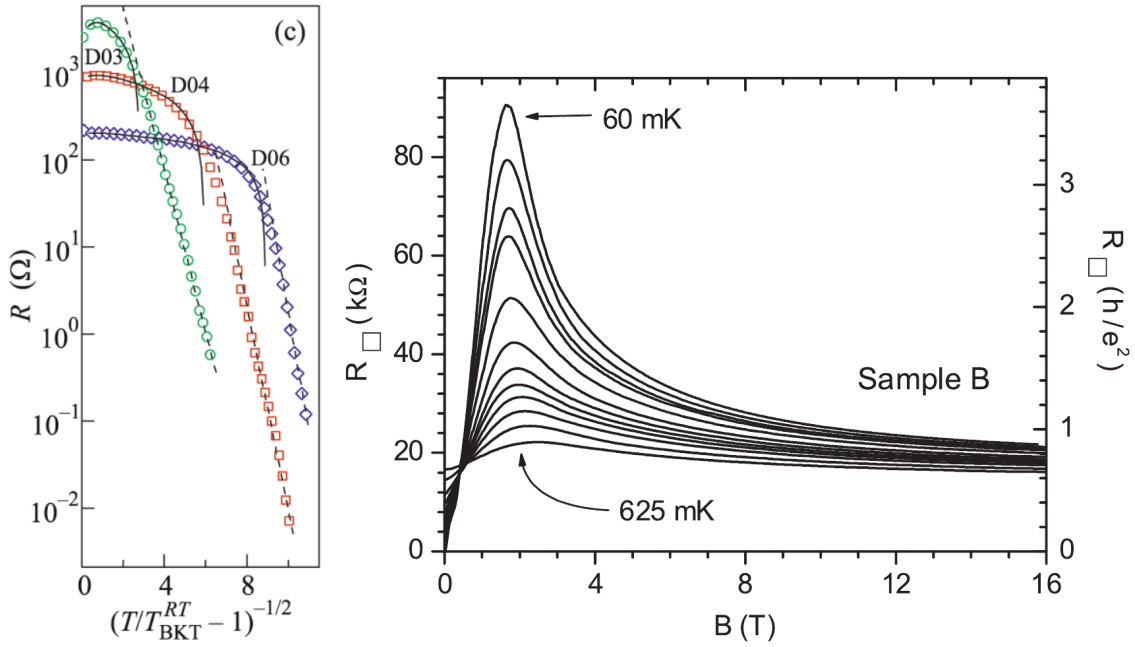

Fig. 2.13: (a) Temperature dependences of the resistance per square of TiN films on a logarithmic scale versus the reduced temperature. $T_{BKT} = 1.145\,\mathrm{K}$ for D03, $T_{BKT} = 2.475\,\mathrm{K}$ for D04 and $T_{BKT} = 3.175\,\mathrm{K}$ for D06 (from [25]). (b) Typical set of magnetoresistance isotherms obtained for a TiN sample on the superconducting side in the vicinity of the D-SIT (from [77]). For more critically disordered superconducting samples and lower temperatures the magnetoresistance peak reaches much higher values in the range of GΩ to TΩ [78].

On the insulating side of the D- and B-SIT a thermally activated temperature de-

pendence of the resistance is observed in TiN and InOx

$$R(T) = R_0 \exp\left(\frac{T_0}{T}\right) \tag{2.62}$$

with the activation energy T_0 and the prefactor R_0. In an Arrhenius plot in which $\log R$ is plotted vs. $1/T$, the thermally activated behaviour of a $R(T)$ curve appears linear. But, as can be seen for the blue curve for zero field in Fig. 2.14a, even at zero magnetic field, the temperature dependence of the resistance on the superconducting side of the D-SIT can be linear in an Arrhenius plot.

In 2008 it was found that for highly insulating samples, a more than thermally activated dependence of the resistance can occur [14]. In Fig. 2.14b Arrhenius plots for different magnetic fields of the sample measured in [14] are shown. In the temperature range $0.3-0.9\,\mathrm{K}$ the $R(T)$s have thermally activated behaviour with activation energies $k_B T_0$ plotted in the inset of Fig. 2.14b. For lower temperatures the deviations from the simple activated behaviour appears, with an upturn in the Arrhenius plots for fields $B <= 1.4\,\mathrm{T}$. This highly insulating phase was called a *superinsulator* [15]

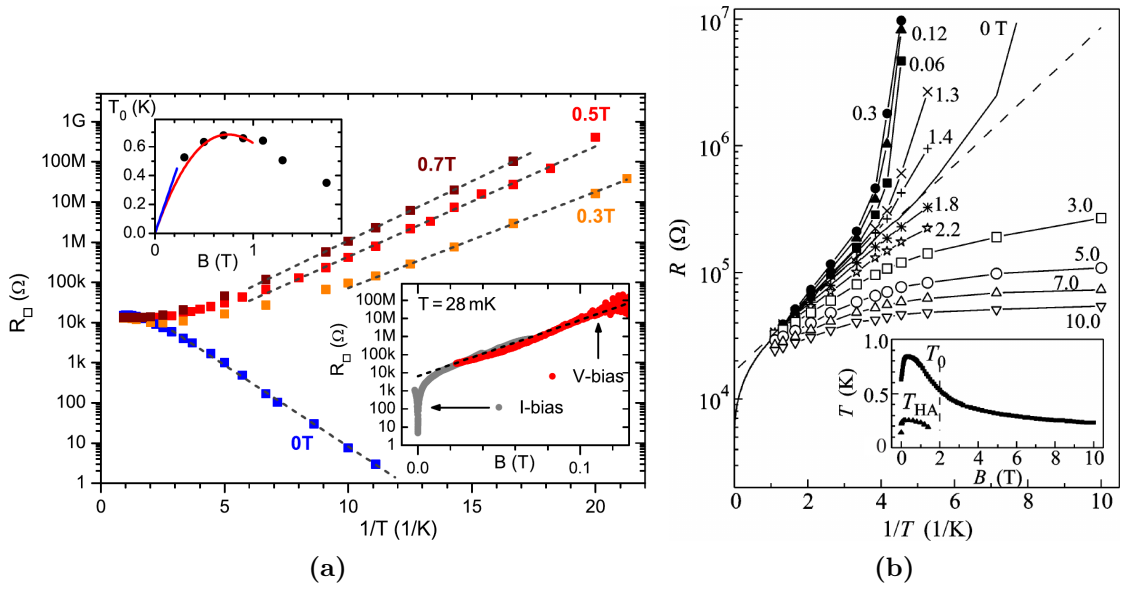

Fig. 2.14: (a) Sheet resistance $R_\square$ on a logarithmic scale vs. $1/T$ at different magnetic fields. Top left corner: the activation temperature T_0 as function of magnetic field B. Bottom right corner inset: magnetoresistance isotherm for $T = 28\,\mathrm{mK}$ for low magnetic fields. The dashed line indicated an exponential increase of the resistance with magnetic field (from [79]). (b) Arrhenius plots of the temperature dependence of the resistance for fixed magnetic fields of a sample that is already insulating at zero magnetic field. Inset: Extracted activation temperatures $T_0(B)$ from the Arrhenius plots in the temperature range $0.3\,\mathrm{K}$ - $0.9\,\mathrm{K}$, since all the $\log R(T, B_i)$ vs. T are linear at all magnetic fields for this temperature range (from [14]).

In InOx there is also an magnetoresistance resistance peak, but typically at much

higher fields (Fig. 2.15a). Like for TiN, in the insulating phase temperature activated behaviour is observed at low temperatures, see Fig. 2.15b.

In TiN as well as in InOx the IV characteristics reveal a highly nonlinear behaviour at low temperatures in the insulating phase. Figs. 2.16a and 2.16b show the differential conductance vs. the applied voltage for insulating TiN and InOx samples respectively. At the higher temperatures the conductance continuously increases with raising bias voltage. At the lower temperatures a jump in the current-voltage characteristics and in the differential conductance emerges.
High-resolution dc measurements could attribute most of these jumps to a decoupling of the electron temperature from the phonon bath temperature [80]. A thorough study of highly insulating TiN samples encouraged an interpretation of the insulating state in terms of Josephson junction arrays [78].

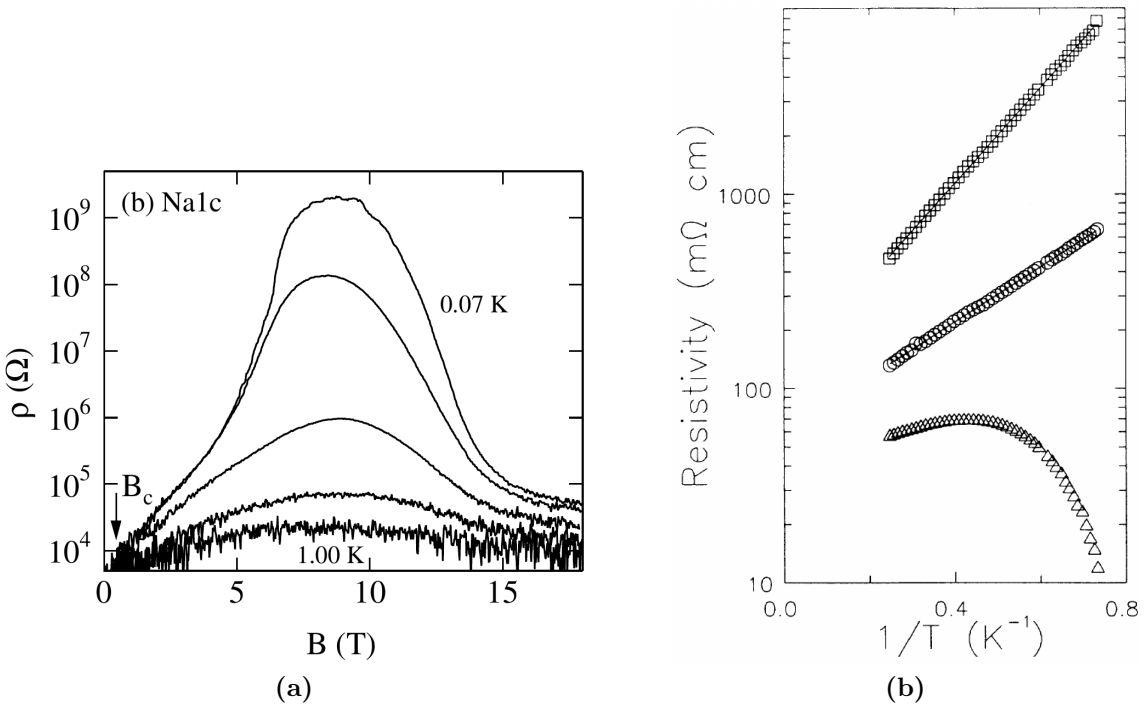

Fig. 2.15: (a) ρ versus B isotherms for a InOx sample at $T = 0.07, 0.16, 0.35, 0.62,$ and $1.00\,\mathrm{K}$ (from [81]). (b) Temperature dependence of the resistance of an amorphous InOx film 2000 Å thick in three states: immediately after deposition (upper curve) and after two subsequent heat treatments. In InOx disorder is reduced due to annealing. (from [63])

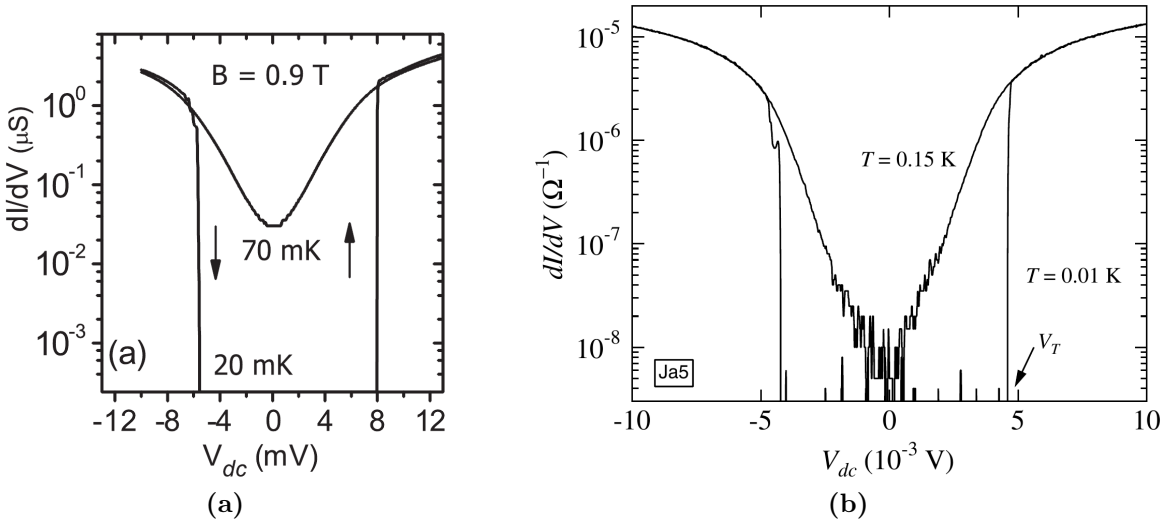

Fig. 2.16: (a) Differential conductance vs. dc voltage $dI/dV(V_{dc}$ for an insulating TiN sample at $B = 0.9\,\mathrm{T}$ at two temperatures $T = 0.02\,\mathrm{K}$ and $T = 0.07\,\mathrm{K}$. Arrows show the direction of the voltage sweep (from [62]). (b) Comparison of IV characteristics of a sample in the B-driven insulating phase at two different temperatures $T = 0.15$, and $T = 0.01\,\mathrm{K}$ (from [82])

2.3.3 The SIT as a quantum phase transition (QPT)

The question if the SIT is a continuous quantum phase transition (QPT) was raised after the studies of homogeneous thin films like a-Bi films grown on a-Ge substrates, for which the $R(T)$ curves are shown in Fig. 2.10a. What set stage for consideration of the SIT as a QPT is the absence of an intermediate metallic regime between the superconducting and insulating regimes. Instead, the superconducting and insulating $R(T)$ curves are divided by a seperatrix to an unstable fixed point at zero temperature. Astonishingly, for the particular set of thin films shown in Fig. 2.10a this fixed point corresponds to the quantum resistance for Cooper pairs $h/4e^2 \approx 6450\,\Omega$. Though in later studies of the SIT in other materials this quantum resistance was found to be not a universal critical resistance, the application of Boson physics to the SIT as an continuous QPT was initiated. The following description of contiuous QPT is taken from Refs. [7, 8].

The partition function Z describes the statistical properties of a quantum system in thermodynamic equilibrium

$$Z(\beta) = \mathrm{Tr}(e^{-\beta H}) \tag{2.63}$$

where H is the Hamiltonian of the system and $\beta = 1/(k_B T)$. It is found that the partition function for a quantum system in d dimensions looks like a partition function for a classical system in $(d + 1)$ dimensions, where the extra dimension is finite in extent $\hbar\beta$ in units of time. In the limit $T \to 0$ the system size in the time dimension diverges and the resulting system is effectively a classical true $(d + 1)$ system.

Here, first an introduction to continuous QPTs in the quantummechanical limit at $T = 0$ is given and then the temperature is introduced, making the system "finite". A quantum system can undergo a continuous QPT at zero temperature as a parameter in the Hamiltonian of the system is changed. A quantum critical point exists which separates two distinct quantum mechanical ground states. Fluctuations in this system are purely quantum mechanical as temperature is not a parameter of this system. Near a QPT there are two diverging correlation length, one for the spatial dimension (ξ) and one for the temporal dimension (ξ_τ). The temporal dimension corresponds to the phase of the quantum mechanical wave function and hence to an energy scale, which vanishes at the critical point. ξ and ξ_τ depend on a control parameter $\delta = (g - g_c)/g_c$ for the transition. For the SIT g can be a measure of disorder, magnetic field or charge carrier density and g_c is the critical value of the control parameter. At $T = 0$ both $\xi(g)$ and $\xi_\tau(g)$ diverge as $\delta \to 0$ in the manner

$$\xi \propto |\delta|^{-\nu} \tag{2.64}$$

$$\xi_\tau \propto \xi^z. \tag{2.65}$$

This defines the correlation length exponent ν and the dynamical critical exponent z. The diverging length and the associated dynamic scaling of physical quantities represent universal behaviour. The scaling of the physical quantities is of particular interest, since this universal behaviour is insensitive to microscopic details and depends only on properties of the system, such as the symmetry breaking associated with the transition, the dimensionality of the system and the range of the interactions. These details define the universality class of the system. The physical quantities in the vicinity of the QPT have dynamic scaling forms. This means that their dependence on the independent variables involves homogeneity relations of the form

$$\mathcal{O}(k, \omega, g) = \xi^{d_\mathcal{O}} O(k\xi, \omega\xi_\tau) \tag{2.66}$$

where $d_\mathcal{O}$ is called the scaling dimension of the observable $\mathcal{O}$ measured at wave vector k and frequency ω

As experimentally only non-zero temperatures are accessible, the above dynamic scaling forms have to be modified for $T > 0$. For a continuous QPT the only effect of introducing finite temperatures $T \neq 0$ on the partition function Eq. 2.63 is to make the temporal dimension finite. As a consequence, the effective classical system resembles a hyperslab with d spatial dimensions with infinite extent and one temporal dimension of size $L_\tau = \hbar\beta$ with $\beta = 1/k_B T$. As temperature is introduced to the system, the energy scale for quantum fluctuations $\Omega \propto \xi_\tau^{-z}$ is cut off by $k_B T$, which results in the cutoff length L_τ. The formal model which is applied for data analysis at $T > 0$ is called finite-size scaling. With finite size scaling the critical exponents and the universality class of the transition can be determined, even at non-zero temperature. The resistance near the QPT in a 2D system obeys the scaling forms

$$R(B, T, E) = R_c \cdot F\left(\frac{\delta}{T^{1/z\nu}}, \frac{\delta}{E^{1/\nu(z+1)}}\right) \tag{2.67}$$

where (B, T, E) are magnetic field, temperature and applied electric field, respectively, and R_c is a prefactor. The function F is system specific and has not to be known for a scaling analysis. It is important to keep in mind that finite-size scaling only works near the QPT and at low enough temperatures, namely $\xi_\tau \sim \xi^z < \hbar\beta$.

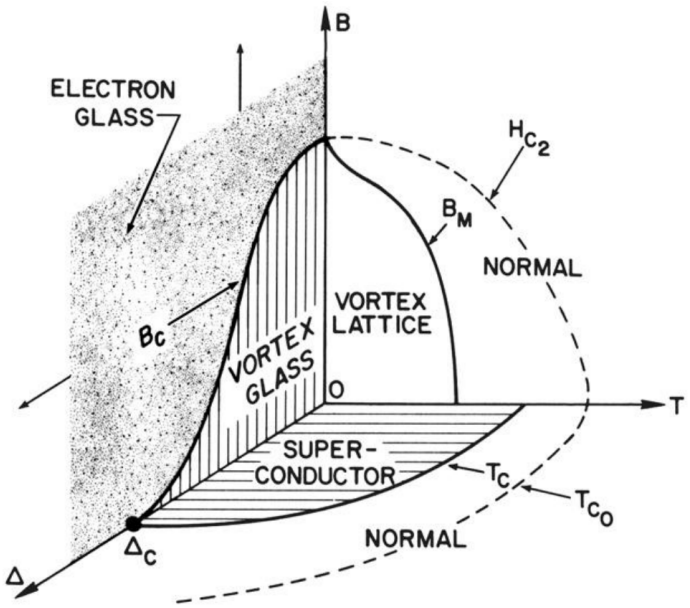

Fig. 2.17: Schematic phase diagram for disordered superconducting films. The SIT quantum phase transition at $T = 0$ occurs at both critical disorder Δ and critical magnetic field B_c. (from [7])

In Refs. [7, 83] a very popular possible description of the SIT as a quantum phase transition is given and finite size scaling predictions for the resistivity near and at the B-SIT/D-SIT are estimated. The insulating phase of the B-SIT is argued to be be described by a dual representation to the superconducting phase. In the superconducting phase Cooper pairs are Bose condensed and vortices are localized in a vortex glass phase. Right at the transition of the field driven SIT the vortices undergo a Bose condensation and delocalize, while the Cooper pairs are localized in the Cooper pair glass phase. At the critical point neither vortices nor Cooper pairs have condensed, they are metallic and diffuse with a finite resistance. The critical point is experimenally not observable since it is of unstable nature, like a pendulum in vertical position with the mass directly above its center of rotation. Under the corresponding duality transformation, from particles to vortices and resistivities to conductivities, it is found that $z = 1$ due to the long ranged Coulomb interaction and $\nu \geq 2/d = 1$ for both the disorder and the magnetic field as control parameter g.

The D-SIT is described by a similar duality picture[7]. The SIT at the critical disorder Δ_c is driven by an vortex binding-unbinding transition, similar to the BKT transition. Vortices are paired in the superconducting phase and unbind in the Cooper-

pair-glass insulator, where the Cooper pairs are localized and the unbound vortices are Bose-condensed.

A scheme of the phase diagram suggested in [7] is shown in Fig. 2.17. An important requirement for the application of the scaling theory developed in [83, 7] is that the microscopic disorder is sufficiently homogeneous. This is fulfilled if the length scale characterizing the uniformity of disorder is longer than the length scale used by the theory to model the superconducting behavior [84].

The first scaling analysis on the SIT was performed by Hebard and Paalanen [84] on the B-SIT of InOx films. They found $z\nu \approx 1.2$ which has been found several times since that (e.g. [45, 85]). $\nu \geq 2/d$ was calculated for the universility class of the (2+1)D XY model in the dirty limit. These findings, and similar results from other materials which obtained $z\nu \geq 1$ and $z = 1$, too, are considered as the signatures of a bosonic system with long ranged Coulomb interactions, like in the duality-based system above from Ref. [7].

In *a*-Bi films the D-SIT (tuned by the film thickness) and the B-SIT were analyzed in the framework of finite size scaling in [86]. Surprisingly, while for the D-SIT once again $z\nu \approx 1.2$ was found, for the B-SIT it was derived that $z\nu \approx 0.7$. This suggests that the B- and the D-SIT belong to two different universality classes. $\nu \leq 2/d$ was calculated for the (2+1)D XY model in the clean limit [87].

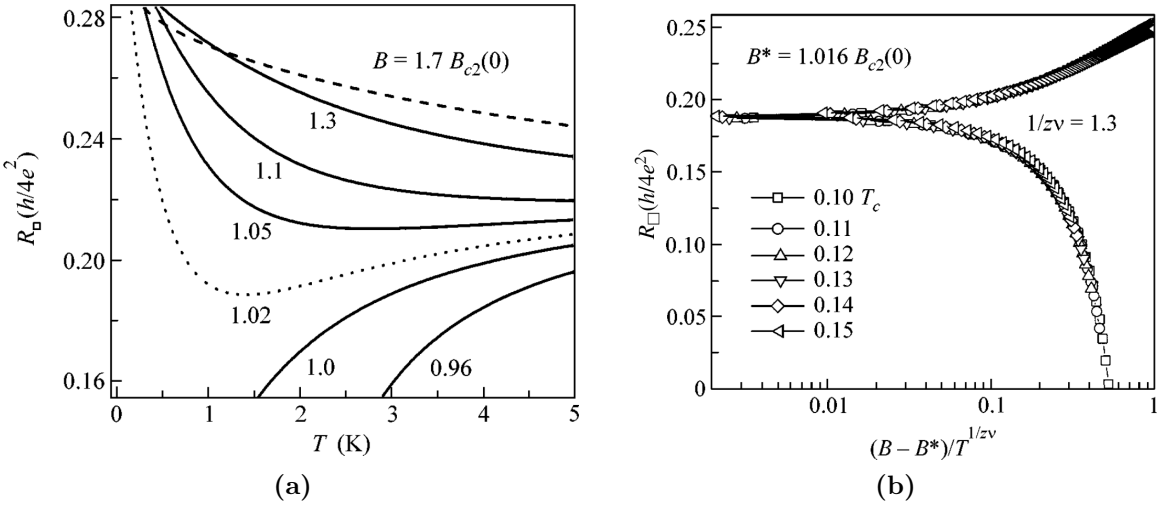

Fig. 2.18: (a) Theoretical $R(T)$ curves for different ratios of $B/B_{c2}(0)$ with a mean field critical temperature $T_{c0} = 11.8\,\mathrm{K}$. The correction to conductivity coming from the Aronov Altshuler interelectron interference is estimeted with $\Delta G^{ID} = -\frac{e^2}{2h}\ln(T/T^*)$ with $T^* = 20\,\mathrm{K}$ (see Eq. 2.41). The Drude conductivity G_0 is set to the value of the conductivity of the NdCeCuO sample under study at $T = 20\,\mathrm{K}$. (from [9]). (b) Scaling of the theoretical $R(T)$ curves around a field $B^* = 1.016 B_{c2}(0)$. The best data collapse is produced with $1/z\nu = 1.3$. [9].

Superconducting fluctuations above the upper critical field $B_{c2}(0)$ produce a crossover of the magnetoresistance isotherms for $T < T_c$ which corresponds to a plateau in the

$R(T)$ curve for the magnetic field at which the $R(B)$ curves intersect. In Fig. 2.18a from Ref. [9] the theoretical $R(T)$ curves for different ratios of $B/B_{c2}(0)$ are shown with a mean field critical temperature $T_{c0} = 11.8\,\mathrm{K}$. The correction to conductivity coming from the Aronov Altshuler interelectron interference was estimeted with $\Delta G^{ID} = -\frac{e^2}{2h}\ln(T/T^*)$ with $T^* = 20\,\mathrm{K}$ (see Eq. 2.41). The Drude conductivity G_0 was set to the value of the conductivity of the NdCeCuO sample under study at $T = 20\,\mathrm{K}$ in Ref. [9]. The total conductivity is given by Eq. 2.40. In Fig. 2.18b a scaling analysis according to the theory of finite size scaling was pursued in a narrow temperature region with $0.1 \leq T/T_{c0} \leq 0.15$. A collapse of the data was achived by choosing $1/z\nu = 1.3$. However, the crossing point in the theoretical $R(B)$ isotherms is clearly not the point of the SIT quantum phase transition and at a zoomed look the crossover of the $R(B)$ curves spreads over a finite field region. The theory of finite size scaling is only applicable for distinct crossing points in the $R(B)$ isotherms, since an approximate crossing point violates the definition of a distinct point for the quantum phase transition. In order to check if an experimental crossing in magnetoresistance isotherms marks the point of the quantum phase transition, the data that collapses in a scaling plot should at least vary by two orders of magnitude in $|R - R_c|$, were R_c is the resistance at the crossing.

2.3.4 Josephson-junction-array model

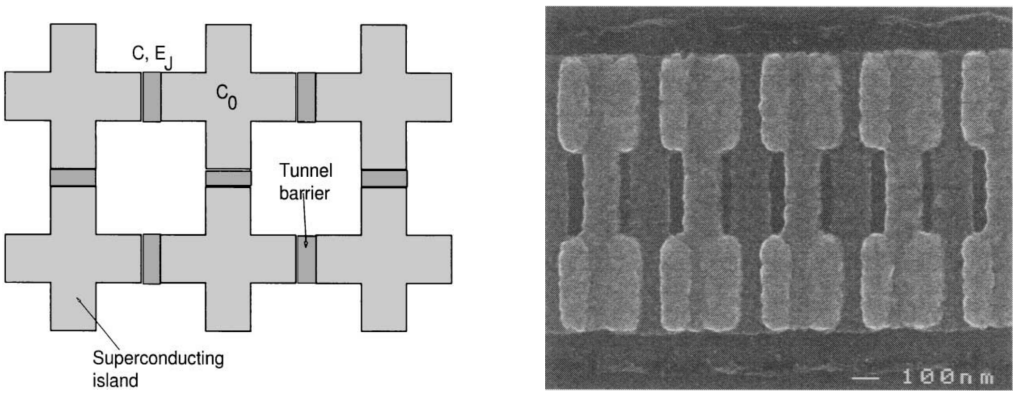

Fig. 2.19: (a) Scheme of a Josephson junction array that consists of a network of superconducting islands weakly coupled by tunnel junctions. The junctions are characterized by the Josephson coupling energy E_J and the junction capacitance C, the islands are characterized each by their capacitance to ground C_0 (from [88]). (b) A scanning-electron microscope image of a SQUID chain (from [89]).

A quantum Josephson junction array consists of a regular network of superconducting islands weakly coupled by tunnel junctions (for a review, see [88, 90]). Artificial Josephson junction arrays are one or two dimensional tunable superconducting systems which can show a SIT quantum phase transition due to tuning two competing

energies: the Josephson junction energy E_J, associated with the tunneling of Cooper pairs between neighbouring islands, and the charging energy E_c, which is the energy needed to add an charge to a neutral island. In Fig. 2.19 a one-dimensional Josephson junction array and a scheme of it are shown.

From the Josephson relations (Eqs. 2.22, 2.23) the Josephson coupling energy is obtained

$$E_J = \frac{\phi_0 I_c}{2\pi} \tag{2.68}$$

where I_c is the maximum junction critical current in the absence of charging effects and thermal fluctuations, and $\phi_0 = h/2e$ is the flux quantum. Ambegaokar and Baratoff estimated it to [91]

$$I_c R_N = \pi \frac{\Delta}{2e} \tanh\left(\frac{\Delta}{2k_B T}\right) \tag{2.69}$$

with R_N the normal-state junction resistance and the energy gap Δ. Each island i of the array has a capacitance C_{ij} to an other island j and a self-capacitance C_0 to ground potential. For an exact determination of the electrostatic energy the capacitance matrix C_{ij} and the gate voltages (if applied) have to be known. The problem simplifies in the nearest neighbour approximation, where only the junction capacitance to the nearest neighbouring islands and the capacitance to ground are considered. The charging energy for two charges, placed on islands i and j of coordinates $\mathbf{r}_i$ and $\mathbf{r}_j$ is then given by

$$E_{ij} = \frac{e^2}{2} C_{ij}^{-1} \sim \frac{e^2}{4\pi C} K_0\left(\frac{|\mathbf{r}_i - \mathbf{r}_j|}{\lambda}\right) \tag{2.70}$$

where K_0 is the modified Bessel function. Up to distances of the order of the electrostatic screening length λ the charging interaction increases logarithmically and then vanishes exponentially. In units of the discrete lattice spacing, the range of the electrostatic interaction between Cooper pairs λ is given by

$$\lambda = \sqrt{C/C_0}. \tag{2.71}$$

The characteristic energy scale is known as the charging energy E_c

$$\text{for electrons :} \quad E_c = \frac{e^2}{2C} \tag{2.72}$$

$$\text{for Cooper pairs :} \quad E_c = \frac{(2e)^2}{2C} \tag{2.73}$$

Quantum effects in Josephson arrays become important when the charging energy is comparable with the Josephson energy. In addition the junction resistance should be of the order of the quantum resistance of pairs $R_Q = h/4e^2$. The Hamiltonian which

describes Cooper pair tunneling in superconducting quantum networks is given by

$$H = H_c + H_J \tag{2.74}$$

$$\sim \frac{1}{2}\sum_{i,j} Q_i C_{ij}^{-1} Q_j - E_J \sum_{\langle i,j\rangle} \cos(\phi_i - \phi_j - A_{ij}). \tag{2.75}$$

The first term considers the charging energy, the second the Josephson tunneling of islands i, j with phases ϕ_i, ϕ_j. The effect of an external gate voltage is omitted. In the second term the effect of a perpendicular magnetic field with vector potential $\mathbf{A}$ is included through $A_{ij} = 2e\int_i^j \mathbf{A}\cdot d\mathbf{l}$. A useful parameter is introduced with the magnetic frustration

$$f = \frac{\phi}{\phi_0} = \frac{1}{2\pi}\sum_P A_{ij} \tag{2.76}$$

where over an elemenatry plaquette of the array is summed. In the Hamiltonian of Eq. 2.75 the two competing contributions favour different ground states. For a dominant Josephson term ($E_J \gg E_C$), a energy minimum is reached if all phases are aligned and a superconducting state is obtained. For the other extreme, a dominant charging energy ($E_J \ll E_C$), each island has zero charge in the ground state. Charge separations or putting an extra charge to an island costs energy of the order of the charging energy. The array is insulating though each island of the array is superconducting.

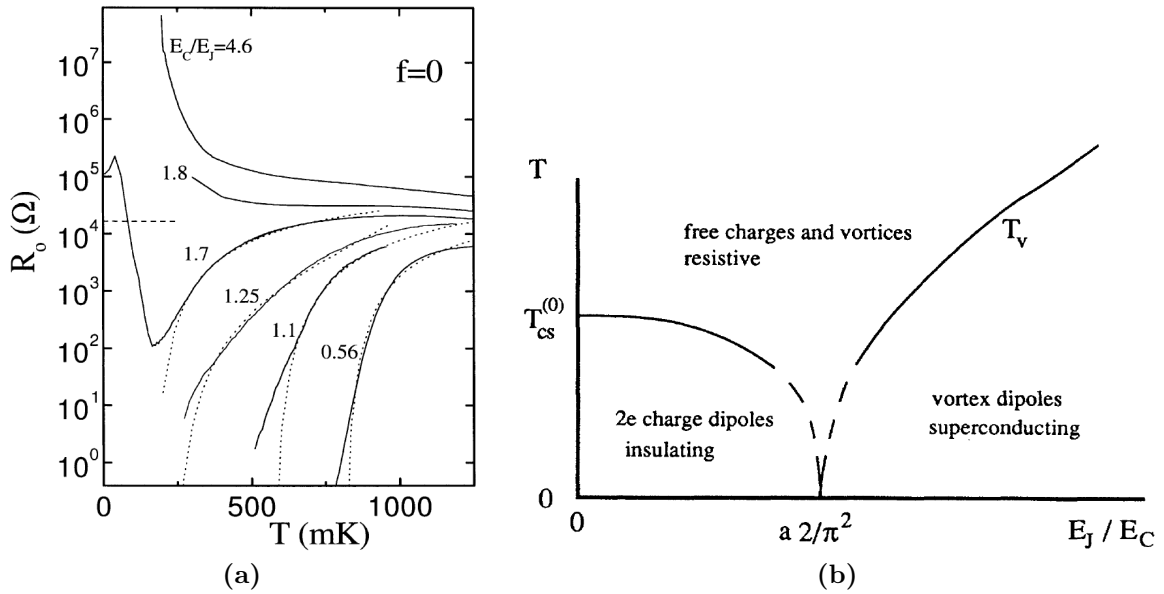

Fig. 2.20: (a) Zero field linear resistance per square vs. temperature for six different square arrays. The curved dashed lines are fits with Eq. 2.27 to the vortex BKT. The dasshed horizontal line indicated an estimated for the zero-temperature universal resistance at the SIT (from [88]). (b) Phase diagram for a quantum Josephson junction array in the limit of long-range (logarithmic) interaction between charges. Dually to a vortex-BKT transition which is indicated by T_V, charges can undergo a charge-BKT transition when the left curved line indicating T_{CS} in the phase diagram is crossed (from [92]).

A transition from the superconducting to the insulating ground state can be achieved by tuning the ratio of E_C/E_J like depicted in Fig. 2.20a. The resistance dependences of temperature were taken for six different square arrays in zero magnetic field. The three arrays that become superconducting undergo a vortex-BKT transition which is already discussed in section 2.2.1. The arrays, to which the upper two $R(T)$-curves belong, show a continous increase of the resistance as temperature is lowered. They undergo a so-called charge BKT transition in which a duality transformation of vortices (in the vortex BKT) to charges (in the charge) can explain the insulating behaviour at low temperatures. The curve corresponding to $E_C/E_J = 1.7$ first has a superconducting-like decrease in resistance with lowering temperature and then an insulating-like increase upon lowering the temperature further. The ratio $E_C/E_J = 1.7$ was estimated to be the critial one for the SIT. On the superconducting side of the SIT in the vortex BKT phase vortex antivortex pairs lead to a finite conductivity for $T > T_{v-BKT}$. In the dual charge BKT phase, local excess and local deficit in the Cooper pair density (called Cooper pair dipoles, abbreviated CPD) cause finite resistivity for $T > T_{c-BKT}$. A qualitative phase diagram is sketched in Fig. 2.20b. With increasing capacitances in a Josephson junction array, the vortex BKT transition temperature T_{v-BKT} is suppressed with [93, 88]

$$k_B T_{v-BKT} = \begin{cases} \frac{\pi E_J}{2}\left(1 - \frac{4}{3\pi}\frac{E_0}{E_J}\right) & \text{for } C_0 \gg C, \quad (2.77) \\ \frac{\pi E_J}{2}\left(1 - \frac{1}{3\pi}\frac{E_C}{E_J}\right) & \text{for } C_0 \ll C \quad (2.78) \end{cases}$$

where $E_0 = e^2/(2C_0)$ is the energy associated with adding a single charge to an island with C_0 the self capacitance of a single island. $E_C = e^2/(2C)$ is associated with the transfer of a charge from an island to a nearby one with C the mutual capacitance between neighbouring islands. Eqs. 2.78 and 2.78 are calculated by a WKB renormalization group analysis where the Josephson energy E_J dominates, leading to a global superconducting state for $T \to 0$. In the charge BKT regime, the transition temperature T_{c-BKT} is given by [92]

$$k_B T_{c-BKT} = \frac{E_C}{\pi} - 0.31\frac{E_J^2}{E_C} \qquad E_J \ll E_C \quad (2.79)$$

An array that undergoes a c-BKT transition is insulating below $T < T_{c-BKT}$. The conductance in the c-BKT should vanish dually to the resistance in the v-BKT with the squareroot dependence of Eq. 2.27. Instead an exponential activated temperature dependence was found to characterize the vanishing conductance

$$\sigma \propto \exp\left[-\frac{E_a}{k_B T}\right] \quad (2.80)$$

with an observed activation energy $E_a \sim \Delta + 0.24E_C$.

In [59] a possible explanation for this activated behaviour is given, based on the

heuristic considerations of Ref. [15]. The starting point is the tunneling current in an Josephson junction array

$$I \propto \exp\left(-\frac{E}{W}\right) \tag{2.81}$$

where E is the characteristic energy barrier controlling the charge transfer betwen superconducting islands, $W = \hbar/\tau_W$, and τ_W is the relaxation time characterizing the rate of the energy exchange between the tunneling charges and the environment. The density of the CPD excitations, which are bosons, is assumed to follow a Bose distribution function and the rate W to be proportional to it

$$\frac{\hbar}{\tau_W} = \frac{E_C}{\exp(E_C/k_BT) - 1} \tag{2.82}$$

The characteristic energy is identified to be $E \simeq E_c \ln(L/a)$ with sample size L. Not too far from the charge BKT transition, $T \gtrsim T_{c-BKT}$, the electrostatic screening length remains longer than the sample size which allows L to scale E like in the charge BKT phase:

$$\sigma \propto \exp\left[-\frac{E_C \ln(L/a)}{T}\right], \quad T \gtrsim T_{c-BKT} \tag{2.83}$$

In the extreme case of very low temperatures, $T \ll T_{c-BKT} \simeq E_C$, the characteristic energy in Eq. 2.82 reduces to $W \simeq E_C \exp(-E_C/T)$ followed by a low-temperature estimate for the conductivity

$$\sigma \sim \exp\left[-\ln(L/a) \cdot \exp\left(\frac{E_C}{T}\right)\right], \quad T \ll T_{c-BKT} \tag{2.84}$$

Up to now it is not taken into account that the correlation length, ξ_{c-BKT}, a measure of the typical distance of the free unbound charges, diverges upon approach of the transition from high temperatures. The resulting temperature dependence of resistance in the vicinity of the transition reads

$$R = R_0 \exp\left(A \cdot \exp\sqrt{\frac{b}{(T/T_{c-BKT}) - 1}}\right) \tag{2.85}$$

where R_0 is a constant in units of resistance, A and b are constants. The measured $R(T)$ curves in Ref. [14] were consistent with Eq. 2.85 treating A and b as free parameters.

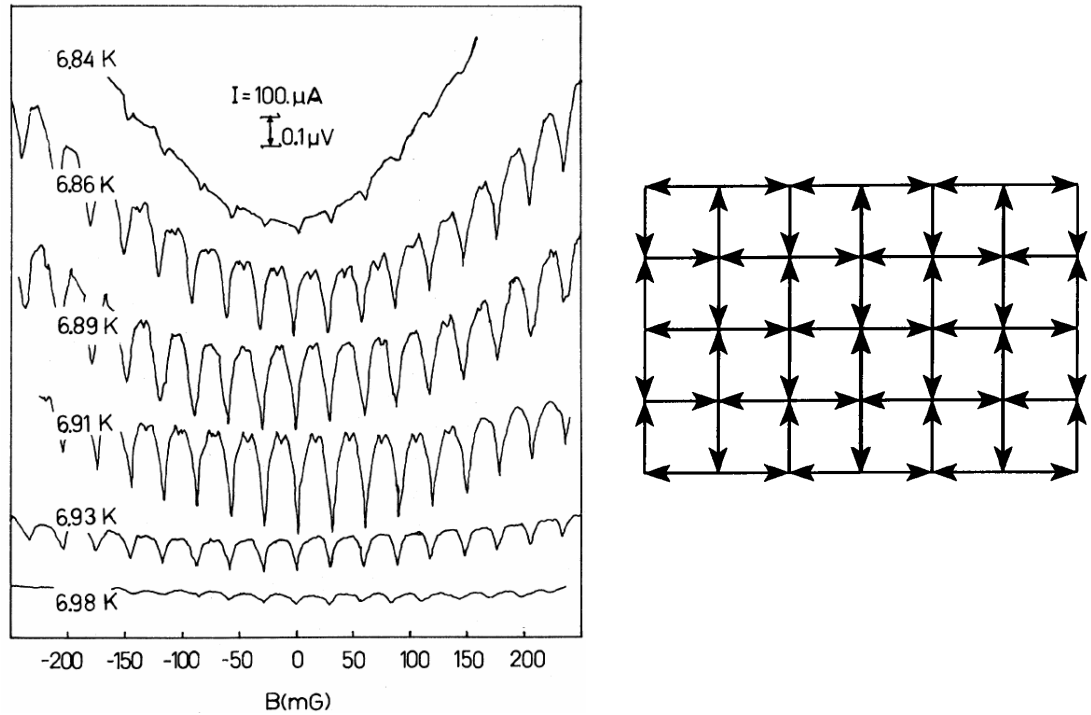

Fig. 2.21: (a) Magnetic field dependence of the resistance at various temperatures for a two-dimensional Pb-Cu 1000 × 1000 array (from [94]). (b) Currents across the Josephson weak links of a fully frustrated array with $f = 1/2$. The arrows indicate the currents flowing in the ground state (from [90].

We now focus on the field dependence of the resistance of a Josephson junction array. It can be seen from the Hamiltonian of Eq. 2.75 that the second term is periodic with magnetic field with a periodicity of integer frustration f. This implies that at integer f, when each plaquette of the array is penetrated by exactly one vortex, the Josephson coupling energy E_J is the same as at zero magnetic field. For $f = p/q$ where p and q are integers, many different ground states with periodic arrangement of vortices can be found. A special case is the maximum frustration at $f = 1/2$ when the ground state is constructed by alternating plaquettes with clockwise and counter-clockwise currents (see Fig. 2.21b). The field dependence of the resistance for a 1000 × 1000 array of superconductor-normal-metal-superconductor Josephson weak links is shown in Fig. 2.21a. The small dips at medium temperatures belong to $f = 1/2$ and the deep dips belong to integer f. Magnetoresistance isotherms with dips in resistivity at $f = p/q$ could be observed, too.

In arrays which are superconducting without an applied magnetic field, but a E_J/E_C ratio close to the critial value, a magnetic field can drive the array to the insulating regime. For such SIT a scaling analysis according to [7] was carried out with the expected values $z = 1$ and $\nu \geq 1$, but the critical resistivities were found not to be universal quantities.

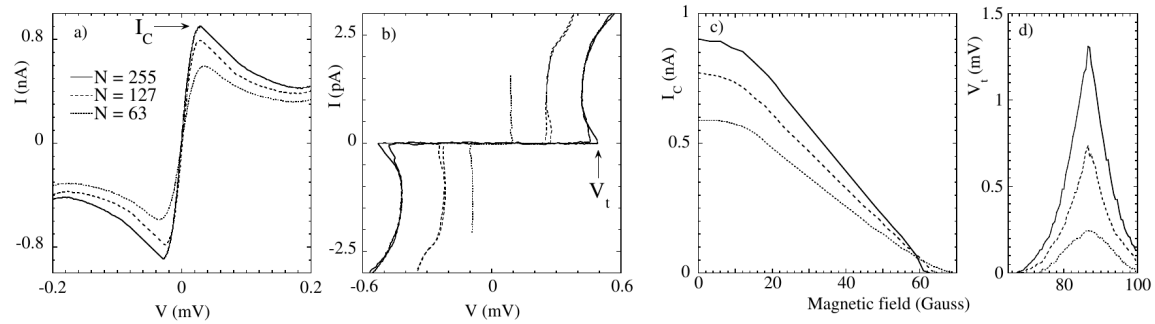

Fig. 2.22: Dependence of IV characteristics on the lenghth N of one-dimensional arrays at $T = 50\,\mathrm{mK}$. (a) At zero magnetic field the shape of the IV curves is Josephson-like with critical current I_C. (b) At $B = 71\,\mathrm{G}$ a threshold voltage V_t indicates Coulomb blockade of Cooper pair tunneling. (c) Magnetic field dependence of I_C. (d) Magnetic field dependence of V_t. (from [89])

A remarkable feature of Josephson junction arrays at low temperatures are the highly non-linear IV characteristics. For superconducting arrays a critical current exists which has its dual analogon for insulating arrays with a threshold voltage. In Fig. 2.22 the shape of the IV characteristics and the magnitude of the critical current and the threshold voltage are plotted vs. magnetic field for one dimensional Josephson junction arrays of different length [89]. The critical current vanishes with increasing magnetic field (Fig. 2.22c). Right when the field the critical value for the B-SIT, the critical current goes to zero and at higher fields a finite threshold voltage appears according to Fig. 2.22d.

A SIT accompanied by a critical current in the superconducting and a threshold voltage in the insulating phase could be observed in two-dimensional arrays and thin films as well. The threshold voltage V_T was estimated to be of the order of the characteristic energy $E = E_c \ln(L/a)$ stemming from the collective Coulomb blockade effect [95]

$$eV_T \simeq E \tag{2.86}$$

In recent years much effort has been devoted to model two dimensional thin films that undergo a SIT with Josephson junction arrays. The theory of regular Josephson junction arrays has been extended and modified, as disordered thin films may exhibit strong inhomogeneities on a mesoscopic scale. In Ref. [96] a numerical study of hopping conductivity on an irregular network of capacitors was pursued, modelling a two-dimensional insulator. The low-temperature $R(T)$ dependence is separated in two subsequent temperature regions with different slopes in the Arrhenius dependence. This is different to the $R(T)$ dependence at low temperatures for a regular network of capacitors, where a single linear slope in the Arrhenius plot is obtained.

3 Materials and Methods

3.1 Sample Properties

The two samples for which measurements are presented in this dissertation are made from the same 3.6 nm thick TiN film D03. The TiN film is grown on a 10 nm thick silicon dioxide layer on a silicon wafer. A detailed characterization of the untreated wafer is given in table 3.1 taken from Ref. [25]. The parameters change upon oxidation of the samples in air.

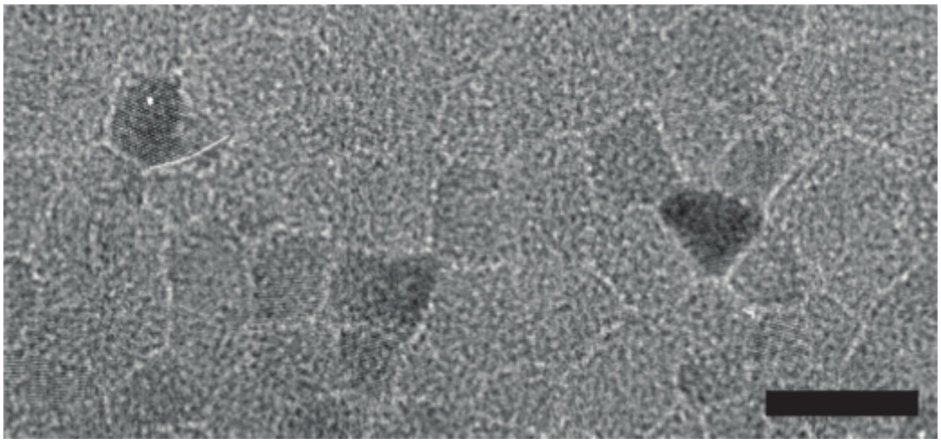

Fig. 3.1: Transmission electron microscope micrograph of a $d \approx 5$ nm thick TiN film made by Gutakovskii and Latyshev, Novosibirsk[97, 78]. Scale bar corresponds to 10 nm.

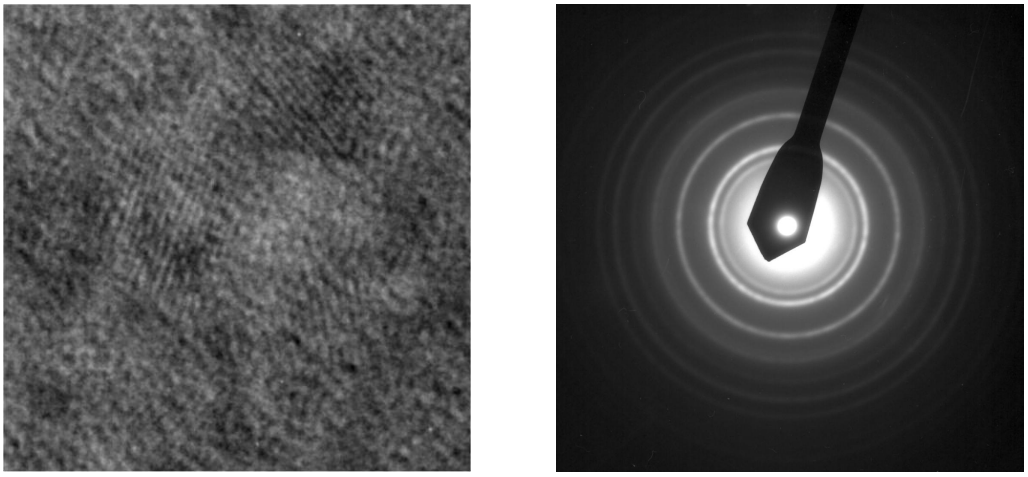

(a) **(b)**

Fig. 3.2: (a) High-resolution transmission electron microscope picture of the D03 wafer and (b) diffraction pattern of the TiN surface of the D03 Wafer, both made by Tatyana Baturina in Novosibirsk. Lateral size of figure (a) is 14 nm.

In previous works [78, 97, 98, 79] the D15 wafer was investigated. In figure 3.1 a transmission electron microscope micrograph of the D15 wafer is shown [97, 98, 78], where the polycristalline structure of the TiN film with a grain size of about 5nm can be seen. Tatyana Baturina provided a high-resolution transmission electron microscope picture of the D03 wafer which is shown in figure 3.2a. There are several areas where the crystal lattice planed are visible with a random orientation. According to these irregularities, the D03 wafer has a polycristalline structure. In figure 3.2b the diffraction pattern of the D03 wafer is shown. The rings are typical for a polycristalline film.

One of the two devices investigated in this thesis consists of a set of TiN squares with different lateral sizes ranging from 0.5 μm to 500 μm named D03_1 which is mapped in figure 3.3. The structure was patterned with optical lithography for the sizes ranging from 5 μm to 500 μm. For the smaller sizes in the middle of the chip with lateral sizes 0.5 μm, 1 μm and 2 μm, electron beam lithography was used to define the structure. First, the contacts were deposited with an 15 nm thick titanium adhesion layer and a 70 nm thick gold layer on top. After another lithography step, the square shaped structure of the TiN film was etched with Argon plasma etching. The resistances at room temperature $R_{\square}^{300\,\mathrm{K}}$ for subsequent oxidation steps are given in table 3.2. The oxidation of the sample was pursued on a 280°C hot plate in dust free air for several minutes. After each oxidation step $R_{\square}^{300\,\mathrm{K}}$ was measured before mounting the devices in the dilution refrigerator.

Parameter	value
$R_{\square}^{300\,\mathrm{K}}[\Omega]$	2520
d[nm]	3.6
l_T[nm] at $T = 4\,\mathrm{K}$	8
$T_{0.5}$[K]	1.411
T_c[K]	1.29
A	2.63
δ	0.23
T_{BKT}^{RT}[K]	1.145
b	2.14
T_{BKT}^{IV}[K]	1.147
D[cm^2/s]	0.34
n[cm^{-3}]	$1.5 \cdot 10^{22}$
$k_F l$	1.8
$\xi_d(0)$[nm]	1.145
$\lambda_d(0)$[μm]	1.7
$E_v(T_{BKT})/(k_B T_{BKT})$	2.3
I_m^+/I_c at 0.2 K	0.06

Table 3.1: Detailled characterization of the untreated wafer from Ref. [25]. $R_{\square}^{300\,\mathrm{K}}$ is the sheet resistance at room temperature, thickness d, thermal coherence length $l_T = (\hbar D/k_B T)^{1/2}$, temperature $T_{0.5}$ at which the resistance is half the normal value, critical temperature T_c of the superconducting transition, coefficient A in Eq. 2.35, pair breaking parameter δ in Eq. 2.38, temperature T_{BKT}^{RT} of the Berezinskii-Kosterlitz-Thouless transition determined by analyzing $R(T)$ measured in the linear regime according to Eq. 2.27, parameter b in Eq. 2.27, temperature T_{BKT}^{IV} of the BKT transition determined by analyzing the VI characteristics, the diffusion constant D, the electron density is n, Fermi wavenumber k_F, mean free path l is $k_F l = 1.8$, superconducting coherence length ξ_d for the "dirty" limit at $T = 0\,\mathrm{K}$, magnetic field penetration depth $\lambda_d(0)$ into a bulk sample at $T = 0\,\mathrm{K}$, screening distance $\lambda_\perp(0) = 2\lambda_d(0)^2/d$ for thin films under an applied perpendicular magnetic field, energy of a vortex $E_v = \phi_0^2/(8\pi^2\lambda_\perp)$, and the ratio I_m^+/I_c of the critical current I_m^+ taken at the maximum of dV/dI and the Ginzburg-Landau depairing current.

A optical microscope picture of the second sample named D03_S is shown in figure 3.4. The motivation to design this sample was to search for a possible screening effect due to a top-gate. The dimensions are larger than one millimeter in order to surely exceed the supposed electrostatic screening length of $\Lambda \simeq 240\,\mu$m [59]. The TiN-film between the gold pads has a length of 1.84 mm and a width of 1.036 mm. The sheet resistance determined from the measured resistance R with $R_\square = \mathrm{width/length} \cdot R = 0.563 \cdot R$. Under the 70 nm thick gold pads a 5 nm thick titanium adhesion layer was applied. Like for sample D03_1 the shape of the TiN-film of sample D03_S was etched with Argon plasma etching.

The big challenge was to measure the sample at low temperatures with and without a top-gate while the resistance at room temperature does not change. If the change

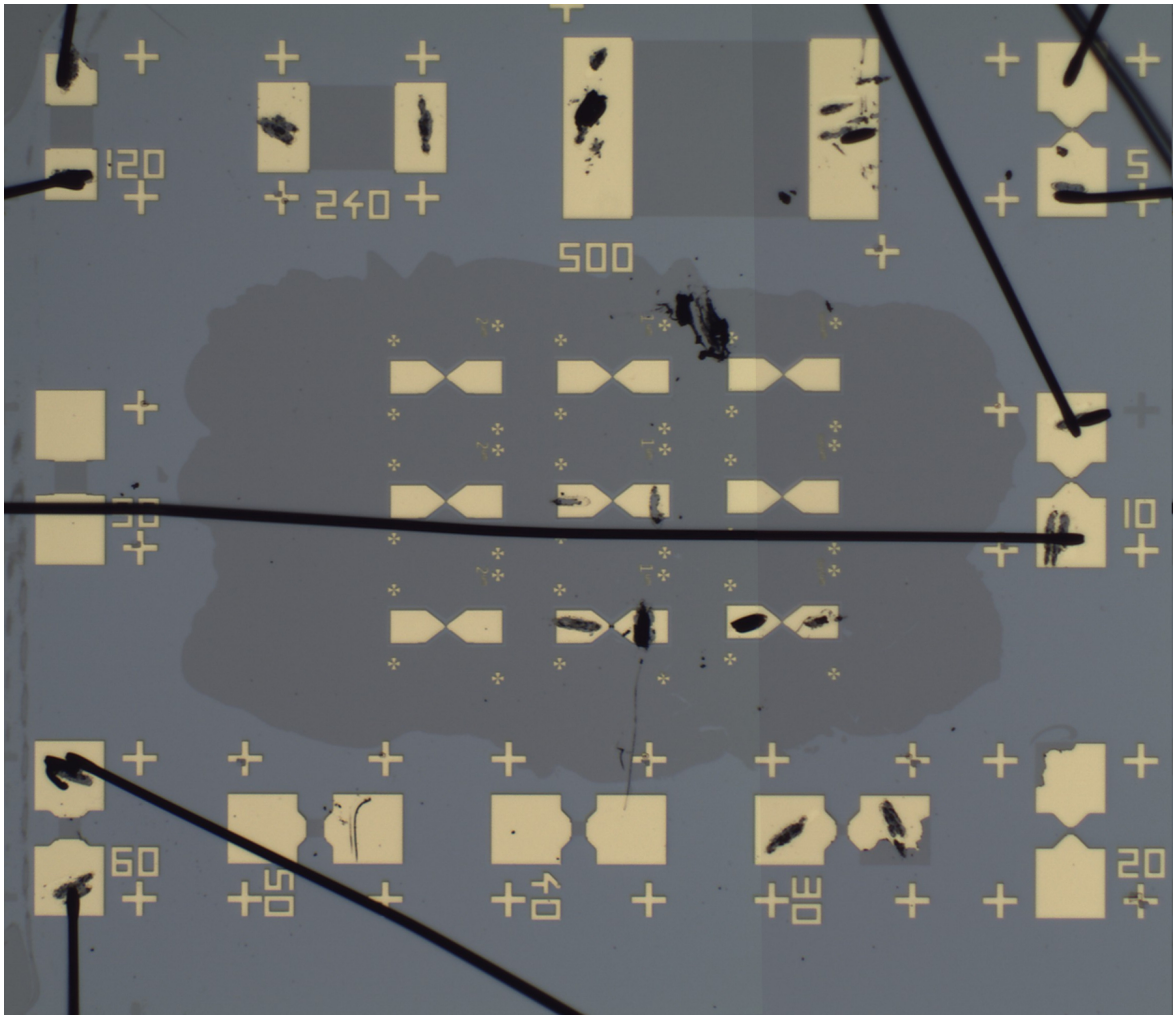

Fig. 3.3: Optical microscope picture of sample D03_1. The darker areas between the gold pads is TiN, the lighter area is the substrate.

of the resistance at room temperature was too strong, it would not be possible to distinguish between a possible screening effect and an effect due to a change of the degree of disorder in the sample. Hence a 30 nm thick layer of Al_2O_3 was put on top of the TiN-film to keep air and water vapor away from the surface of the TiN-film when it is warmed up to room temperature between the measurement periods and to electrically insulate the TiN-film from the metallic top-gate. The metallic top-gate was not evaporated directly on top of the Al_2O_3. In order to be able to remove the top-gate and measure the uncovered film again a about 30 nm thick PMMA-layer was coated on top of the Al_2O_3. On top of this PMMA-layer the 70 nm thick palladium top-gate was evaporated which completely covers the TiN-film and overlaps with the Au contact-pads without an electrical contact. There is no uncovered region of the TiN-film which would not be screened by the top-gate. The top-gate can be lifted off with dichloromethane which solves the PMMA-layer.

Both samples were glued into 20 pin chip-carriers and bonded with aluminum wires.

Fig. 3.4: Optical microscope picture of sample D03_S after eight cool-downs with and without a top-gate. The gold contacts are partially destroyed, but the TiN-film is still undamaged. The darker area between the gold pads is the TiN film, the lighter area is the substrate.

All the structuring of the samples was done by Klaus Kronfeldner in the clean room facilities at the Prof. Weiss chair at the University of Regensburg. The bonding of both samples was done with a Westbond bonder with very smooth parameters. Instead of the usual power 180, a power of 100-120 was set at the bonder in order to avoid bonding through the bond pads to the silicon substrate. Experience showed that for the standard bonding parameters a parallel conduction channel through the silicon substrate was established which essential to be avoided.

Size	untreated	1st	2nd	3rd	4th	5th
240 μm	2422	3085	3461	3740	4110	4320
120 μm	2529	3022	3521	3800	4220	4450
90 μm	-	-	-	3890	4180	4420
30 μm	2887	3114	3568	3850	4190	4500
10 μm	2436	3203	3641	3890	4220	4650
5 μm	-	-	-	4130	4400	5180
1 μm	2343	3047	3519	3483	-	4340

Table 3.2: The sheet resistance at room temperature $R_{\square}^{300\,\mathrm{K}}[\Omega]$ is given for sample D03_1 for different lateral sizes. The values for $R_{\square}^{300\,\mathrm{K}}$ were measured before the measurements in the dilution refrigerator.

3.2 Measurement Setup

Within this thesis the superconductor-insulator transition is measured. From the superconducting regime to the insulating regime resistances appear, ranging form zero resistance up to $> 100\,\mathrm{G\Omega}$ which can not be measured with the same circuitry. For low resistances a current-bias setup with a four-point geometry is needed. Line resistances and contact resistances can be avoided in the measurement. Additionally a current-bias setup is recommendable to measure superconductivity not only to see whether the sample resistivity approaches zero, but also to be able to resolve very small critical currents. Critical currents in a range of $< 1\,\mathrm{nA}$ can easily be exceeded by noise if it is measured with a voltage-bias setup. A scheme of the ac current bias setup used for measurements of the resistance in the thrid oxidation step of sample D03_1 is shown in Fig. 3.5. The Lock-in amplifier SR 830 from Stanford research systems supplied a ac voltage with a frequency below 20 Hz in order to avoid capacative effects from the leads into the cryostat. A series resistor in MΩ range defines the ac current applied to the sample. The Femto DLPVA-S voltage amplifier is connected to the voltage probes in the four terminal setup. The output of the DLPVA-S is connected to the input of the Lock in.

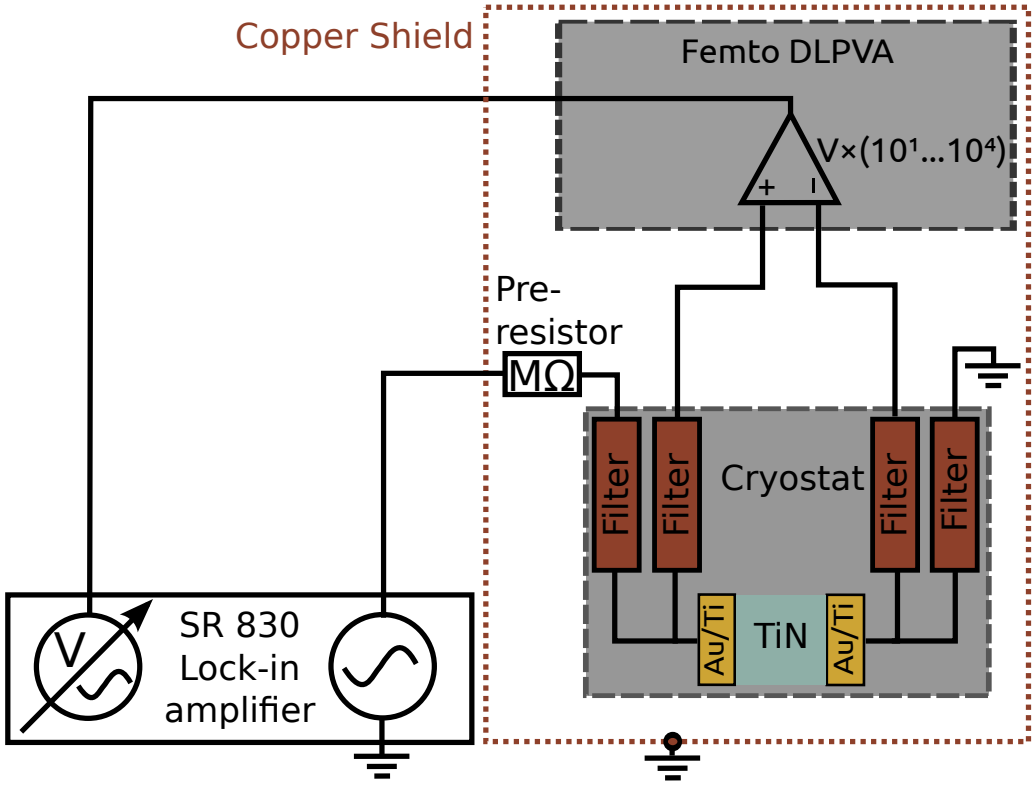

Fig. 3.5: Ac current bias setup for the measurement of low resistances.

The region focused on in this thesis is not the deeply superconducting regime, but the transition from the superconducting state to the insulating state with a resistance range of $100\,\Omega \lesssim R \lesssim 10\,\mathrm{G\Omega}$.

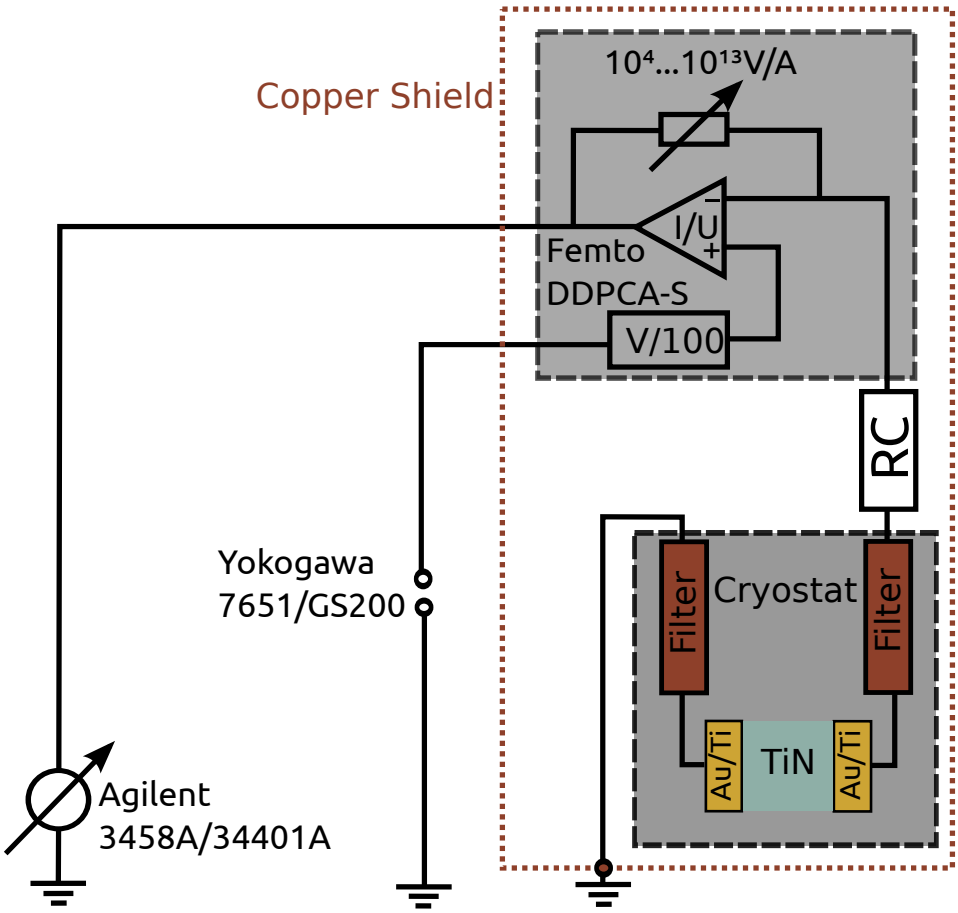

Fig. 3.6: Dc voltage bias setup for the measurement of high resistances. The rectangle marked with RC between the sample and the Femto amplifier is the optional RC-filter to protect the sample from the noise of the amplifier.

For these quite high resistances a voltage-bias setup is used which is schematically shown in figure **??**. The Yokogawa 7651 or the newer Yokogawa GS 200 are used for a dc voltage source. The GS 200 allows to make faster voltage-sweeps, where the bias voltage is set according to a voltage-list, since the time to set a voltage is shorter. These instruments were set to a fixed range mode with a voltage range which is adjusted to the applied bias range. A change of the range within a running measurement of an IV curve produces voltage peaks and therefore artefacts in the measurement. The room temperature wiring was built with coaxial cables with BNC connectors. All lines that access the copper box are fed through π filters at room temperature. Since the lines pick up noise from outside of the cryostat, a voltage divider is directly connected to the connector box of the cryostat with a division factor of at least 100. In our measurement equipment we have the Femto DDPCA-300-S, a transimpedance amplifier that converts current to voltage and additionally divides a bias voltage by 100 which is applied to the non-inverting input of the operation amplifier. For stable biasing a 8 Hz low pass filter and a voltage buffer are used. The voltage buffer transfers the voltage between two circuits, where a voltage source with a high output impedance is connected to

the input of the voltage buffer and a low impedance measurement circuit is connected to the output of the voltage buffer. The bias voltage in the measurement circuit is hence protected against an uncorrect operation due to a loading of the voltage source. No additional voltage divider is needed as in usual setups. The biasing and the conversion from current to voltage are thus provided by a single instrument. The input of the Femto preamplifier is connected to the input line of the cryostat, the other cryostat line to the sample is grounded at room temperature. The output of the Femto preamplifier is connected to a dc voltmeter, either the Agilent 3458A or the Agilent 34401A. The 3458A has a higher resolution and a higher sampling rate which is useful for faster IV sweeps. The connection between the measurement computer and the instruments is done via GPIB-cables, an optocoupler electrically decouples the computer from the instruments. Grounding is one of the biggest possibilities how to reduce noise. To avoid noise, especially at 50 Hz, usually one uses a star-point grounding to avoid ground loops through which noise from electromagnetic radiation gets picked up. However, this is not always possible. For example, the shielding of the coaxial cables with BNC connectors is on ground potential and hence ground loops are easily constructed. Since the resistance of the shielding of these coaxial cables is often too high (for example for voltage dividers), an additional grounding with a thick copper cable has to be established. This surely causes ground loops, but it is better than to work with a bad connection to ground potential. Mostly it is not the best solution to ground everything additionally with copper wires, a way in the middle has to be found in order to minimize the noise level.

Measurements performed by Ina Schneider and Klaus Kronfeldner showed that an additional RC low pass filter between the Femto preamplifier and the input lines of the cryostat affects the behaviour of the sample. Weakly superconducting states and weakly insulating states suffer from noise coming from the input of the preamplifier because the current or voltage levels in the IV curve, respectively, are similar to the noise level emitted from the preamplifier. To avoid this, an additial RC low pass filter was added between preamplifier and sample. An effect on the IV curves as well as on the resistances extracted from the IV curves was observed (for more details on the effect see Ref. [99]). Sample D03_S was measured with an RC low pass filter with $R = 20\,\mathrm{k}\Omega$ and $C = 1\,\mu\mathrm{F}$ with a cut-off frequency of $\approx 8\,\mathrm{Hz}$. Resistances below $\approx 100\,\Omega$ are not possible to measure with the setup that is optimized for high resistances due to the relatively high series resistor.

After the fourth oxidation step, a ac voltage bias measurement setup like shown in Fig. 3.7 was used to measure the zero-bias linear resistance vs. magnetic field and temperature. The bias input of the Femto DDPCA-S transimpedance amplifier was grounded with a $50\,\Omega$ cap. The superconducting as well as the insulating features in the IV characteristic are very sensitive to small offset voltages that are applied by the input of the Femto preamplifier. Therefore, the Femto amplifier offset has to be exactly zero. It is quite difficult to measure the offset voltage at the input of the amplifier with a connected multimeter. However, the offset voltage at the input can be estimated indirectly. In a first step the output offset voltage has to be adjusted to zero. Therefore the bias input gets grounded with a $50\,\Omega$ cap and the input is floating.

The voltage that is measured at the output can now be adjusted to zero. The offset screw for the offset of the output has to be adjusted carefully to reach this. After this step a resistor is connected to the input of the Femto. The other side of the resistor is grounded. The output voltage of the Femto gives a measure of the current flow through the resistor. This current is flowing due to the offset voltage at the input. The input offset voltage can now be set to zero with the input offset screw. Zero voltage at the output translates to zero voltage at the input. After this adjustment, the Femto preamplifier is ready for the measurement. For the ac voltage bias measurement, the output frequency of the Lock-in was set to $\lesssim 5\,\mathrm{Hz}$. The voltage divider had a ratio of about 1000 to keep the excitation voltage at the sample small, but the signal from the lock in to the voltage divider high. The ratio of the picked up noise to the signal is reduced in this way.

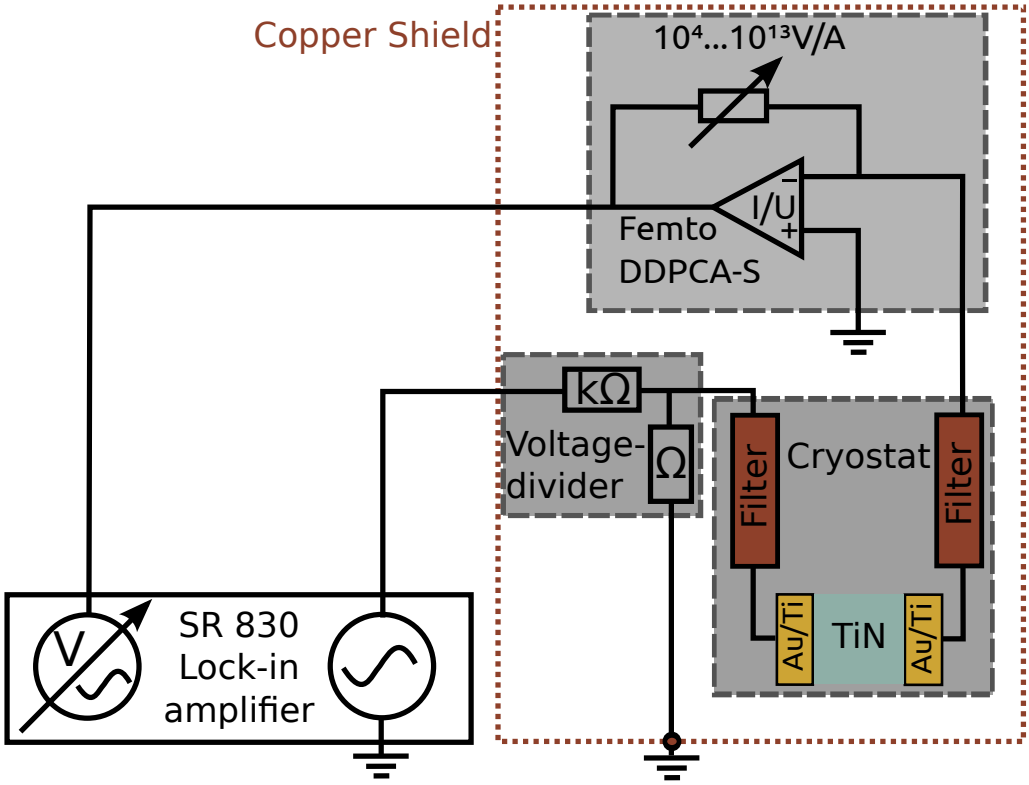

Fig. 3.7: Ac voltage bias setup for the measurement of high resistances.

All measurements were performed in two different dilution cryostats with base temperatures of $25 - 35\,\mathrm{mK}$. Cryostat I is surrounded with a grounded copper box to shield radiation, all lines are filtered with π-filters at room temperature and copper powder filters at the mixing chamber level with a base temperature of $\approx 35\,\mathrm{mK}$ and at the $T = 100\,\mathrm{mK}$-level. The superconducting magnet allows to apply fields ranging from $-8\,\mathrm{T} \leq B \leq 8\,\mathrm{T}$. In cryostat II all lines have π filters at room temperature and copper powder filters at the mixing chamber level with a base temperature of $\approx 25\,\mathrm{mK}$. In this cryostat fields up to $|B| = 17\,\mathrm{T}$ can be applied. Sample D03_S was measured

exclusively in cryostat I. Sample D03_1 was measured in cryostat I for all oxidation steps, except the fourth which was pursued in cryostat II.

4 Multiple crossovers of magnetoresistance isotherms

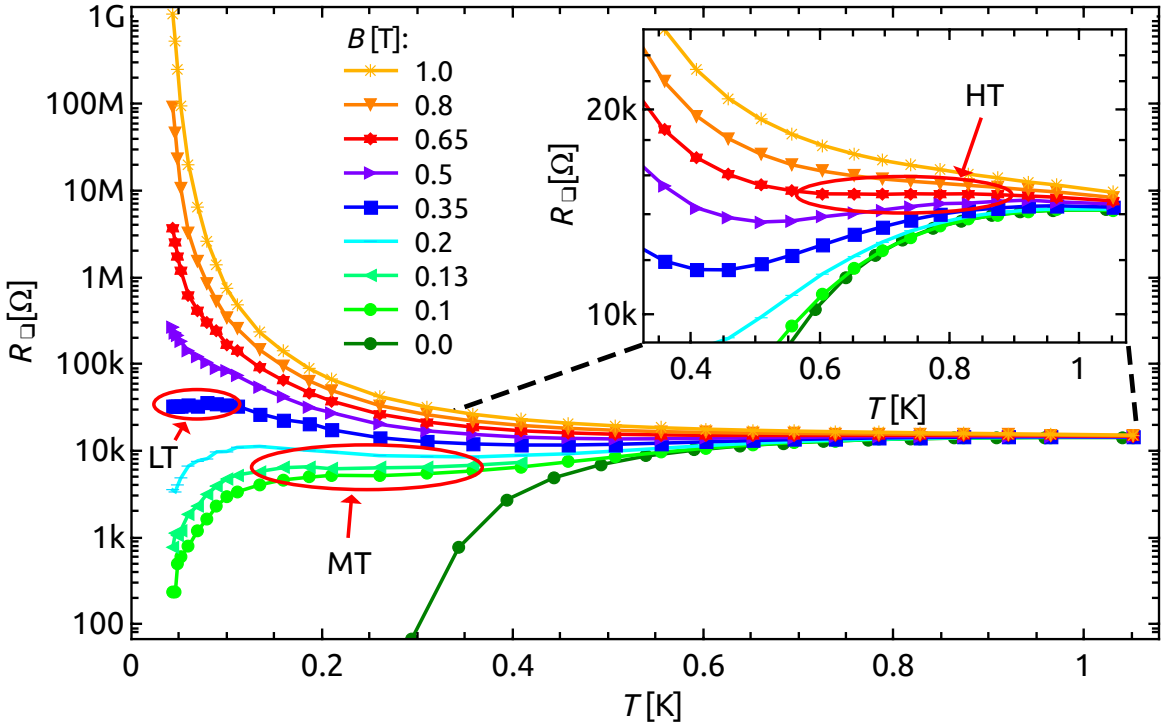

Fig. 4.1: $R(T)$ curves of sample D03_S for several magnetic fields for temperatures ranging from 37 mK to 1.04 K. The sample is superconducting for zero field and low temperatures and showes a transition to an insulating state for low temperatures at highest fields shown here. Three plateaus in the $R(T)$ curves can be observed, marked with red ellipses.

The $R(T)$ curves of sample D01_S shown in Fig. 4.1 reveal a magnetic field induced SIT at lowest measured temperatures. The zero field $R(T)$ dependence indicates a superconducting transition with a vanishing resistance for temperatures below ≈ 300 mK. Upon increasing the magnetic field, the temperature at which the resistance vanishes is lowered. For $B = 0.13$ T the $R(T)$ develops a plateau for temperatures ranging from 120 mK to 350 mK. This medium-temperature (MT) plateau in the $R(T)$ corresponds to the crossing point in the magnetoresistance isotherms shown in Fig. 4.2b at $B_{cM} = 0.15$ T. Upon exceeding a magnetic field of about $B = 0.35$ T, the decrease of the resistance at lowest temperatures turns to an increase of the resistance at lowest temperatures. The magnetic field that corresponds to the seperatrix in the $R(T)$

curves between the superconducting and insulating tendencies at low temperatures (LT), is revealed as the magnetic field of the crossing point in the $R(B)$ isotherms in Fig. 4.2a at $B_{cL} = 0.36\,\mathrm{T}$. The low-temperature crossing-point (LT) in the magnetoresistance isotherms emerges at temperatures below 100 mK and persists down to the lowest measured temperature with 36 mK. For magnetic fields in a range of $0.15\,\mathrm{T} < B < 0.65\,\mathrm{T}$ the $R(T)$ curves develop a minumum which emerges from the MT plateau at $B_{cM} = 0.15\,\mathrm{T}$ and vanishes with the formation of another plateau in the $R(T)$ curves for $B = 0.65\,\mathrm{T}$ in a high temperature (HT) range of about 590 mK to 950 mK.

In total, three plateaus are identified in the $R(T)$ curves with corresponding crossing points in the magnetoresistance isotherms. In Fig. 4.2d a zoom into the positive magnetoresistance is depicted for the magnetoresistance isotherms within the complete temperature range. The position of the LT-, MT- and HT crossing points are marked by red circles.

In the next sections the crossing points in the magnetoresistance istherms are analyzed as follows:

- The found plateaus in the $R(T)$ curves and the corresponding crossing points in the magnetoresistance isotherms motivated a phenomenological description of the $R(T, B)$ in the three temperature regimes LT, MT and HT with respect to magnetic fields $B_{cL,cM,cH}$ and the associated resistances $R_{cL,cM,cH}$.

- Based on the theory of finite size scaling [7, 8], a crossing point in the magnetoresistance isotherms might be the point of the SIT quantum phase transition. A scaling analysis allows to gain information about the physics of the system at a quanum phase transition, without the knowledge of microscopic details.

- In order to test for alternative phenomenological descriptions of the $R(T, B)$ in the MT and LT regimes, a modified scaling approach is pursued.

- The LT regime reveals highly nonlinear IV characteristics that show insulating steps and superconducting features at the same time for $0.2 \lesssim B \lesssim B_{cL} = 0.36\,\mathrm{T}$.

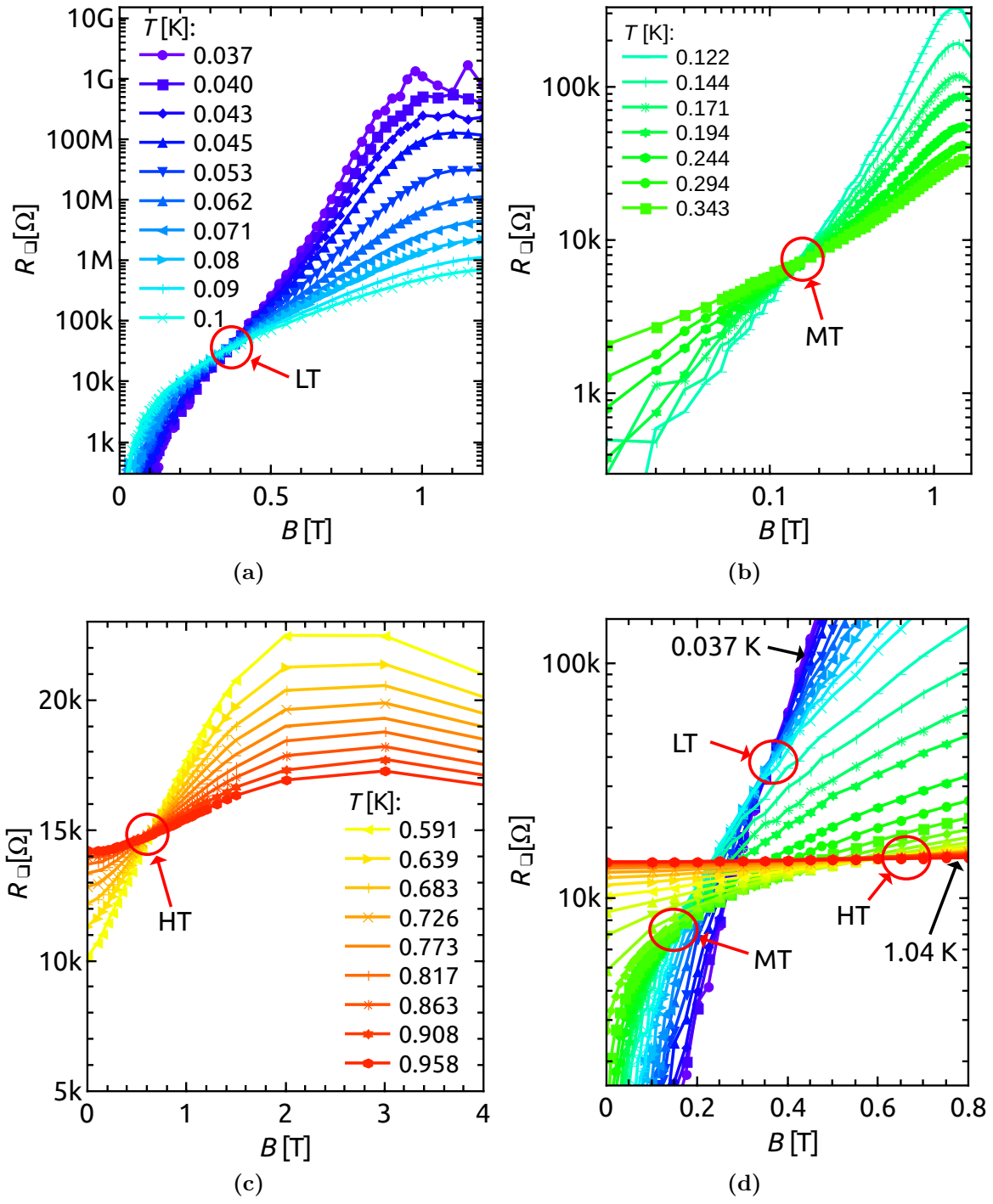

Fig. 4.2: Magnetoresistance isotherms of sample D03_S with marked crossing points. (a) shows the LT region of the $R(B)$ curves, (b) shows the MT region of the $R(B)$ curves and (c) shows the HT region of the $R(B)$ curves. In (d) a zoom into the positive magnetoresistance for all measured temperatures is shown to visualize the relative position of the crossing points to each other.

4.1 Phenomenological description of the three crossing points

4.1.1 Low temperatures (LT)

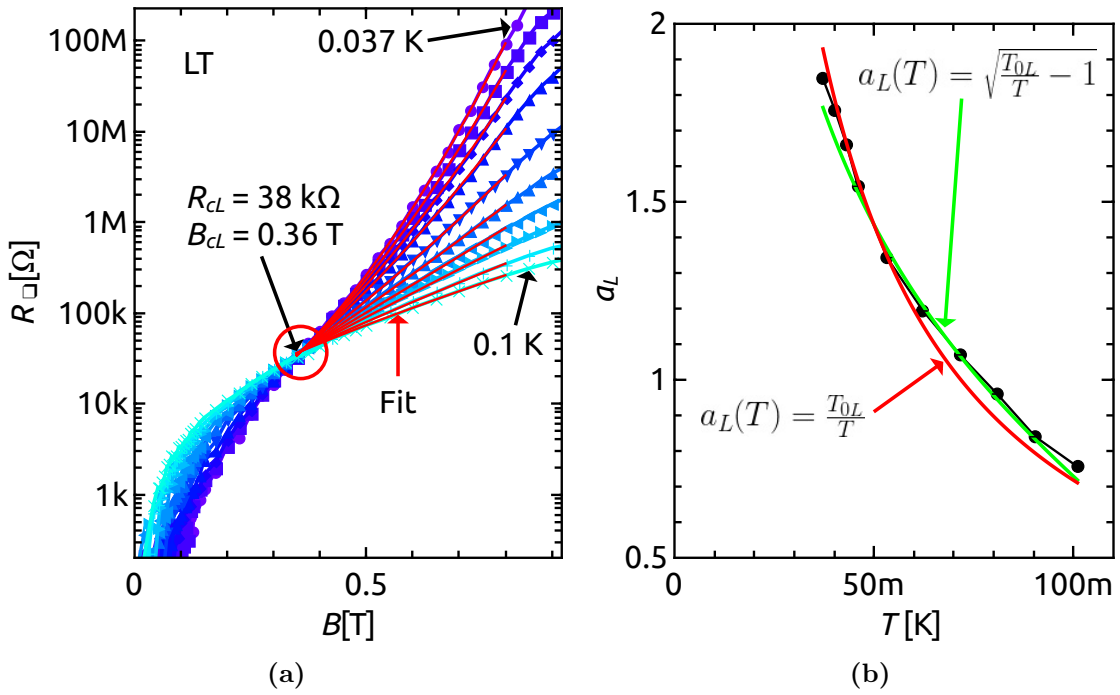

Fig. 4.3: (a) Fit of the magnetoresistance isotherms at low temperatures (LT) with Eq. 4.1. (b) Temperature dependence of the exponent a_L. Two fits with different fitting functions are shown.

Below 100 mK the low-temperature (LT) crossing point appears at $B_{cL} = 0.36\,\mathrm{T}$ and at $R_{cL} = 38\,\mathrm{k\Omega}$. Fig. 4.3a shows the corresponding magnetoresistance isotherms for the LT crossing point. While for zero field the sample is superconducting, the resistance $R_\square$ increases to $\approx 1\,\mathrm{G\Omega}$ at $B_{peak} \approx 1\,\mathrm{T}$. For $B_{cL} \leq B \lesssim 0.8\,\mathrm{T}$ the data can be described by the following phenomenological expression:

$$R(T,B) = R_{cL} \cdot \exp\left\{A \cdot \left[\left(\frac{B}{B_{cL}}\right)^{a_L(T)} - 1\right]\right\} \tag{4.1}$$

where $A \approx 2.4$ is a dimensionless parameter that is kept constant, while $a_L(T)$ was adjusted for each curve seperately. The red lines in Fig. 4.3a correspond to the B-dependence of Eq. 4.1. The phenomenological fit works for resistances ranging from 38 kΩ upt to 100 MΩ which are more than three orders of magnitude in resistance.

The temperature dependence of $R(T,B)$ is in the exponent $a_L(T)$ which is plotted in Fig. 4.3b. Two fits with different functions for $a_L(T)$ are shown in Fig. 4.3b.

The red curve is a fit to $a_L(T) \propto 1/T$ which corresponds to a double exponential activated behaviour: $R(T) \propto \exp(\exp(T_{0L}/T))$. The fit works best for $T \lesssim 50\,\mathrm{mK}$. The activation energy for this fit is $T_{0L} = 0.072\,\mathrm{K}$. In accordance with the double exponential $R(T)$ dependence, the Arrhenius plot of the $R(T)$ curves for $B_{cL} < B \leq 1\,\mathrm{T}$ reveals a more than thermally activated behaviour below $T \lesssim 50\,\mathrm{mK}$ (see Fig. 4.4). The try to fit $a_L(T)$ with the temperature dependence in Eq. 2.85 [59], does not reproduce the data points properly. Instead $a_L(T) = \sqrt{T_{0L}/T - 1}$, which is the green curve in Fig. 4.3b, fits the data points for $50\,\mathrm{mK} \lesssim T \lesssim 100\,\mathrm{mK}$ with $T_{0L} = 0.153\,\mathrm{K}$. We are not aware of any theory which could explain this dependence of a_L on temperature.

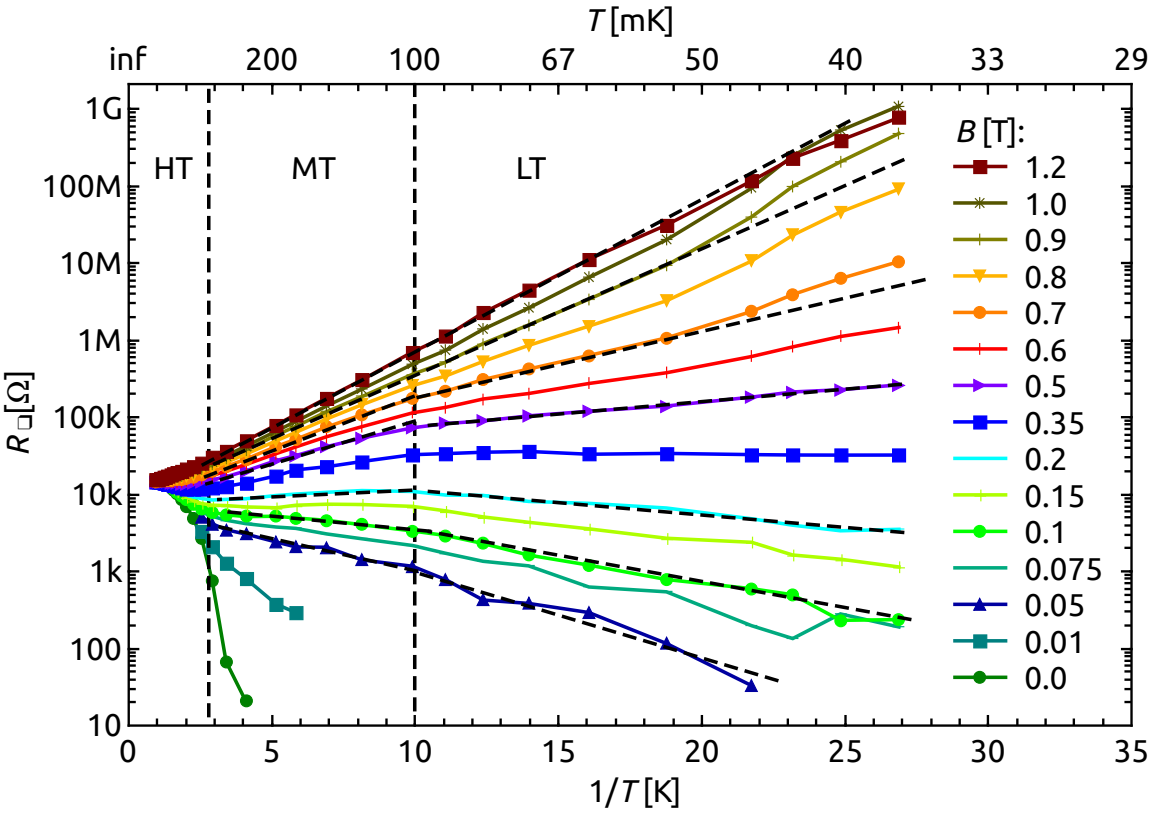

Fig. 4.4: $R(T)$ curves of sample D03_S for several magnetic fields in an Arrhenius plot where the R is scaled logarithmically and temperature as $1/T$. The separations of the LT, MT and HT temperature regimes are indicated by the dashed vertical lines at $T = 100\,\mathrm{mK}$ and $T = 350\,\mathrm{mK}$. The straight dashed black lines on top of the measured $R(T)$ curves are a guide to the eye to check for thermally activated behaviour. In the MT regime thermally activated behaviour for magnetic fields ranging from $B = 0.05\,\mathrm{T}$ up to $B = 1.2\,\mathrm{T}$ is observed. This is consistent with $a_M(T) \propto 1/T$ in Eq. 4.2. In the LT regime for $B_{cL} < B \leq 1\,\mathrm{T}$, the $R(T)$ curves evolve a more than activated behaviour. However, when the temperature window in the Arrhenius plot is restricted to $50\,\mathrm{mK} \lesssim T \lesssim 100\,\mathrm{mK}$, the $R(T)$ curves for $B_{cL} < B \leq 1\,\mathrm{T}$ indicate thermally activated behaviour.

In the latter temperature regime $50\,\mathrm{mK} \lesssim T \lesssim 100\,\mathrm{mK}$, the $R(T)$ curves behave

linear in the Arrhenius plot in Fig. 4.4. This $R(T)$ dependence indicates thermally activated behaviour. However, this linear $R(T)$ in the Arrhenius plot for this rather small temperature interval can also be produced by a change from the activated behaviour in the MT regime to a more than activated behaviour in the LT regime and a corresponding change from a concave shape around $T = 100\,\mathrm{mK}$ to a convex shape at lowest temperatures. The continuous change from concave to convex, forms a linear region in the Arrhenius plot within the measurement accuracy. Both, the change of curvatures and thermally activated behaviour are possible explanations for the linear regions in the Arrhenius plot. But the phenomenological description of the temperature dependence by Eq. 4.1 describes a more than thermally activated behaviour. The change of curvatures hence seems to be the appropriate reson for the linear region in the Arrhenius plots.

4.1.2 Medium temperatures (MT)

At medium temperatures (MT) $120\,\mathrm{mK} \lesssim T \lesssim 350\,\mathrm{mK}$ there is another common intersection point for the $R(B)$-curves at $B_{cM} = 0.148\,\mathrm{T}$ and $R_{cM} = 7\,\mathrm{k\Omega}$ (figure 4.5a). The behaviour of the $R(T, B)$-curves on both sides of the crossing point for $400\,\Omega \lesssim R \lesssim 100\,\mathrm{k\Omega}$ can be described with the expression:

$$R(T,B) = R_{cM} \cdot \exp\left\{ a_M(T) \cdot \left[\left(\frac{B}{B_{cM}} \right)^{1/4} - 1 \right] \right\} \tag{4.2}$$

The function $a_M(T)$ is well described by $a_M \propto 1/T$ (see figure 4.5b), e.g. Eq. 4.2 corresponds to a simple activated behaviour with a magnetic field dependent activation energy of

$$T_{0M}(B) = T_{0M} \cdot \left[\left(\frac{B}{B_{cM}} \right)^{1/4} - 1 \right] \tag{4.3}$$

where $T_{0M} = 0.73\,\mathrm{K}$ which is about double the value of the upper temperature limit (350 mK) for the MT regime. The thermally activated behaviour can also be seen for the $R(T)$ curves in the MT regime (see Fig. 4.4. In figure 4.5c the magnetoresistance isotherms for the MT region are plotted as $\log(\log R)$ vs. $\log B$. The dashed black lines in figure 4.5c are a guide to the eye and show a linear behaviour of the $R(B)$ curves in the given plot. This means that the logarithm of R follows a powerlaw dependence on B: $R \propto \exp(B^\alpha)$. From the fit in figure 4.5a the exponent α can be evaluated to be 1/4 with an error of two percent. The fitting-range, where formula 4.2 is fitted to the measured $R(B)$ curves, reaches from 0.03 T up to 0.8 T. This corresponds to a variation in resistance from $\approx 1\,\mathrm{k\Omega}$ up to $\approx 150\,\mathrm{k\Omega}$ which is more than two orders of magnitude.

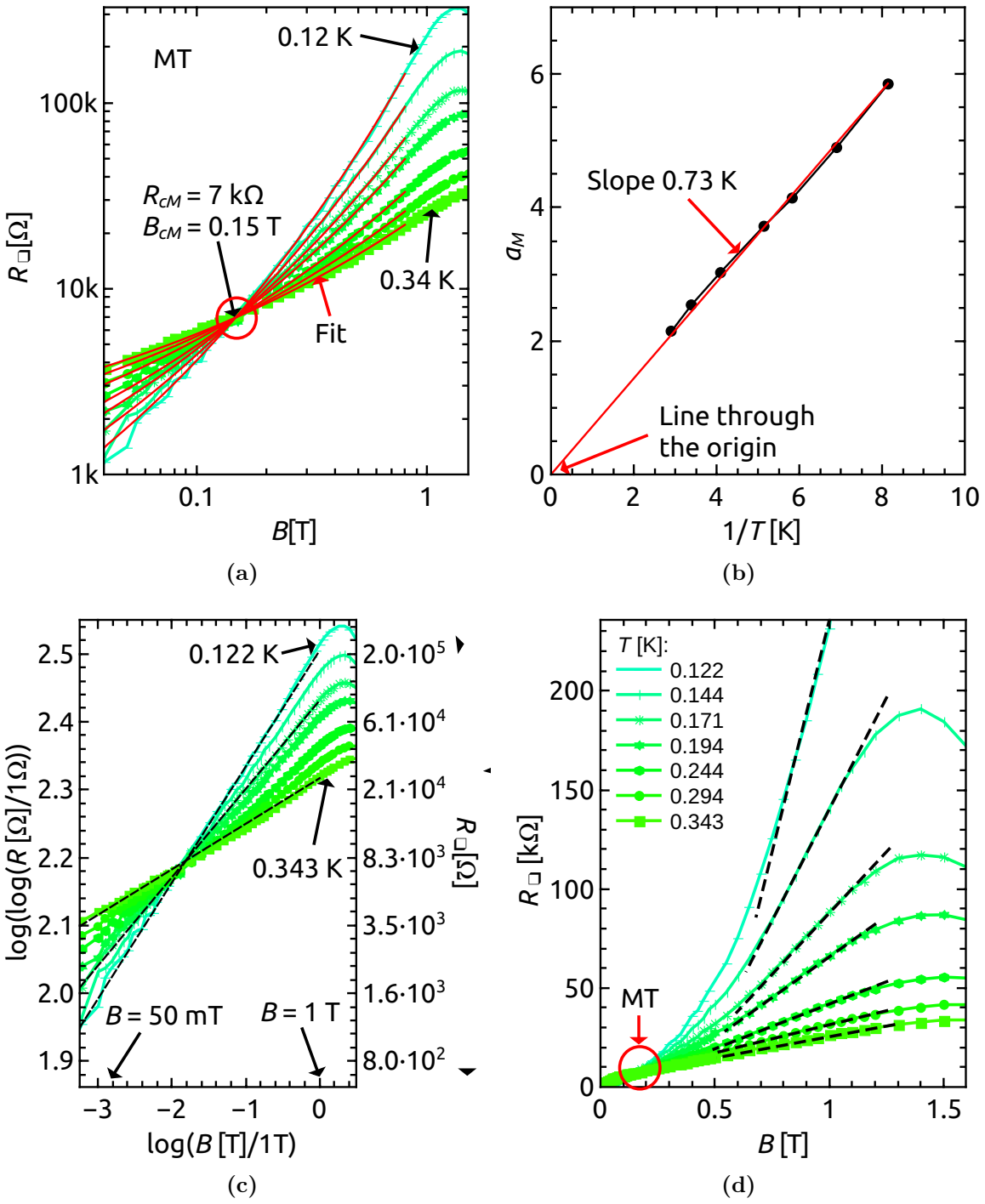

Fig. 4.5: (a) Fit of the magnetoresistance isotherms at medium temperatures (MT) with formula 4.2 A linear behaviour of the $R(T)$ curves in the presented double logarithmic plot indicate a powerlaw with $R \propto B^{\alpha}$. The alternative scaling analysis in Fig. 4.8b allows for the description of the $R(B)$ isotherms with the latter powerlaw for resistances up to $\lesssim 20\,\mathrm{k\Omega}$. However, the alternative scaling presented in Fig. 4.8a, corresponding to Eq. 4.2, shows that Eq. 4.2 promises a more appropriate description of the $R(T, B)$ from lowest measured resistances up to almost the magnetoresistance maximum than a simple powerlaw. (b) Temperature dependence of a_M vs. $1/T$. As $a_L(T) = 0.73\,\mathrm{K}/T$, $R(T)$ has temperature activated behaviour. (c) shows a plot of $\log(\log R)$ vs. B. (d) $R(B)$ in a linear plot. At high fields $B \gg B_{cM}$ the dashed black lines indicate a linear $R(B)$ (see section 9.1).

4.1.3 High temperatures (HT)

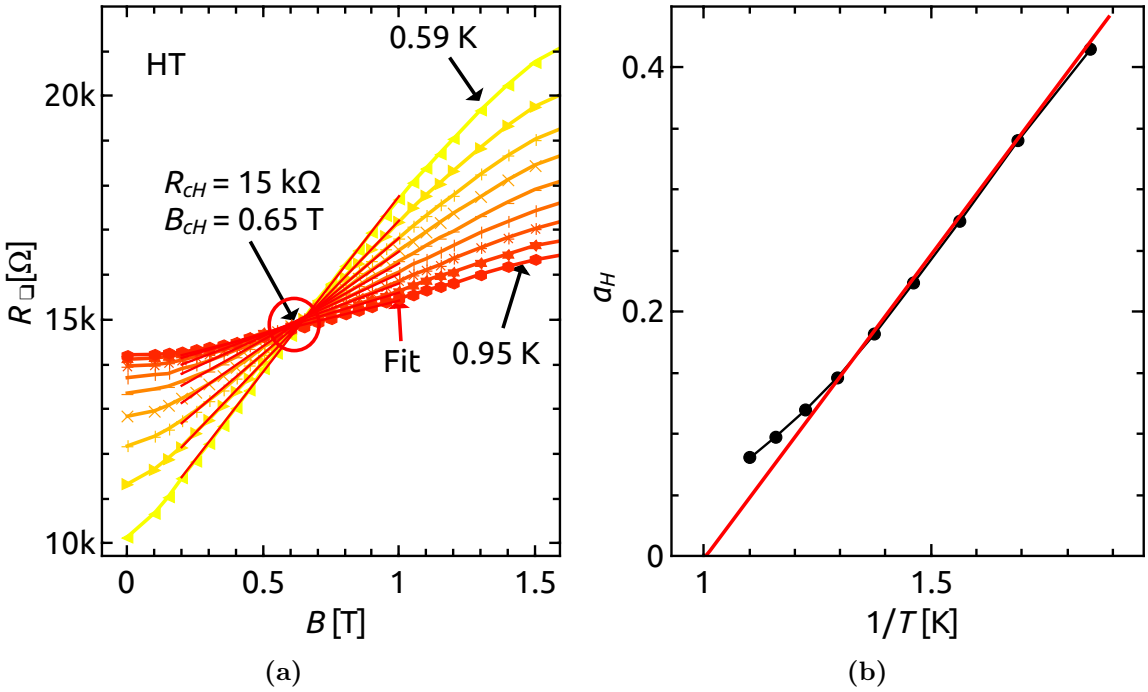

Fig. 4.6: (a) Fit of the magnetoresistance isotherms for high temperatures (HT) with formula 4.4 which is linear in B. (b) Temperature dependence of a_H vs. $1/T$. $a_L(T) = (0.96\,\mathrm{K} - T)/2T$ is depicted by the red line.

The third crossing point (HT) appears at relatively high temperatures between 0.59 K and 0.95 K at $B_{cH} = 0.65\,\mathrm{T}$ and $R_{cH} = 15\,\mathrm{k\Omega}$ (see figure 4.6a). Around B_{cH} the magnetoresistance isotherms are linear with magnetic field:

$$R(T,B) = R_{cH} \cdot \left[1 + a_H(T) \cdot \left(\frac{B}{B_{cH}} - 1\right)\right] \tag{4.4}$$

with $a_H(T) = (T_{0H} - T)/2T$ and $T_{0H} = 0.96\,\mathrm{K}$ (see figure 4.6b) which coincides with about the upper temperature limit (0.95 K) for the HT crossing point. The fit of formula 4.4 works for a small resistance range compared to the above LT and MT fits, i.e. from 12 kΩ to 18 kΩ. This corresponds to a clearly metallic-like regime, as opposed to the strongly insulating behaviour at lower temperatures.

4.2 Scaling behaviour near the crossing points

4.2.1 The finite size scaling approach

Around a critical point finite size scaling should be possible [7, 8]. For each of the three crossing points finite size scaling is possible as shown in figure 4.7. The value for $z\nu$ was estimated on the basis of the following considerations. The dependence of the resistance on the scaling variable $|B - B_{cL,cM,cH}|/T^{1/z\nu}$ is given by

$$R = R_{cL,cM,cH} \cdot f\left(\frac{|B - B_{cL,cM,cH}|}{T^{1/z\nu}}\right) \tag{4.5}$$

where f is an unknown scaling function. The derivative $\partial R/\partial B$ at $B = B_{cL,cM,cH}$ reads

$$\left.\frac{\partial R}{\partial B}\right|_{B=B_{cL,cM,cH}} = R_{cL,cM,cH} \cdot f'(0) \cdot T^{-1/z\nu} \tag{4.6}$$

The exponent $z\nu$ is then given by the linear slope in the plot of $\log\left\{\left.\frac{\partial R}{\partial B}\right|_{B=B_{cL,cM,cH}}\right\}$ vs. $\log T$. The scaling plots that are obtained by these exponents $z\nu$ for the LT, MT and HT crossing points, are depicted in Fig. 4.7.

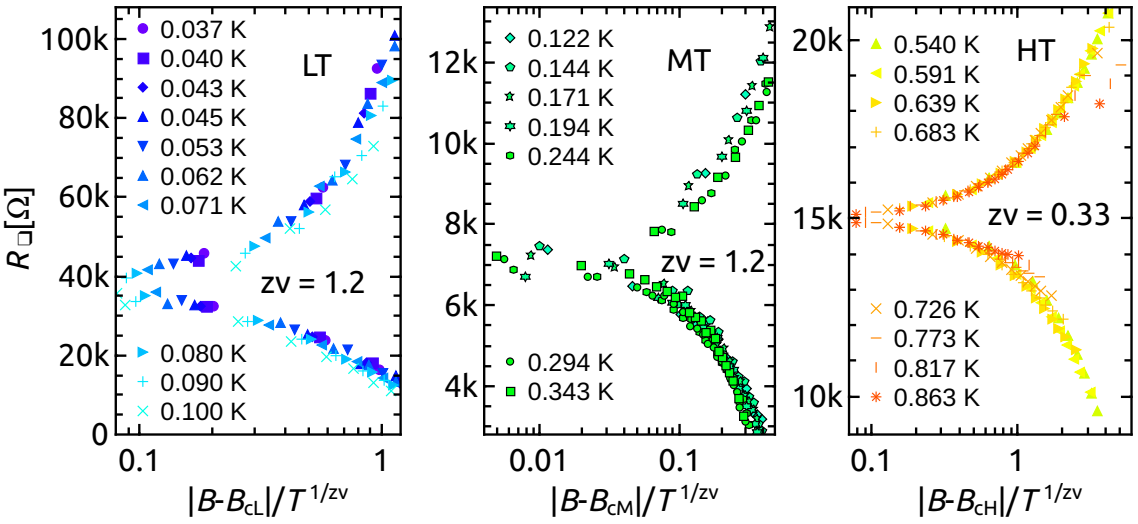

Fig. 4.7: Finite size scaling for the LT (left), MT (middle) and HT (right) crossing points in the magnetoresistance isotherms. The abscissa is scaled according to the scaling variable $|B - B_{cL,cM,cH}|/T^{1/z\nu}$ with the values for zv given in the plots.

For the LT and MT crossing points the obtained critical exponents $z\nu \approx 1.2$ are similar to what has been found previously in indium oxide [84, 45]. $z = 1$ would be expected for a bosonic system with long ranged Coulomb interactions independent of dimensionality d, and $\nu \geq 2/d = 1$ is believed to be in the universality class of the SIT in two dimensions in the dirty limit, as described by the (2+1)D XY model, for

the magnetic field driven as well as for the disorder driven SIT [83, 7, 8]. The long ranged Coulomb interaction, which corresponds to a logarithmic charging interaction up to the electrostatic screening length in the system and an exponential decrease of the charging energy for larger distances, is a key feature in the vortex charge duality picture for the SIT proposed in Ref. [7]. For the HT crossing point a much smaller $z\nu \approx 0.33$ is found. This is not expected for a disordered system with long ranged Coulomb interactions. From the standpoint of finite size scaling the MT crossing point as well as the LT crossing point are candidates for a SIT quantum phase transition originating from vortex charge duality at the SIT with $z\nu \geq 1$ [7].

4.2.2 Alternative scaling approach for the MT regime

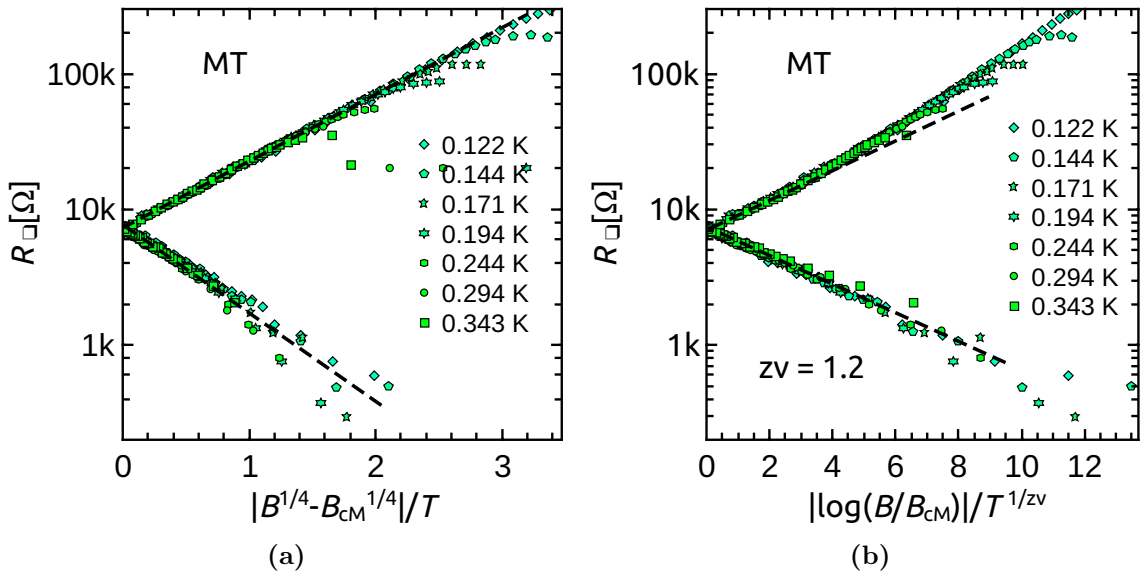

Fig. 4.8: Alternative scaling plots for the MT regime. (a) The argument of Eq. 4.2 is taken for the scaling variable. Dashed lines on the upper and lower branch indicate the linear behaviour in the logarithmic plot. (b) To test for a powerlaw behaviour of the $R(B)$ isotherms, the logarithmic scaling variable used here would lead to a linear slope in the presented logarithmic plot. Dashed lines indicate deviations in the upper branch.

We begin a more detailled analysis of the phenomenological description of the $R(T, B)$ with the MT regime. Though $(B - B_c)/T^{1/z\nu}$ from [7] is commonly taken to be the the scaling variable for the magnetic field driven SIT, it is possible to find other scaling variables which produce a much better collapse of the $R(B, T)$ data in a scaling plot. In the MT regime the phenomenological Eq. 4.2 contributes a different scaling function. A collapse of the $R(T, B)$ data can be achieved on the basis of Eq. 4.2 when for the scaling variable $|B^{1/4} - B_{cM}^{1/4}|/T$ is taken instead of $|B - B_{cM}|/T^{1/z\nu}$. The quality of the corresponding scaling plot can be viewed in Fig. 4.8a. A collapse of the $R(T, B)$ data is obtained for a resistance range of more than two orders of magnitude, from

lowest measured resistances of around $\approx 1\,\mathrm{k}\Omega$ almost up to the temperature dependent magnetoresistance maximum. A second alternative scaling variable provides an equally well collapse of the $R(T,B)$ data in an scaling plot presented in Fig. 4.8b. There, the scaling variable $|\log(B/B_{cM})|/T^{1/z\nu}$ with $z\nu = 1.2$ forces the $R(T,B)$ curves to lie on top of each other for the same resistance and field ranges than in the $|B^{1/4} - B_{cM}^{1/4}|/T$ case. A difference between the two latter scaling plots occurs for the upper branches in Figs. 4.8a and 4.8b, where for the scaling variable $|B^{1/4} - B_{cM}^{1/4}|/T$ a linear dependence in the logarithmic plot (log-scale for $R_\Box$) resembles the phenomenological Eq. 4.2. In Fig. 4.8b an upturn in the upper branch indicates that a simple powerlaw behaviour for the magnetoresistance isotherms is too weak to serve as a scaling function. This upturn was interpreted as "breakdown of duality" in Ref. [45].

4.2.3 Alternative scaling approach for the LT regime

For the LT regime a alternative scaling analysis that is similar that for the MT regime allows us to distinguish between different phenomenological descriptions of the $R(T,B)$. A scaling analysis for the LT crossing point with the scaling variables $|B^{1/4} - B_{cL}^{1/4}|/T^{1/z\nu}$ and $|\log(B/B_{cM})|/T^{1/z\nu}$ is depicted in Fig. 4.9. For the former scaling variable the $R(T,B)$ data collapses for a resistance range from $\approx 1\,\mathrm{k}\Omega$ to a few hundred $k\Omega$ (see Fig. 4.9a), while for the logarithmic scaling in B the $R(T,B)$ curves stay at the same trace up to $M\Omega$ range (see Fig. 4.9b).

We first take a look at the lower branches in Figs. 4.9a and 4.9b and in doing so we consider $B < B_{cL}$. A powerlaw dependence of the magnetoresistance seems to underestimate the increase in resistance, since there is an upturn in the scaling plot for the logarithmic scaling variable in Fig. 4.9b. However, the lower branch in Fig. 4.9a for the scaling variable $|B^{1/4} - B_{cL}^{1/4}|/T^{1/z\nu}$ exhibits a linear slope and therefore resembles the phenomenological formula Eq. 4.2 for the MT regime with the critical parameters for the LT crossing point B_{cL} and R_{cL}.

The upper branches in the two alternative scaling plots show a similar shape, apart from the difference in the resistance range up to which scaling produces a collapse in $R(T,B)$. For both upper branches the upturn excludes a powerlaw behaviour as well as Eq. 4.2 to serve as scaling functions.
Instead, Eq. 4.1 can be taken as the scaling function for the LT $R(T,B)$ for $B > B_{cL}$. But in order to obtain a collapse of the $R(T,B)$ data in the according scaling plot, the temperature dependence of the scaling variable has to be known. We are not sure about the physics of the temperature dependence of the LT regime, as already discussed above. The best fit for $a_L(T)$ was achieved by the square-root temperature dependence $a_L(T) = \sqrt{T_0/T - 1}$ with $T_{0L} = 0.153\,\mathrm{K}$. In Fig. 4.9c a scaling plot with the scaling variable $B/B_{cL}^{a_L(T)} - 1$ with the square-root $a_L(T)$ is presented. The data collapses well over more than four orders of magnitude in resistance. From the linear slope of the upper branch the phenomenological Eq. 4.1 is verified.

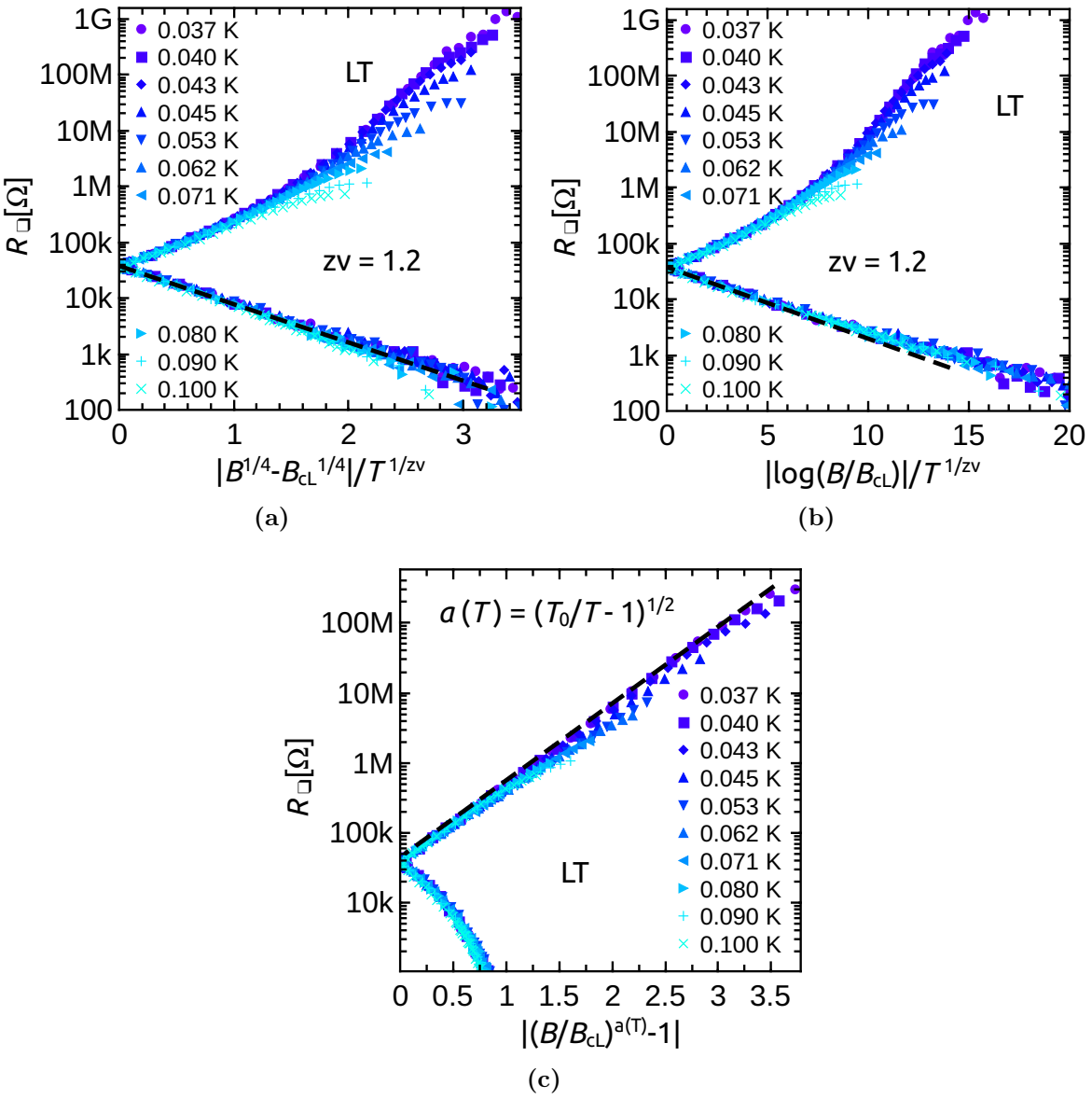

Fig. 4.9: Alternative scaling plots for the LT regime. (a) The argument of Eq. 4.2 is taken for the scaling variable. The dashed line in the lower branch is in accordance with the finding that Eq. 4.2 fits well for the LT regime for $B < B_{cL}$. (b) Analogous scaling plot to 4.8b, adapted for the LT regime. The powerlaw of $R(B)$ even underestimates the lower branch not just the upper one. (c) The argument of Eq. 4.1 served as scaling function for this scaling plot. The dashed line in the upper branch indicates that Eq. 4.1 is resembled.

As a concluding remark to the alternative scaling plots presented here it must be said that these scaling plots should not be taken as an alternative way to investigate the SIT as a quantum phase transition. For the latter purpose finite size scaling like presented in Fig. 4.7 is the only known possibility up to now. The alternative scaling plots with their corresponding scaling variables are used to verifiy the phenomenological Eqs. 4.2 and 4.1 against a powerlaw behaviour, and to give an impression about the quality of

the fits of Eqs. 4.2 and 4.1 to the measured data, with the tool of scaling plots.

4.2.4 Coexistence of superconducting and insulating behaviour in IV curves near to B_{cL}

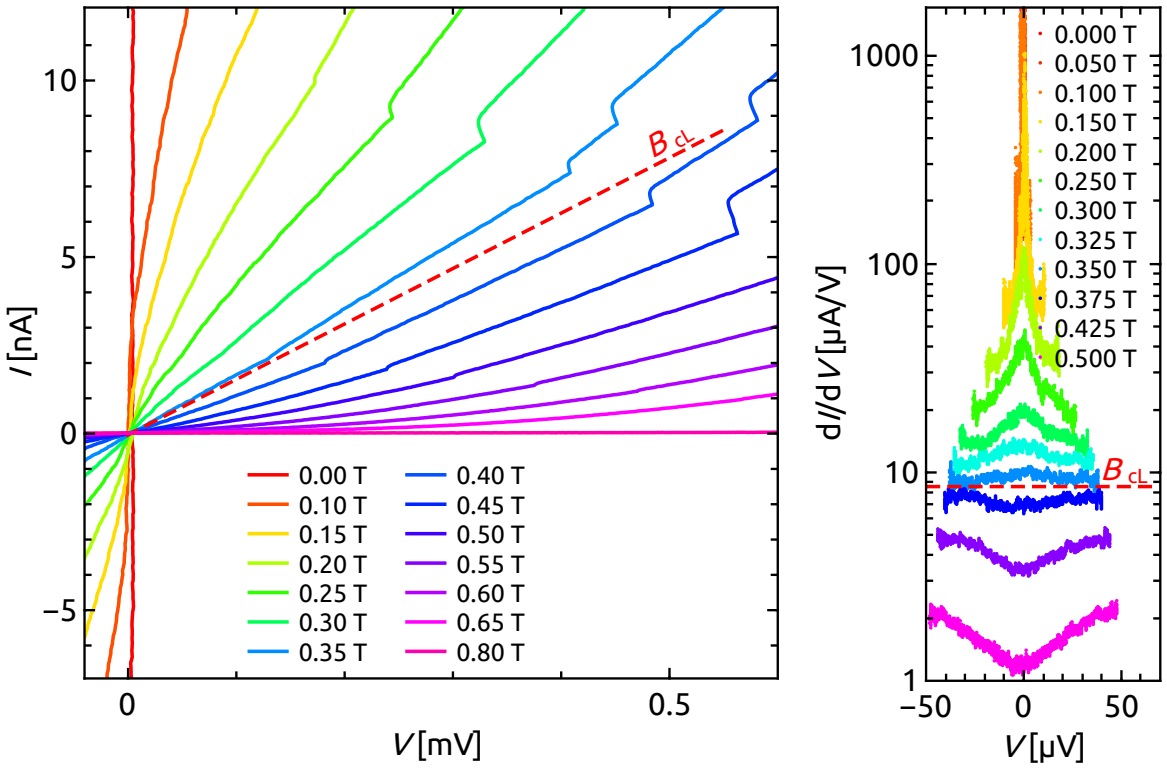

Fig. 4.10: In the IV characteristics for $T = 36\,\mathrm{mK}$ (left) current steps from higher resistive to lower resistive are visible, even for fields $B < B_{cL}$. The differential conductivity dI/dV (right) for smaller bias voltages than in the left figure exhibits a transition from a superconducting to an insulating feature around zero bias right at B_{cL}.

The resistance data presented so far were extracted from the linear region around zero bias of a dc voltage bias measurement. The shape of the IV characteristics for each point of the $R(T, B)$ provides additional information with regard to the superconducting and insulating features. The $I - V$ characteristics are linear in the HT and MT regime up to the maximally applied bias voltage of 1 mV. In the LT regime they develop strong nonlinearities.

A set of $I - V$ curves for fields around the LT crossing point is shown in Fig. 4.10 for the lowest measured temperature of $T = 36\,\mathrm{mK}$. In the left part of Fig. 4.10 we observe jumps in the $I-V$ from higher resistive to lower resistive parts of the $I-V$ for increasing bias voltage for $B \gtrsim 0.2\,\mathrm{T}$. This can be identified as an insulating feature like in [100], where, similar to our observations, multiple jumps within the same IV curve were measured. The authors of Ref. [100] attributed these multiple jumps to the

emergence of inhomogeneities in the electronic structure of the studied indium oxide film near the SIT. They argued that the jumps indicate a current breakdown that proceeds via percolative paths spanning from one electrode to the other. On the other hand a vortex breakdown should be reflected in a voltage rather than a current jump. The differential conductance (right side of Fig. 4.10) calculated from high resolution $I - V$ curves, exhibits at very low bias a switch from a superconducting feature to an insulating feature right at B_{cL} for increasing field B. From the linear resistance of these high resolution IV curves around zero bias, the above presented $R(T, B)$ data points are extracted.

When we put the two informations obtained from Fig. 4.10 together, we observe in the field range $0.2\,\mathrm{T} < B < 0.36\,\mathrm{T}$ that the $I - V$ characteristics reveal a superconducting feature at low bias and an insulating feature at higher bias at the same time.

5 Superconducting fluctuations above B_{c2}

Above the upper critical field B_{c2} the electrical conductivity is not completely described by the Drude expression Eq. 1.1, it is strongly affected by superconducting fluctuations. For magnetic fields much higher than B_{c2} the correction ΔG^{ID} originated from the Aronov-Altshuler interelectron interference is dominating the quantum corrections to the Drude conductivity G_0. For fields near but above B_{c2} the superconducting fluctuations can dominate even G_0 and G^{ID}. In section 2.2.2 the theoretical work of Galitski and Larkin [16] is introduced. The total conductivity is given by Eq. 2.40

$$G(T, B) = G_0 + \Delta G^{ID} + \Delta G^{SF}. \tag{5.1}$$

where the contributions of superconducting fluctuations to conductivity ΔG^{SF} are estimated by Eq. 2.39

$$\Delta G^{SF} = \frac{4}{3} G_{00} \left[-\ln \frac{r}{h} - \frac{3}{2r} + \psi(r) + 4[r\psi'(r) - 1] \right] \tag{5.2}$$

where $G_{00} \simeq (81\,\mathrm{k\Omega})^{-1}$, $r = (1/2\gamma)h/t$, $\gamma = 1.781$ is Euler's constant, $h = (B - B_{c2}(T))/B_{c2}(0)$ and $t = T/T_{c0}$. $B_{c2}(T) = B_{c2}(0) \cdot \cos(\pi(T/T_{c0})^{0.87}/2)$ is an approximation of the Werthamer-Helfand $B_{c2}(T)$ [22] for TiN (Eq. 2.20). ψ is the digamma function with $\psi(x) = \frac{d}{dx}\ln(\Gamma(x)) = \frac{\Gamma'(x)}{\Gamma(x)}$, where Γ is the gamma function. ψ' is the trigamma function with $\psi'(z) = \frac{d^2}{dz^2}\ln(\Gamma(z))$.

ΔG^{ID} the correction to conductivity due to Aronov Altshuler type of interelectron interference Eq. 2.41[5]:

$$\Delta G^{ID} = G_{00} B \ln\left(\frac{k_B T \tau}{\hbar}\right) \tag{5.3}$$

where B is a constant which depends on the Coulomb screening and it remains of the order of unity.

In Figs. 5.1, 5.2 and 5.3 the magnetoresistance isotherms for three different samples were fitted with 2.40. The temperature dependence of the critical magnetic field $B_{c2}(T)$ was given by the Werthamer-Helfand-Hohenberg dependence which is approximated

for TiN films by Eq. 2.21[22]

$$B_{c2}(T) = B_{c2}(0) \cdot \cos\left(\frac{\pi}{2} \cdot \left(\frac{T}{T_c}\right)^{0.87}\right) \tag{5.4}$$

For the fitting procedure a least-square algorithm was written in the scripting language python under usage of the scientific packages scipy and numpy. The parameters $B_{c2}(0)$ and T_c were adjusted by hand. The only fitting parameter was $G_0 + \Delta G^{ID}$ which sets the height of the fitting curve in the $R(B)$ isotherms. A change in the choice of $B_{c2}(0)$ shifts the peak of the fitted magnetoresistance curve in the horizontal direction. The parameter T_c affects the fit in a more complex way, a higher T_c produces a sharper magnetoresistance peak and at the same time a higher peak. Additionally the peak migrates nearer to $B_{c2}(T)$ for increasing T_c. $B_{c2}(0)$, T_c and $G_0 + \Delta G_{ID}$ can not be used as independent free fit parameters at the same time, because they affect the curves in a similar way. The errors obtained from the diagonal of the covariance matrix are almost of the order of the values itself when $B_{c2}(0)$, T_c and $G_0 + \Delta G_{ID}$ are all used as independent fit parameters. Hence we decided to choose fix values for T_c and $B_{c2}(T)$ by try and error in order to produce a best possible fit for a set of different measured magnetoresistance isotherms. To estimate the error, it was checked whether the fitting curves followed the traces of the measured $R(B)$ isotherms. The fitting range for the leastsquare fit started from a few hundred mT smaller than the magnetoresistance peak up to the highest measured magnetic fields.

Sample	$R_{\square}^{300K}[\Omega]$	$B_{c2}(0)$[T]	T_c[K]
D03_S	4228	0.88	0.83
D03_1 240 μm	4110	1.3	1.1
D03_1 120 μm	4220	0.93	0.7
D03_1 90 μm	4180	1.1	0.85
D03_1 30 μm	4190	1.5	1.1
D03_1 5 μm	4400	1.7	0.85

Table 5.1: Set parameters T_c and $H_{c2}(0)$ for a best fitting of the superconducting fluctuations according to Eq. 2.40 on the measured $R(B)$ isotherms. The sheet resistance at room temperature $R_{\square}^{300K}$ is given for the different samples of different sizes.

This procedure resulted in very good agreement with the data what can be viewed in Fig. 5.1a for sample D03_S, in Fig. 5.2a for the 90 μm size of sample D03_1 in the fourth oxidation step and in Fig. 5.3a for the 5 μm size of sample D03_1 in the fourth oxidation. Up to resistances of a few ten kΩ the fit according to the superconducting fluctuations reproduces the measured data with great accuracy. The highest temperatures for which the fit succeeded are close to the critical temperature T_c estimated from the fits. As a result of fitting a whole set of magnetoresistance isotherms for different temperatures, the error for the estimation of both T_c and $H_{c2}(0)$ is below $\approx 10\%$.

In table 5.1 the parameters T_c and $H_{c2}(0)$ from the fitting procedure and the sheet resistance at room temperature $R_{\square}^{300K}$ are given for different samples. For other samples or other oxidation degrees of the present samples, the fitting procedure did not succeed well due to too few points in the $R(B)$ isotherms beyond the magnetoresistance peak, too few measured temperatures, or inaccurate ac measurements where an dc bias offset originating from the current preamplifier shifted the differential resistance measurement out of the linear resistance region around zero bias voltage.

Now we turn to the behaviour of the only free fitting parameter $G_0+\Delta G_{AA}$, where the normal state conductivity and the Aronov Altshuler type of corrections to conductivity are concerned. Exemplarily, in Fig. 5.1c for sample D03_S, and in Fig. 5.2c for the $90\,\mu$m size of sample D03_1 in the fourth oxidation, the temperature dependence of the normalized conductivity $(G_0 + \Delta G_{AA})/G_{00}$ with $G_{00} = e^2/(2\pi^2\hbar) \simeq (81\,\mathrm{k\Omega})^{-1}$ is shown on a logarithmic T-scale. All points in these plots lie on a line with a slope of ≈ 1 what is expected for the Aronov-Altshuler type of electron-electron interaction. G_0 and G_{AA} were not plotted seperately, since the exact value of the normal state resistance is not known exactly. The sheet resistance at room temperature $R_{\square}^{300K}$ is probabily the best choice for R_0 as $\Delta G_{AA} \to 0$ for high temperatures. The value of the correction term ΔG_{AA} can be estimated when $(R_{\square}^{300\,\mathrm{K}})^{-1}/G_{00} \approx (4\,\mathrm{k\Omega})^{-1}/G_{00} \simeq 20$ is subtracted in the combined plots in Figs. 5.1c 5.2c. The dashed horizontal lines at $(G_0 + \Delta G_{AA})/G_{00} = 1$ indicate where the value $G_{00} \simeq (81\,\mathrm{k\Omega})^{-1}$ is crossed.

In Figs. 5.1b, 5.2b and 5.3b we zoom into the region of the HT crossing points of the magnetoresistance isotherms and their corresponding Galitski-Larkin fits. It can be seen that not only the measured magnetoresistance isotherms intercept at B_{cH}, but also the fitting curves at B_{cGL}. This crossing of the Galitski-Larkin fits was already realized in Ref. [9] where a similar analysis of superconducting fluctuations after the theory of Galitski and Larkin was pursued for NdCeCuO (see Fig. 2.18). Here we argue that the HT crossing point can be linked to the Galitski-Larkin fits. For samples which are deeper in the superconducting regime, the determined critical field $B_{c2}(0)$ increases. This increase of $B_{c2}(0)$ corresponds to the arrangement of Figs. 5.1b, 5.2band 5.3b. The crossing fields B_{cH} and B_{cGL} more and more coincide, the deeper the sample is in the superconducting regime. The deviations of the measured crossing from the Galiski-Larkin crossing for an increase in disorder might be explained by resistive mechanisms below the critical field $B_{c2}(0)$ such as vortex motion. A discussion of crossover from resistive mechanisms below $B_{c2}(0)$ due to vortices to superconducting fluctuations above $B_{c2}(0)$ is examined in section 9.1.

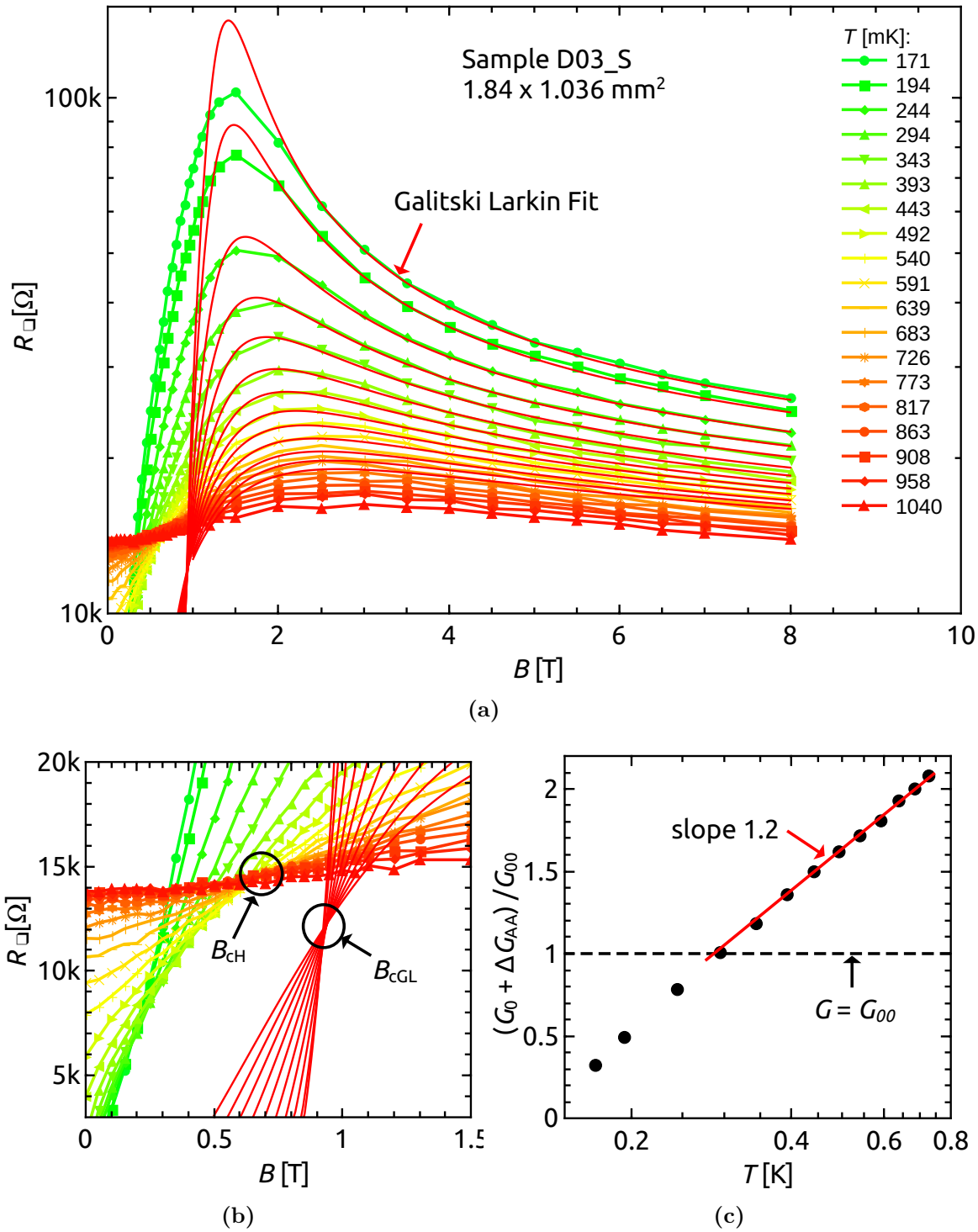

Fig. 5.1: Analysis of superconducting fluctuations for the large sample D03_S with $R_{\square}^{300K} = 4228\,\Omega$. (a) Fit of the magnetoresistance isotherms as explained in the text with parameters $B_{c2}(0) = 0.88\,\mathrm{T}$ and $T_c = 0.83\,\mathrm{K}$. (b) Zoom of the low-field side of the magnetoresistance isotherms and the corresponding fits. The measured (B_{cH}, R_{cH}) and the crossing that emerges from the fit at B_{cGL} are marked by black circles. (c) The temperature dependence of the normalized conductivity $(G_0 + \Delta G_{AA})/G_{00}$ with $G_{00} = e^2/(2\pi^2\hbar) \simeq (81\,\mathrm{k}\Omega)^{-1}$ is shown on a logarithmic T-scale to reveal the Aronov-Altshuler type of correction to conductivity. The dashed horizontal line marks $G_{00} \simeq (81\,\mathrm{k}\Omega)^{-1}$.

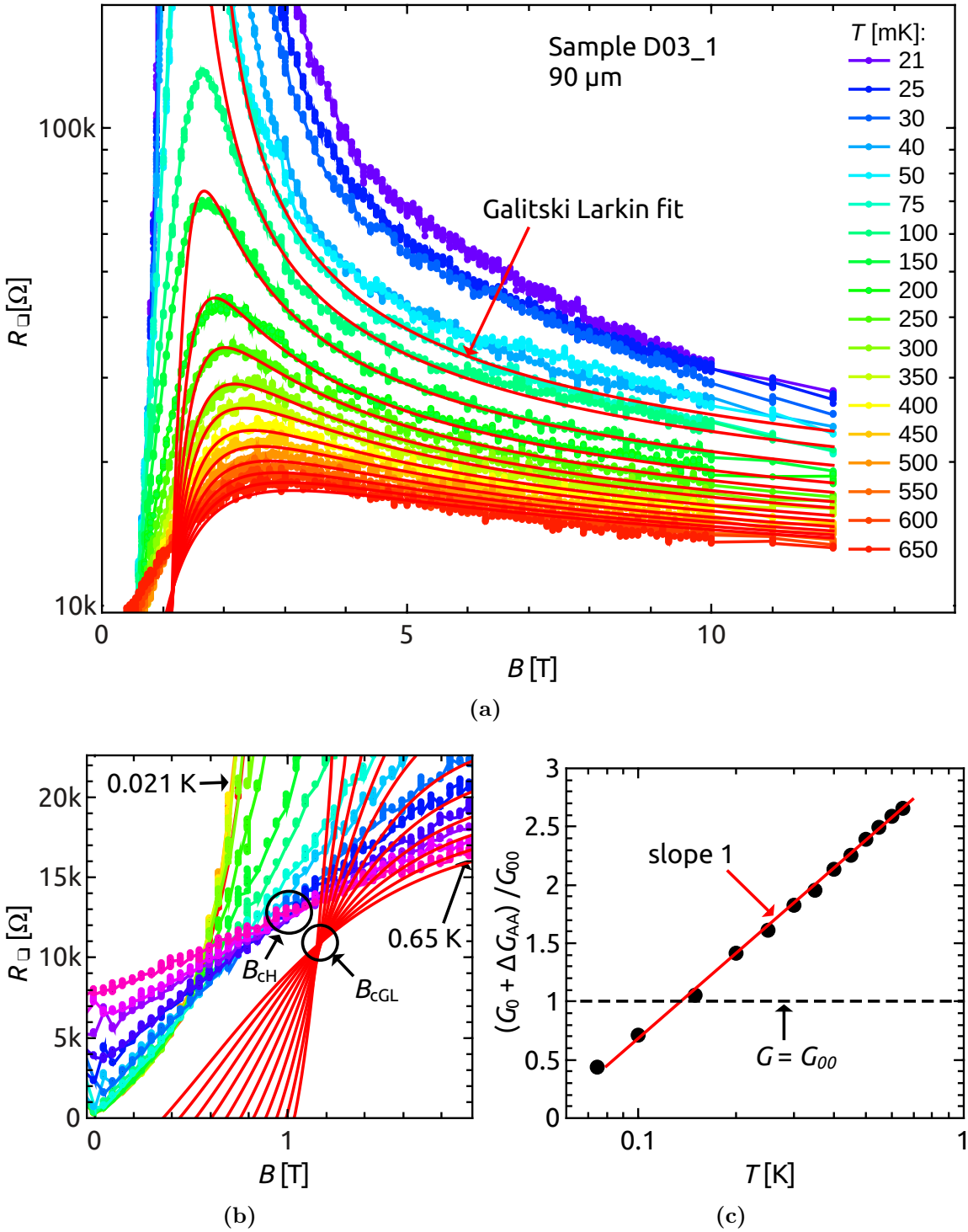

Fig. 5.2: Analysis of superconducting fluctuations for the 90 μm size of sample D03_1 with $R_{\square}^{300K} = 4180\,\Omega$. (a) Fit of the magnetoresistance isotherms as explained in the text with parameters $B_{c2}(0) = 1.1\,\mathrm{T}$ and $T_c = 0.85\,\mathrm{K}$. (b) Zoom of the low-field side of the magnetoresistance isotherms and the corresponding fits. The measured (B_{cH}, R_{cH}) and the crossing that emerges from the fit at B_{cGL} are marked by black circles. (c) The temperature dependence of the normalized conductivity $(G_0 + \Delta G_{AA})/G_{00}$ with $G_{00} = e^2/(2\pi^2\hbar) \simeq (81\,\mathrm{k}\Omega)^{-1}$ is shown on a logarithmic T-scale to reveal the Aronov-Altshuler type of correction to conductivity. The dashed horizontal line marks $G_{00} \simeq (81\,\mathrm{k}\Omega)^{-1}$.

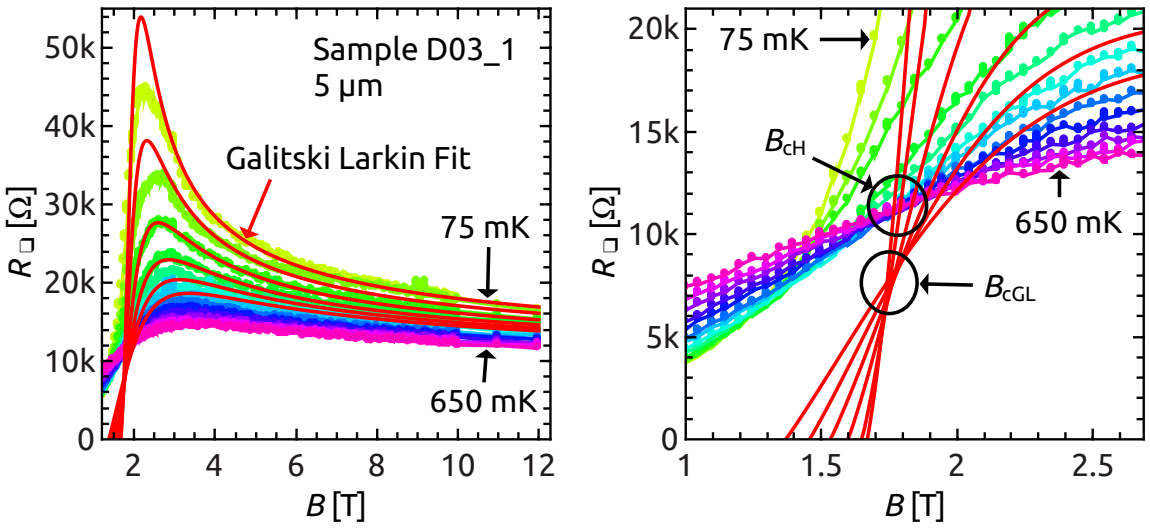

Fig. 5.3: Analysis of superconducting fluctuations for the 5 μm size of sample D03_1 with $R_\square^{300K} = 4400\,\Omega$. (a) Fit of the magnetoresistance isotherms as explained in the text with parameters $B_{c2}(0) = 1.1\,\mathrm{T}$ and $T_c = 0.85\,\mathrm{K}$. (b) Zoomed view of the low-field side of the magnetoresistance isotherms and the corresponding fits. TThe measured (B_{cH}, R_{cH}) and the crossing that emerges from the fit at B_{cGL} are marked by black circles. The fields B_{cH} and B_{cGL} coincide for this sample.

In Fig. 2.3b taken from Ref. [32] can be seen that the crossing point in the magnetoresistance isotherms for a TiN sample more deeply in the superconducting regime is consistent with the theory of superconducting fluctuations. Additionally can be seen, how the crossing point in the measured $R(B)$ isotherms shifts for a more critically disordered sample (Fig. 2 of Ref. [32]). The magnetic field and the resistance at which the curves intersect are comparable to the values of the HT crossing point obtained in this thesis for the most disordered samples. This allows us to assign the crossing of $R(B)$ isotherms in Fig. 2 of Ref. [32] to the HT crossing point. In Ref. [32] the authors did not succeed to fit the magnetoresistance isotherms of their Fig. 2 with the theory of Galitski and Larkin at that time. It would be worth to try the latter. From the comparably big difference of the crossing-point field and the magnetoresistance-peak field, we expect that deviations between the measured crossing point to the Galitski-Larkin crossing point in both the field and the resistance at the crossing will occur, similar to what we observe.

6 Test for long-ranged interactions with a screening top-gate

It is well-known that vortices interact logarithmically in a two dimensional superconducting film with thickness $d \ll \xi$ (see Eq. 2.25) [19]. Beyond the magnetic screening length $\lambda_\perp$ the interaction energy falls of as $1/r$ with increasing vortex separation r [26]. As long as the sample size is smaller than $\lambda_\perp$, a superconducting state with zero resistance emerges below a finite $T_{BKT} > 0$. However, when the sample size exceeds the screening length $\lambda_\perp$, unbound vortices are present for all finite temperatures with $T_{BKT} = 0$, and the resistance remains finite.

Based on the model of Josephson junction arrays, the insulating regime is expected to be accompanied by a charge BKT transition, dual to the vortex BKT transition in the superconducting regime. The charges interact logarithmically according to Eq. 2.70 up to the electrostatic screening length $\lambda_C = a\sqrt{C/C_0}$, where C is the capacitance between neighbouring islands, C_0 is the self-capacitance to ground potential and a is the lattice spacing [88]. According to Eq. 2.70, the charging interaction is negative and increases logarithmically up to distances of the order of the screening length λ_C and then exponentially goes to zero for distances larger than λ_C. A two dimensional character of the electric field in the Josephson junction array is essentially required for the logarithmic interaction between charges. In Ref. [59] a simple electrostatic approach is pursued to demonstrate the two-dimensional trapping of the electric field lines in a dielectric film with dielectric constant ϵ and thickness d. The latter film is sandwiched between two dielectric media with dielectric constants ϵ_1 and ϵ_2. The electrostatic potential in the plane of the film of a charge q depends on distance $r \gg d$ with

$$\phi(r) = \frac{q}{4\epsilon_0\epsilon d}\left[H_0\left(\frac{\epsilon_1+\epsilon_2}{\epsilon}\frac{r}{d}\right) - N_0\left(\frac{\epsilon_1+\epsilon_2}{\epsilon}\frac{r}{d}\right)\right] \tag{6.1}$$

where H_0 and N_0 are the Struve and Neumann functions, respectively. The electrostatic screening length in the dielectric film is given by

$$\lambda_C = \frac{\epsilon d}{\epsilon_1+\epsilon_2} \tag{6.2}$$

Similarly to Eq. 2.70, the potential increases logarithmically up to distances of the order of the screening length λ_C and then exponentially goes to zero. The electrostatic energy for a Cooper pair dipole, which consists of a Cooper pair and a local deficit of

a Cooper pair, for short distances $d \ll r \ll \lambda_C$ is given by

$$V(r) = \frac{(2e)^2}{2\pi\epsilon_0\epsilon d} \ln\left(\frac{r}{d}\right) \tag{6.3}$$

Indeed, such a logarithmic dependence of the activation energy in the insulating state was found in TiN thin films [78, 98] and indium oxide [101] films as well. The activation energy T_0 was related to $V(\min\{L, \lambda_C\})$ with sample length L in Ref. [59]. From the linear slope in the plot of T_0 vs. $\ln L$ the dielectric constant of the TiN film of Ref. [78, 98] was calculated to $\epsilon = 4 \cdot 10^5$. With the dielectric constant $\epsilon_1 = 4$ for SiO_2 and $\epsilon_2 = 1$ for vaccum, the electrostatic screening length was calculated to $\lambda_C = 240\,\mu$m. In Ref. [59] from this macroscopic value of λ_C was concluded that samples with a width w of less than λ_C seem to be well-described by two-dimensional electrostatics. However, the more relevent scale in the charge BKT phase is the length of the sample L. This is consistent with the logarithmic dependence of the activation energy T_0 on the film length L at a fixed width w in Ref. [101]. If the sample width w was the relevant length scale, the activation energy T_0 would logarithmically depend on $\min\{\lambda_C, w\}$ and not on the expermenatlly found $\min\{\lambda_C, L\}$.

Svitlana Kondovych [102] extended the model of the sandwiched dielectric film by adding a metal electrode in the distance h. The electrostatic potential for $\epsilon \gg (\epsilon_1 + \epsilon_2)$ and $r \gg d$ is given by

$$\phi(r) = \frac{q}{4\pi\epsilon_0\epsilon d} \int_0^\infty \frac{\tanh(kh) J_0(kr)}{k \tanh(kh) + \frac{\epsilon_1 + \epsilon_2 \tanh(kh)}{d\epsilon}} dk. \tag{6.4}$$

Practically, the metal electrode can be realized with a metal top-gate that is electrically isolated from the TiN film and the contacts by Al_2O_3. An Al_2O_3 layer of tickness $h \simeq 30\,$nm already achieves a substantial isolation. For an expected electrostatic screening length of $\lambda_C = 240\,\mu$m in the TiN film that is not covered with a metal top-gate, the electrostatic potential of the top-gated film with $h \ll \lambda_C$ is approximated by

$$\phi(r) = \frac{q}{4\pi\epsilon_0\epsilon d} K_0\left(\frac{1}{\sqrt{2}} \frac{r}{\sqrt{h\lambda_C}}\right). \tag{6.5}$$

Here, $\lambda_C^* = \sqrt{h\lambda_C}$ is the reduced electrostatic screening length due to the metal top-gate. For $d \ll r \ll \lambda_C^*$ the charge interaction potenial $V(r)$ of a Cooper pair and a local deficit of a Cooper pair increases logarithmically with separation r. When the reduced screening length λ_C^* is exceeded, the interaction energy vanishes according to $V(r) \propto r^{-1/2} e^{-r}$.

We now turn to the question, what changes in the charge BKT scenario for a reduced electrostatic screening length λ_C^*? In Ref. [59] the charge bound phase below a finite T_{c-BKT} is expected to vanish for an electrostatic screenning length that decreases below the sample size. The duality to the vortex bound regime below T_{v-BKT} becomes apparent, where the zero resistance state is absent for the sample size exceeding $\lambda_\perp$. Dually to that, the reduction of λ_C to $\lambda_C^* = \sqrt{h\lambda_C} \ll L$ due to an applied top-gate,

would result in finite conductivity below the charge BKT temperature T_{c-BKT} of the uncovered film.
In addition, since the activation energy in the charge unbound phase above T_{c-BKT} is expected to depend on λ_C^* with $T_0^* \simeq V(\min\{L, \lambda_C^*\})$, the activation energy should decrease with shrinking λ_C^* according to $T_0^* \propto \ln(\lambda_C^*)$ [95, 59], when $\lambda_C, \lambda_C^* \ll L$:

$$T_0^* = E_C \cdot \ln\left(\frac{\sqrt{h\lambda_C}}{d}\right), \quad h \ll \lambda_C \tag{6.6}$$

where $E_C = (2e)^2/(4\pi\epsilon_0\epsilon d)$ [59].

A few general properties of TiN thin films have to be considered before the sample is patterned. TiN thin films slowly oxidize if they are exposed to air at room temperature. The resistance $R_\square^{300\,\mathrm{K}}$ of a D03 sample increases by more than $\gtrsim 200\,\Omega$ after a exposure time of two years. Every time a sample is mounted in a cryostat, cooled down and warmed up again, the resistance $R_\square^{300\,\mathrm{K}}$ increases by a few ten Ω. The deposition of 30 nm Al_2O_3 on top of the TiN film decreases the resistance $R_\square^{300\,\mathrm{K}}$ by $\approx 200\,\Omega$. However, a TiN film with a Al_2O_3 covering, retains its $R_\square^{300\,\mathrm{K}}$ in spite of cooling the sample down and warming it up again, and in spite of long exposure times to air. Hence, we decided to cover the TiN film of sample D03_S with a 30 nm thick Al_2O_3 coating and an additional 30 nm thick PMMA layer on top of that. The deposited palladium top-gate above this PMMA layer thus easily can be removed again. $R_\square^{300\,\mathrm{K}}$, which is a measure of the disorder in the film, was only slightly lowered by $22\,\Omega$ for the successive measurements of the sample with and without the top-gate.

We now estimate the screening effect due to the metallic top-gate. From measurements of the size-dependent sample D03_1 presented in chapter 8, the electrostatic screening length λ_C was estimated to $\lambda_C \simeq 180\,\mu$m from the logarithmic size dependence of the activation energy T_0. The size of sample D03_S with a length of $L = 1.84$ mm well exceeds the estimated λ_C. The reduced screening length due to electrostatic screening is given by $\lambda_C^* = \sqrt{h\lambda_C} = \sqrt{60\,\mathrm{nm} \cdot 180\,\mu\mathrm{m}} \simeq 3.3\,\mu$m. According to Eq. 6.6, the activation energy is reduced by the ratio

$$\frac{T_0^*}{T_0} = \frac{\ln(\lambda_C^*/d)}{\ln(\lambda_C/d)} = 0.63. \tag{6.7}$$

This surprisingly small effect of the large reduction of the screening length on the activation energy is associated with the logarithmic interaction of charges in the 2D film. For increasing intercharge distance r, the potential energy of the charges grows more and more slowly. Within a intercharge distance of $r = 100 \cdot d = 360$ nm the potenial energy has already increased to $V(r = 360\,\mathrm{nm}) = 0.43 \cdot T_0$. The expected effect of the screening top-gate on T_0 hence is of the same order like the the change of T_0 due to a change of $R_\square^{300\,\mathrm{K}}$ by $\approx 120\,\Omega$ in the vicinity of the D-SIT (see Fig. 8.6a).

Below, the $R(T)$ curves and the $R(B)$ curves of sample D03_S, which was measured with and without a top-gate, are analyzed with respect to the expected electrostatic screening effect.

6.1 General characterization of the sample properties at low temperatures

First we focus on the temperature dependence of the resistance at zero magnetic field and at the highest field measured at $B = 8\,\mathrm{T}$.

At zero field (see Fig. 6.1a) the sample is superconducting for both configurations (covered with the top-gate and after removing the top-gate). The maximum resistance R_{max} that is reached in the $R(T)$ curves at zero field decreased by $\approx 500\,\Omega$ upon the removal of the top-gate. This strong decrease of R_{max} compared with the small decrease of $R_{\square}^{300K}$ by just $22\,\Omega$ indicates the close vicinity to the disorder driven SIT.

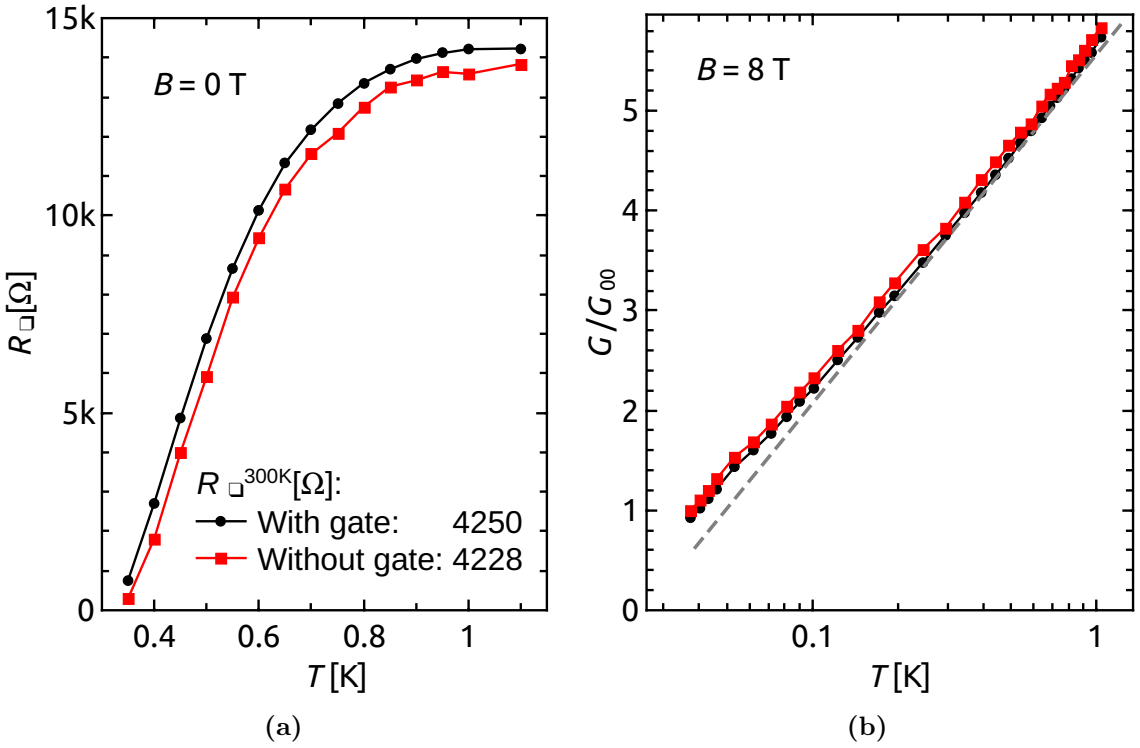

Fig. 6.1: Temperature dependences of the resistance at zero and high magnetic field. The black curves are taken with a top-gate in a distance of $\approx 60\,\mathrm{nm}$ from the TiN film. The red curves were measured after the removal of the top-gate with 30 nm aluminum oxide on top of the TiN film. (a) Temperature dependence of the resistance at zero magnetic field. (b) Test for Aronov-Altshuler type of correction to conductivity and weak localization at $B = 8\,\mathrm{T}$.

By an applied large magnetic field of $B = 8\,\mathrm{T}$, superconductivity and most of the superconducting fluctuations are destroyed and the behaviour of the film is predominantely characterized by a metallic behaviour. In Fig. 6.1b the normalized conductance G/G_{00} with $G_{00} \simeq (81\,\mathrm{k}\Omega)^{-1}$ is plotted vs. the temperature on a logarithmic scale. A linear dependence in this plot is related to weak localization and an Aronov-Altshuler type of electron localization. The slope of both curves in this plot is ≈ 1.4, close to

the slope of ≈ 1 found for $(G_0 + \Delta G_{AA})/G_{00}$ in Figs. 5.1c 5.2c. The slope of unity was attributed to a pure Aronov-Altshuler type of correction to conductivity at the analysis of superconducting fluctuations. We can interpret the slightly higher slope of 1.4 with a small contribution of superconducting fluctuations which has not vanished completely at $B = 8\,\mathrm{T}$ (see chapter 5). The curves for the sample with and without a top-gate lie almost on top of each other. This is expected in the metallic regime, when the resistance at room temperature $R_{\square}^{300K}$ changes by just $22\,\Omega$.

The close vicinity to the D-SIT on the one hand is essential to observe a magnetic field driven SIT and possible effects of a screening top-gate on electrostatically couples droplet-like superconducting domains in the flim. On the other hand the critically disordered samples are extremely sensitive to slight changes in the resistance at room temperature which makes it hard to distinguish between an effect due to the top-gate and an effect due to a change of disorder.

6.2 Experimental test for a screening effect due to a metallic top-gate

In Fig. 6.2 the temperature dependence of the resistance for several set magnetic fields is displayed in an Arrhenius plot. For zero magnetic field the sample is superconducting in both configurations, as already shown in Fig. 6.1a. For the upper set of curves for $B = 1\,\mathrm{T}$, the field of the magnetoresistance peak (see Fig. 6.4), the resistance increases monotonically with decreasing temperature. At $B = 1\,\mathrm{T}$ and lowest measured temperatures of $T = 36\,\mathrm{mK}$ the resistance of the configuration with gate exceeds the one without gate by $\sim 350\mathrm{M}\Omega$ what corresponds to a factor of ≈ 3 between the two highest resistances.

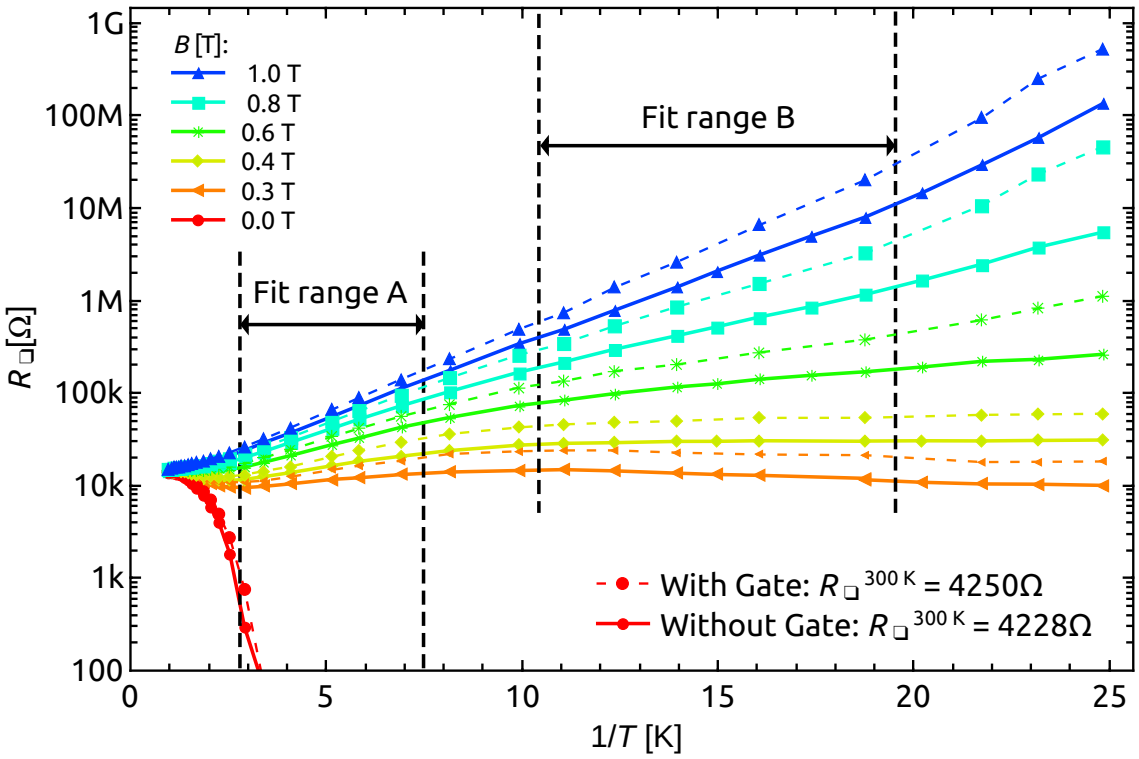

Fig. 6.2: Arrhenius plot of the measured temperature dependence of the resistance for sample D03_S in the two different configurations. The dashed lines correspond to the $R(T)$ curves for sample with a top-gate in a distance of $\approx 60\,\mathrm{nm}$ from the TiN film. The solid lines show the $R(T)$ curves for the sample after the removal of the top-gate with 30 nm aluminum oxide on top of the TiN film. The activation energies presented in Fig. 6.3 are obtained from linear fits of the $R(T)$ curves in the Arrhenius plot here. Fit range A reaches from 150 mK to 350 mK (Fig. 6.3a), and fit range B reaches from 50 mK to 90 mK (Fig. 6.3b).

A further analysis of all measured $R(T)$ curves in matters of activated behaviour is shown in Fig. 6.3. In a range from $150\,\mathrm{mK} - 350\,\mathrm{mK}$ (the MT regime) the $R(T)$ curves show activated behaviour with the activation energies T_0 depited in Fig. 6.3a. For all measured temperatures, the activation energies T_0 are nearly the same for the two different configurations.
The analysis that lead to Fig. 6.3b was motivated by numerical study of hopping conductivity on an irregular network of capacitors [96]. In this model system for a two-dimensional insulator, the low-temperature $R(T)$ dependence is separated in two subsequent temperature regions with different slopes in the Arrhenius dependence. For our $R(T)$ curves this would mean that the activated behaviour at moderate temperatures is replaced by another activated behaviour with a different activation energy at low temperatures. Indeed, a linear region in the Arrhenius plots can be observed in a limited temperature range from $50\,\mathrm{mK} - 90\,\mathrm{mK}$ with activation energies T_0 shown in Fig. 6.3b. Over the whole field range T_0 for the configuration without gate is lower by about 50 mK compared to the configuration with gate.

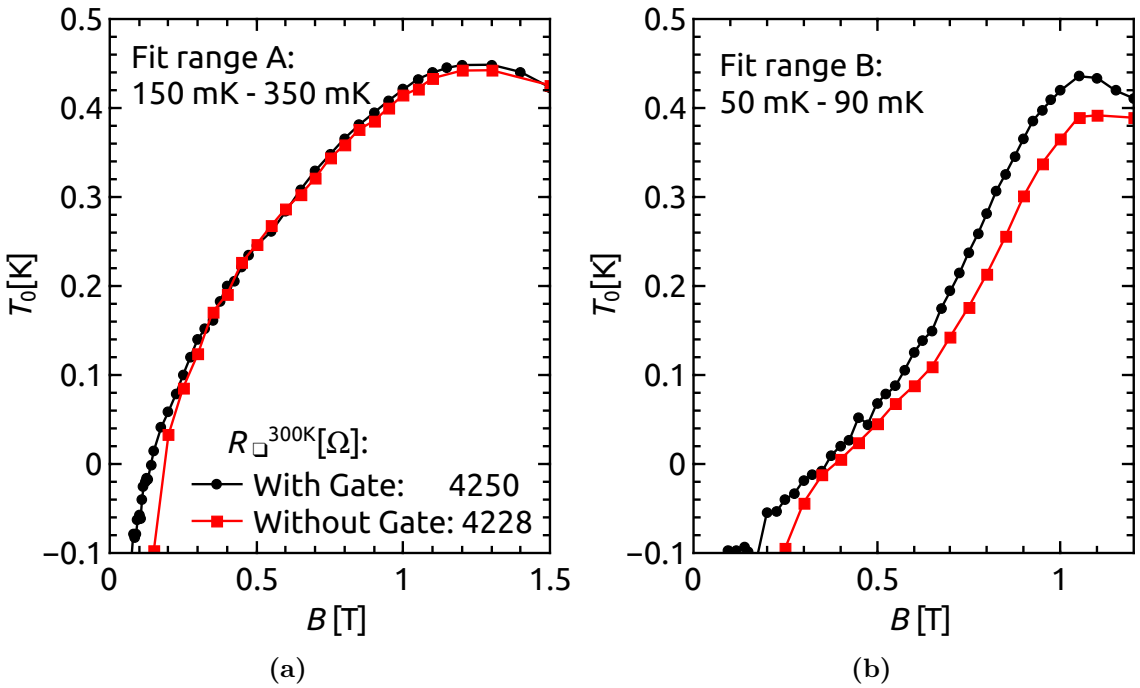

Fig. 6.3: The extracted activation energies from the $R(T)$ curves for to different temperature regions. The black data points correspond to the sample with top-gate, the red points to the sample without top-gate. Activation energies obtained from linear fits of the $R(T)$ curves in the Arrhenius plots for temperatures ranging from (a) 150 mK − 350 mK and (b) 50 mK − 90 mK.

For temperatures lower than 50 mK an upturn in the Arrhenius plots of the $R(T)$ curves for the three highest fields in Fig. 6.2 can be observed. It is not clear whether this is due to an erroneous temperature calibration which is extrapolated below $T \approx 42$ mK, or it is really an upturn like in [14] corresponding to hyperactivated behaviour. Future measurements have to clarify this issue.

The magnetoresistance isotherms with and without gate differ slightly in the positive magnetoresistance region and the peak height for lowest temperatures. The difference in resistance at the peak is the previously mentioned factor of ≈ 3. At higher temperatures ($\gtrsim 100$ mK) and at high fields, the $R(B)$ isotherms almost collapse. This is expected for the normal metal state where small changes in disorder have not such a huge effect on the electron-dominated conductivity like on the Cooper-pair dominated conductivity at lower fields.

Altogether we could not observe a significant screening effect due to a top-gate. The change in resistance at low temperatures upon the removal of the metal top-gate can be explained by the small but relevant change in resistance at room temperature of the critically disordered sample.

This indicates that the relevant energy scales in the sample are not governed by long-range electrostatics, in contrast to the expectation from the anaysis in Ref. [59].

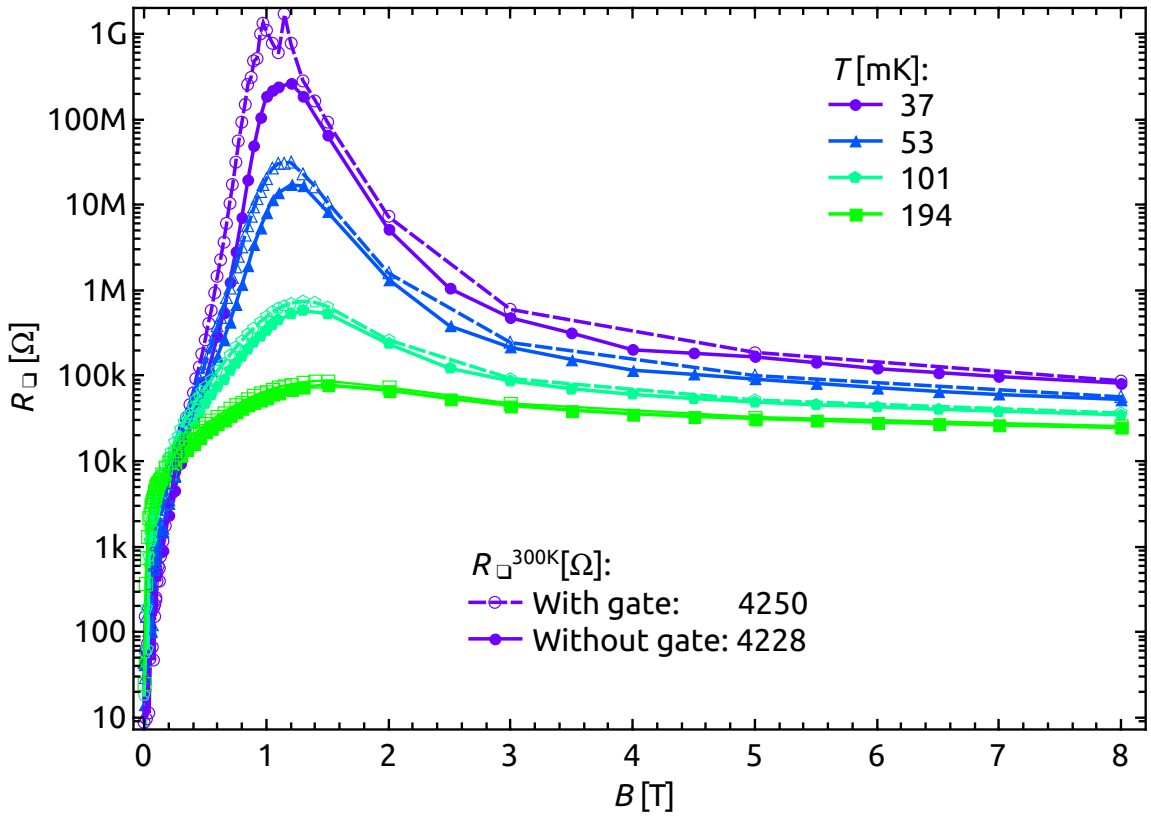

Fig. 6.4: Magnetoresistance isotherms at four different temperatures for sample D03_S for the configurations with and without top-gate. The open symbols that are connected by dashed lines were obtained for a measurement of the top-gated sample, the closed symbols that are connected by solid lines correspond to data points that were measured after the removal of the top-gate.

7 Disorder driven Superconductor-Insulator transition in TiN

In this chapter we will first focus on the IV characteristics at zero magnetic field, followed by a section where insulating IV characteristics with dual shape to the ones at zero field are shown. The dual shape of the IV characteristics on the insulating side of the B-SIT is achieved by the exchange of voltage and current axes. A wide spectrum of differently disordered samples has been measured and this serves as a basis for the evolution of the critical temperature with increasing disorder. A BKT analysis is attached, to explain different results for T_c for different theoretical approches.

7.1 Heating phenomena at zero magnetic field for differently disordered samples

Astonishing features in the IV characteristics attracted our attention, when we recorded IV characteristics at zero magnetic field. We observe two successive current plateaus in our voltage-biased measurements. After the bias voltage exceeds the critical current according to Ohm's law with $V = R_L I_C$, with R_L the line resistance of the cryostat ($\approx 7\Omega$), the current drops to the upper plateau with very noisy current. At some higher voltage the current drops to the lower plateau. When the bias voltage is increase further, the IV characteristics develops a linear behaviour. In this high-voltage regime the IV curve asymptotically approches $I(V) = V/R_N$ with the normal state resistance R_N.
The formation of the upper plateau is attributed to circuit-controlled relaxation oscillations [53, 49]. An example for this relaxation oscillation plateau can be viewed in Fig. 7.1c. Here, the peak of the critical current (at $I_c \approx 180\,\mathrm{nA}$) is not much higher than the height of the relaxation oscillation plateau (at $I \approx 160\,\mathrm{nA}$). The formation of the lower plateau (the hotspot plateau) is explained by by the hotspot theory [49] (see chapter 2.2.4). With increasing bias voltage, a normal-conducting hotspot grows in the middle of the sample. The mechanism of relaxation oscillations strongly depends on parameters of the cryostat as well as of the sample. Hence, we do not analyze the relaxation oscillation plateaus in detail. Instead, we thoroughly investigate the observed hotspot plateaus. From the analysis of the hotspot plateaus according to the

hotspot theory, we can estimate thermal conductivities within the film to the leads and the thermal conductivity from the film to the substrate.

In section 2.2.4 it was explained how the values for the thermal conductivity $K_{N,S}$ in the normalconducting and superconducting parts of the film, respectively, the surface thermal conductivity α from the film to the substrate, the temperature difference between the critical temperature and the bath temperature $T_c - T_b$, and the normal state resistance R_N can be estimated from the IV characteristics. Additionally the thermal healing length η_N and η_S, for the normalconducting and superconducting parts of the film, respectively, are obtained [49].

For our calculations the normal thermal conductivity K_N is approximated by the Wiedemann-Franz thermal conductivity. For the sample dimension W the lateral sizes are taken. The position of the normalconducting/superconducting interface x_0 is expressed by a list of 1000 entries with equidistant spacings from zero to $L/2$. In a python script, under usage of the module scipy, a least-square problem with Eqs. 2.57, 2.58 with the free fitting variables R_N, $T_c - T_b^*$, K_S and α is solved. Here, the bath temperature T_b is exchanged by the variable T_b^*. It is not possible to reproduce the measured IV characteristics with the hotspot theory under usage of a set parameter $T_c - T_b$, due to the saturation of the shape of the IV characteristics which is discussed below. This saturation behaviour motivated the introduction of the free fitting variable $T_c - T_b^*$.

The according fits that are obtained by the solution of the least-square problem for different IV characteristics are shown in Figs. 7.1, 7.2, 7.3. The values obtained for the fitting variables are shown in Fig. 7.4.
The left panels of Figs. 7.1, 7.2, 7.3 show IV characteristics for the smallest measured sizes of sample D03_1 for the different oxidation degrees. The behaviour of the IV curves for the untreated sample (Fig. 7.1a) and after the first oxidation (Fig. 7.1c) can be explained by the hotspot theory for long microbridges. For the further oxidation steps the hotspot theory is not applicable since the superconducting critical current peak vanishes. The behaviour of these IV characteristics is similar to that of overdamped Josephson junctions [103, 104]. A thorough analysis of IV characteristics of very small samples with a minimum width of 16 nm is worked out by Ina Schneider in Ref. [99].
In the right columns of Figs. 7.1, 7.2, 7.3 the IV characteristics for the largest sizes of sample D03_1 are depicted that were measured in a sufficient wide bias voltage range to pursue an analysis with respect to heating. In Fig. 7.1b a current plateau at $\approx 9\,\mu$A is visible. It was not possible to match the hotspot theory with the measured data. The so called "excess" currents like shown by the dashed line in Fig. 7.1b among others can be explained by the hotspot theory. However it was not possible to reproduce the curvature to the left and the right of the plateau with the leastsquare fit. The wavy structure of the hotspot plateau might be the key feature to explain.

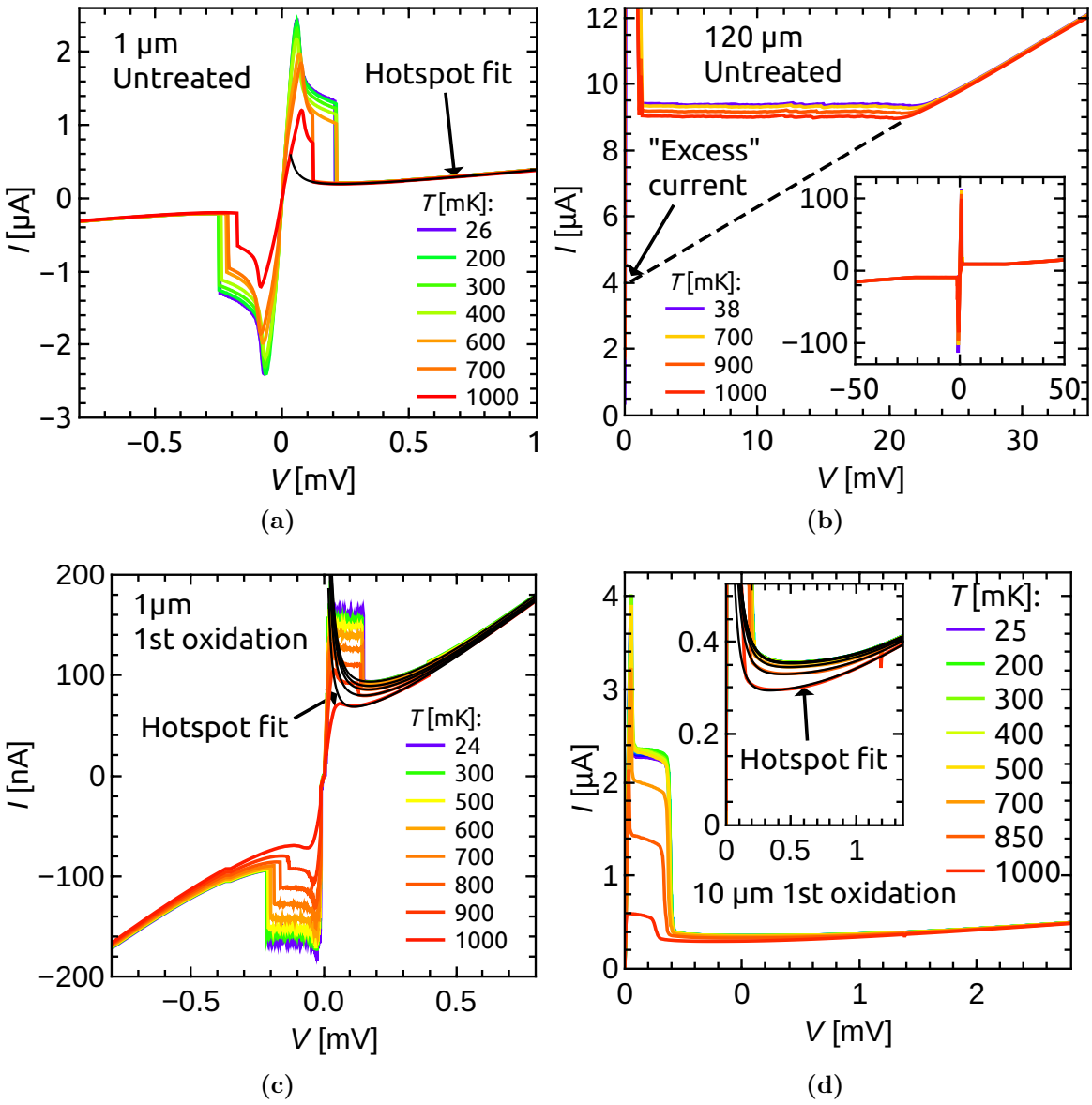

Fig. 7.1: *IV* characteristics for zero magnetic field for (a), (b) the untreated and (c), (d) the first oxidation step. The black solid lines correspond to a fit of the *IV* characteristics according to the theory of self-heating in superconducting long microbriges [49]. (b) It was not possible to fit the *IV* characteristics of the untreated 120 μm size with the hotspot-theory. The large "excess" current of $\approx 4\,\mu$A, which is indicated by the intercept of the dashed black line with the current axis, was not able to fit with the hotspot theory. Relaxation oscillation plateaus are visible in (a), (c) and (d) at low voltage bias. In (b) the relaxation oscillation plateau at low biases is not resoluted in the current plot.

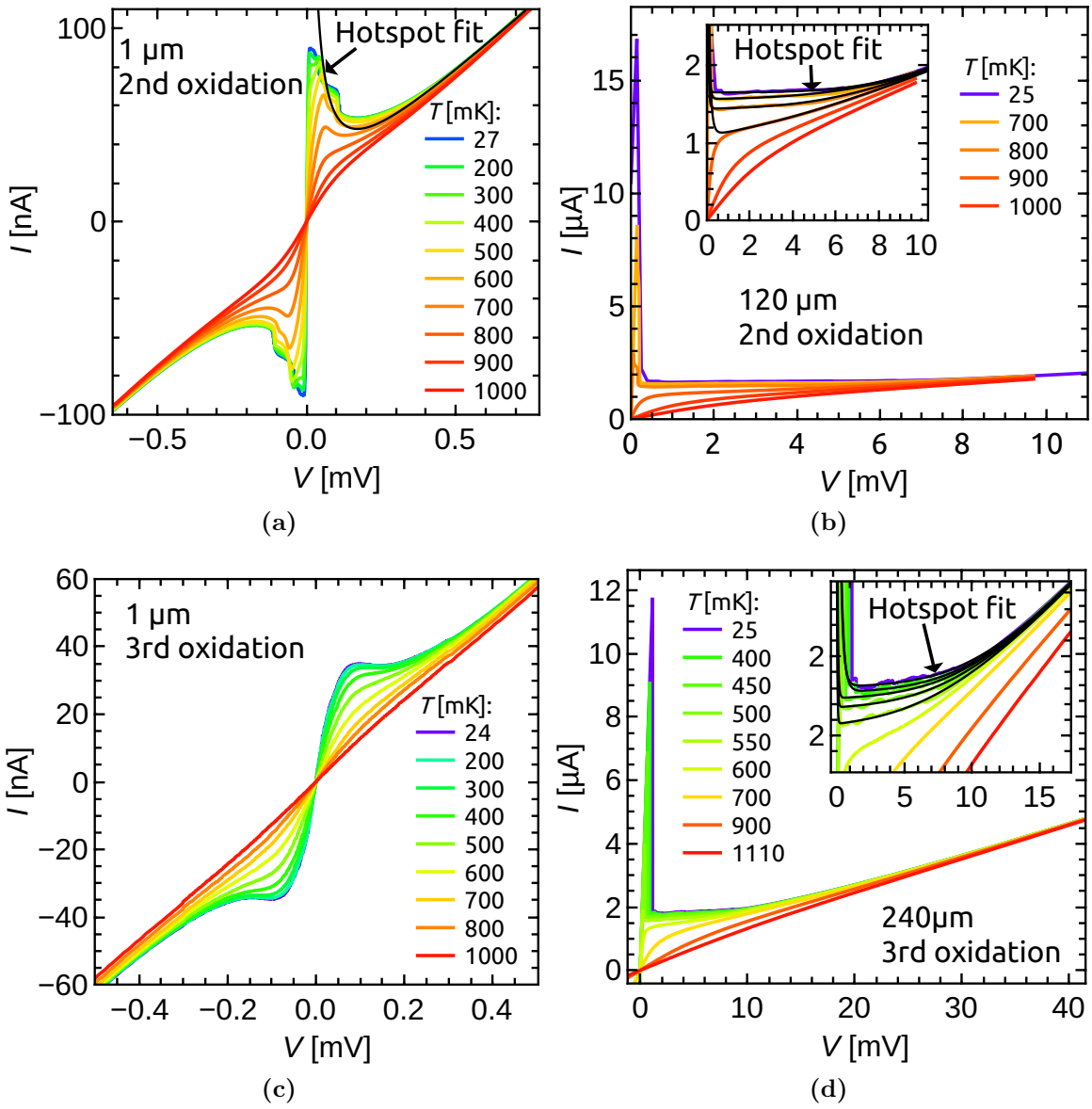

Fig. 7.2: *IV* characteristics for zero magnetic field for (a), (b) the second oxidation step and (c), (d) the third oxidation step. The black solid lines correspond to a fit of the *IV* characteristics according to the theory of self-heating in superconducting long microbriges [49]. (a) The shape of the *IV* characteristics for the 1 μm size in the second oxidation step is not possible to be properly fitted by the hotspot-theory. The shape of the *IV* characteristics of this sample turns to that of an overdamped Josephson junction from (a) the second to (c) the third oxidation step (see. [99]). An alternative interpretation of the latter shape of the *IV* characteristics could be given by homogeneous heating since η_S is comparable with the size of the sample. Relaxation oscillation plateaus are visible in (a), in (b) and (d) the existing relaxation oscillation plateaus at low bias voltages are not resoluted in the current plots for the benefit of a better visualization of the hotspot plateaus.

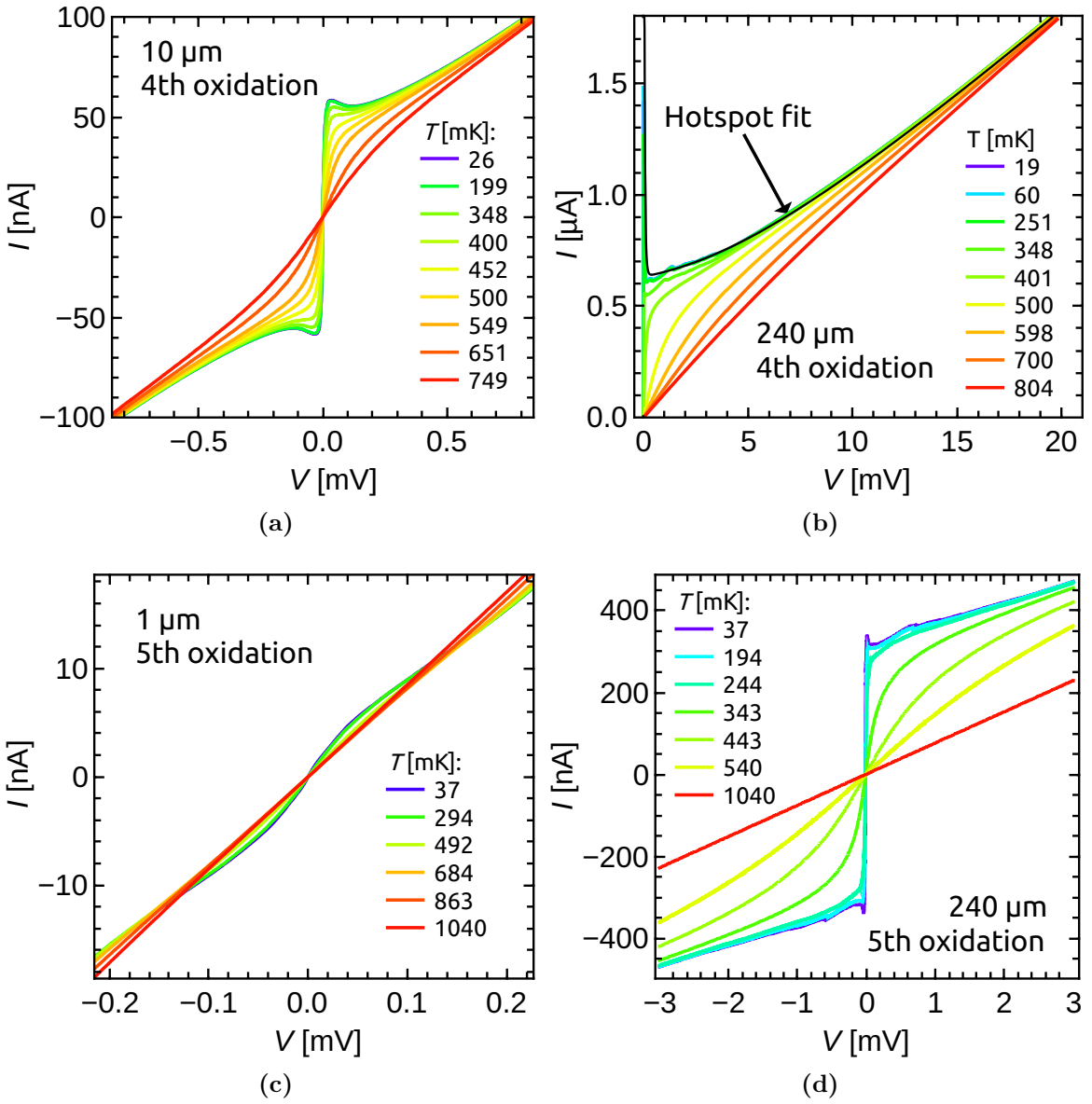

Fig. 7.3: *IV* characteristics for zero magnetic field for (a), (b) the fourth oxidation step and (c), (d) the fifth oxidation step. The black solid lines in (b) correspond to a fit of the *IV* characteristics according to the theory of self-heating in superconducting long microbriges [49]. (d) In the fifth oxidation step the superconducting current-peak in the *IV* characteristics almost disappears what prevents a fit according to the hotspot-theory. (c) The shape of the *IV* characteristics for the 1 μm for the highest oxdation step tends to become almost linear compared to the former oxidation steps. A higher influence of thermal or quantum fluctuations on the Josephson junction and at the same time the phase slip junction could be the reason for that. In (b) relaxation oscillations can be oberved at low bias voltage at a zoomed look. In (d) the relaxation oscillations vanish due to a vanishing superconducting peak in the *IV* characteristics.

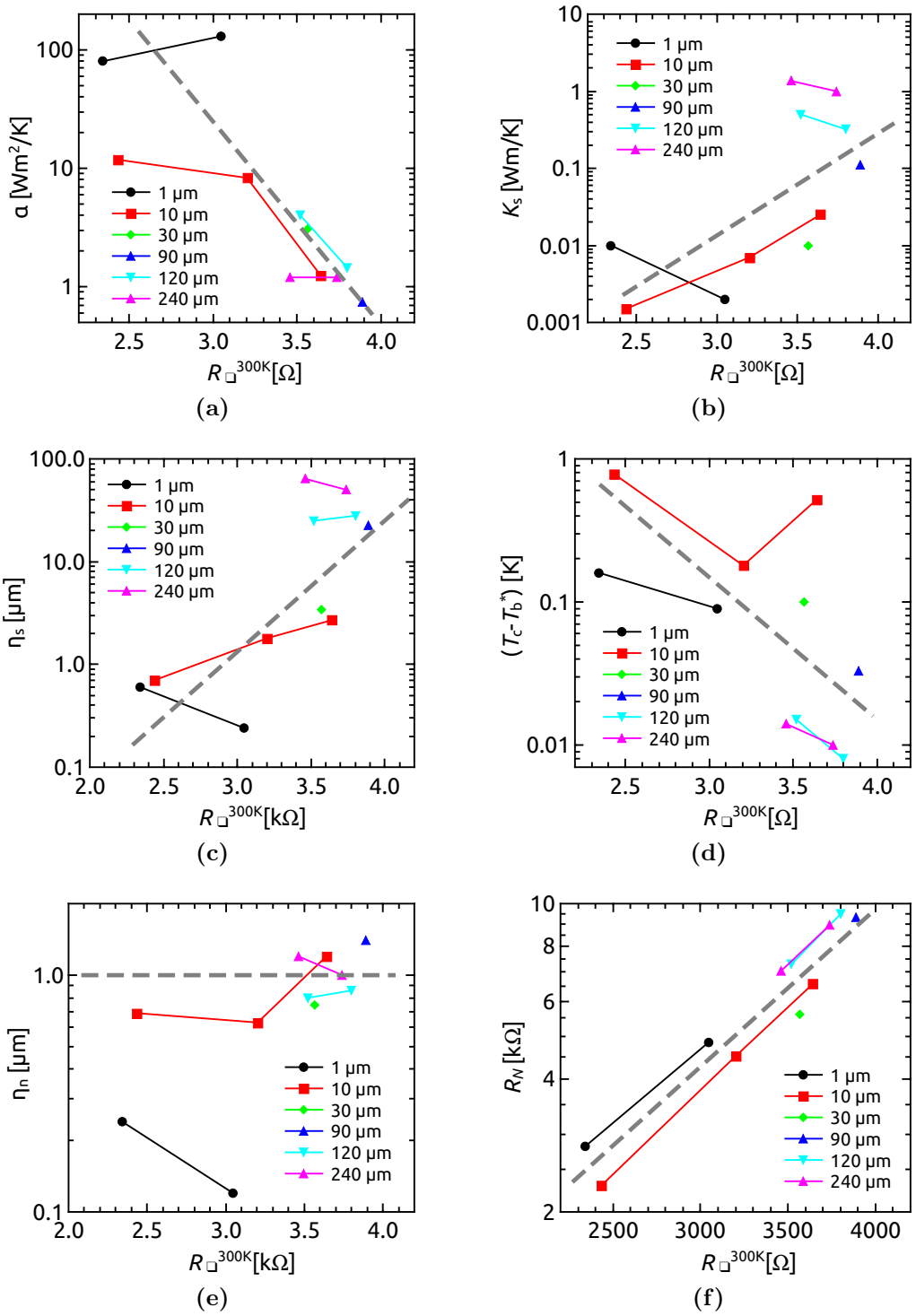

Fig. 7.4: Fitting variables for the fits of IV characteristics according to the hotspot theory vs. $R_{\square}^{300\,\mathrm{K}}$. (a) Surface thermal conductivity α, (b) thermal conductivity K_S in the superconducting parts of the film, (c) thermal healing length $\eta_S = K_S/\alpha$ in the superconducting parts of the film, (d) Difference $T_c - T_b$ between bath temperature T_b and T_c, (e) thermal healing length $\eta_N = K_N/\alpha$ in the normalconducting parts of the film, (f) normalconducting resistance R_N at high bias voltages.

The fits of the IV characteristics according to the hotspot theory reveal a remarkable variation of the fitting variables with the oxidation degree. The distinct plateau for low oxidation degrees develops a convex shape with different curvatures above and below the region of the minimum current which is adjusted by $\eta_S = K_S/\alpha$ and $\eta_N = K_N/\alpha$ in the fit, respectively. While η_N (see Fig. 7.4e) stays the same with $\approx 1\,\mu$m, η_S increases from below $\approx 1\,\mu$m to nearly $\approx 100\,\mu$m (see Fig. 7.4c) with a change in sheet resistance at room temperature of $\approx 1.5\,\mathrm{k}\Omega$. This strong increase of the extracted thermal healing length in the superconducting part of the films is accompanied by an apparent decrease of the surface thermal conductivity by two orders of magnitude (see Fig. 7.4a) and an increase of the thermal conductivity K_S in the superconducting part of the film by about three orders of magnitude (see Fig. 7.4b).

An eye-catching feature of the IV characteristics is the temperature-saturation of the shape as well as of the fitting variables at quite high temperatures. All IV curves lie on top of each other below an approximate saturation temperature of $\approx 700\,\mathrm{mK}$ for the first oxidation degree (see Fig. 7.1d). Upon further oxidations, the saturation temperature successively decreases to $\approx 200\,\mathrm{mK}$ for the fifth oxidation degree (see Fig. 7.3d).

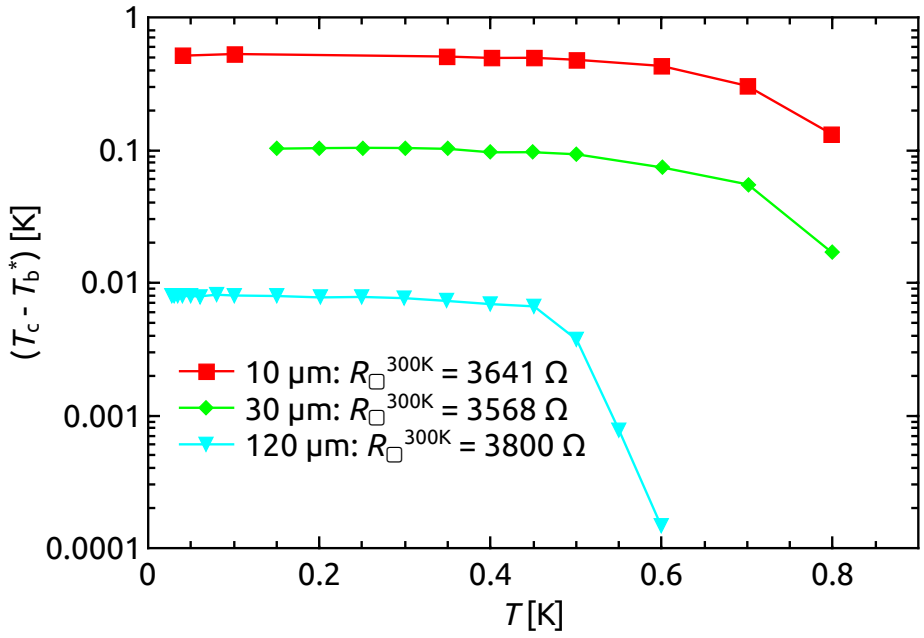

Fig. 7.5: Saturation behaviour of the fitting variable $T_c - T_b$ for differently disordered samples. The upper red squares correspond to the second oxidation step of the $10\,\mu$m size. The middle green diamonds belong to the second oxidation step of the $30\,\mu$m size. The lowest cyan triangles depict a saturation behaviour of the IV characteristics for the third oxidation step of the $120\,\mu$m size at less than 10 mK below T_c.

The temperature saturation manifests itself in a saturation of the the fitting variables, where $T_c - T_b^*$ serves to estimate the temperature difference between the critical

temperature T_c and the temperatue T_b^* (see Fig. 7.5). Here, T_b^* is not the bath temperature, instead it might be a measure for the temperature near to the edges of the contacts. A possible explanation for the large difference between the fit variable T_b^* and the bath temperature T_b is given below (see p. 96). In Fig. 7.4d the saturation values for $T_c - T_b^*$ are shown on a logarithmic temperature scale vs. $R_\square^{300\,\mathrm{K}}$. The critical temperature for the untrated sample was estimated to $T_c = 1.29\,\mathrm{K}$ in Ref. [25]. This value for T_c is about $\approx 0.6\,\mathrm{K}$ higher than the observed saturation temperature below which the IV curves of the untreated samples lay on top of each other (see Fig. 7.1b). At this saturation temperature, the temperature difference between the bath temperature and the critical temperature is expressed by the parameter $T_c - T_b \approx 0.6\,\mathrm{K}$. The saturation value for $T_c - T_b^*$ of a few hundred mK for the untreated samples (see Fig. 7.4d) roughly coincides with the estimated $T_c - T_b$. Astonishingly, $T_c - T_b^*$ shrinks by two orders of magnitude to $\approx 10\,\mathrm{mK}$ for higher oxidation degrees.

Last but not least, the evolution of the normal state resistance R_N is plotted in Fig. 7.4f. This is the fitting variable with the highest accuracy, the error for R_N is much below 1 %. From Fig. 7.4f an exponential increase vs. $R_\square^{300\,\mathrm{K}}$ is observed.

To check for mutual dependence of the fitting variables yield the same fit curve, the errors of all variables were estimated from the leastsquare fit. The errors are always below $\lesssim 10\,\%$ for all variables. The latter suspicion is averted, as the expected errors would have been a few hundred percent at least. In the normalconducting parts of the thin film it is expected that the corresponding parameters do not vary over several orders of magnitude, since the resistance R_N and the saturation temperatures do not either. This expectation is in agreement with the almost constant $\eta_N \approx 1\,\mu\mathrm{m}$. An exception is formed by the $1\,\mu\mathrm{m}$ size which is thus rather a short microbridge and cannot consistently by analized by the theory of self-heating in long microbridges.

Since R_N is the most reliable fitting variable with the smallest error of all fitting variables, we start the discussion of the accuracy of the fitting variables here. From R_N, the Wiedemann-Franz thermal conductivity K_N was calculated which is contained in the thermal healing length $\eta_N = (K_N d/\alpha)^{1/2}$. Hence η_N depends only on one fitting variable, namely α. From the regular behaviour of η_N the reliability of α can be deduced. The next variable in sequence to be verified is K_S via $\eta_S = (K_S d/\alpha)^{1/2}$ which adjusts the curvature above the region of the minimum current in the fit. The excellent match of the fitting curves to the measured curves in this region and the accuracy of η_S and K_S are sufficient to take K_S seriously. For the fitting variable $T_c - T_b$ it is not possible to decuce its reliability from other variables. A plausible argument for such a sharp saturation at a distance of minimum $\approx 10\,\mathrm{mK}$ below T_c can be given from the sharp saturation of the current plateau at temperatures of a few hundred mK.

The most peculiar results from the hotspot-theory are the strongly decreasing α and the extreme increase in K_S with increasing disorder.

The first, the decrease of the surface thermal conductance α, was already reported in the original work of Ref. [49] when the temperature T_b was decreased. Here we have a similar lowering of temperature, in particular of the saturation temperature

which decreases for higher $R_{\square}^{300\,\mathrm{K}}$. A possible explanation for that is the weak electron-phonon coupling in the film which makes a temperature decoupling of the film from the substrate possible. An analysis of electron-phonon decoupling in critically disordered TiN films can be found in Ref. [78]. A quantitative analysis is not possible here due to not known critical temperatures and due to too few and too scattered data points for α.

In order to give possible explanations for the second result, the strong increase of the thermal conductivity below the critical temperature in the superconducting regime, a few existing theories are listed below. The main question is: can superconductivity provide large thermal conductivities?

In the normal state electron-phonon scattering limits the phonon mean free path Λ_{Ph}. Upon Cooper pairing Λ_{Ph} increases, since Cooper pairs do not scatter phonons. At the same time the number of quasiparticle excitations decreases quickly below T_c and thus the electron-mediated thermal conductivity rapidly vanishes below T_c. The overall thermal conductivity is determined by a competition of the rapidly vanishing electron-caused thermal conductivity and the increasing phonon-mediated thermal conductivity below T_c [105]. In pure superconductors the total thermal conductivity disappears slightly below T_c. But for sufficiently disordered superconductors, where the phonon-mediated thermal conductivity dominates the the total thermal conductivity in the normal state near to T_c, a rise of the total thermal conductivity below T_c can happen. For $T \to 0$ the total thermal conductivity decreases due to a decrease of the phonon population at low temperatures. At lowest temperatures phonon-defect scattering starts to dominate the heat transfer.

For high-T_c superconductors, similarly resistive like our TiN-films, an increase of the total thermal conductivity by a factor of $\approx 2-3$ below T_c was observed. In our TiN-films we observe an increase of the thermal conductivity in the superconducting regime by about four orders of magnitude. With increasing disorder, the Wiedemann-Franz thermal conductivity decreases by about one order of magnitude, while the thermal conductivity in the superconducting state K_S increases by three orders of magnitude starting from $K_S \simeq K_N \approx 0.0015\,\mathrm{Wm/K}$ for the least disordered samples.

Deppe and Feldman [106] calculated the thermal conductivity of a Josephson junction array when the temperature is lowered across the order-disorder phase transition at T_{v-BKT} below which the sample becomes globally superconducting. The heat transport in the Josephson junction array is argued to be theoretically enhanced due to noncommuting capacative terms in the Hamiltonian. They found under the usage of two different theoretical approches that the thermal conductivity increases by one order of magnitude as the temperature is lowered below T_{v-BKT}. The parameters they used were adjusted for granular aluminum films with a resistivity of $1.75\,\Omega\mathrm{cm}$ which is about three orders of magnitude lower than the resistivity of our TiN-films. An adjustment of the parameters to the TiN-films measured here would be a future task.

Another effect in Josephson junction arrays in considered by Andreas Andersson and Jack Lidmar in Ref. [107]. The Nernst effect can produce a vortex motion under

an applied temperature gradient. Generally, the Nernst effect describes the creation of an electric field in y-direction perpendicular to a temperature gradient in x-direction and a transverse magnetic field in z-direction.

$$\nu = \frac{E_y}{B_z(-\Delta_x T)} \tag{7.1}$$

where ν is called the Nernst coefficient. Vortices in a 2D superconductor intrinsically generate a transverse magnetic field. The electric field established by the Nernst effect can cause a flux-flow of vortices via the Lorentz force in the direction of the temperature gradient. Since vortices are associated with finite entropy, they carry heat when they are moved along a temperature gradient.
The contribution of vortex motion to the heat conductivity K_S was calculated in numerical simulations. At low temperatures $T \ll T_{v-BKT}$ the contribution of spin waves dominates K_S. This contribution is temperature independent and depends logarithmically on the size of the array or rather on the screening length, depending on which one is smaller. On approach of the BKT transition K_S rapidly increases, as the thermal conductivity is enhanced by the unbinding of thermally induced vortex-antivortex pairs. A maximum of K_S in the region $T_{v-BKT} \ll T \ll T_c$ was observed. A comparison of the thermal conductivity calculated in Ref. [107] to the thermal conductivities found here is hardly possible, because in Ref. [107] the evolution of the thermal conductivity across the critical temperature T_c is not evaluated. Therefore it is not possible to estimate if the thermal conductivity in the superconducting phase is actually higher than in the normalconducting phase.

The three above mechanisms are surely not the only possibilities to enhance the thermal conductivity in the superconducting regime compared to the thermal conductivity in the normalconducting regime. A combination of different mechanisms may finally cause the drastic effects that we deduce from the hotspot theory.

About the origin of the saturation behaviour of the IV characteristics at relatively high temperatures and the decrease of $T_c - T_b^*$ down to $\approx 10\,\mathrm{mK}$ we just can speculate. The highly non-monotonic temperature behaviour of the thermal conductivity across the critical temperature surely causes a change of the temperature distribution of Fig. 2.6 in the film that is assumed for the hotspot model. Under the assumption that the thermal conductivity rises drastically as T is lowered below T_c till it reaches a maximum and decreases again for $T \to 0$, the thermal healing length $\eta_S(x,T)$ strongly depends on the temperature and therefore on the site on the superconducting film.
For lowest bath temperatures T_b, $\eta_S(\frac{1}{2}L, T_b)$ near the electrical contacts is short compared to $\eta_S(x_0, T_c)$ near the normalconductor/superconductor interface. This results in a much steeper temperature gradient at the edges of the film than near the hotspot. With the exception of the edges, the temperature gradient is smooth, with temperatures slightly lower than T_c up to distances from the center $x = \frac{1}{2}L - \Delta_L$. If Δ_L, the size of the edge region where the temperature gradient is steep, is much smaller than the sample length L, the region $-\frac{1}{2}L + \Delta_L < x < \frac{1}{2}L - \Delta_L$ dominates the behaviour of the IV characteristics. The effective bath temperature T_b^* at the edges of this middle region will be much higher than the temperature T_b of the contact pads. Additionally,

the surface heat transfer is very weak and makes a thermalization of the film via the substrate inefficient. The criterion for the position of Δ_L is the position on the film where the local temperature crosses the value of the fitting variable $T_c - T_b^*$ from the hotspot-fits.
This mechanism would explain the saturation behaviour, but it is not possible to determine the temperature dependence of K_S for $T \to 0$ with the hotspot theory. A temperature gradient between two temperatues that are both much lower than T_c would be essential for this determination, which is obviously not possible for a normalconducting hotspot in the middle of the film.

It is important to be aware of the simplifications that are made in the hotspot-model. The $R(T)$ dependence is taken to be a step-function at T_c which is not the case for the highly disordered TiN films where the transition is broadened due to superconducting fluctuations and the BKT physics. K_S and K_N are assumed to be temperature independent in the hotspot-model. However, particularly K_S seems to behave highly non-monotonic with temperature. The solution of an extended hotspot-model that is adapted to the latter deviations from the model in [49] would require numerical simulations with recursive convergence methods.

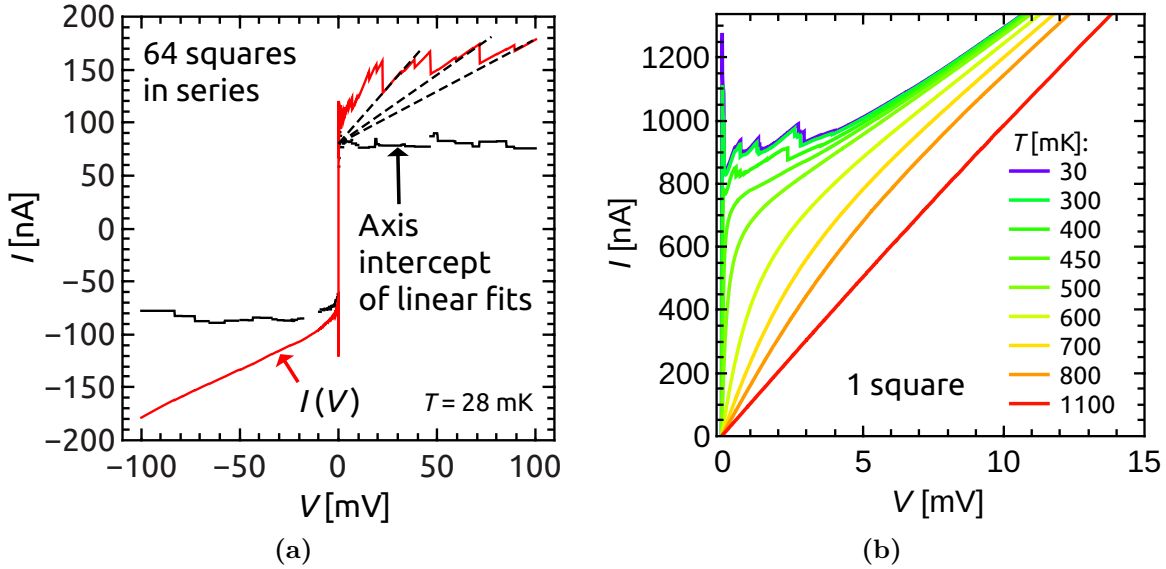

Fig. 7.6: IV characteristics taken from samples with different aspect ratios. (a) The step-shape of the IV characteristics for a very long TiN film with 64 squares in series is due to a subsequent formation of phase slip centers with increasing bias voltage. The extrapolated intercept of the linear fits indicated by the black dashed lines at $V = 0$ is taken to be half the critical current $\frac{1}{2}I_c \simeq 80\,\mathrm{nA}$. The length of the sample is 1.6 mm and the width is 25 μm. (b) The step structure due to the formation of hotspots is sustained even for the square shaped sample with a width and length of 200 μm.

In Fig. 7.6 we now switch to IV characteristics where the dissipated Joule power is not sufficient to establish a normalconducting hotspot. In this case phase slip centers control the shape of the IV curves (see chapter 2.2.4). The voltage steps that usually

occur in a current biased measurement (see Fig. 2.5) here translate to current steps in the voltage biased measurement in Fig. 7.6a. The measured sample has 64 squares in a row. The sample is 1.6 mm long and 25 μm wide and patterned on the wafer D03 with a tuned sheet resistance at room temperature of $R_{\square}^{300\,\mathrm{K}} = 4025\,\mathrm{k}\Omega$. According to the theory of Ref. [48], the linear fits of the linear regions in the IV curve between the steps should extrapolate all to the same point at $V = 0$ with the magnitude $I_c/2$. This obviously is the case in Fig. 7.6a. Heating effects should occur at higher bias voltage, but this is beyond the measurement range. In Fig. 7.6b the IV characteristics of a square-shaped sample with lateral size 200 μm, patterned on the same sample like the 64 square size, with $R_{\square}^{300\,\mathrm{K}} = 4181\,\mathrm{k}\Omega$, shows phase slip behaviour at lowest bias voltage which changes over to a shape that is deterimined by heating at higher voltages. The observation that there are much more PSCs established in long films rather than short films coincides with the energetically more favourable placement of PSCs with a higher distance to each other.

7.2 Hysteretic jumps in insulating IV characteristics

In the previous section IV characteristics at zero magnetic field were analyzed. By increasing the magnetic field, we now turn from the superconducting side of the B-SIT to the insulating side. Here, we notice a remarkable similarity of the shape of the IV characteristics when the voltage and the current axes are changed (compare e.g. Fig. 7.1 on the superconducting side). In Fig. 7.7 the IV characteristics for the 120 μm size of sample D03_1 are shown for a set of low temperatures at the magnetic field of $B = 1\,\mathrm{T}$. Current jumps are visible in these IV curves which are measured with a voltage-biased setup (dashed lines in Fig. 7.7). The resistance in the linear region around zero bias at lowest measured temperatures is $R_{max}(T = 37\,\mathrm{mK} \approx 2\,\mathrm{G}\Omega$. It is important to note that the IV characteristics are linear around zero bias down to lowest temperatures and no powerlaw behaviour $I \propto V^{\alpha}$ with $\alpha > 3$ is observed. For more disordered samples investigated in Ref. [98], this $\alpha > 3$ was attributed to a charge BKT regime at low temperatures.

Here, we reveal for the fist time the complete shape of the IV characteristics, including the behaviour on the hysteretic branch which usually is hidden by the jump. With a $R_{series} = 1\,\mathrm{M}\Omega$ series resistor between the current preamplifier and the sample, a measurement setup is assembled which is a voltage-bias setup for high sample resistances and a current-bias setup for low sample resistances. In the further description of the trace of the IV we first focus on the lowest temperature at $T = 37\,\mathrm{mK}$ and the sweep direction of the applied voltage from zero in the positive direction. Since the resistance around zero bias voltage is 2000 times higher than the series resistor, the measurment is voltage-biased in this regime. As soon as the maximum voltage at $V_{peak} = 0.65\,\mathrm{mV}$ is reached (see Fig. 7.7c), the characteristics of the measurement successively changes to current-bias. The voltage drop V_s across the sample is then given by

$$V_s = V_{source} - I \cdot R_{series} \tag{7.2}$$

where V_{source} is the voltage that is applied to the high-impedance system comprised by the series resistor with $R_{series} = 1\,\mathrm{M\Omega}$ and the sample.

Above V_{peak}, the IV characteristics turns from its highly insulating part into a constant-voltage plateau with a voltage $V_{plateau1} \approx 0.5\,\mathrm{V}$ (see Fig. 7.7c). The voltage does not immediately drop to $V_{plateau1}$ after V_{peak} is exceeded. Instead, the IV curves follows the load-line with differential resistance $-R_{series}$ starting from V_{peak} and entering into the voltage plateau at $V_{plateau1}$ (compare Fig. 2.9). At a current of $0.2\,\mathrm{nA}$ and a voltage of $0.5\,\mathrm{mV}$, the IV characteristics turns into a second constant-voltage plateau with $V_{plateau2} \approx 0.43\,\mathrm{V}$ (see Fig. 7.7c). Again, the second voltage plateau is approached across the load line with differential resistance $-R_{series}$, starting from $V_{plateau1}$ and entering into the voltage plateau at $V_{plateau2}$. The measurement has now already rather a current-biased than a voltage biased character. This can be seen from the point in the IV curve, where the upper plateau is left at current of $0.2\,\mathrm{nA}$ and a voltage of $V_{plateau1} = 0.5\,\mathrm{mV}$. This corresponds to an effective resistance of the sample of $0.5\,\mathrm{mV}/0.2\,\mathrm{nA} = 0.25\,\mathrm{M\Omega}$. The series resistor at this point already is four times as high as the effective sample resistance. Hence, the applied current rather than the applied voltage V_s is changed by a change of V_{source}. After a series of smaller steps to less and less resistive regions in the IV characteristic, a linear behaviour at high biases occurs where the IV curves for all the presented temperatures in Fig. 7.7a collapse. This linear region extrapolates to $\approx 0.3\,\mathrm{mV}$ at zero current. For higher temperatures, the voltage-height of the voltage plateaus is lowered, until the plateau feature vanishes completely at the highest shown temperature of $T = 81\,\mathrm{mK}$.

A plateau usually refers to a horizontal line. Here, we apply the word "plateau" to emphasize the dual shape of the constant-voltage regions in the insulating IV characteristics to the current plateaus in the superconducting IV characteristics (section 7.1).

In the negative bias region the shape of the IV characteristics is completely identical with respect to a point symmetry around the origin. There is no hysteresis in the measured IV characteristics that are obtained under usage of the special measurement setup with the $1\,\mathrm{M\Omega}$ series resistor.

The non-hysteretic behaviour is different to what is usually seen in IV characteristics, where jumps in the voltage biased IV curves occur due to electron-phonon decoupling (see eg. [80, 108] and [78] for the insulating IV characteristics above the charge BKT transition temperature). The bistability of the electron temperature causes strongly hysteretic IV characteristics. In terminology, the retrapping voltage V_{trap} is defined as the voltage at which the highly resistive state is reached by a jump starting from the low resistive state at high biases. In the other direction, the escape voltage is defined as the voltage at which a jump occurs from the highly resistive state into the low resistive state. In Figs. 7.7b and 7.7c the retrapping- and escape-behaviour of the IV characteristics is shown, respectively,. These curves were obtained in a voltage-biased measurement without a series resistor. At high biases the IV characteristics of the two different measurement setups lie on top of each other.

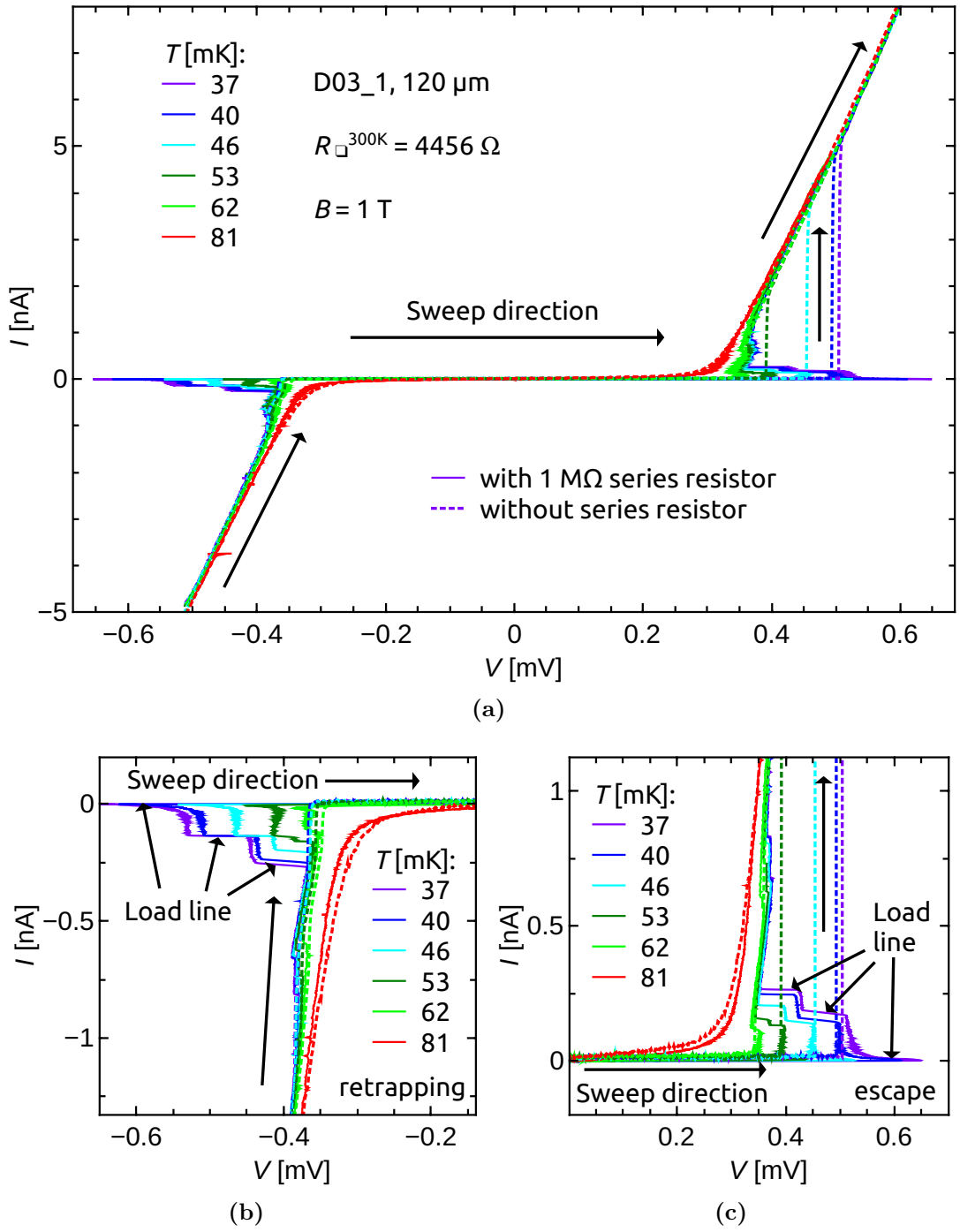

Fig. 7.7: (a) Comparison of IV characteristics obtained from a voltage-bias measurement with a 1 MΩ series resistor between current preamplifier and sample (solid lines) and a measurement obtained from a regular voltage-bias measurement without a series resistor (dashed lines). The sweep direction is in the positive direction. The device under test was the 120 μm size of the sample $D03\_1$ after the fifth oxidation step with a sheet resistance at room temperature of $R_{\square}^{300\,\mathrm{K}} = 4456\,\Omega$ with an applied magnetic field of $B = 1\,\mathrm{T}$. (b) Zoom of (a) into the negative bias region where the switch from the low resistive state to the highly resistive state occurs, labelled with "retrapping". (c) Zoom of (a) into the positive bias region where the switch from the highly resistive state to the low resistive state ocurrs, labelled with "escape".

This serves as a verification of the reliability of the IV curves that were obtained from the measurement setup with the series resistor where the voltage drop at the sample was calculated according to Eq. 7.2.

A comparison of the IV characteristics originating from the two different measurements reveals remarkable details. It is surprising that the escape-voltage, corresponding to the vertical dashed lines in Fig. 7.7c, is not equal to the voltage peak V_{peak} obtained by the high-impedance measurement. A close look reveals a connection between the escape-voltage and the constant-voltage plateaus that are observed in the high-impedance IV characteristics. Over the whole range of temperatures, where the plateaus occur, the escape-voltage V_{escape} coincides with the voltage-height $V_{plateau1}$ of the plateaus very well. Only for the lowest temperature of $T = 37\,\mathrm{mK}$ the escape-voltage appears to be a bit lower than the height of the plateau. The most probable reason for this difference is the slightly higher base temperature by $\approx 1\,\mathrm{mK}$ of the cryostat for the measurement without the series resistor.
In Fig. 7.7b the focus is on the jump in the IV characteristics of the measurement without a series resistor at the retrapping-voltage V_{trap}. With this low-impedance measurement setup, it is only possible to sweep the voltage in one direction. Here in Fig. 7.7b the voltage is sweeped from negative to positive. Hence, it is not possible to trace the voltage-plateaus and the voltage-peak in the IV characteristics that are obtained by the high-impedance measurement. Instead, a jump from the low resistive state to the highly resistive state appears in the IV characteristic of the low-impedance measurement. The value of V_{escape} coincides with the minimum voltage value in the plateau-shaped region of the IV characteristics that are measured in the high-impedance setup.

Most recently, the discontinuities in the IV characteristics of insulating indium oxide films attracted attention in Ref. [109]. Therein, Doron *et al.* discuss the dependence of the escape-voltage and the trap-voltage on temperature and magnetic field. With their standard voltage-bias measurement setup they obtained for $B = 9.5\,\mathrm{T}$ an increase of the escape-voltage vs. temperature upon lowering temperature, followed by a sharp increase at a certain temperature that enters a temperature independent plateau at lowest temperatures. Due to this observation the question was raised whether there actually is a highly resistive state in the IV characteristics that is experimenally accessible down to lowest temperatures $T \to 0$.

Altshuler *et al.* argued that jumps in the IV characteristics of disordered films occur due to a decoupling of the electron temperature from the phonon temperature. The theoretically obtained IV characteristics reveal a bistability in which the experimental IV curves are predicted to follow a hysteretic behaviour. According to Ref. [108], the escape-voltage is smaller than the upper bistability boundary of the theoretically derived IV characteristics, since the switch is determined by kinetics of the decay of metastable states. We argue, that by virtue of the high-impedance measurement, we are now able to fully resolve the theoretically predicted IV characteristics, as there appears no bistability region in the IV characteristics measured in the high-impedance setup. The peak-voltage V_{peak} then coincides with the upper bistability boundary.

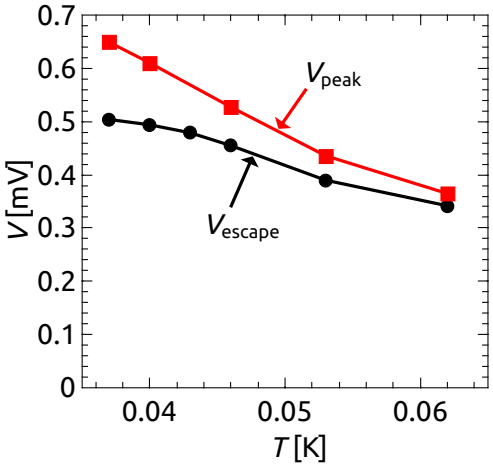

Fig. 7.8: Comparison of the peak-voltage V_{peak} and the escape-voltage V_{escape} extracted from the IV characteristics in Fig. 7.7. V_{peak} raises linearly down to the lowest measured temperature of $T = 37\,\mathrm{mK}$. Instead, V_{escape} seems to saturate upon lowering temperature.

We now compare the results of Ref. [109] to our observations depicted in Fig. 7.7. In Fig. 7.8 the peak-voltage V_{peak} obtained with the high-impedance setup is compared to the escape-voltage V_{escape} extracted from the IV characteristics of Fig. 7.7 that were measured without the series resistor. While V_{escape} seems to saturate at low temperatures, V_{peak} raises linearly upon lowering temperature. The the saturation behaviour of V_{escape} is similar to what is observed in Ref. [109]. For magnetic fields below $B \leq 8\,\mathrm{T}$ the temperature dependence of V_{escape} in Ref. [109] saturates, too. This saturation behaviour was attributed to the effect of inhomogeneity on the electron-heating model. The sample's inhomogeneity is argued to favour the nucleation of local normalconducting hotspots (see section 7.1).
It would be of great interest to know how the IV characteristics of the indium oxide samples measured in Ref. [109] evolve in a similar high-impedance measurement setup like the one used here. We speculate that the jumps in the IV curves may be absent and a peak-voltage V_{peak} which is higher than the measured escape-voltage V_{escape} will appear. If the physics observed in Ref. [109] is indeed the same as in our experiments, the steep increase of V_{escape} with lowering temperature to 60 mK at $B = 9.5\,\mathrm{T}$, may collapse with the increasing peak-voltage V_{peak}. For even lower temperatures, the measured V_{escape} decreases and finally saturates at lowest measured temperatures down to 11 mK. However, V_{peak} might rise even further upon lowering temperature below 60 mK, similar to the behaviour of V_{peak} in our measurements (see Fig. 7.8).

It seems advantageous to pursue measurements with the high-impedance setup, because valuable insights might be gained from IV characteristics if the discontinuities are avoided.

7.3 $R(T)$ and critical temperature at zero magnetic field on approach of the D-SIT

To find the critial temperature T_c at which a finite order parameter occurs, is by no means trivial in a disordered thin film. The temperature dependence of the resistance $R(T)$ displays a non-monotonic behaviour when the temperature is lowered. For the samples discussed here, the resistance usually rises upon lowering temperature until a maximum in the resistance is reached typically at $1-2\,\mathrm{K}$. The lower the temperature is at which the maximum occurs, the higher is the resistance at the maximum. This can exemplarily be seen in Fig. 7.9 which shows $R(T)$ curves for TiN films at different oxidation levels and zero magnetic field. The maximum temperatures up to which the cryostat was operated were too low to record the maxima for the lower disordered samples.

The focus in Fig. 7.9 lies on the broad temperature range within which the resistance vanishes upon lowering the temperature below the $R(T)$ maximum. In this region no sharp drop of resistance occurs, like it is usually observed for clean bulk-superconductors in zero field. In disordered thin films superconducting fluctuations and the vortex BKT physics broaden the transition from normal to zero resistance. In addition, thin disordered metal films undergo localization effects at low temperatures due to the weak localization and the Aronov-Altshuler effect [5].

The combined fluctuation corrections to conductivity have been calculated theoretically e.g. in Ref. [30] and were applied to thin TiN films in Ref. [27, 25] (see chapter 2.2.2). Additional corrections to conductivity were added to the theoretical expressions in Ref. [30] due to weak localization and the Aronov-Altshuler effect [5]. A fit to measured $R(T)$ curves at zero magnetic field was possible under the variation of three fitting parameters. One parameter described the Maki-Thomson term, the second the localization effects of the electrons and the third was the critical temperature T_c. At T_c the remaining resistance was estimated to $R(T_c) \simeq (0.08-0.13)\cdot R_{max}$, where R_{max} is the resistance at the maximum of the $R(T)$ curve. In a private communication, Tatyana Baturina recommended the $T_{c,0.2}$-criterion for a quick estimation of the critical temperature. Here, the temperature $T_{c,0.2}$ is determined at 20 % of R_{max}: $R(T_{c,0.2}) \simeq 0.2\cdot R_{max}$.

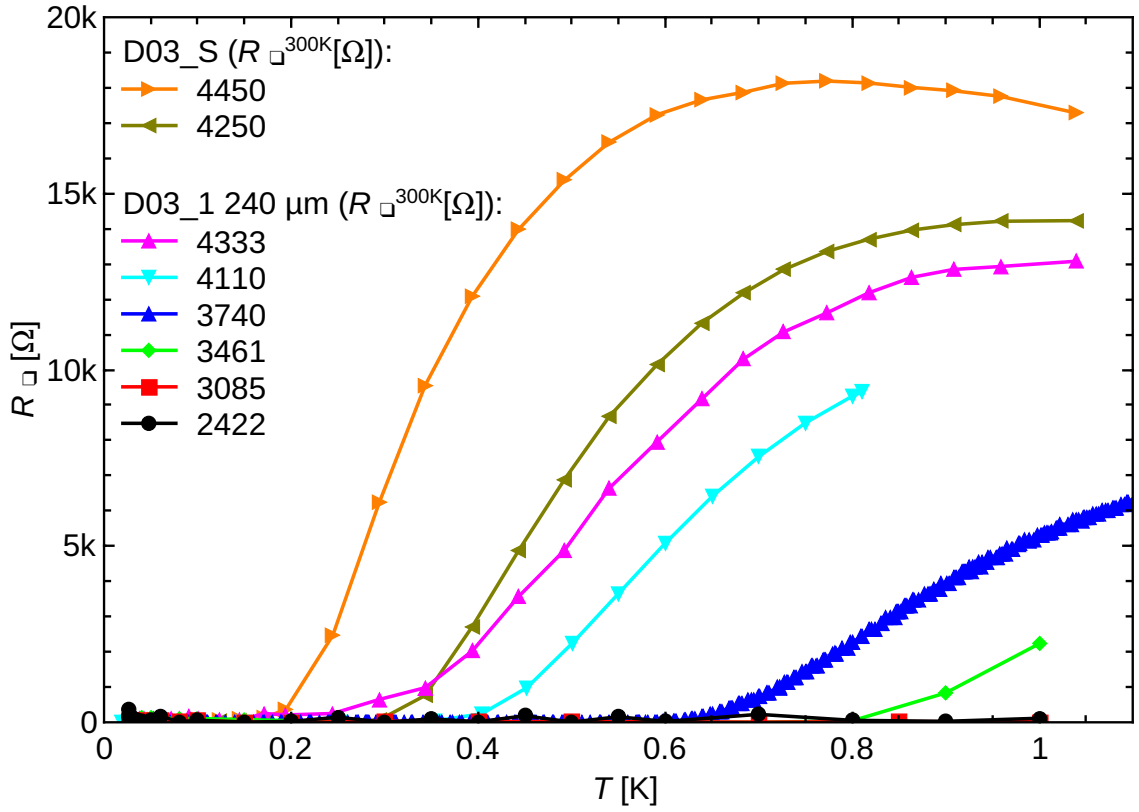

Fig. 7.9: $R(T)$ characteristics at zero magnetic field for differently disordered samples patterned from the wafer D03. The upper two curves are measured from sample D03_S with a length of 1.84 mm and a width of 1.036 mm. The lower six curves correspond to measurements of sample D03_1 for the untreated sample to the fifth oxidation steps in the order from low to high $R_{\square}^{300\,\mathrm{K}}$. For the untreated sample and the fist oxidation step the sample is superconducting over the whole measured temperature range. The second and thrid $R(T)$ curves from above cross at $\approx 1\,\mathrm{k}\Omega$. A reason for this can be the increase of the parameter b in the Halperin-Nelson fit with Eq. 2.27 for increasing sample sizes L in the fifth oxidation step of sample D03_1 (see section 8.1). Since sample D03_S is much bigger than the 240 μm size of sample D03_1, the steeper slope in the $R(T)$ at superconducting transition of sample D03_S possibly can be attributed to a higher b in the Halperin-Nelson fit.

The purpose of this section is to test for the validity of the $T_{c,0.2}$-criterion. In chapter 5 we already obtained values for the critical temperature and the upper critical magnetic field from the theory of Galitski and Larkin. There, the input-information is a set of magnetoresistance isotherms for a number of different temperatures and a field range of $\approx 1\,\mathrm{T} - 8\,\mathrm{T}$.

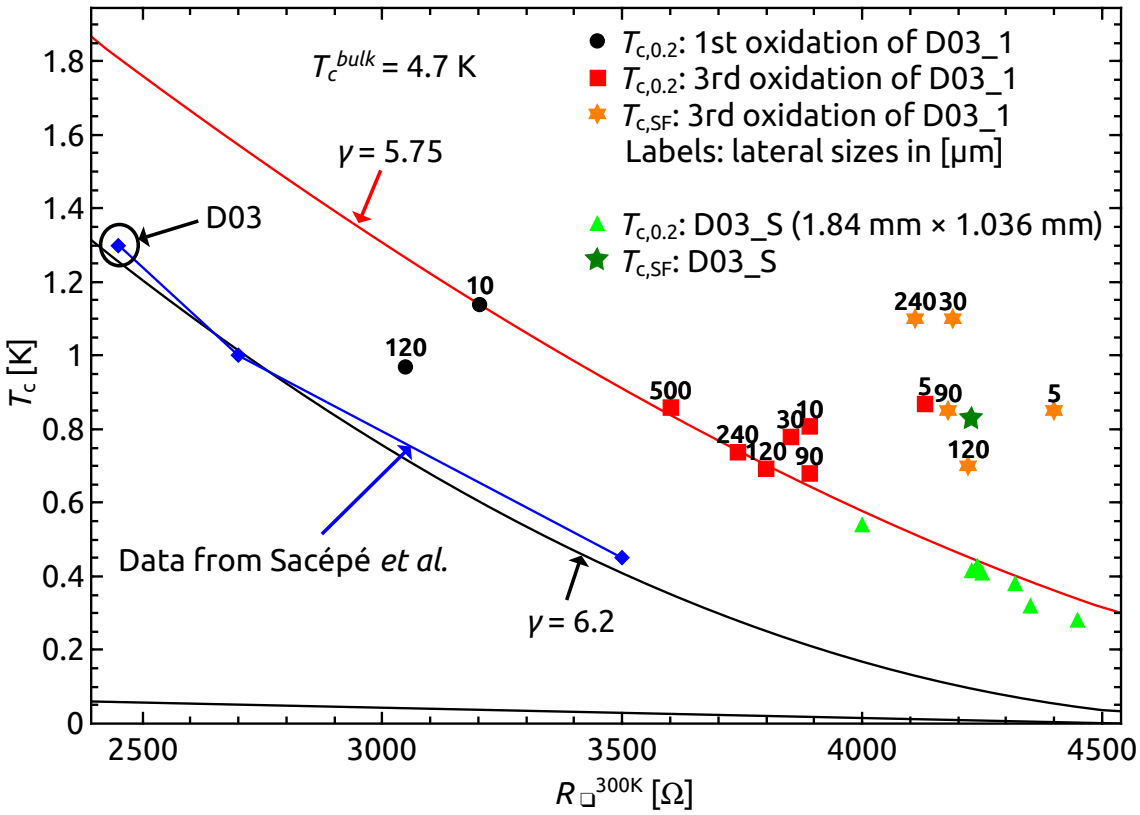

Fig. 7.10: The critical temperature of the superconducting transition at zero magnetic field vs. $R_\square^{300\,\mathrm{K}}$ determined from different approaches. The blue diamonds are taken from Sacépé *et al.* [6] where the critical temperature was estimated by a best fit of the measured $R(T)$ to the theory of superconducting fluctuations above T_c. Finkelstein's formula Eq. 2.60 reproduces the suppression of T_c according to the blue diamonds for increasing disorder with the parameters $T_c^{bulk} = 4.7\,\mathrm{K}$ and $\gamma = 6.2$. The black dots, red squares and green triangles were obtained from $R(T_{c,0.2}) = 0.2 \cdot R_{max}$ where R_{max} is the maximum resistance in the $R(T)$ curve at zero magnetic field. $T_{c,0.2}$ thus is set to 20 % of R_{max}. The red curve shows Finkelstein's formula for $T_c^{bulk} = 4.7\,\mathrm{K}$ and $\gamma = 5.75$. The orange stars and the green star correspond to the transition temperatures $T_{c,SF}$ that were found from simultaneous fits of the magnetoresistance isotherms for many different temperatures according to the theory of Galitski and Larkin [16] (see Fig. 5.1, 5.2, 5.3).

In Fig. 7.10 the critical temperatures determined by using different methods are plotted in the same graph against $R_\square^{300\,\mathrm{K}}$. The blue data points are taken from Sacépé *et al.* [6] where Finkelstein's formula Eq. 2.60 was adjusted with the parameter $\gamma = 6.2$. These points were obtained by a fit according to the theory of superconducting fluctuations. The black points, the red squares and the green triangles are the result for $R(T_{c,0.2}) = 0.2 \cdot R_{max}$. For $\gamma = 5.75$ Finkelstein's formula fairly describes the supression of $T_{c,0.2}$ for increasing disorder with an exception of the smallest samples measured in the third oxidation step (red squares).
The orange stars and the green star display the critical temperatures obtained from the Galitski-Larkin fits. They are scattered around $T_{c,SF} \sim (0.9 \pm 0.2)\,\mathrm{K}$. Hence, they

lie double as high as expected from the Finkelstein-formula with $\gamma = 5.75$. Altogether, we compare three different possible choices for the critical temperature, originating either from a fit according to superconducting fluctuations, or from setting $T_{c,0.2}$ to $R(T_{c,0.2}) = 0.2 \cdot R_{max}$, or from the Galitski-Larkin fits at high magnetic fields.

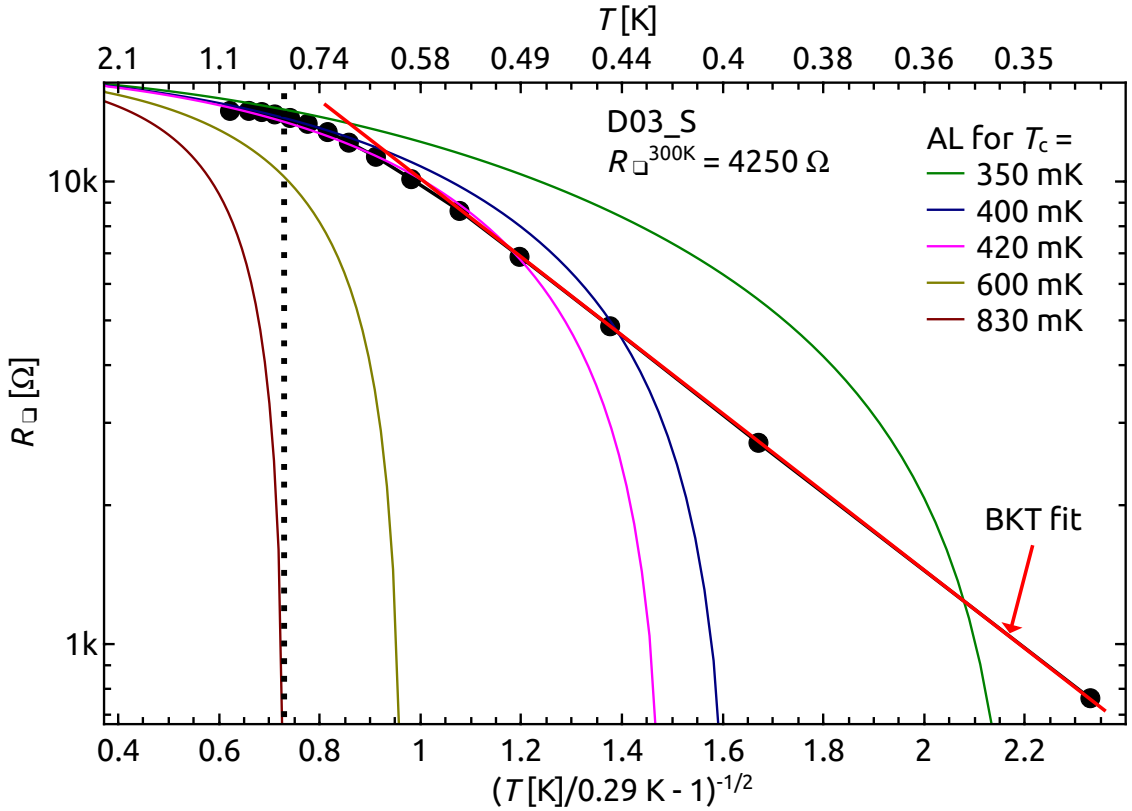

Fig. 7.11: Temperature dependence of the resistance of sample D03_S with $R_{\square}^{300\,\mathrm{K}} = 4250\,\mathrm{k\Omega}$. The abscissa is scaled in the form $(T/T_{BKT} - 1)^{-1/2}$ with $T_{BKT} = 290\,\mathrm{mK}$ and the resistance is scaled logarithmically in order to test for a temperature dependence of the resistance according to the theory of Halperin and Nelson for the BKT regime (Eq. 2.27). The red straight line demonstrates a BKT dominated regime up to resistances of $\approx 10\,\mathrm{k\Omega}$. The dashed vertical line indicates the superconducting transition temperature $T_c = 0.83\,\mathrm{K}$ found by the $R(B)$-fits according to Galitski and Larkin. The concave coloured lines show the Aslamazov-Larkin type of drop of the resistance at different critical temperatures. For a thorough discussion of the right determination of T_c see text.

Now, we turn to the analysis of the $R(T)$ curves with respect to the vortex BKT physics according to the Halperin-Nelson formula (Eq. 2.27). The $R(T)$ curve in Ref. [25] is well described by the theory of superconducting fluctuations, with $R_{v-BKT}(T_c) \simeq (0.08 - 0.13) \cdot R_{max}$. Here, $R_{v-BKT}(T_c)$ refers to the resistance at T_c, originating from the physics of the vortex BKT regime. However, the samples measured in Ref. [25] are deeply on the superconducting side of the disorder-driven SIT. Here, we will reveal the increasing importance of the vortex BKT with increasing disorder. We argue on the basis of Halperin-Nelson fits to the $R(T)$ curves at zero field, that almost the complete

drop in resistance occurs in the vortex BKT phase for critically disordered TiN films. This vortex BKT dominated scenario is depicted in Fig. 7.11. The red line corresponds to a fit of the Halperin-Nelson formula (Eq. 2.27) with $T_{v-BKT} = 0.29\,\mathrm{K}$. Up to $\approx 10\,\mathrm{k\Omega}$ the $R(T)$ dependence is well described by the vortex BKT physics. This corresponds to about $2/3 \cdot R_{max}$! $T_{c,SL} = 0.83$ from the fits of the magnetoresistance isotherms according to the theory of the superconducting fluctuations above B_{c2} by Galitski and Larkin, is indicated by the vertical dashed line. The drop of the resistance according to the theory of Aslamazov and Larkin is shown by the coloured lines in Fig. 7.11 for different values of the parameter T_c (see expression for AL in table 2.1). This emphasizes the difficulty to explain the $R(T)$ curves at zero field according to the theories of superconducting fluctuations above T_c. Near to T_c, the Aslamazov-Larkin term dominates the superconducting fluctuations and yields a sharp drop of the resistance near T_c with $R^{-1} = R_N^{-1} + R_0^{-1}/(T/T_c - 1)$ (from Ref. [110]), where $R_0 = e^2/16\hbar = 6.58 \cdot 10^4\,\Omega$ and R_N is the normal resistance.
The concave shape of the Aslamazov-Larkin curves in Fig. 7.11 obviously excludes the Aslamazov-Larkin effect as an alternative explanation of the vortex BKT like behavior of the $R(T)$ curve. The best fit of the Aslamazov-Larkin behaviour to our data for $R \gtrsim 6\,\mathrm{k\Omega}$ is found for $T_c = 420\,\mathrm{mK}$. This conflicts with the BKT behaviour up to $\approx 600\,\mathrm{mK}$ which may serve as a lower bound for T_c. However, for $T_c = 600\,\mathrm{mK}$ as well as for $T_{c,SF} = 830\,\mathrm{mK}$, it is not possible to describe the $R(T)$ curve with the theory of superconducting fluctuations.

In Fig. 7.12 the $R(T)$ curves of four differently disordered samples are fitted according to the Halperin-Nelson formula Eq. 2.27 with the abscissa scaled to $(T/T_{BKT} - 1)^{-1/2}$. Fig. 7.12c shows the BKT fit for the least disordered sample and Fig. 7.12d the BKT fit for the most disordered sample. The maximum resistance up to which the $R(T)$ curves follows a BKT behaviour grows from $\approx 5\,\mathrm{k\Omega}$ to $\approx 15\,\mathrm{k\Omega}$ with increasing disorder. This translates to $1/2 \cdot R_{max}$ and $5/6 \cdot R_{max}$, respectively.

The existing theories either describe the temperature dependence of the resistance in the region $T_{v-BKT} < T < T_c$ with the vortex BKT physics or the region $T > T_c$ with superconducting fluctuations. In the vortex BKT regime the $R(T)$ follows Eq. 2.27, with a finite resistance $R_{v-BKT}(T_c)$ at T_c. But superconducting fluctuations are only present at temperatures higher than T_c what results in zero resistivitiy at T_c according to the theory of superconducting fluctuations. The central problem is the lack of a theory that describes the $R(T)$ continuously from T_{v-BKT} over T_c up to high temperatures. The impossibility of a fit of the $R(T)$ curve at zero magnetic field solely considering superconducting fluctuations (see Fig. 7.11) by no means negates the validity of the critical temperature $T_{c,SF}$ obtained from the Galitski-Larkin fits. When $T_{c,SF}$ was obtained from the Galiski-Larkin fits, the high-field behaviour of the magnetoresistance isotherms ensured a destroyed vortex BKT phase. The superconducting fluctuations are therefore not distorted by the vortex BKT physics. In our opinion, the value of $T_{c,SF}$ from the Galitski-Larkin fits hence provides a better estimation of the mean field transition temperature than the value of T_c obtained from fits according to superconducting fluctuations at zero field.

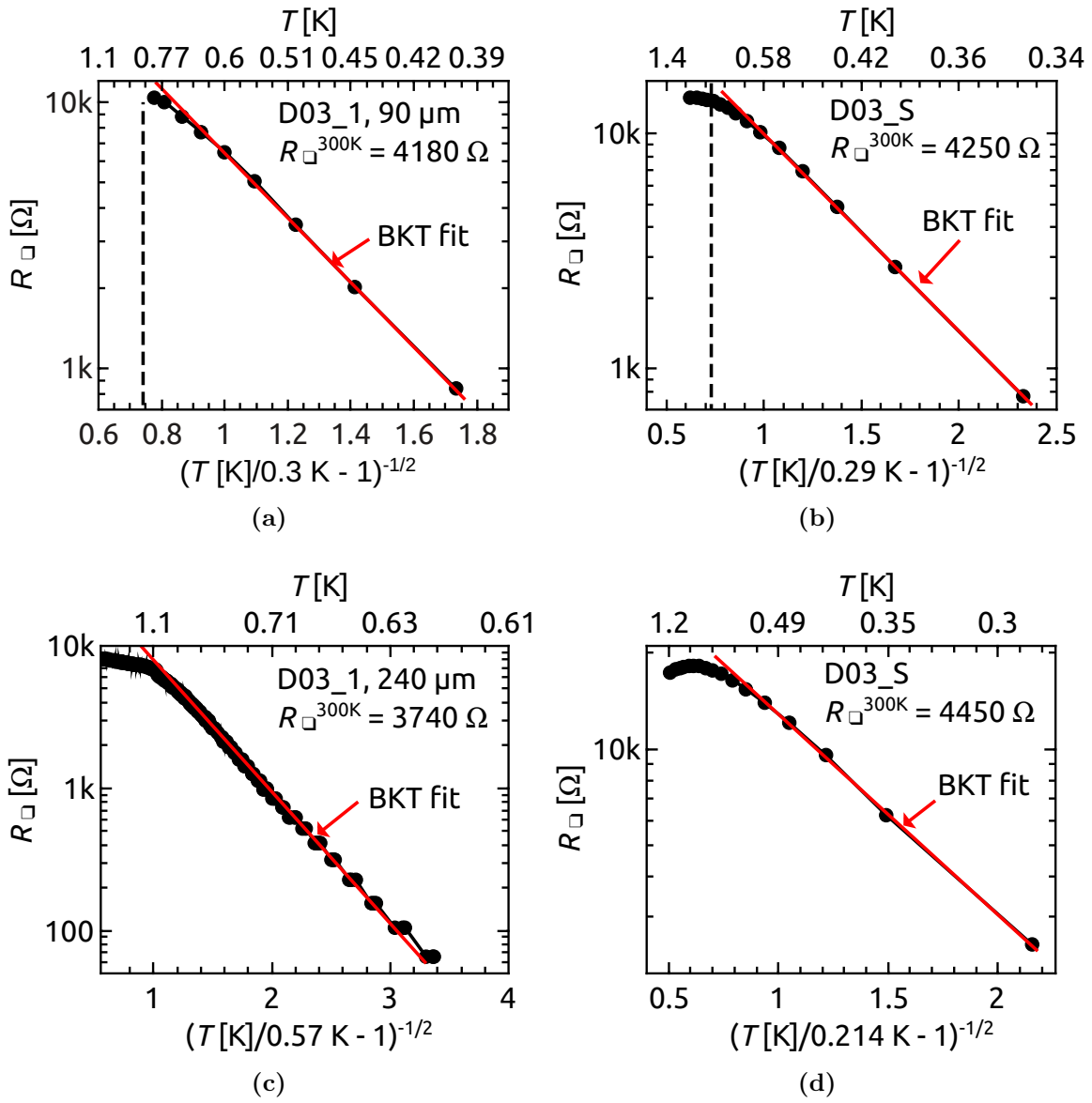

Fig. 7.12: Temperature dependence of the resistance for differently disordered TiN films. The abscissa is scaled in the form $(T/T_{v-BKT}-1)^{-1/2}$ and the resistance is scaled logarithmically in order to test for a temperature dependence of the resistance according to the theory of Halperin and Nelson for the BKT regime (Eq. 2.27). (a) 90 μm size of sample D03_1 in the fourth oxidation step. The dashed vertical line indicates T_c from the Galitski-Larkin fits. (b) The same as in Fig. 7.11 but without the Aslamazov-Larkin lines. (c) 240 μm size of sample D03_1 in the third oxidation step. For this least disordered sample of the four samples presented in this figure, the highest value of $T_{v-BKT} = 0.57\,\mathrm{K}$ is found. (d) Sample D03_S for a higher degree of disorder than in (b). For this most disordered sample of the four samples presented in this figure, the lowest value of $T_{v-BKT} = 0.214\,\mathrm{K}$ is found. The dependence of T_{v-BKT} on $R_{\square}^{300\,\mathrm{K}}$ (Fig. 8.3) is discussed in chapter 8.

Now we return to the three different criteria for T_c visualised in Fig. 7.10. The

BKT physics is consistent with the temperature dependence of the resistance up to $5/6 \cdot R_{max}$. Hence we argue, that the criterion for a quick estimation of the transition temperature with $T_{c,0.2}$ significantly underestimates the transition temperature for critically disordered samples. Still, there are two other criteria for the estimation of T_c. The blue diamonds depict the critical temperatures that are found in Ref. [6] by fits of the $R(T)$ curves at zero magnetic field according to the theory of superconducting fluctuations. The samples investigated there were deeply in the superconducting regime, far from the D-SIT. In this regime, the vortex BKT behaviour does not dominate the $R(T)$ up to almost R_{max} and the theory of superconducting fluctuations at zero field well describes the $R(T)$ curves. The second criterium is provided by the theory of Galitski and Larkin. Above, we already argued that the value of $T_{c,SF}$ approximates the value of the mean field transition temperature quite well.

In the plot shown in Fig. 7.10, only the blue diamonds, the orange stars and the green star remain according to the latter two criteria. The positions of these remaining values for T_c in Fig. 7.10 can not be properly reproduced with Finkelstein's formula Eq. 2.60. Instead they rather lie on a horizontal line. The values of $T_{c,SF}$ might be scattered due to predicted giant mesoscopic fluctuations in critically disordered samples [71]. These fluctuations lead to a smearing of T_c due to the formation of localized islands. Our observations are consistent with a non-vanishing mean field transition temperature at the disorder-driven SIT which is found to occur at $R_{\square}^{300\,\mathrm{K}} \approx 4.6\,\mathrm{k\Omega}$ [6].

In a personal communication with Tatyana Baturina, she suggested to apply the phenomenological parameter $(T_{0.8} - T_{0.2})/T_{0.5}$ for a estimation for the width of the temperature range of the superconducting transition in the $R(T)$ curves at zero field. The temperatures $T_{0.2}$, $T_{0.5}$ and $T_{0.8}$ are determined at 20 %, 50 % and 80 % of R_{max}, respectively. She observed that below $R_{\square}^{300\,\mathrm{K}} \lesssim 4\,\mathrm{k\Omega}$ the parameter $(T_{0.8} - T_{0.2})/T_{0.5}$ increased smoothly with increasing $R_{\square}^{300\,\mathrm{K}}$. Surprisingly, in the range $R_{\square}^{300\,\mathrm{K}} \approx (4 - 4.5)\,\mathrm{k\Omega}$ this parameter starts to increase dramatically with increasing disorder. This evolution remains unexplained up to now.

Here, we argue that the strong increase of the parameter $(T_{0.8} - T_{0.2})/T_{0.5}$ is consistent with the growing importance of the vortex BKT physics with increasing disorder. From Fig. 7.11 the latter statement easily can be explained. The superconducting fluctuations cause a faster decrease of the resistance than the BKT physics which can be seen from the concave shape of the Aslamazov-Larkin $R(T)$ compared with the linear BKT fit (Eq. 2.27). The parameter $(T_{0.8} - T_{0.2})/T_{0.5}$ is not affected by the vortex BKT phase for samples deeply in the superconducting regime with a BKT dominated behaviour of the $R(T)$ below $0.2 \cdot R_{max}$. In these samples the $R(T)$ curves are well described by the theory of superconducting fluctuations at zero field down to resistances below $0.2 \cdot R_{max}$. With increasing disorder first $T_{0.2}$, then $T_{0.5}$ and finally $T_{0.8}$ fall into the vortex BKT dominated part of the $R(T)$ dependence. The BKT phase broadens the superconducting transition with respect to the temperature range. A strong increase of the parameter $(T_{0.8} - T_{0.2})/T_{0.5}$ is consistent with a vortex BKT phase that more and more dominates the superconducting transition at zero field with increasing disorder.

8 Size-dependent superconductor-insulator transition

A few years ago it was found by D. Kalok that the $R(T)$ curves for a disorder driven insulating state at zero magnetic field show thermally activated behaviour, with a activation energy $k_B T_0$ that logarithmically increases with sample size L [78, 98]. This logarithmic size dependence of the activation energy was first found in indium oxide films with a common width of $500\,\mu$m and different length L [101].

The latter observations from Refs. [78, 98, 101] were consistently described by the two-dimensional character of the electric field in the charge BKT phase of a Josephson junction array [95]. The logarithmic interaction of charges in the charge BKT phase is thoroughly described in chapter 6. In the charge BKT phase, charges interact logarithmically according to Eq. 2.70 up to the electrostatic screening length $\lambda_C = a\sqrt{C/C_0}$. Here, C is the capacitance between neighbouring islands in the Josephson junction array, C_0 is the self-capacitance of a single island and a is the lattice spacing. Beyond the screening length λ_C, the charging interaction vanishes exponentially. The electrostatic energy of a Cooper pair dipole, which consists of a Cooper pair and a local deficit of a Cooper pair, for short distances $d \ll r \ll \lambda_C$ with film thickness d is given by

$$V(r) = \frac{(2e)^2}{4\pi C} \ln\left(\frac{r}{d}\right). \tag{8.1}$$

The latter expression for $V(r)$ is similar to Eq. 6.3. Eq. 6.3 describes the electrostatic potential of charges in a film with dielectric constant ϵ, sandwiched between two dielectric media with dielectric constants ϵ_1 and ϵ_2. Here, in Eq. 8.1 the dielectric constants are replaced by the corresponding capacitances in a Josephson junction array. The activation energy $k_B T_0$ is related to the barrier for the Cooper pair propagation $\Delta_C = V(\min\{L, \lambda_C\}$. Hence, Δ_c is derived to

$$k_B T_0 = \Delta_C = \frac{E_C}{2} \ln\left(\frac{\min(\lambda_C, L)}{d}\right) \tag{8.2}$$

where $E_C = e^2/(2C)$.
Thus for $\lambda_C > L$, the activation energy $k_B T_0$ depends logarithmically on the sample size.

On the superconducting side of the D-SIT, the vortex BKT transition temperature of a Josephson junction array depends on E_C and E_J according to Eq. 2.78 for $C_0 \ll C$.

$$k_B T_{v-BKT} = \frac{\pi E_J}{2}\left(1 - \frac{1}{3\pi}\frac{E_C}{E_J}\right) \quad \text{for } C_0 \ll C \tag{8.3}$$

The calculation of Eq. 2.78 included a quasiclassical approximation, where the temperature is much higher than the charging energy, e.g. $k_B T \gg E_C$. According to Eq. 8.3, an increase of the ratio of E_C/E_J, which is related to increasing disorder, causes a suppression of the vortex BKT transition temperature T_{v-BKT}.

In this chapter the $R(T)$ and $R(B)$ curves of differently disordered square shaped TiN films on the superconducting side of the D-SIT are investigated. In section 8.1 the $R(T)$ curves at zero magnetic field are analysed in the framework of a vortex BKT transition. The $R(T)$ curves are fitted with the Halperin-Nelson expression for $T_{v-BKT} < T < T_{c0}$ (Eq. 2.27). The obtained vortex-BKT transition temperatures T_{v-BKT} are discussed with respect to Eq. 8.3 and a size dependence.
The sample D03_1 was oxidized step-by-step to approach the D-SIT. After the fourth and fifth oxidation steps a magnetic field induced SIT was observed in a perpendicular magnetic field. In section 8.2, the thermally activated behaviour of the resistance in the field-induced insulating state is analysed with respect to the sample size L and the degree of disorder $R_\square^{300\,\mathrm{K}}$.

8.1 Size dependence of the superconducting transition at zero magnetic field

The superconducting transition temperature T_c was found to correlate much better with the sheet resistance at room temperature $R_\square^{300\,\mathrm{K}}$ than with the resistivity or the film thickness. The quantitative dependence of T_c on $R_\square^{300\,\mathrm{K}}$ is given by Finkelstein's Eq. 2.60. In order to compare the measured $R(T)$ and $R(B)$ curves with respect to a size dependence at low temperatures, $R_\square^{300\,\mathrm{K}}$ has to be the same for all sizes at a certain oxidation step. In Fig. 8.1 $R_\square^{300\,\mathrm{K}}(L)$ is shown for the third, fourth and fifth oxdidation steps. Similar to the behaviour of $R_\square^{300\,\mathrm{K}}(L)$ found in Refs. [78, 98] we observe an increase of $R_\square^{300\,\mathrm{K}}(L)$ for $L \lesssim 10\,\mu\mathrm{m}$. A plausible explanation for this increase is given in Refs. [78, 98] where the higher $R_\square^{300\,\mathrm{K}}$ for low samples is attributed to a locally suppressed conductivity at the sample edges. There, $R_\square^{300\,\mathrm{K}}$ was increased by soft plasma etching, which might be more efficient at the edges of the samples. This more strongly affects the smaller samples. The largest sample with $L = 240\,\mu\mathrm{m}$ has an $\approx 200\,\Omega$ below-average $R_\square^{300\,\mathrm{K}}$ and thus $R_\square^{300\,\mathrm{K}}(240\,\mu\mathrm{m})$ is settled somewhere between the size-average $R_\square^{300\,\mathrm{K}}$ of the current and the previous oxidation steps.

First, we turn to the $R(T)$ dependence at zero magnetic field to analyse the superconducting transition. It is well-known that superconducting thin films undergo a vortex BKT transition with a vortex BKT phase where the $R(T)$ curves can be

described by the Halperin-Nelson Eq. 2.27 within the interval $T_{BKT} < T < T_{c0}$:

$$R = R_0 \exp\left(-\frac{b}{(T/T_{v-BKT} - 1)^{-1/2}}\right) \tag{8.4}$$

where b is a constant of the order of unity. As already discussed in chapter 7.3, it is difficult to find the critical temperature T_c since there is no feature in the $R(T)$ curves right at T_c. For the determination of T_{v-BKT}, the vortex binding-unbinding transition temperature, the determination is similarly difficult. Usually a description of the $R(T)$ curves with Eq. 2.27 is tried to be obtained at the onset of resistance in the $R(T)$ [25], but inhomogeneities and finite size effects can shift T_{BKT} from the onset of resistance to some higher value [111].

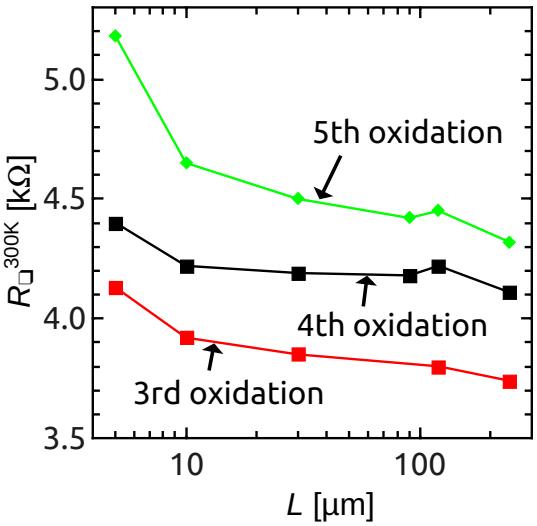

Fig. 8.1: Sheet resistance at room temperature $R_\square^{300\,\mathrm{K}}$ for square shaped TiN films of different lateral sizes L for three different oxidation degrees. $R_\square^{300\,\mathrm{K}}$ serves as a good estimation of the disorder and the suppressed T_c [69]. For $L \leq 10\,\mu$m, $R_\square^{300\,\mathrm{K}}$ tends to raise with decreasing L. For the largest sample with $L = 240\,\mu$m, $R_\square^{300\,\mathrm{K}}$ is $\approx 200\,\Omega$ lower than the size-averaged $R_\square^{300\,\mathrm{K}}$.

Here, we start our analysis with fitting the Halperin-Nelson formula to the $R(T)$ curve for the $240\,\mu$m sample (see section 7.3, Fig. 7.12c). The depicted $R(T)$ curve was measured in a four-terminal current bias setup with an excitation of 10 nA which enabled a reliable measurement of the resistance down to a few ten Ohm. The obtained parameters for the fit with the Halperin-Nelson formula are $T_{v-BKT} = 0.57\,\mathrm{K}$, $R_0 = 60\,\mathrm{k}\Omega$ and $b = 2.09$. The black solid line in Fig. 8.2a that resembles the $R(T)$ curve of the $240\,\mu$m length corresponds to a Halperin-Nelson fit with the latter parameters. The other fits in Fig. 8.2a are obtained with the fixed parameters $R_0 = 60\,\mathrm{k}\Omega$ and $b = 2.09$ which are the same parameters as obtained from Fig. 7.12c. Only the value for T_{v-BKT} is changed in order to obtain the best fit to the measured data. In Figs. 8.2b and 8.2c the Halperin-Nelson fits to the measured $R(T)$ curves for the fourth and

fifth oxidation steps are displayed, respectively. For the fourth oxdidation step the parameters $R_0 = 80\,\mathrm{k\Omega}$ and $b = 2.42$ were kept fixed.

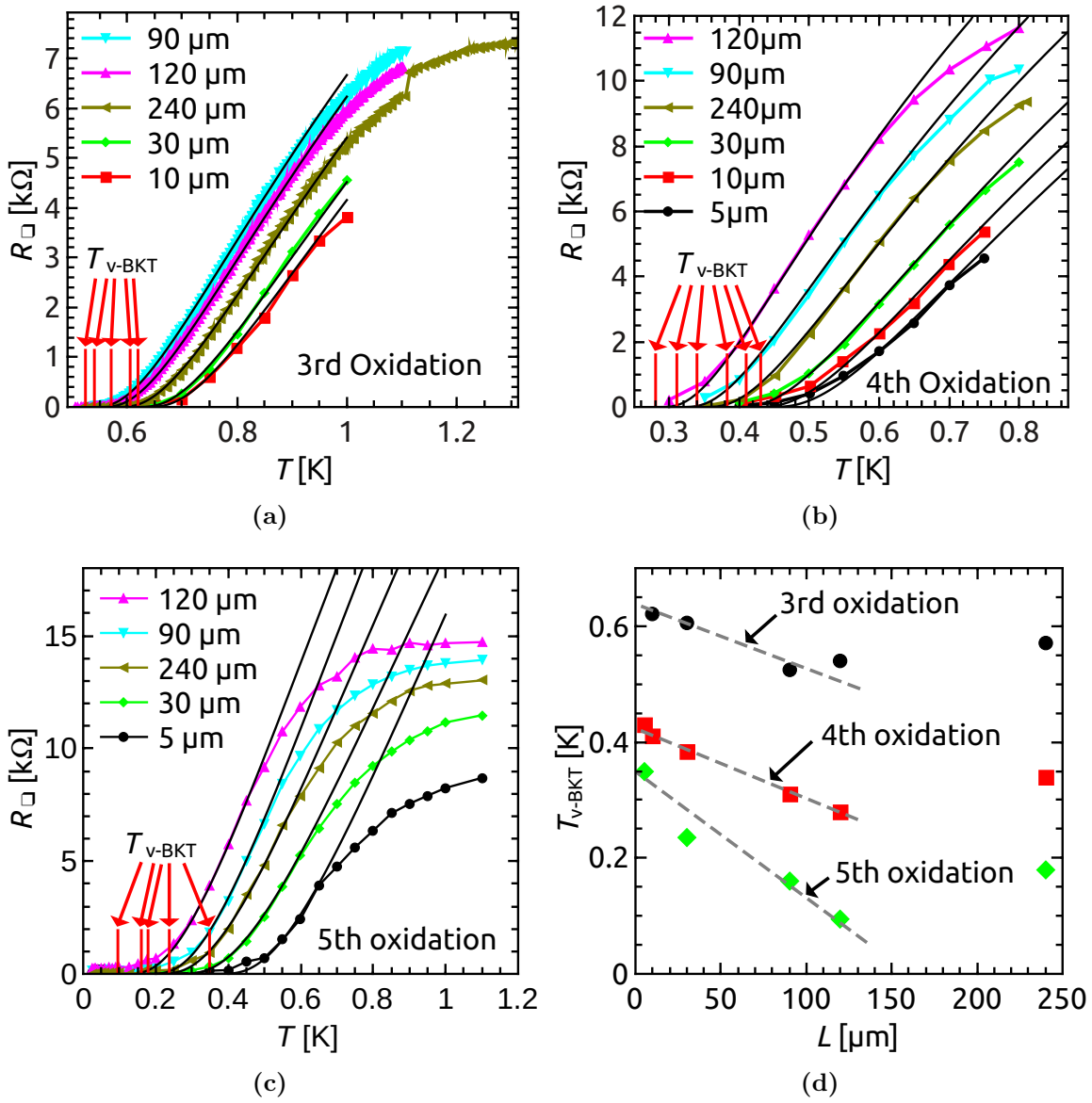

Fig. 8.2: $R(T)$ dependences for three different oxidation degrees at zero magnetic field. The black lines correspond to fits of the $R(T)$ data to the Halperin-Nelson estimation for the resistance in the BKT regime with Eq. 2.27. (a) For the third oxidation step the fixed parameters are $R_0 = 60\,\mathrm{k\Omega}$ and $b = 2.09$. A variation of T_{v-BKT} is sufficient to match the $R(T)$-curves for all different sizes. (b) $R_0 = 80\,\mathrm{k\Omega}$ and $b = 2.42$ were kept fixed in the fits for the fourth oxidation step while T_{v-BKT} was adjusted. (c) In the fifth oxidation step it was required to adapt b, too. The paramters are: $b = 7.1$ for $L = 120\,\mu$m, $b = 5.5$ for $L = 90\,\mu$m, $b = 5.5$ for $L = 240\,\mu$m, $b = 5$ for $L = 30\,\mu$m and $b = 4$ for $L = 5\,\mu$m. $R_0 = 370\,\mathrm{k\Omega}$ is the fixed paramter. (d) Fitting variable T_{BKT} vs. L. For explanations see text.

The Halperin-Nelson fits of the $R(T)$ curves for the fifth oxidation step required a variation of the parameter b for the different lenght L. Sorted from highest to lowest values for b it was obtained: $b = 7.1$ for $L = 120\,\mu$m, $b = 5.5$ for $L = 90\,\mu$m, $b = 5.5$ for $L = 240\,\mu$m, $b = 5$ for $L = 30\,\mu$m and $b = 4$ for $L = 5\,\mu$m. The parameter $R_0 = 370\,\mathrm{k}\Omega$ was kept fixed for all L.

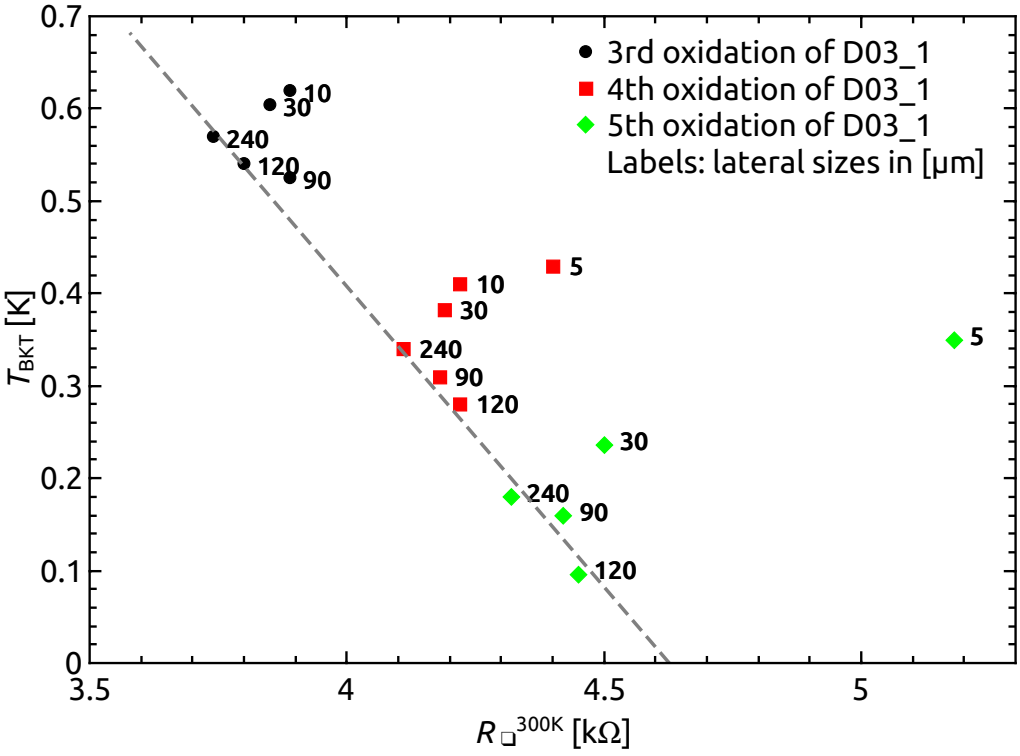

Fig. 8.3: The fitting variable T_{BKT} from Fig. 8.2d vs. $R_{\square}^{300\,\mathrm{K}}$. The points obtained from Halperin-Nelson fits of the $R(T)$-curves at zero magnetic field for the largest samples follow the trend indicated by the grey dashed line. The extrapolated $R_{\square}^{300\,\mathrm{K}}$ for $T_{BKT} \to 0$ marks the point of the D-SIT at $R^* \approx 4.6\,\mathrm{k}\Omega$. The points for the smallest samples strongly deviate from the dashed grey line due to the size depenence of the BKT transition.

The values for T_{v-BKT} for the three different oxidation steps are plotted versus L in Fig. 8.2d. At first sight a decrease of T_{v-BKT} upon subsequent oxidation can be observed. From the third to the fifth oxidation step, T_{v-BKT} is reduced by $\approx 400\,$mK. This strong decrease to almost zero motivates the plot of the dependence of T_{v-BKT} on $R_{\square}^{300\,\mathrm{K}}$ in Fig. 8.3. The data points for the sizes $L = 90, 120, 240\,\mu$m remarkably well lie on a straight line that extrapolates to $\approx 4.6\,\mathrm{k}\Omega$ at $T_{v-BKT} = 0$. The data points for the smaller samples $L = 5, 10, 30\,\mu$m deviate from this apparently linear behaviour. This deviation corresponds to an increase of T_{v-BKT} with a decrease of L within the same oxidation step indicated by the grey dashed lines in Fig. 8.2d. The vortex BKT transition temperature seems to be increased for small sample sizes. For the largest sample with $L = 240\,\mu$m, T_{v-BKT} is higher in accordance with the change of $R_{\square}^{300\,\mathrm{K}}$. The value of $R_{\square}^{300\,\mathrm{K}}$ for the $240\,\mu$m size is $\approx 200\,\Omega$ below the average of the other sizes

at the same oxidation step. In Fig. 8.3, the comparable large value of T_{v-BKT} for the 240 μm sample is consistent with its lower $R_{\square}^{300\,\mathrm{K}}$ for each oxidation step. Hence, the smooth increase of T_{v-BKT} with decreasing sample size is masked by the strong decrease of T_{v-BKT} with increasing $R_{\square}^{300\,\mathrm{K}}$ in the case of the 240 μm size.

In Fig. 8.3 the distinct trend of $T_{v-BKT} \to 0$ for a critical resistance $R^* \approx 4.6\,\mathrm{k\Omega}$ is shown for the very first time. Up to now, the value of $R \approx 4.5\,\mathrm{k\Omega}$ served for an estimate, where the mean-field critical temperature T_{c0} vanishes [6] and above which the "first" insulating sample with $R_{\square}^{300\,\mathrm{K}} = 4.6\,\mathrm{k\Omega}$ was found. In fact, from the discussion in section 7.3 we conclude that the critical temperature T_{c0} does not tend to vanish at R^*. Here we uncover the crucial importance of the vortex BKT transition temperature T_{v-BKT} for the disorder-driven SIT. While T_{c0} stays finite across the D-SIT, the vanishing $T_{v-BKT} \to 0$ at $R^* \approx 4.6\,\mathrm{k\Omega}$ seems to mark the critical point of the D-SIT.

We now turn to the discussion of the decrease of T_{v-BKT} with increasing $R_{\square}^{300\,\mathrm{K}}$ and the increase of T_{v-BKT} with decreasing sample size L. In the introduction to this chapter, the suppression of the vortex BKT transition temperature T_{v-BKT} with increasing disorder was predicted according to Eq. 8.3

$$k_B T_{v-BKT} = \frac{\pi E_J}{2}\left(1 - \frac{1}{3\pi}\frac{E_C}{E_J}\right) \quad \text{for } C_0 \ll C \tag{8.5}$$

The corresponding supression T_{v-BKT} in artificial Josephson junction arrays can be viewed in Fig. 2.20a. The decrease of T_{v-BKT} with growing $R_{\square}^{300\,\mathrm{K}}$ (Fig. 8.3) and hence a growing E_C/E_J, can qualitatively be explained by Eq. 8.3. Though, Eq. 8.3 describes the suppression of T_{v-BKT} in the quasiclassical limit, where $k_B T \gg E_C$. The TiN samples investigated here are in the close vicinity to the D-SIT. It is not possible to accurately describe the behaviour of our samples with the quasiclassical approximation, since the ratio of E_J/E_C, and hence $2k_B T_{v-BKT}/(\pi E_C)$, is approximated with $E_J/E_C = 2a/\pi^2$ at this critical disorder, where $a \gtrsim 1$ is larger but close to one [92]. In addition, a fit of Eq. 8.3 to the data in Fig. 8.3 would require a known dependence of E_J/E_C on $R_{\square}^{300\,\mathrm{K}}$.

Nevertheless, Eq. 8.3 demonstrates that the ratio of E_C/E_J is the relevant parameter for the calcultion of the suppression of T_{v-BKT}. In Ref. [93], the charging energy E_C is the energy associated with the transfer of a charge from an island to a nearby one. However, in a critically disordered film where the screening length λ_C is of the order of the sample size L, the characteristic energy for thermally activated conductivity is given by the collective Coulomb barrier Δ_C (Eq. 8.2)

$$k_B T_0 = \Delta_C = \frac{E_c}{2}\ln\left(\frac{\min(\lambda_c, L)}{d}\right). \tag{8.6}$$

When E_C in Eq. 8.3 is exchanged by Δ_C, the observed increase of T_{v-BKT} for decreasing sample size L is consistent with a decrease of Δ_C for decreasing sample size L (see section 8.2).

In this work the disorder-driven insulating state was not reached. Nevertheless, in Refs. [6, 27] it is shown that the samples from the D03 wafer we use here behave quite similar to the samples from the wafer D15. The lower two blue points in Fig. 7.10 are obtained from fits according to the theory of superconducting fluctuations to the $R(T)$ curves, for differently disordered samples that were patterned on the D15 wafer. Despite the fact that the neglection of the influence of the vortex BKT physics on the $R(T)$ dependence might affect in the absoute value of T_c, it is possible to achieve a common fit of all points for T_c with Finkelstein's Eq. 2.60 with γ as the only free fitting parameter. The "first" insulating sample stemming from the D15 wafer with $R_{\square}^{300\,\mathrm{K}} = 4.6\,\mathrm{k}\Omega$ thus serves as a good approximation for the "first" insulating sample from the D03 wafer as well. The statement that a vanishing vortex BKT transition temperature T_{v-BKT} accompanies the D-SIT is thus strengthened.

8.2 Size dependence of the magnetic-field-driven SIT

After the fourth and fifth oxidation steps a magnetic field induced SIT appeared with a magnetoresistance peak at $B = 1 - 2\,\mathrm{T}$ and up to resistances of $> 100\mathrm{M}\Omega$ for the fourth oxidation step and $> 1\mathrm{G}\Omega$ for the fifth oxidation step. The magnetoresistance isotherms for the lowest measured temperatures for a set of different sample sizes are depicted in Fig. 8.4. The magnitude of the magnetoresistance maxima of the three largest samples $L = 90, 120, 240\,\mu\mathrm{m}$ is almost the same within the same oxidation step. But for the smaller samples $L = 5, 10, 30\,\mu\mathrm{m}$ the height of the magnetoresistance maxium is suppressed. For the smallest sample with $L = 5\mu\mathrm{m}$ the maximum resistance value is already suppressed by three orders of magnitude, compared with that of the largest three samples in the fourth oxidation step. For the fifth oxidation step this difference increases to four orders of magnitude.

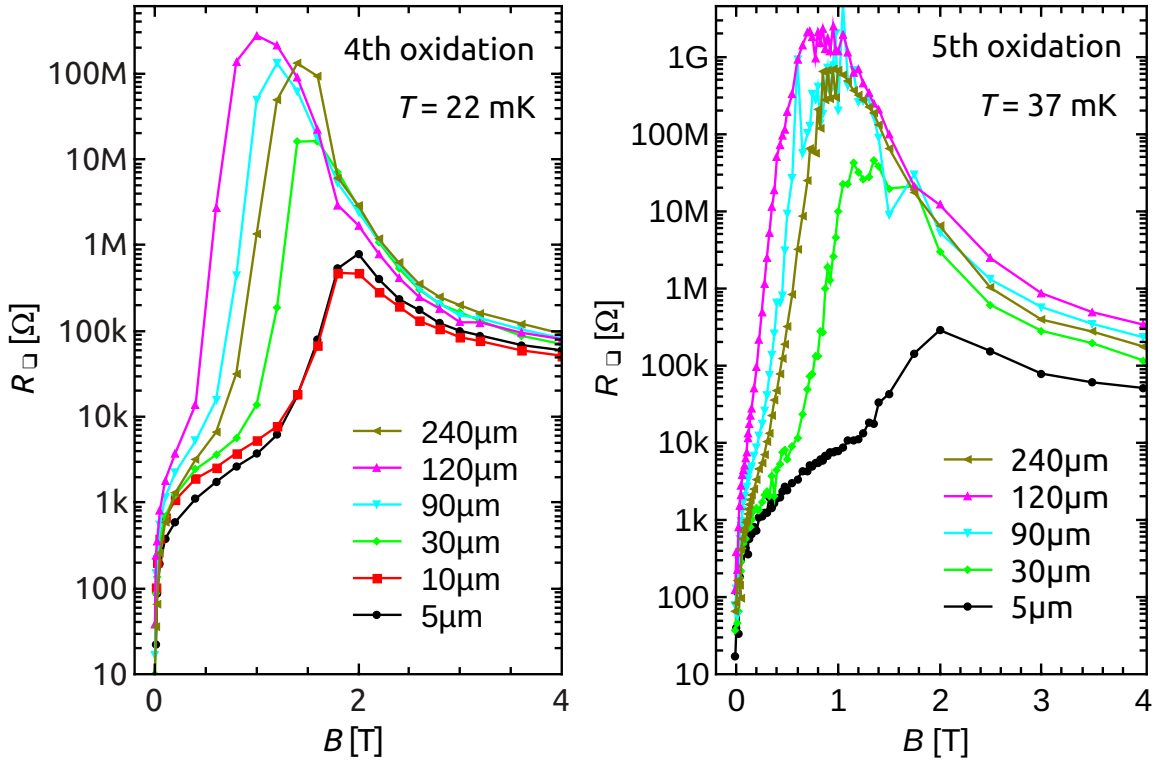

Fig. 8.4: Magnetoresistance isotherms for the (a) fourth oxidation step at a temperature of $T = 22\,\mathrm{mK}$ and (b) fifth oxidation step for a temperature of $T = 37\,\mathrm{mK}$. The $R(B)$-maximum shrinks and is shifted to higher fields for smaller sample sizes. The $R(T)$-curves presented in Fig. 8.5 are taken at the $R(B)$-maxima.

Due to the different temperatures at which the $R(B)$ isotherms were recorded, a quantitative analysis with respect to a comparison of the different oxidation steps is difficult. Here we choose a comparison of the $R(T)$ dependences at the fields of

the magnetoresistance maxima to a gain a quantitative insight into the dependences of the SIT on disorder and sample size. In Fig. 8.5 the $R(T)$ dependences at the $R(B)$-maxima are shown in an Arrhenius-plot. The dashed black lines indicate where temperature activated behaviour appears with

$$R(T) = R_0 \cdot \exp\left(\frac{T_0}{T}\right) \tag{8.7}$$

where T_0 is the activation energy and R_0 is a prefactor.

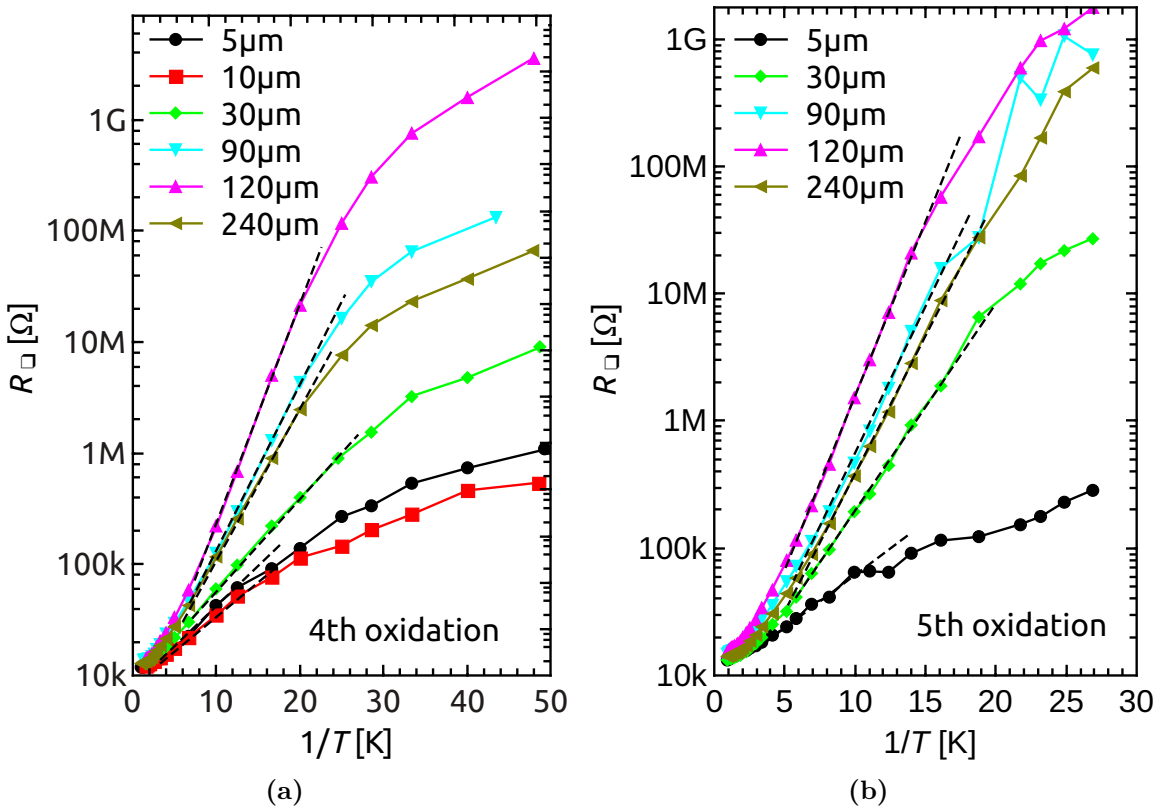

Fig. 8.5: Arrhenius-plots of the $R(T)$-curves for a set of different sample sizes in the (a) fourth and (b) fifth oxidation steps. The black dashed lines indicate the region where temperature activated behaviour is found and the activation energy T_0 is extracted. (a) Due to a higher amplification factor of the transimpedance current-amplifier and hence less noise from the amplifier imposed on the sample, the maxima resistances here exceed the $R(B)$-maxima of the magnetoresistance curves in Fig. 8.4a. The noise from the operational amplifier is less for a higher amplification factor, because the input impedance increases with an increasing amplification factor. The input impedence in combination with the input capacitance to ground forms a RC low-pass filter and damps the noise originating from the amplifier. This kind of filtering works better for higher amplification factors. In the measurements for (b) a RC-lowpass filter between the preamplifier and the sample prevented the influence of the noise from the preamplifier on the sample.

Below the temperature region corresponding to the dashed black lines in Fig. 8.5, a saturation-like behaviour of the $R(T)$ in the Arhhenius plot can be observed. However, the apparent saturation behaviour differs from that found in Ref. [78, 98]. There, the $R(T)$ curves of the smallest samples at lowest temperatures were horizontal. Here, the $R(T)$ curves reveal a a finite slope in the Arrhenius plot down to lowest measured temperatures. The acheived lowest temperatures are not low enough to check if another low-temperature Arrhenius behaviour emerges with a different activation energy, like predicted for a irregular network of capacitors in Ref. [96]. However, the measurement for the fourth oxidation step was conducted in the Cryostat II. According to recent measurements, the temperature calibration of the thermometer has to be checked.

The activation energies T_0 that are extracted from Fig. 8.5, are plotted in Fig. 8.6 against two different parameters, $R_{\square}^{300\,\mathrm{K}}$ and L. The dependence of T_0 vs. $R_{\square}^{300\,\mathrm{K}}$ shown in Fig. 8.6a is intended to give an impression of how T_0 evolves in the B-SIT regime with increasing disorder. The activation energies, obtained from the linear regions in the Arrhenius plots of the $R(T)$ curves corresponding to the $R(B)$-maxima of differently disordered states of sample D03_S, are added to Fig. 8.6a. For the largest sizes of sample D03_1 and for sample D03_S T_0 vs. $R_{\square}^{300\,\mathrm{K}}$ remarkably well lie on a line which extrapolates to $\approx 4\,\mathrm{k\Omega}$. A disappearance of T_0 for less disoredered samples with $R_{\square}^{300\,\mathrm{K}} \lesssim 4\,\mathrm{k\Omega}$ is consistent with the observation of an absent thermally activated behaviour in magnetic field for the third oxidation step, where $R_{\square}^{300\,\mathrm{K}} \approx 3.8\,\mathrm{k\Omega}$. The $R(B)$ isotherms for the third oxidation step were fitted with the theory of Galitsi and Larkin. The weak magnetoresistance peak hence is attributed to superconducting fluctuations above the upper critical field and not to insulating-like thermally activated behaviour.

We now combine the observation that T_0 vanises below $R_{\square}^{300\,\mathrm{K}} \lesssim 4\,\mathrm{k\Omega}$, with the one of the last section that T_{v-BKT} vanishes above $R_{\square}^{300\,\mathrm{K}} \gtrsim 4.6\,\mathrm{k\Omega}$. Samples within the window $4\,\mathrm{k\Omega} \lesssim R_{\square}^{300\,\mathrm{K}} \lesssim 4.6\,\mathrm{k\Omega} = R^*$ become superconducting at zero magnetic field and undergo a field-induced SIT in perpendicular field. For less disoredered samples it is not possible to tune the sample insulating under an applied field. They simply turn normalconducting at B_{c2} with a weak magnetoresistance peak due to superconducting fluctuations. More disordered samples with $R_{\square}^{300\,\mathrm{K}} \gtrsim 4.6\,\mathrm{k\Omega}$ are not superconducting at zero magnetic field even for $T \to 0$. However, the validity of the window holds only for the largest samples.

Now we turn to the observed deviations of the data from the grey dashed line that resembles T_0 vs. $R_{\square}^{300\,\mathrm{K}}$ in Fig. 8.6a by the activation energies obtained from the smallest samples with $L = 5, 10, 30\,\mu\mathrm{m}$. Since already the T_{v-BKT} vs. $R_{\square}^{300\,\mathrm{K}}$ of these small samples deviated from the behaviour of the largest samples, the test for a size dependence of the activation energy motivated the plot of T_0 vs. L in Fig. 8.6b. L is logarithmically scaled. For the fifth oxidation step even better than for the fourth oxidation step, a logarithmic dependence of T_0 on L can be observed (indicated by the black dashed lines). The insulating state in the fifth oxidation step seems to be more robust against a scatter of $R_{\square}^{300\,\mathrm{K}}$ of the particular sizes. This presumably leads to a more precise logarithmic behaviour of T_0 in the higher oxidation degree.

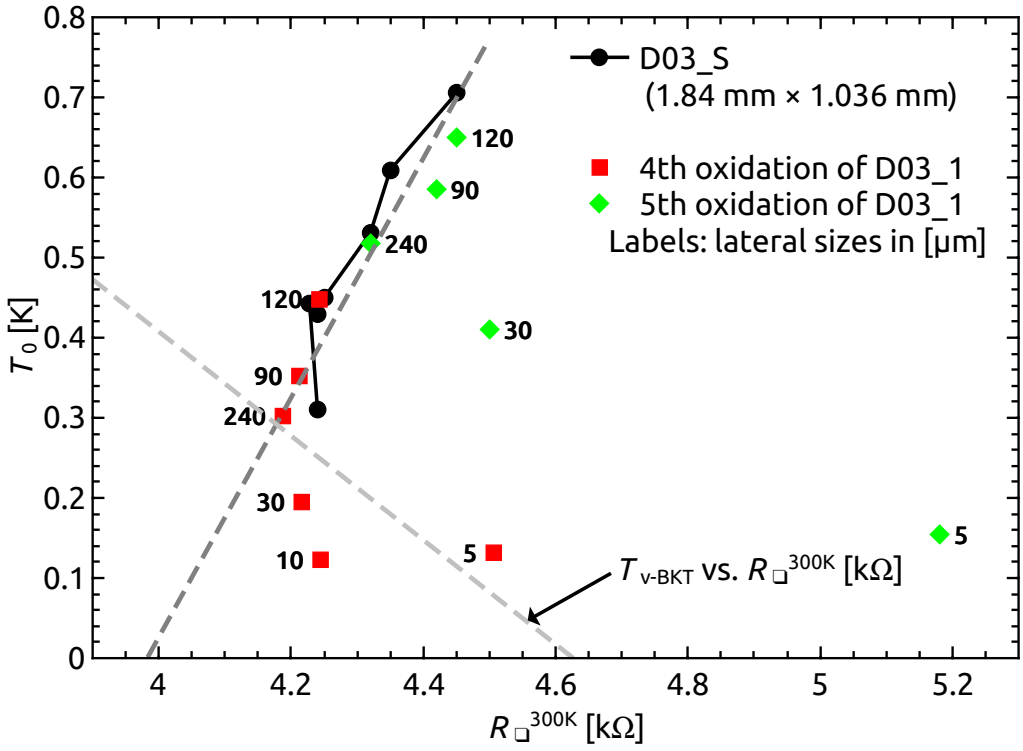

(a)

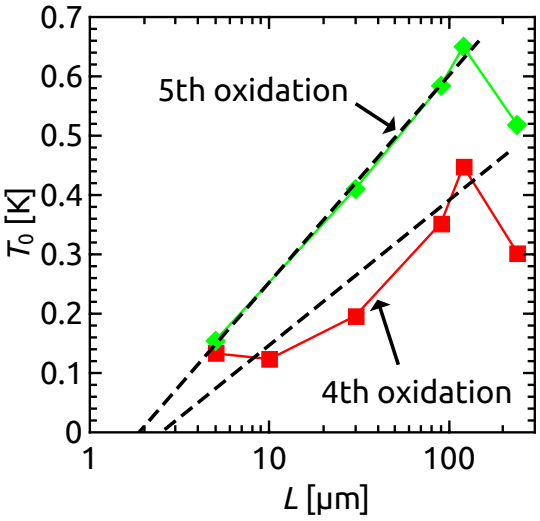

(b)

Fig. 8.6: Activation energy T_0 extracted from the Arrhenius-plots in Fig. 8.5. (a) T_0 vs. $R_{\square}^{300\,\mathrm{K}}$ for the fourth and fifth oxidation steps of sample D03_1 and for the different degrees of disorder of sample D03_S. T_0 for the largest sizes of sample D03_1 and all T_0 for sample $D03\_S$ approximately lie on a line which extrapolates to $\approx 4\,\mathrm{k\Omega}$. This resistance marks the lower bound for $R_{\square}^{300\,\mathrm{K}}$, above which a magnetic field induced SIT can be found. The grey dashed line labelled with T_{v-BKT} vs. $R_{\square}^{300\,\mathrm{K}}$ reproduces the grey dashed line of Fig. 8.3. The deviations of T_0 for the smallest samples are explained by the size dependence of T_0 on $\ln(L)$ in (b). The black dashed lines extrapolate to $L^* \approx 2-3\,\mu$m which is identified as the low-distance cutoff [59]. The slope of the line corresponding to the fifth oxidation step is $\approx 0.15\,\mathrm{K}$.

The $T_0 \propto \ln L$ dependence was already found for samples on the insulating side of the D-SIT in Refs. [101, 78, 98]. This logarithmic size dependence again is consistent with the model of Josephson junction arrays. The collective charging energy Δ_C, described in Eq. 8.2, logarithmically depends on $\min\{L, \lambda_C\}$ with the electrostatic screening length λ_C. This served already as a basis for the explanation of the size-dependent superconducting transition at zero magnetic field (section 8.1), but a quantitative analysis failed. Now, at the insulating side of the SIT we explicitly obtain the logarithmic dependence of the activation energy on the sample size. Since only the activation energies from the $R(T)$ curves of the smallest samples with $L = 5, 10, 30\,\mu$m deviate from the grey dashed line in Fig. 8.6a and show a distinct reduction with respect to the activation energies for the largest samples in Fig. 8.6b, the screening length λ_C can be roughly estimated to $30\,\mu\text{m} \lesssim \lambda_C \lesssim 90\,\mu$m. The black dashed lines in Fig. 8.6b extrapolate to $L^* \approx 2 - 3\,\mu$m. A vanishing T_0 would predict the absence of an insulating state for smaller samples than L^*. Samples with sizes $L = 0.5, 1, 2\,\mu$m were measured during this work, but due to a much too high resistance for $T \gg T_c$, we assume that the geometries of these samples were not well-defined, which may be caused by bad contacts.

In Ref. [59] the T_0 vs. L dependence found in Refs. [78, 98] was analyzed with respect to the electrostatic energy of charges in a two-dimensional film, sandwiched between dielectric media (see chapter 6). The extrapolated value for $L^* = 3\,$nm was attributed to a low-distance cutoff which is equal to the thickness d. In Fig. 8.6b L^* exceeds the thickness $d = 3.6\,$nm by almost three orders of magnitude. The slope of T_0 vs. $\ln(L)$ was taken to evaluate the dielectric constant of the TiN film and to calculate the screening length λ_C. The interaction energy between a Cooper pair and a local deficit of a Cooper pair with a distance r was estimated to (Eq. 6.3)

$$V(r) = \frac{(2e)^2}{2\pi\epsilon_0\epsilon d} \ln\left(\frac{r}{d}\right) \tag{8.8}$$

as long as $r \lesssim \lambda_C$. Here ϵ is the effective dielectric constant of the TiN film. For the fifth oxidation step we obtain $\epsilon \simeq 2.5 \cdot 10^5$. The screening length λ_C was given by [59]

$$\lambda = \frac{\epsilon d}{\epsilon_1 + \epsilon_2} \tag{8.9}$$

where ϵ_1 and ϵ_2 are the effective dielectric constants of the dielectric media that surround the TiN film. For vacuum $\epsilon_1 = 1$ and for SiO_2 $\epsilon_2 = 4$. For the fifth oxidation step we obtain $\lambda_C \simeq 180\,\mu$m. This is at least double the value compared to the rough estimate of $90\,\mu$m made above. Nevertheless, the difference between the two obtained screening length is small under consideration of the variation of $R_\square^{300\,\text{K}}$ for the different sizes.

The measurements for the fourth oxidation step were performed in a dilution refrigerator which allows to apply $B = 17\,$T to the sample. The obtained $R(T)$-curve for this immense magnetic field are presented in Fig. 8.7. The normalized conductance G/G_{00} vs. T on a logarithmic scale allows a test for an Aronov-Alshuler type of con-

ductivity. The grey dashed lines indicate logarithmic behaviour in the semi-log plot with slopes between $1 - 1.4$. This would indicate an almost purely Aronov-Altshuler dominated type of conductivity. Though, due to the saturation at low temperatures in the G/G_{00} vs. T plot, it is not clear what dominates the behaviour of the $R(T)$. From a maximally reached resistance of $< 30\,\mathrm{k\Omega}$ it is at least clear that at $B = 17\,\mathrm{T}$ the TiN films behave metallic.

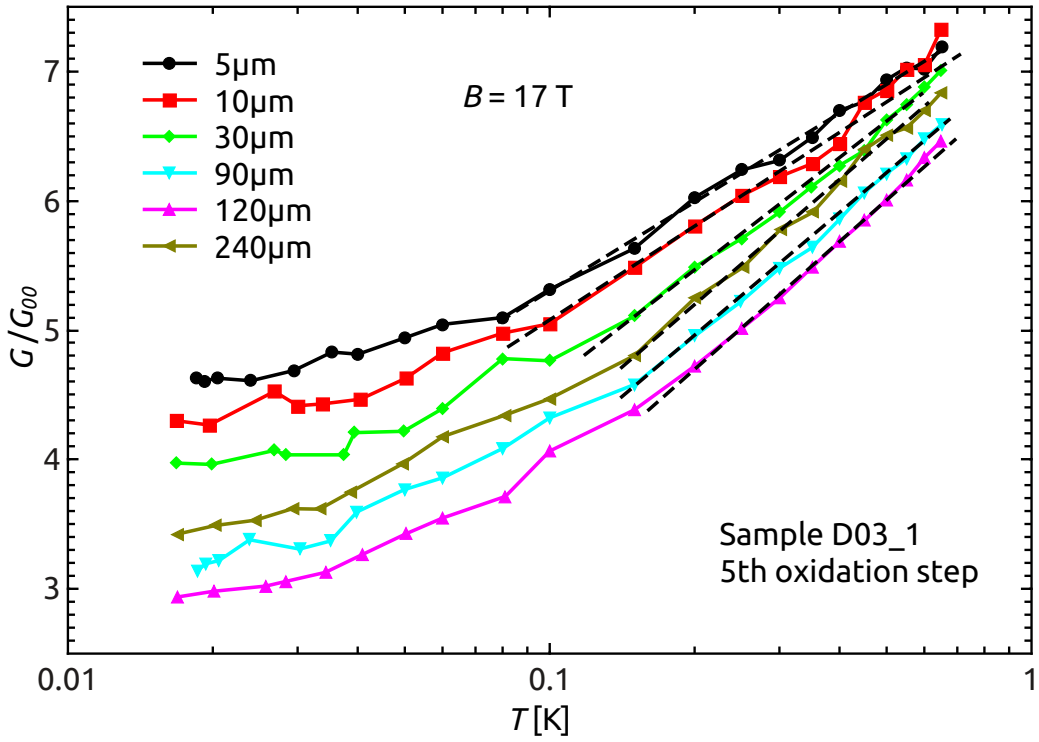

Fig. 8.7: Temperature dependence of the normalized conductance G/G_{00} vs. T on a logarithmic scale at a magnetic field of $B = 17\,\mathrm{T}$. A linear behaviour in this type of plot corresponds to weak localization or Aronov-Alshuler contributions to conductivity. The dashed black lines indicate linear regions at highest measured temperatures with slopes ranging from 1 for $L = 5\,\mu$m to 1.4 for $L = 90, 120, 240\,\mu$m. The usage of the lambda-stage of the dilution refrigerator lowered the temperature of the helium-bath to $T_{He} = 2.2K$. In consequence of the thermal coupling, the temperature of the still was lowered by $\approx 100\,\mathrm{mK}$. It was tried to sustain the cooling power by heating up the still to the usual temperature of $\approx 800 - 900\,\mathrm{mK}$. Though, there were problems with stabilizing the temperature which caused the scattered shape of the $R(T)$ curves. The saturation-like behaviour at lowest temperatures may be due to a not calibrated thermometer at $B = 17\,\mathrm{T}$. The sample thermometer reveals a positive magnetoresistance, hence the used calibration law produces too low temperature values at high magnetic fields. At $B = 17\,\mathrm{T}$, the base temperature that is obtained with the used calibration law, is $\approx 4\,\mathrm{mK}$ lower than for zero field. The latter value allows an estimation of the error due to the applied magnetic field. However, only for the lowest temperature. Additionally, a calibration of the thermometer is needed also at zero magnetic field, due to recent measurements that casted doubts on the calibration of the sample thermometer in Cryostat II.

A surprising observation is the size dependence in Fig. 8.7. The order of the sample sizes with respect to the resistances at lowest temperatures for $B = 17\,\mathrm{T}$ is the same like that for the highly insulating sate at lowest temperatures in Fig. 8.5a. As there is still a slope in the magnetoresistance curves at the highest measured fields, superconducting fluctuations above B_{c2} may sustain the size dependence up to these fields.

The observed size dependence both on the superconducting side as well as the insulating side of the B-SIT seems to be inconsistent with the absence of a screening effect (chapter 6). However, the capacitance in $\lambda_C = a\sqrt{C/C_0}$ might not be of a purely electrostatic origin. Mesoscopic Josephson junctions are usually associated with a competition between the Josephson and the Coulomb effects. Due to the localization of charges by the Coulomb effect, the Hamiltonian of a Josephson junction describes a system with a non-linear capacitance (see Ref. [112]). The so called "Josephson-capacitance" was successfully measured in a Cooper pair box [113]. Hence, the geometric capacitance C_{geo} of the Josephson junction might be enhanced by the dynamic Josephson-capacitance C_J. The resulting total capacitance $C = C_{geo} + C_J$ for $C_J \gg C_{geo}$ would thus hardly be affected by a screening top-gate, since the top-gate only screens electrostatically. However, a reduction of the sample size to $L < \lambda_C = a\sqrt{(C_{geo} + C_J)/C_0}$ is expected to influence the activation energy with $k_B T_0 = \Delta_C = \frac{E_C}{2} \ln\left(\frac{\min(\lambda_C, L)}{d}\right)$ (Eq. 8.2).
The absent screening effect due to a electrostatically screening top-gate therefore does not negate the presence of long-range Coulomb interactions in the critically disordered TiN films investigated in this thesis. Further studies have to be pursued on the possible effects of the Josephson-capacitance on the localization of Cooper pairs in disordered superconductors.

9 Discussion

In this thesis the disorder-driven as well as the magnetic-field-driven SIT are investigated by means of transport measurements. The results of the preceding chapters are now discussed with respect to recent publications.

9.1 Multiple criticality vs. multiple crossovers - finding the point of the QPT

There are still many open questions to the characterization of the field-induced SIT and the three found crossing points in the magnetoresistance isotherms at three different temperature regimes. As the SIT is considered a quantum phase transition, the field-induced SIT is expected to occur at a crossing point in the magnetoresistance isotherms (see section 2.3.3). However, a common crossing of several magnetoresistance isotherms is not sufficient to associate the observed crossing point with the SIT quantum phase transition. In this section, the phenomenological expressions Eq. 4.1, 4.2, 4.4 are discussed with respect to recent publications. In addition, the here observed crossing points are compared to those found in Ref. [10]. There, each of the two crossing points in the magnetoresistance isotherms was associated with a quantum phase transition. However, we doubt that all of the three crossing points observed in this thesis are associated with a quantum phase transition.

We start with the discussion of the HT crossing point, as this is the best understood one. In chapter 2.2.2 the HT crossing point could be connected to the approximate crossing of the fits according to the theory of superconducting fluctuations above B_{c2} from Galitski and Larkin [16]. This explanation excludes the HT crossing point to be the point of the quantum phase transition. The surprisingly small scaling exponent $z\nu = 0.33$ therefore has no physical meaning. A similar approximate crossing point in the magnetoresistance isotherms has been found for a NdCeCuO sample in Ref. [9]. There, a scaling analysis of the $R(T, B)$ that could be fitted by the theory of Galitski and Larkin was found to be possible, but a not sufficient element of the analysis of the SIT.
The deviations of the HT crossing point from the Galiski-Larkin crossing point for more disordered samples might be attributed to vortex physics. In chapter 7 it is found that $T_{v-BKT} = 0.29\,\mathrm{K}$ and $T_{c0} = 0.83\,\mathrm{K}$. For temperatures $T_{v-BKT} < T < T_{c0}$ the vortices in the BKT regime determine the physics at zero magnetic field and lead to a resistance below T_{c0}. If only the contribution from the theory of superconducting fluctuations above B_{c2} is considered for the total corrections to conductivity, the resistance at

$B < B_{c2}$ is zero. However, a finite resistance occurs already at zero magnetic field at $T_{BKT} < T < T_{c0}$, due to flux-flow of vortices in the vortex BKT phase. Both, the $R(B)$ dependence from the Galitski-Larkin fits around the approximate crossing point and the $R(B)$ dependence expected from flux-flow of vortices are linear. Hence, the linear behaviour of the magnetoresistance isotherms in the HT regime for $B < B_{c2}$ described by Eq. 4.4 is consistent with a flux flow of BKT vortices and magnetic field induced vortices.

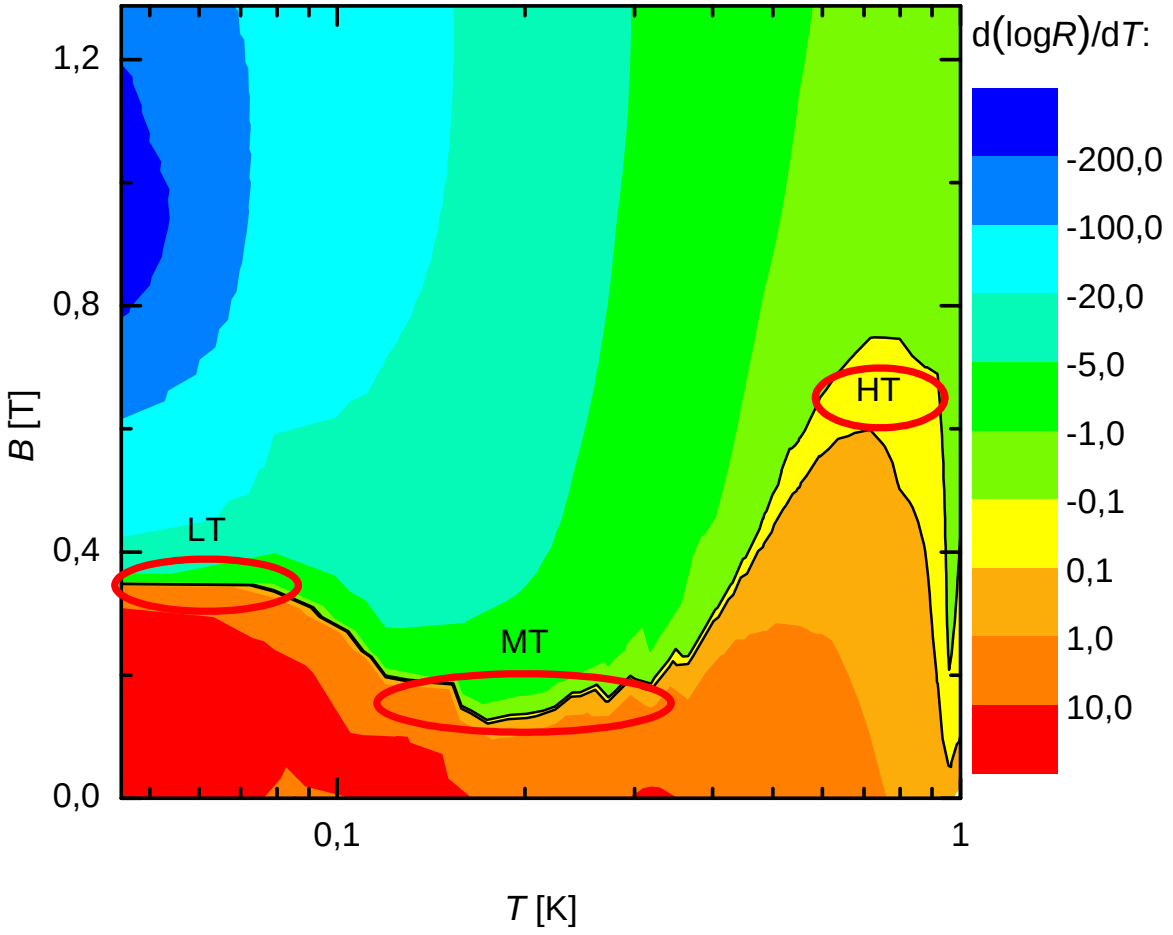

Fig. 9.1: $d \log R/dT$ colour plot vs. B and T for sample D03_S. The sample is superconducting for zero field and low temperatures (red area). The insulating state is indicated by the blue areas. The seperatrix for $R(T)$ curves tending down or up in resistance is marked by the yellow area. In this area a crossing of $R(B)$ isotherms and a plateau in the $R(T)$ dependence for the corresponding temperature and field range occurs. The three found crossing points in the magnetoresistance isotherms are highlighted with red ellipses. The width of the ellipses resembles the temperature ranges for the LT, MT and HT regimes.

Below $\lesssim 350\,\mathrm{mK}$ the MT crossing point emerges in the $R(B)$ isotherms. In Fig. 9.1 this can be seen by a change from the region marked with HT to the region marked with MT. The yellow area in Fig. 9.1 indicates where the derivative of $d(\log R)/dT$ is near to zero what is associated with a plateau in the $R(T)$ dependence at the cor-

responding field. The temperature range of the plateau is given by the width of the yellow area in the horizontal direction.
Apparently the upper temperature limit for the MT regime with $\approx 350\,\mathrm{mK}$ is approximately the temperature $T_{v-BKT} = 290\,\mathrm{mK}$ below which the vortices are bound in vortex-antivortex pairs and the sample is superconducting at zero magnetic field. The phenomenological Eq. 4.2 describes the $R(T,B)$ behaviour in the MT regime for $0.03\,\mathrm{T} \lesssim B \lesssim 0.8\,\mathrm{T}$ and resembles the MT crossing point very well. At zero magnetic field Eq. 4.2 fails to reproduce the vanishing resistance in the superconducting state with $R = 0$. Instead, a finite resistance of $R(T, B = 0) = R_{cM} \cdot \exp(-a_M(T))$ remains for $B = 0$ in Eq. 4.2.
The powerlaw $R(B) \propto (B/B_c)^{T_0/T}$ proposed in Refs. [44, 45, 40] avoids this problem. At zero magnetic field it produces zero resistance. For $B \lesssim B_{cM}$ the magnetoresistance isotherms in Fig. 4.5a are quite straight in the double logarithmic plot. Hence for $B \lesssim B_{cM}$, the $R(B)$ curves are well described by the powerlaw $R(B) \propto (B/B_c)^{T_0/T}$. In section 2.2.3 several possibilities were named that can cause the $R(B) \propto (B/B_c)^{T_0/T}$ dependence. According to Inui et al. [37] the powerlaw can be understood from thermally activated depinning of single vortices from homogeneous and densely distributed pinning centers. Opposed to this single-vortex physics, the motion of pairs of dislocations in the vortex flux lattice also produces a powerlaw behaviour of $R(B)$ within the collective pinning model [39, 40, 46].

But the power-law underestimates the increase in resistance for $B > B_{cM}$. On the other hand, the phenomenological description of the magnetoresistance proposed here (Eq. 4.2) varies stronger than a simple $T_0 \propto \ln B$ dependence suggested in [45]. There are two options to interprete the remarkable well fit of Eq. 4.2 to the magnetoresistance isotherms in the MT regime (see Fig. 4.5a). The first option is that Eq. 4.2 explains the physics of the MT regime on both sides of the crossing point on the basis of a model that is not found yet. The second option is that there is a crossover from low-field behaviour (e.g. powerlaw behaviour) to a high field behaviour with a different field dependence. The crossover might happen at the point where the measured $R(B)$ isotherms deviate from the powerlaw $R(B) \propto (B/B_c)^{T_0/T}$ for $B > B_{cM}$. Indeed, for $0.5\,\mathrm{T} \lesssim B \lesssim 1\,\mathrm{T}$ a rather linear behaviour of the $R(B)$ isotherms in the MT regime can be observed (see Fig. 4.5d). Whether Eq. 4.2 originates from a single physical effect or traces the crossover from a powerlaw to a linear behaviour is not clear. Neither there is an explanation for a linear $R(B)$ dependence for resistances up to $\approx 100\,\mathrm{k}\Omega$ to our knowledge. A linear $R(B)$ dependence due to flux-flow raises the resistance maximally to the normal state resistance.

At about $T \lesssim 100\,\mathrm{mK}$ the MT plateau blurs and the LT plateau emerges in Fig. 9.1. The magnetoresistance isotherms for $B > B_{cL}$ are described by the phenomenological Eq. 4.1. Between $70\,\mathrm{mK} < T \lesssim 100\,\mathrm{mK}$ a less than exponential $R(B)$ dependence is found with $a_L < 1$ in Eq. 4.1. At $T = 70\,\mathrm{mK}$ an exponential magnetoresistance $R \propto \exp(B)$ is observed with $a_L = 1$. This exponential behaviour has been seen earlier in [79] for a similarly disordered TiN sample from a slightly different starting wafer. There $R(T,B) \propto \exp(T_0(B)/T)$ could be derived self-consistently starting from $T_0(B) \propto B$ and $R(B) \propto \exp B$ for $T = 28\,\mathrm{mK}$ in terms of Josephson junction network

physics.

For $T < 70\,\mathrm{mK}$, the $R(B)$ grows more than exponential with $a_L > 1$. At lowest temperatures of $T = 37\,\mathrm{mK}$, a_L approches 2 with $R(B) \propto \exp[(B/B_{cL})^2]$. The latter $R(B)$ dependence was theoretically obtained by Sankar and Tripathi [114]. They studied the influence of a perpendicular magnetic field on a critically and homogeneously disordered 2D superconductor. In the regime of quantum phase fluctuations originating from Coulomb blockade they calculated based on a Josephson junction model that the magnetoresistance obeys the law $R(B) \propto \exp[(B/B_0)^2]$ with some constant B_0. This regime is restricted to $E_c/E_J, E_c/T \gg 1$ with E_c the charging energy for incoherent sequential hopping of charges between neighbouring islands and E_J the Josephson coupling energy between the islands. Shankar and Tripathi showed that experimantal data fits to the calculated $R(B)$ for highly disordered InO_x films.

Though our magnetoresistance isotherms for lowest temperatures can be interpreted with numerical calculations of an homogeneously disordered superconductor forming a Josephson junction array at strong enough disorder [114], the $I - V$ characteristics reveal strong inhomogeneity around the LT crossing point (see Fig. 4.10). However, this is consistent with the observations in Ref. [6]. There it was found that even for uniformly disordered systems, strong inhomogeneities emerge on a mesoscopic scale. These inhomogeneities may lead to a percolation network with different loop sizes. We argue that the coexistence of superconducting and insulating features in our $I-V$ characteristics are consistent with the physics of a percolation network. For small fields the larger loops are filled with a flux quantum, inducing an insulating background for embedded fragile superconducting paths. Exceeding $B = B_{cL}$, all superconducting regions are destroyed by filling smaller loops, forming a globally insulating state.

It is not clear if theory of finite size scaling around a quantum critical point is applicable in the presence of strong mesoscopic inhomogeneities of the superconducting properties, e.g. the spatial fluctuations of the superconducting gap [6]. According to Hebard and Paalanen [84] the theory of finite size scaling is applicable to an experimental system, if the length scale characterizing the uniformity of disorder exceeds the length scale used by the theory to model the superconducting behaviour. In the case of the LT crossing point, finite size scaling may be inappropriate due to the strong mesoscopic inhomogeneities.

Multiple crossing points in the magnetoresistance isotherms were already observed before. In Ref. [10] two crossing points for $B_1^* = 3.63\,\mathrm{T}$ in a high-temperature range $4.795\,\mathrm{K} \lesssim T_1^* \lesssim 9.675\,\mathrm{K}$ (Fig. 2 in [10]) and for $B_2^* = 13.45\,\mathrm{T}$ in a low-temperature range $0.121\,\mathrm{K} \lesssim T_2^* \lesssim 0.313\,\mathrm{K}$ (Fig. 3 in Ref. [10]) were found in a $La_{2-x}Sr_xCuO_4$ film with $x = 0.07$. The there presented zero-resistance critical temperature $T_{c,0} = (3.8 \pm 0.1)\,\mathrm{K}$ is closer to the vortex BKT transition temperature T_{v-BKT} than to the critical temperature T_{c0} in this thesis. The authors of Ref. [10] did not estimate T_c under from the theories on superconducting fluctuations above B_{c2} or T_{c0}. Therefore T_{c0} is not known for the measured $La_{2-x}Sr_xCuO_4$ sample. The upper critical B_{c2} field was determined assuming a quadratic dependence $R(B) \propto B^2 + C$ for the normal state resistance with some constant C. On a plot of R vs. B^2, B_{c2} was set to the point where

deviations to a linear behaviour in the present plot occur for lowering the magnetic field. Under usage of this criterion the zero-temperature upper critical field was estimated to $B_{c2}(T = 0) = (15 \pm 1)\,\mathrm{T}$ (from Ref. [115]). The latter criterion sets B_{c2} to a field above which all superconducting fluctuations are fully suppressed. Contrary to this reasoning for the criterion used in Ref. [10], superconducting fluctuations are expected above B_{c2}. The in Ref. [10] found $B_{c2}(T = 0) = (15 \pm 1)\,\mathrm{T}$ hence might differ from the exact upper critical field B_{c2}.

Nevertheless, a scaling analysis is pursued for both crossing points. For the low-temperature regime $z\nu = 1.15 \pm 0.05$ and for the high-temperature-regime $z\nu = 0.737 \pm 0.006$ was found. Both crossing points were taken as the signature of quantum critical points. At $T = 0$ the following phases are described for increasing field B: For $B < B_1^*$ the vortices are pinned in a vortex solid, a Bragg glass, for $B_1^* < B < B_2^*$ the vortices are ordered in a vortex glass with an irregular structure and above B_2^* the sample is insulating. For finite temperature a complex phase diagram was eleborated, based on the latter zero temperature phases.

Since it is not known how the $R(T, B)$ can be explained in terms of superconducting fluctuations and vortex BKT physics, and without the knowledge of B_{c2} and T_c, it is difficult to find the connection between the crossing points found in Ref. [10] and in this thesis. However, more reliable values for $B_{c2}(x = 0.069) = 17\,\mathrm{T}$ and $T_{c0} = 12\,\mathrm{K}$ are found from specific heat measurements in Ref. [116]. They serve as a good approximation for the upper critical field B_{c2} and critical temperature T_{c0} in $La_{2-x}Sr_xCuO_4$ with $x = 0.07$. The $R(T)$ dependence for different magnetic fields in Fig. 9.2 for the LaSrCuO sample from Ref. [10] is very similar to what we observe in Fig. 4.1 with respect to the sample specific T_{c0} and B_{c2}. At zero magnetic field the resistance at $T_{c0} = 12\,\mathrm{K}$ is almost at the maxium of the $R(T)$ dependence, similar to our observations. For the highest presented fields with $B = 18\,\mathrm{T} \approx B_{c2}$, an monotonic increase of the resistance with decreasing temperature corresponds to our observations at the magnetic field of magnetoresistance maximum. The non-monotonic $R(T)$ dependence for intermediate fields of $4\,\mathrm{T} \lesssim B \lesssim 12\,\mathrm{T}$ is similar to the non-monotonic $R(T)$ curves (see Fig. 4.1) that we observe for fields between the MT and the LT regimes for $0.15\,\mathrm{T} \lesssim B \lesssim 0.36\mathrm{T}$.

From the comparison of the $R(T)$ dependences shown in Figs. 9.2 and 4.1 the low-temperature crossing point in the $La_{2-x}Sr_xCuO_4$ sample most likely can be connected to the LT crossing point in our TiN films. In both cases the crossing field, which is smaller than B_{c2}, marks a transition from a downturn in the $R(T)$ to an upturn in the $R(T)$ curves with lowering temperature and increasing field. The high-temperature crossing point in the $La_{2-x}Sr_xCuO_4$ sample most likely can be connected to the MT crossing point in our TiN films. In this regime the the resistance vanishes for the crossing field for $T \to 0$ and a plateau in the $R(T)$ curves can be seen for a temperature region well below T_c. A counterpart to the HT crossing point found here was not found for the LaSrCuO sample. This is not surprising since for the corresponding fields and temperatures there were measured too few data points in the $R(T)$ curve to identify a plateau. Due to the similarity of the $R(T)$ dependences from Ref. [10] to the $R(T)$ dependences for sample D03_S, the colour plot in Fig. 9.1 may describe the behaviour of the LaSrCuO sample as well with differently scaled axes.

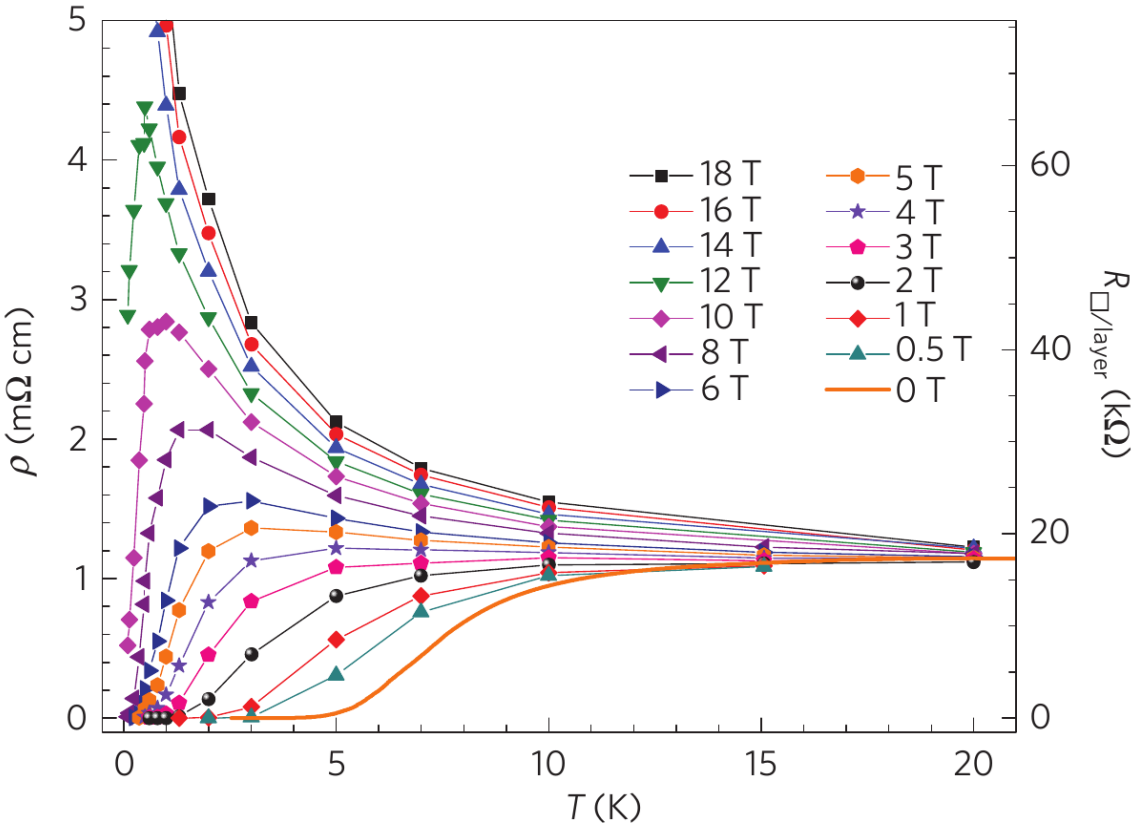

Fig. 9.2: Temperature dependence of the resistivity ρ for different magnetic fields perpendicular to the CuO_2 layers in a $La_{2-0.07}Sr_{0.07}CuO_4$ sample. The sheet resistance per layer $R_\square$ is given on the right axis. The low-temperature crossing point in the $R(B)$ isotherms occurs at $B_2^* = 13.45\,\mathrm{T}$, the corresponding plateau in the $R(T)$ dependence is above of the shown resistance range. The high-temperature crossing point in the $R(B)$ isotherms occurs at $B_1^* = 3.63\,\mathrm{T}$ which corresponds to a plateau in the $R(T)$ curves between 5 K and 10 K, near the starred violet curve for $B = 4\,\mathrm{T}$. The $R(T)$ dependence for sample D03_S in Fig. 4.1 looks very similar, under consideration of the different values for the critical magnetic fields and temperatures for TiN and $La_{2-0.07}Sr_{0.07}CuO_4$. (from [10])

After we refered the crossing points in Ref. [10] to the ones observed in this thesis, we can discuss differences and similarities. The scaling exponents $z\nu > 1$ are similar for the low-temperature crossing points in both works, that is $B_2^* = 13.45\,\mathrm{T}$ in Ref. [10] and $B_{cL} = 0.36\,\mathrm{T}$ here. The systems are thus assigned to the univerality class of the $(2+1)\,\mathrm{D}\,XY$ model in the dirty limit. For the high-temperature crossing point at $B_1^* = 3.63\,\mathrm{T}$ in the LaSrCuO sample, $z\nu = 0.737$ is attributed to the univerality class of the $(2+1)\,\mathrm{D}\,XY$ model in the clean limit. The proposed transition from the vortex Bragg glass to the vortex glass was reasoned with $z\nu < 1$ that is associated to a clean-limit transition. This is in contrast to the found $z\nu = 1.2$ for the MT crossing point indicating the dirty case. In our case we would have three dirty systems separated by the LT and MT crossing points at zero temperature. A phase diagram like presented in Ref. [10] is not yet elaborated for the two found crossing points in our TiN film.

Nevertheless, it is doubtful that a scaling analysis like in Ref. [10] as a stand-alone argument is sufficient to provide compelling evidence for a quantum phase transition at an observed crossing point in the magnetoresistance isotherms. In order to verify if an experimental crossing in magnetoresistance isotherms is associated with the point of the quantum phase transition, the $R(T)$ data that collapses in a scaling plot should at least vary by two orders of magnitude in $|R - R_c|$, were R_c is the resistance at the crossing. Based on the scattered and flat magnetoresistance isotherms shown in Fig. 2a of Ref. [10] for the high-temperature crossing point at $B_1^* = 3.63\,\mathrm{T}$, we argue that the latter criterion for validation of a quantum phase transition is presumably not fulfilled. If we apply the criterion to the scaling plots obtained here (see Fig. 4.7), it is doubtful if the MT crossing point passes the criterion. The LT crossing point probably passes the criterion, but the measured $R(T, B)$ was measured in too large B steps. In order to test for critical behaviour, further high-resolution $R(T, B)$ measurements are needed around the LT and the MT crossing points.

9.2 Disorder driven SIT and the vortex BKT physics

In chapter 7 the importance of the vortex BKT physics was emphasized for the determination of the critical temperature T_{c0} at zero magnetic field. Apparently the vortex BKT transition also influences the IV characteristics at $B = 0$. When we compare the values for T_{v-BKT} from the Halperin-Nelson fits displayed in Fig. 8.2d with the saturation behaviour of the IV characteristics in Figs. 7.2 and 7.3, we observe that the temperature at which the shape of the IV characteristics saturates with lowering temperature approximately coincides with T_{v-BKT}. This leads to the assumption that the parameter T_c used in the fits according to the hotspot theory has to be replaced by T_{v-BKT}. T_c in the hotspot theory is defined as the temperature where the resistance increases from zero resistance in the superconducting regime to the normal resistance in the normalconducting regime. Hence the fitting parameter T_c resembles the vortex BKT transition temperature T_{v-BKT}, as T_{v-BKT} is approximately at the onset of a finite resistance in the $R(T)$ dependence with increasing temperature.

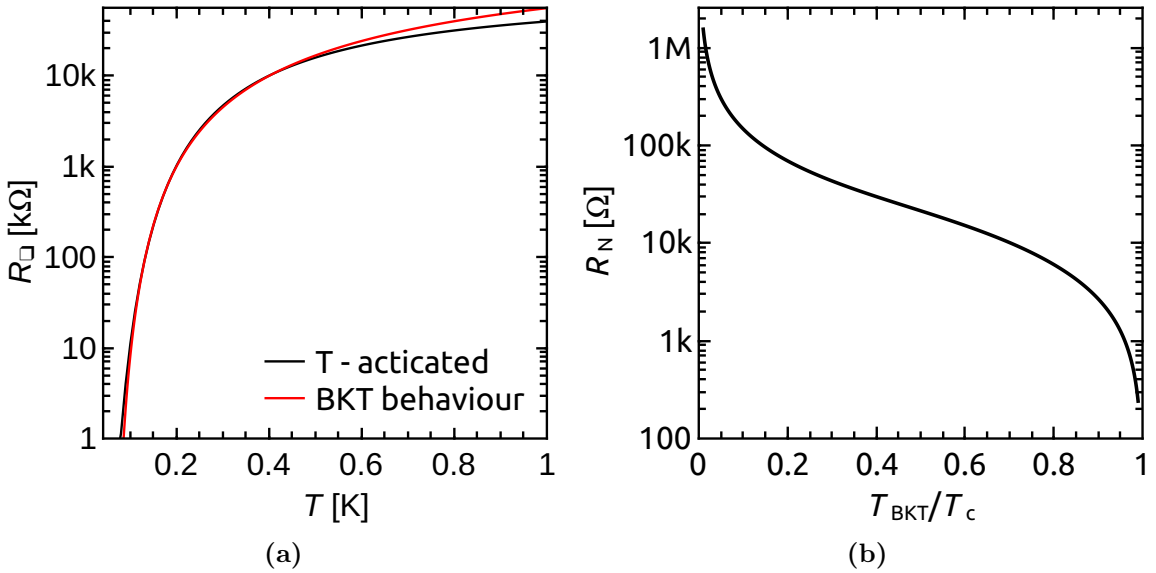

Fig. 9.3: (a) Comparison of temperature activated behaviour and BKT behaviour according to the Halperin-Nelson formula Eq. 2.27. The black solid line corresponds to the temperature activated behaviour (Eq. 9.1) where $R_0 = 100\,\mathrm{k\Omega}$ and $T_{J0} = 0.92\,\mathrm{K}$. The parameters for the red solid line that corresponds to the vortex BKT behaviour are $R_0 = 800\,\mathrm{k\Omega}$, $T_{v-BKT} = 0.05\,\mathrm{K}$ and $b = 11.6$. (b) Dependence of R_N on the ratio of T_{v-BKT}/T_c according to Beasley, Mooij and Orlando with Eqs. 2.28 and 2.29 from Ref. [26]. R_N is plotted vs. T_{v-BKT}/T_c to demonstrate how the parameter R_N, which is used as a free fitting parameter in the Halperin-Nelson fits, grows with decreasing T_{v-BKT}/T_c. (from Ref. [10])

In Ref. [79] in Fig. 2 the $R(T)$ dependence was presented in an Arrhenius plot to

test for temperature activated behaviour with

$$R_\Box = R_0 \cdot \exp\left(-\frac{T_{J0}}{T}\right) \tag{9.1}$$

It was possible to extract the activation energy $T_{J0} = 0.92\,\mathrm{K}$. From the extrapolation of the dashed grey line to $1/T = 0$ in Fig. 2 of Ref. [79] we can extract $R_0 \approx 100\,\mathrm{k\Omega}$. The prefactor R_0 in the Arrhenius law Eq. 9.1 reproduces the resistance at very high temperatures $R(T \gg T_{J0}) \simeq R_0$. In our opinion, a resistance of $R_0 \approx 100\,\mathrm{k\Omega}$ can not be produced by the dissipation meachnism of thermally activated phase slips as suggested in Ref. [79], since it is much higher than the quantum resistances for Cooper pairs ($R_Q \approx 6.45\,\mathrm{k\Omega}$) and much higher than $R_\Box^{300\,\mathrm{K}} = 4.26\,\mathrm{k\Omega}$. The latter R_Q and $R_\Box^{300\,\mathrm{K}}$ values approximately determine upper bounds for the resistance which can be produced by phase slips [19]. In Ref. [79] the parameter T_{J0} was identified as the Josephson coupling energy E_{J0} of an overdamped Josephson junction with $k_B T_{J0} = 2E_{J0}$. However, the sample length of $450\,\mu\mathrm{m}$ is too long for associating the thin film with a single Josephson junction.

In Fig. 9.3a we demonstrate the possibility to fit the zero field $R(T)$ dependence of Ref. [79] with the Halperin-Nelson formula Eq. 2.27. The black curve reproduces the temperature activated behaviour (Eq. 9.1) with the values $T_{J0} = 0.92\,\mathrm{K}$ and $R_0 = 100\,\mathrm{k\Omega}$ from Ref. [79]. The red curves is a Halperin-Nelson fit that traces the temperature activated behaviour from $1\,\Omega$ up to more than $10\,\mathrm{k\Omega}$ with $R_0 = 800\,\mathrm{k\Omega}$, $b = 11.6$ and $T_{v-BKT} = 0.05\,\mathrm{K}$. The prefactor R_0 in the Halperin-Nelson formula has not the meaning of a physical resistance, it is a product of the constant b^* and the normal state resistance R_N: $R_0 = b^* R_N/0.37$ [24]. The constant b^* differs from the parameter b with $b = \sqrt{b^*(T_{c0} - T_{v-BKT})}$ [24]. For $(T_{c0} - T_{v-BKT}) \ll 1$ which is the case for the samples measured in this thesis and in Ref. [79], we estimate $b^* \gg b$. Hence the normal state resistance R_N is expected to have a much lower value than the prefactor R_0 in the Halperin-Nelson Eq. 2.27 with $R_0 = b^* R_N/0.37 = b^2 R_N/(0.37 \cdot (T_{c0} - T_{v-BKT})) \gg R_N$. An exact caluclation of R_N from the fitting parameter R_0 is not possible due to a not exactly known $T_{c0} - T_{v-BKT}$. On top of that the normal state resistance R_N expected from the BMO Eqs. 2.28 and 2.29 from Ref. [26] allows for a very high R_N for $T_{v-BKT}/T_c \ll 1$ (see Fig. 9.3b). Huge prefactors R_0 and huge values for R_N have been found earlier, too. In Ref. [25] for the $R(T)$ curve of sample D04 in Fig. 1c of Ref. [25] we extracted $R_0 \approx 5.3\,\mathrm{G\Omega}$. In Ref. [28] it was found that the T_{v-BKT}/T_{c0} and the R_N for amorphous indium oxide films are in good agreement with the BMO Eqs. 2.28,2.29 up to $R_N \sim 50\,\mathrm{k\Omega}$. The value for R_N was determined by extrapolating to $R_N(T = 0)$ to zero temperature in a plot of $1/R$ vs. $T^{1/4}$, since $1/R \propto T^{1/4}$ was found to describe the $R(T)$ dependence best in the normal state [29].

We argue that the onset of the resistance in the $R(T)$ curves at zero magnetic field is mainly deterimined by vortex BKT physics for our critically disordered samples as well as the sample investigated in Ref. [79]. To verify the estimation of the vortex BKT transition temperature T_{v-BKT} and to demonstrate the existance of a vortex

BKT transition, an additional analysis of the IV characteristics is needed. The powerlaw $V \propto I^{\alpha}$ with $\alpha = 3$ marks T_{v-BKT} in the IV characteristics. However, ín this thesis we performed no high resolution dc current bias measurements on which such a vortex BKT analysis can be pursued. Hence, we analyse the IV characteristics for the similarly disorderd sample depicted in Fig. 1e of Ref. [79]. There obviously occurs a vortex BKT transition approximately above 50 mK where the IV characteristics bend down in the double logarithmic plot. The powerlaw $V \propto I^{\alpha}$ with $\alpha > 3$ for $T \lesssim 50\,\mathrm{mK}$ verifies a vortex BKT controlled $R(T)$ dependence at zero magnetic field. Thus, the Ambegaokar-Halperin description of phase diffusion through an overdamped junction proposed in Ref. [79] is not applicable for the disorderded thin films investigated here and in Ref. [79]. The proposed single Josephson junction physics may find its application for very small TiN films with a size of less than $\lesssim 1\,\mu\mathrm{m}$.

9.3 Duality of superconducting and insulating states

M. P. A. Fisher [7] characterized the duality of the superconducting phase, where Cooper pairs are condensed and vortices are localized, to the insulting phase, where Bose-condensed vortices are delocalized and electron pairs are localized. From the theory of finite size scaling around the SIT it is possible to describe a narrow region around the critical point of the SIT by a single scaling variable and a single scaling function on both sides of the transition [7, 8]. The scaling function $R(T, B)$ in the theory of finite size scaling reproduces the measured $R(T, B)$ only very close to the SIT. Far away from the SIT, thermal fluctuations are expected to distort the $R(T, B)$ described by the scaling function. Thus, the duality of the superconducting to the insulating state proposed in Ref. [7] does not necessarily result in a simultaneous description of the $R(T, B)$ deeply in the superconducting regime as well as deeply in the insulating regime by a single expression. Indeed, the latter statement works in the other direction, too: A possible phenomenological description of the $R(T, B)$ around a crossing point in the magnetoresistance isotherms is not sufficient to associate the apparent crossing point with the SIT quantum phase transition. Though the latter phenomenological expression for $R(T, B)$ may describe the measured $R(T, B)$ even far away from the apparent crossing point at B^*, a finite size analysis with the scaling variable $(B - B^*)/T^{1/z\nu}$ might lead to the conclusion that the apparent crossing at B^* is not the point of the quantum phase transition. The latter conclusion is based on the criterion that the $R(T)$ data that collapses in a scaling plot should at least vary by two orders of magnitude in $|R - R_c|$, were R_c is the resistance at the crossing.

We now focus on apparent crossing points in the magnetoresistance isotherms and the duality of the superconducting and insulating states at the SIT which is associated with these crossing points in the literature. In Ref. [45] a crossing point in the magnetoresistance isotherms similar to the MT crossing point here is found. Both sides of the crossing point, the superconducting as well as the insulating side, could phenomenologically be described by the powerlaw $R \propto B^{T_0/T}$. Based on the latter powerlaw which described both sides of the apparent crossing, a vortex-charge duality-symmetry was

attributed to this crossing point. Deviations to this powerlaw at low temperatures to a $R(B)$ dependence that is stronger were taken as the arrival of a highly insulating state in which the $R(B)$-duality-symmetry between the superconducting and the insulating side of the SIT is violated. It is important to emphasize the difference between the duality of Cooper pairs and vortices proposed in Ref. [7], and the misleading term duality-symmetry used in Ref. [45] which means the possibility to describe the $R(T, B)$ around the apparent crossing by a phenomenological expression. However, the finite size scaling analysis depicted in Fig. 4 of Ref. [45] hardly passes the criterion that the $R(T)$ data collapsing in a scaling plot should at least vary by two orders of magnitude in $|R - R_c|$. We therefore doubt that the crossing point in Ref. [45], and also the MT crossing point here (see discussion in section 9.1), can be associated with a quantum phase transition on the basis of finite size scaling.

In Ref. [45] the magnetoresistance isotherm for the lowest shown temperature of $T = 0.15\,\mathrm{K}$ deviates from the common crossing point for the $R(B)$ curves at higher temperatures. This blurred crossing point at higher temperatures is similar to the change from the MT to the HT crossing point here. For $T < 0.15\,\mathrm{K}$ the IV characteristics evolve strong nonlinearities, what is similar to the IV characteristics that accompany the LT crossing point in this thesis. From a private communication with Benjamin Sacepe we know that a low-temperature crossing point emerges in indium oxide below $T < 0.15\,\mathrm{K}$, too. A thorough scaling analysis has not been perforemd yet for the reported low-temperature crossing point in indium oxide. On the basis of the scaling analysis that we performed on the LT crossing point, we just can speculate about the results of such a scaling analyis on the corresponding low-temperature crossing point in indium oxide. In the LT regime, each side of the crossing point was described by a different phenomenological expression. For $B < B_{cM}$ a powerlaw behaviour was found with $R(B) \propto (B/B_{cM})^{\alpha(T)}$ with $\alpha(T) \sim a_M(T)$, where $a_M(T) \propto 1/T$ is shown in Fig. 4.5b. On the other side for $B > B_{cM}$, the phenomenological Eq. 4.1 was found to well describe the $R(T, B)$. Thus, these two different phenomenological expressions for the different sides of the crossing point show the absence of a $R(B)$-duality-symmetry for the complete LT regime. However, the finite size scaling analysis works quite well for the LT crossing point with the scaling exponents $z\nu = 1.2$, which is repeatedly found in indium oxide [84, 45] and LaSrCuO ($z\nu = 1.15$ for the low-temperature crossing point at B_2^*) [10]. The exponent $z\nu = 1.2$ is expected in the universality class of the 2D SIT in the dirty limit, where $z = 1$ is associated with long-range Coulomb interaction between charges [7]. The possible scaling analysis for the LT crossing point allows for a vortex-charge duality at the LT crossing point. The absence of a $R(B)$-duality-symmetry thus is not sufficient to deduce a "breakdown of duality" for the vortex-charge duality around the SIT like it was interpreted in Ref. [45].

The finding of the crossing point at which a SIT occurs that is accompanied by vortex-charge duality, is therefore not possible by finding a $R(B)$-duality symmetry like described in Ref. [45]. Only a finite size scaling analysis can reveal if a crossing point in the magnetoresistance isotherms marks the quantum critical point of an SIT that is accompanied by vortex-charge duality.

10 Summary and Outlook

In this thesis the disorder-driven as well as the magnetic field induced SIT in TiN thin films are investigated. Three crossing points in the magnetoresistance isotherms at different temperature regimes are discussed in the framework of zero temperature quantum phase transitions and superconducting fluctuations. For each of these crossing points a phenomenological description of the temperature and magnetic field dependence of the resistance $R(T, B)$ is given at magnetic fields below the magnetoresistance peak. The $R(T, B)$ dependence at high magnetic fields is explained by superconducting fluctuations above the upper critical field B_{c2}.

Motivated by the model of Josephson junction arrays, measurements with a screening top-gate are performed, in order to test for long-ranged Coulomb interactions. The charging energy between superconducting islands that are embedded in a normal-conducting matrix is expected to depend logarithmically on the minimum of sample size and electrostatic screening length. Though an apparent screening effect due to a screening top-gate could not be observed, a size dependence of the activation energy for the thermally activated resistance is revealed for the magnetic field induced SIT. An astonishing new result is the size dependence of the BKT transition temperature on the superconducting side of the SIT (see Fig. 8.2d). Both size dependences are consistent with the model of Josephson junction arrays.

The analysis of the temperature dependences of the resistance at zero field and the magnetoresistance maximum were performed for differently disordered samples with respect to the sheet resistance at room temperature $R_{\square}^{300\,\mathrm{K}}$. It is found that both the activation energy T_0 at the magnetoresistance maximum and the BKT transition temperature T_{v-BKT} depend on the sample size. Besides a size dependence also a disorder dependence is observed for T_0 and T_{v-BKT}. The activation energy $k_B T_0$ is found to vanish below $R_{\square}^{300\,\mathrm{K}} \lesssim 4\,\mathrm{k\Omega}$. Hence it is not possible to induce an insulating state with activated behaviour by a perpendicular magnetic field for samples with $R_{\square}^{300\,\mathrm{K}} \lesssim 4\,\mathrm{k\Omega}$.
At zero magnetic field the BKT transition temperature tends to zero at $R_{\square}^{300\,\mathrm{K}} \gtrsim 4.6\,\mathrm{k\Omega}$. Thus, in the disorder range associated with $4\,\mathrm{k\Omega} \lesssim R_{\square}^{300\,\mathrm{K}} \lesssim 4.6\,\mathrm{k\Omega}$ and sufficient low temperature, the sample is superconducting at zero magnetic field and undergoes a field induced SIT with termally activated behaviour of the resistance in the insulating state.

The critical temperature T_{c0} obtained from the theory of superconducting fluctuations above B_{c2} motivated a discussion about the determination of T_{c0} from the temperature dependence of the resistance $R(T)$ at zero magnetic field. It is found that the vortex BKT phase determines the onset of the resistance in the $R(T)$ up to a resistance

that subsequently approximates the resistance of the $R(T)$ maximum with increasing disorder. Thus, a determination of T_{c0} according to available theories for superconducting fluctuations above T_{c0} produces a too low value for T_{c0}, as the $R(T)$ is strongly affected by the vortex BKT behaviour. To our knowledge, there is no comprehensive theory to describe the $R(T)$ curves at zero field that includes both superconducting fluctuations above T_{c0} and vortex BKT physics.

Highly non-linear IV characteristics at zero magnetic field for differently disordered square-shaped samples with different lateral sizes L are explained by the theory of self-heating in superconducting microbridges. The vortex BKT temperature T_{v-BKT}, which is found to resemble the fitting parameter T_c, decreases with increasing disorder. The fitting parameters in the fits of the hotspot theory to the measured IV characteristics saturate very near to T_{v-BKT}. A possible explanation for the strong decrease of the surface thermal counductance is the weakened electron-phonon coupling in the film at low temperatures which allows for a temperature decoupling of the film from the substrate. Hence, the observed decrease of the surface thermal conductivity with increasing disorder is consistent with a decreasing T_{v-BKT}. The thermal conductivity in the superconducting parts of the thin film drastically increases with increasing disorder. A possible explanation includes the heat transfer due to vortices in the BKT phase. A dual picture to the superconducting IV characteristics is found on the insulating side of the B-SIT with interchanged current and voltage axes.

A number of ideas for future measurements arises from this thesis. To test for the presence of the LT crossing point for temperatures down to zero, the measurement of sample D03_S should be performed in a dilution refrigerator with a much lower base temperature. In order to verify the vortex BKT transition temperature T_{v-BKT} extracted from the $R(T)$ dependences, a current-biased four terminal measurement with an accuracy down to mΩ is required. With this data the vortex BKT transition can be identified from the IV characteristics and from the $R(T)$ dependence at the same time. The samples that are investigated in this thesis may undergo a charge BKT transition in the insulating state, however the charge BKT transition temperature T_{c-BKT} might be lower than the temperatures that are accessible in our systems. The measurement of the insulating IV characteristics at lower temperatures near the charge BKT transition gains further insight into the physics of the insulating side of the SIT. The new features, that are revealed under the usage of a high-impedance measurement setup in order to obtain insulating IV characteristics without hysteretic jumps, have to be analysed further. They possibly enable to distinguish between heating effects and Josephson junction network physics. First experiments have been pursued to test for a gate effect due to an applied voltage on a top-gate with a perfectly insulating dielectric medium between top-gate and TiN film. The resistance at lowest achieved temperatures for the magnetic field induced insulating state changed by $\approx 25\,\%$ due to an applied gate voltage $V_{Gate} = \pm 10\,\mathrm{V}$. Very near to the disorder driven SIT a change of the charge carrier density might enable to switch between the superconducting and the insulating regimes.

It would be a breakthrough to proove the charge BKT phase in the $R(T)$ dependence of the insulating state. In Fig. 9.3a it was shown that the temperature activated

behaviour of the resistance on the superconducting side can also be interpreted as a vortex BKT transition under the usage of the Halperin-Nelson formula Eq. 2.27. This alternative explanation of a linear slope in the Arrhenius plot can be transferred to the insulating side, where temperature activated behaviour in the MT regime is followed by a more than temperature activated increase of the resistance with decreasing temperature in the LT regime. It was possible to fit some $R(T)$ curves for the latter description with a modified Halperin-Nelson formula where conductance is exchanged by resistance and by a change of the sign of parameter b. However, further independent evidence is needed to verify the charge BKT transisiton for $R(T)$ curves in the highly insulating regime. This finding of the charge BKT remains a task for future generations of PhD students.

Bibliography

[1] J. M. Kosterlitz and D. J. Thouless. Long range order and metastability in two dimensional solids and superfluids. (Application of dislocation theory). *Journal of Physics C: Solid State Physics*, 5(11):L124, 1972.

[2] J. M. Kosterlitz and D. J. Thouless. Ordering, metastability and phase transitions in two-dimensional systems. *Journal of Physics C: Solid State Physics*, 6(7):1181, 1973.

[3] V.L. Berezinskii. Destruction of Long-range Order in One-dimensional and Two-dimensional Systems having a Continuous Symmetry Group I. Classical Systems. *JETP*, 32(3):493, 1971.

[4] V.L. Berezinskii. Destruction of Long-range Order in One-dimensional and Two-dimensional Systems Possessing a Continuous Symmetry Group II. Quantum Systems. *JETP*, 34(3):610, 1972.

[5] B. L. Altshuler and A. G. Aronov. Electron–Electron Interaction In Disordered Conductors. In A. L. Efros and M. Pollak, editors, *Electron–Electron Interactions in Disordered Systems*, volume 10 of *Modern Problems in Condensed Matter Sciences*, pages 1–153. Elsevier, 1985.

[6] B. Sacépé, C. Chapelier, T. I. Baturina, V. M. Vinokur, M. R. Baklanov, and M. Sanquer. Disorder-Induced Inhomogeneities of the Superconducting State Close to the Superconductor-Insulator Transition. *Phys. Rev. Lett.*, 101(15):157006, Oct 2008.

[7] M. P. A. Fisher. Quantum phase transitions in disordered two-dimensional superconductors. *Phys. Rev. Lett.*, 65(7):923–926, Aug 1990.

[8] S. L. Sondhi, S. M. Girvin, J. P. Carini, and D. Shahar. Continuous quantum phase transitions. *Rev. Mod. Phys.*, 69:315–333, Jan 1997.

[9] V. F. Gantmakher, S. N. Ermolov, G. E. Tsydynzhapov, A. A. Zhukov, and T. I. Baturina. Suppression of 2D superconductivity by the magnetic field: Quantum corrections vs. The superconductor-insulator transition. *Journal of Experimental and Theoretical Physics Letters*, 77(8):424–428, 2003.

[10] X. Shi, V. Lin Ping, T. Sasagawa, V. Dobrosavljevic, and D. Popovic. Two-stage magnetic-field-tuned superconductor-insulator transition in underdoped $La_{2-x}Sr_xCuO_4$. *Nat. Phys.*, 10(6):437–443, jun 2014.

[11] Biscaras J., Bergeal N., Hurand S., Feuillet-Palma C., Rastogi A., Budhani R. C., Grilli M., Caprara S., and Lesueur J. Multiple quantum criticality in a two-dimensional superconductor. *Nat Mater*, 12(6):542–548, jun 2013.

[12] T. Yamaguchi, R. Yagi, S. Kobayashi, and Y. Ootuka. Two-Dimensional Arrays of Small Josephson Junctions with Regular and Random Defects. *Journal of the Physical Society of Japan*, 67(3):729–731, 1998.

[13] A. Kanda and S. Kobayashi. Precursor of Charge KTB Transition in Normal and Superconducting Tunnel Junction Array. *Journal of the Physical Society of Japan*, 64(1):19–21, 1995.

[14] T. I. Baturina, A. Yu. Mironov, V. M. Vinokur, M. R. Baklanov, and C. Strunk. Hyperactivated resistance in TiN films on the insulating side of the disorder-driven superconductor-insulator transition. *JETP Letters*, 88(11):752–757, 2008.

[15] V. M. Vinokur, T. I. Baturina, M. V. Fistul, A. Yu. Mironov, M. R. Baklanov, and C. Strunk. Superinsulator and quantum synchronization. *Nature*, 452(7187):613–615, apr 2008. 10.1038/nature06837.

[16] V. M. Galitski and A. I. Larkin. Superconducting fluctuations at low temperature. *Phys. Rev. B*, 63:174506, Apr 2001.

[17] H. Kamerlingh Onnes. Further experiments with liquid helium. C. On the change of electric resistance of pure metals at very low temperatures etc. IV. The resistance of pure mercury at helium temperatures. *Leiden Comm.*, 120b, 1911.

[18] W. Meissner and R. Ochsenfeld. Ein neuer Effekt bei Eintritt der Supraleitfähigkeit. *Naturwissenschaften*, 21(44):787–788, 1933.

[19] M. Tinkham. *Introduction to Superconductivity*. Dover Publications, Inc., Mineola, New York, USA, 2004.

[20] C. Enns and S. Hunklinger. *Low-Temperture Physics*. 2000.

[21] J. Bardeen, L. N. Cooper, and J. R. Schrieffer. Theory of Superconductivity. *Phys. Rev.*, 108:1175–1204, Dec 1957.

[22] N. R. Werthamer, E. Helfand, and P. C. Hohenberg. Temperature and Purity Dependence of the Superconducting Critical Field, H_{c2}. III. Electron Spin and Spin-Orbit Effects. *Phys. Rev.*, 147:295–302, Jul 1966.

[23] K. D. Usadel. Generalized Diffusion Equation for Superconducting Alloys. *Phys. Rev. Lett.*, 25:507–509, Aug 1970.

[24] B. I. Halperin and David R. Nelson. Resistive transition in superconducting films. *Journal of Low Temperature Physics*, 36(5):599–616, 1979.

[25] S. V. Postolova, A. Yu. Mironov, and T. I. Baturina. Nonequilibrium transport near the superconducting transition in TiN films. *JETP Letters*, 100(10):635–641, 2015.

[26] M. R. Beasley, J. E. Mooij, and T. P. Orlando. Possibility of Vortex-Antivortex Pair Dissociation in Two-Dimensional Superconductors. *Phys. Rev. Lett.*, 42:1165–1168, Apr 1979.

[27] T. I. Baturina, S. V. Postolova, A. Yu. Mironov, A. Glatz, M. R. Baklanov, and V. M. Vinokur. Superconducting phase transitions in ultrathin TiN films. *EPL*, 97(1):17012, 2012.

[28] A. F. Hebard and G. Kotliar. Possibility of the vortex-antivortex transition temperature of a thin-film superconductor being renormalized by disorder. *Phys. Rev. B*, 39:4105–4109, Mar 1989.

[29] A. T. Fiory and A. F. Hebard. Electron Mobility, Conductivity, and Superconductivity near the Metal-Insulator Transition. *Phys. Rev. Lett.*, 52:2057–2060, Jun 1984.

[30] A. Glatz, A. A. Varlamov, and V. M. Vinokur. Fluctuation spectroscopy of disordered two-dimensional superconductors. *Phys. Rev. B*, 84:104510, Sep 2011.

[31] J. M. B. Lopes dos Santos and E. Abrahams. Superconducting fluctuation conductivity in a magnetic field in two dimensions. *Phys. Rev. B*, 31:172–176, Jan 1985.

[32] T. I. Baturina, J. Bentner, C. Strunk, M. R. Baklanov, and A. Satta. From quantum corrections to magnetic-field-tuned superconductor–insulator quantum phase transition in TiN films. *Physica B: Condensed Matter*, 359–361:500–502, 2005. Proceedings of the International Conference on Strongly Correlated Electron Systems.

[33] K. S. Tikhonov, G. Schwiete, and A. M. Finkel'stein. Fluctuation conductivity in disordered superconducting films. *Phys. Rev. B*, 85:174527, May 2012.

[34] I. S. Burmistrov, I. V. Gornyi, and A. D. Mirlin. Superconductor-insulator transitions: Phase diagram and magnetoresistance. *Phys. Rev. B*, 92:014506, Jul 2015.

[35] B. Tarasinski and G. Schwiete. Fluctuation conductivity of disordered superconductors in magnetic fields. *Phys. Rev. B*, 88:014518, Jul 2013.

[36] Y. B. Kim, C. F. Hempstead, and A. R. Strnad. Flux-Flow Resistance in Type-II Superconductors. *Phys. Rev.*, 139:A1163–A1172, Aug 1965.

[37] M. Inui, P. B. Littlewood, and S. N. Coppersmith. Pinning and thermal fluctuations of a flux line in high-temperature superconductors. *Phys. Rev. Lett.*, 63:2421–2424, Nov 1989.

[38] T. T. M. Palstra, B. Batlogg, L. F. Schneemeyer, and J. V. Waszczak. Thermally Activated Dissipation in $Bi_{2.2}Sr_2Ca_{0.8}Cu_2O_{8+\delta}$. *Phys. Rev. Lett.*, 61:1662–1665, Oct 1988.

[39] W. R. White, A. Kapitulnik, and M. R. Beasley. Collective vortex motion in *a* -MoGe superconducting thin films. *Phys. Rev. Lett.*, 70:670–673, Feb 1993.

[40] D. Ephron, A. Yazdani, A. Kapitulnik, and M. R. Beasley. Observation of Quantum Dissipation in the Vortex State of a Highly Disordered Superconducting Thin Film. *Phys. Rev. Lett.*, 76:1529–1532, Feb 1996.

[41] C. Attanasio, C. Coccorese, V.N. Kushnir, L. Maritato, S.L. Prischepa, and M. Salvato. Magnetic field depedennce of pinning mechanisms in Bi2Sr2Ca1Cu2O8+x thin films. *Physica C: Superconductivity*, 255(3):239–246, 1995.

[42] J. A. Chervenak and J. M. Valles. Evidence for a quantum-vortex-liquid regime in ultrathin superconducting films. *Phys. Rev. B*, 54:R15649–R15652, Dec 1996.

[43] A. W. Tsen, B. Hunt, Y. D. Kim, Z. J. Yuan, S. Jia, R. J. Cava, J. Hone, P. Kim, C. R. Dean, and A. N. Pasupathy. Nature of the quantum metal in a two-dimensional crystalline superconductor. *Nat. Phys.*, 12(3):208–212, mar 2016.

[44] G. Sambandamurthy, A. Johansson, E. Peled, D. Shahar, P. G. Björnsson, and K. A. Moler. Power law resistivity behavior in 2D superconductors across the magnetic field-tuned superconductor-insulator transition. *EPL (Europhysics Letters)*, 75(4):611, 2006.

[45] M. Ovadia, D. Kalok, B. Sacepe, and D. Shahar. Duality symmetry and its breakdown in the vicinity of the superconductor-insulator transition. *Nat. Phys.*, 9(7):415–418, jul 2013.

[46] M.V. Feigel'man, V.B. Geshkenbein, and A.I. Larkin. Pinning and creep in layered superconductors. *Physica C: Superconductivity*, 167(1):177–187, 1990.

[47] G. Blatter, M. V. Feigel'man, V. B. Geshkenbein, A. I. Larkin, and V. M. Vinokur. Vortices in high-temperature superconductors. *Rev. Mod. Phys.*, 66:1125–1388, Oct 1994.

[48] W. J. Skocpol, M. R. Beasley, and M. Tinkham. Phase-slip centers and nonequilibrium processes in superconducting tin microbridges. *Journal of Low Temperature Physics*, 16(1):145–167, 1974.

[49] W. J. Skocpol, M. R. Beasley, and M. Tinkham. Self-heating hotspots in superconducting thin-film microbridges. *Journal of Applied Physics*, 45(9):4054–4066, 1974.

[50] A. G. Sivakov, A. M. Glukhov, A. N. Omelyanchouk, Y. Koval, P. Müller, and A. V. Ustinov. Josephson Behavior of Phase-Slip Lines in Wide Superconducting Strips. *Phys. Rev. Lett.*, 91:267001, Dec 2003.

[51] I. M. Dmitrenko. Experimental studies of weakly coupled superconductors (Review). *Low Temperature Physics*, 30(7):522–527, 2004.

[52] V. M. Dmitriev, I. V. Zolochevskii, T. V. Salenkova, and E. V. Khristenko. Critical currents, phase slip centers, and phase slip lines in superconducting films in the absence of external magnetic field. *Low Temperature Physics*, 31(2):127–136, 2005.

[53] F. L. Vernon and R. J. Pedersen. Relaxation Oscillations in Josephson Junctions. *Journal of Applied Physics*, 39(6):2661–2664, 1968.

[54] F. Marsili, D. Bitauld, A. Fiore, A. Gaggero, F. Mattioli, R. Leoni, M. Benkahoul, and F. Lévy. High efficiency NbN nanowire superconducting single photon detectors fabricated on MgO substrates from a low temperature process. *Opt. Express*, 16(5):3191–3196, Mar 2008.

[55] C. Delacour, B. Pannetier, J. Villegier, and V. Bouchiat. Quantum and Thermal Phase Slips in Superconducting Niobium Nitride (NbN) Ultrathin Crystalline Nanowire: Application to Single Photon Detection. *Nano Letters*, 12(7):3501–3506, 2012. PMID: 22694480.

[56] W. Zhang, P. Khosropanah, J. R. Gao, E. L. Kollberg, K. S. Yngvesson, T. Bansal, R. Barends, and T. M. Klapwijk. Quantum noise in a terahertz hot electron bolometer mixer. *Applied Physics Letters*, 96(11), 2010.

[57] E. L. Kollberg and K. S. Yngvesson. Quantum-noise theory for terahertz hot electron bolometer mixers. *IEEE Transactions on Microwave Theory and Techniques*, 54(5):2077–2089, May 2006.

[58] V. F. Gantmakher and V. T. Dolgopolov. Superconductor-insulator quantum phase transition. *Physics-Uspekhi*, 53(1):1–49, 2010.

[59] T. I. Baturina and V. M. Vinokur. Superinsulator–superconductor duality in two dimensions. *Annals of Physics*, 331:236–257, 2013.

[60] Y. Lin, J. Nelson, and A. M. Goldman. Superconductivity of very thin films: The superconductor–insulator transition. *Physica C: Superconductivity and its Applications*, 514:130–141, 2015. Superconducting Materials: Conventional, Unconventional and Undetermined.

[61] D. B. Haviland, Y. Liu, and A. M. Goldman. Onset of superconductivity in the two-dimensional limit. *Phys. Rev. Lett.*, 62:2180–2183, May 1989.

[62] T. I. Baturina, A. Bilušić, A. Yu. Mironov, V. M. Vinokur, M. R. Baklanov, and C. Strunk. Localized Superconductivity in the Quantum-Critical Region of the Disorder-Driven Superconductor-Insulator Transition in TiN Thin Films. *Physica C*, 468:316, Nov 2008.

[63] D. Shahar and Z. Ovadyahu. Superconductivity near the mobility edge. *Phys. Rev. B*, 46:10917–10922, Nov 1992.

[64] S. R. Khan, E. M. Pedersen, B. Kain, A. J. Jordan, and R. P. Barber. Superconductor-insulator transition in granular Pb films near a superconducting ground plane. *Phys. Rev. B*, 61:5909–5912, Mar 2000.

[65] X. Leng, J. Garcia-Barriocanal, S. Bose, Y. Lee, and A. M. Goldman. Electrostatic Control of the Evolution from a Superconducting Phase to an Insulating Phase in Ultrathin $YBa_2Cu_3O_{7-x}$ Films. *Phys. Rev. Lett.*, 107:027001, Jul 2011.

[66] J. Garcia-Barriocanal, A. Kobrinskii, X. Leng, J. Kinney, B. Yang, S. Snyder, and A. M. Goldman. Electronically driven superconductor-insulator transition in electrostatically doped $La_2CuO_{4+\delta}$ thin films. *Phys. Rev. B*, 87:024509, Jan 2013.

[67] P.W. Anderson. Theory of dirty superconductors. *Journal of Physics and Chemistry of Solids*, 11(1):26–30, 1959.

[68] P. A. Lee and T. V. Ramakrishnan. Disordered electronic systems. *Rev. Mod. Phys.*, 57:287–337, Apr 1985.

[69] A. M. Finkel'stein. Suppression of superconductivity in homogeneously disordered systems. *Physica B: Condensed Matter*, 197(1):636–648, 1994.

[70] N. Hadacek, M. Sanquer, and J.-C. Villégier. Double reentrant superconductor-insulator transition in thin TiN films. *Phys. Rev. B*, 69:024505, Jan 2004.

[71] M. A. Skvortsov and M. V. Feigel'man. Superconductivity in Disordered Thin Films: Giant Mesoscopic Fluctuations. *Phys. Rev. Lett.*, 95:057002, Jul 2005.

[72] P. W. Anderson. Special Effects in Superconductivity. In E. R. Caiabiello, editor, *Lectures on the Many-body Problems*, pages 113–135. Academic Press, 1964.

[73] Y. Dubi, Y. Meir, and Y. Avishai. Nature of the superconductor-insulator transition in disordered superconductors. *Nature*, 449(7164):876–880, oct 2007. 10.1038/nature06180.

[74] B. Sacepe, T. Dubouchet, C. Chapelier, M. Sanquer, M. Ovadia, D. Shahar, M. Feigel'man, and L. Ioffe. Localization of preformed Cooper pairs in disordered superconductors. *Nat Phys*, 7(3):239–244, mar 2011. 10.1038/nphys1892.

[75] D. Sherman, G. Kopnov, D. Shahar, and A. Frydman. Measurement of a Superconducting Energy Gap in a Homogeneously Amorphous Insulator. *Phys. Rev. Lett.*, 108:177006, Apr 2012.

[76] Y. M. Strelniker, A. Frydman, and S. Havlin. Percolation model for the superconductor-insulator transition in granular films. *Phys. Rev. B*, 76:224528, Dec 2007.

[77] T. I. Baturina, C. Strunk, M. R. Baklanov, and A. Satta. Quantum Metallicity on the High-Field Side of the Superconductor-Insulator Transition. *Phys. Rev. Lett.*, 98:127003, Mar 2007.

[78] D. Kalok. Non-linear conductance at the superconductor-insulator transition in titanium nitride. *Dissertation*, 2013.

[79] T. I. Baturina, D. Kalok, A. Bilušić, V. M. Vinokur, M. R. Baklanov, A. K. Gutakovskii, A. V. Latyshev, and C. Strunk. Dual threshold diode based on the superconductor-to-insulator transition in ultrathin TiN films. *Applied Physics Letters*, 102(4), 2013.

[80] M. Ovadia, B. Sacépé, and D. Shahar. Electron-Phonon Decoupling in Disordered Insulators. *Phys. Rev. Lett.*, 102(17):176802, Apr 2009.

[81] G. Sambandamurthy, L. W. Engel, A. Johansson, and D. Shahar. Superconductivity-Related Insulating Behavior. *Phys. Rev. Lett.*, 92(10):107005, Mar 2004.

[82] G. Sambandamurthy, L. W. Engel, A. Johansson, E. Peled, and D. Shahar. Experimental Evidence for a Collective Insulating State in Two-Dimensional Superconductors. *Phys. Rev. Lett.*, 94(1):017003, Jan 2005.

[83] M. P. A. Fisher, G. Grinstein, and S. M. Girvin. Presence of quantum diffusion in two dimensions: Universal resistance at the superconductor-insulator transition. *Phys. Rev. Lett.*, 64:587–590, Jan 1990.

[84] A. F. Hebard and M. A. Paalanen. Magnetic-field-tuned superconductor-insulator transition in two-dimensional films. *Phys. Rev. Lett.*, 65(7):927–930, Aug 1990.

[85] S. Mitra, G. C. Tewari, D. Mahalu, and D. Shahar. Finite-size effects in amorphous indium oxide. *Phys. Rev. B*, 93:155408, Apr 2016.

[86] N. Marković, C. Christiansen, and A. M. Goldman. Thickness˘Magnetic Field Phase Diagram at the Superconductor-Insulator Transition in 2D. *Phys. Rev. Lett.*, 81:5217–5220, Dec 1998.

[87] J. Kisker and H. Rieger. Bose-glass and Mott-insulator phase in the disordered boson Hubbard model. *Phys. Rev. B*, 55:R11981–R11984, May 1997.

[88] R. Fazio and H. van der Zant. Quantum phase transitions and vortex dynamics in superconducting networks. *Physics Reports*, 355(4):235–334, 2001.

[89] E. Chow, P. Delsing, and D. B. Haviland. Length-Scale Dependence of the Superconductor-to-Insulator Quantum Phase Transition in One Dimension. *Phys. Rev. Lett.*, 81:204–207, Jul 1998.

[90] R. S. Newrock, C. J. Lobb, U. Geigenmüller, and M. Octavio. The Two-Dimensional Physics of Josephson Junction Arrays. volume 54 of *Solid State Physics*, pages 263–512. Academic Press, 2000.

[91] V. Ambegaokar and A. Baratoff. Tunneling Between Superconductors. *Phys. Rev. Lett.*, 10:486–489, Jun 1963.

[92] R. Fazio and G. Schön. Charge and vortex dynamics in arrays of tunnel junctions. *Phys. Rev. B*, 43(7):5307–5320, Mar 1991.

[93] J. V. José and C. Rojas. Superconducting to normal state phase boundary in arrays of ultrasmall Josephson junctions. *Physica B: Condensed Matter*, 203(3):481–489, 1994.

[94] M. Tinkham, D. W. Abraham, and C. J. Lobb. Periodic flux dependence of the resistive transition in two-dimensional superconducting arrays. *Phys. Rev. B*, 28:6578–6581, Dec 1983.

[95] M. V. Fistul, V. M. Vinokur, and T. I. Baturina. Collective Cooper-Pair Transport in the Insulating State of Josephson-Junction Arrays. *Phys. Rev. Lett.*, 100(8):086805, Feb 2008.

[96] M. Ortuño, A. M. Somoza, V. M. Vinokur, and T. I. Baturina. Electronic transport in two-dimensional high dielectric constant nanosystems. *Scientific Reports*, 5:9667, apr 2015.

[97] D. Kalok, A. Bilušić, T. I. Baturina, A. Yu. Mironov, S. V. Postolova, A. K. Gutakovskii, A. V. Latyshev, V. M. Vinokur, and C. Strunk. Non-linear conduction in the critical region of the superconductor-insulator transition in TiN thin films. *Journal of Physics: Conference Series*, 400(2):022042, 2012.

[98] D. Kalok, T. I. Baturina, V. M. Vinokur, and C. Strunk. Intrinsic non-linear conduction in the super-insulating state of thin TiN films. *arXiv:1004.5153*, page 4, 2010.

[99] I. A. Schneider. *Dissertation*, to be published.

[100] O. Cohen, M. Ovadia, and D. Shahar. Electric breakdown effect in the current-voltage characteristics of amorphous indium oxide thin films near the superconductor-insulator transition. *Phys. Rev. B*, 84:100507, Sep 2011.

[101] D. Kowal and Z. Ovadyahu. Scale dependent superconductor insulator transition. *Physica C Superconductivity*, 468:322–325, February 2008.

[102] S. Kondovych. Private communication. 2015.

[103] Yu. M. Ivanchenko and L. A. Zil'berman. The Josephson Effect in Small Tunnel Contacts . *JETP*, 28(6):1272, 1969.

[104] V. Ambegaokar and B. I. Halperin. Voltage Due to Thermal Noise in the dc Josephson Effect. *Phys. Rev. Lett.*, 22:1364–1366, Jun 1969.

[105] C. Uher. Thermal conductivity of high-T c superconductors. *Journal of Superconductivity*, 3(4):337–389, 1990.

[106] J. Deppe and J. L. Feldman. Energy current and thermal conductivity for Josephson-junction array models of granular superconductors. *Phys. Rev. B*, 50:6479–6482, Sep 1994.

[107] A. Andersson and J. Lidmar. Influence of vortices and phase fluctuations on thermoelectric transport properties of superconductors in a magnetic field. *Phys. Rev. B*, 83:174502, May 2011.

[108] B. L. Altshuler, V. E. Kravtsov, I. V. Lerner, and I. L. Aleiner. Jumps in Current-Voltage Characteristics in Disordered Films. *Phys. Rev. Lett.*, 102(17):176803, Apr 2009.

[109] A. Doron, I. Tamir, T. Levinson, M. Ovadia, B. Sacépé, and D. Shahar. Transport Catastrophe Near the Superconductor-Insulator Transition. *ArXiv e-prints*, June 2016.

[110] L. G. Aslamazov and A. I. Larkin. *Fiz. Tverd. Tela*, 10(4):1104–1111, 1968.

[111] L. Benfatto, C. Castellani, and T. Giamarchi. Broadening of the Berezinskii-Kosterlitz-Thouless superconducting transition by inhomogeneity and finite-size effects. *Phys. Rev. B*, 80:214506, Dec 2009.

[112] K. K. Likharev and A. B. Zorin. Theory of the Bloch-wave oscillations in small Josephson junctions. *Journal of Low Temperature Physics*, 59(3):347–382, 1985.

[113] M. A. Sillanpää, T. Lehtinen, A. Paila, Yu. Makhlin, L. Roschier, and P. J. Hakonen. Direct Observation of Josephson Capacitance. *Phys. Rev. Lett.*, 95:206806, Nov 2005.

[114] S. Sankar and V. Tripathi. Low-field magnetoresponse of strongly disordered two-dimensional superconductors. *Phys. Rev. B*, 94:054520, Aug 2016.

[115] X. Shi, G. Logvenov, A. T. Bollinger, I. Božović, C. Panagopoulos, and D. Popović. Emergence of superconductivity from the dynamically heterogeneous insulating state in $La_{2-x}Sr_xCuO_4$. *Nature Materials*, 12(1):47–51, jan 2013. 10.1038/nmat3487.

[116] Y. Wang and H.-H. Wen. Doping dependence of the upper critical field in $La_{2-x}Sr_xCuO_4$ from specific heat. *EPL (Europhysics Letters)*, 81(5):57007, 2008.

Acknowledgement

I would like to thank

- My advisor Prof. Dr. Strunk. He gave me this very interesting topic and lead my work to the right direction. The discussions about the SIT and my measurements were very helpful. I am very thankful for the incredible length of the measurement time I got at three different dilution fridges, and for the freedom to pursue measurements on features which looked interesting in my opinion. I was allowed to join several conferences, where I could present my results to leading experts in the SIT. First of all, the low temperatures conference (LT27) in Buenos Aires, and the workshop on localization, interactions and superconductivity in the Landau institute in Chernogolovka in 2016, were highlights after years of measurements and data analysis.
- Prof. Dr. Evers, who agreed to act as referee for my thesis
- Dr. Tatyana Baturina, who introduced me to the topic of superconducting fluctuations and helped me to understand my data. Her suggestions were the basis for several topics in this thesis.
- Dr. Valerii Vinokur, who helped us to understand the phenomenological expressions for the $R(T, B)$ at the three found crossing points. Thank you for spending time on explaining the gigantic review of Ref. [47].
- Dr. David Kalok, who introduced me to the measurement techniques, the cryostat handling, the perl programming, the python scripting and who helped me with the data analysis. Though he had to finish his PhD thesis, he took the time to help me.
- Prof. Dr. Weiss, who let me use his clean room facilities, his dilution fridge and the infrastructure of the chair.
- The He-station for the supply of liquid Helium.
- The electronic and machine workshop for their support.
- Our technicians Thomas Haller and Michael Weigl for the assistance on many technical problems at the fridges and at the sample preparation.
- Our secretaries Claudia Rahm and Elke Haushalter for their reliability and for solving all my administrative problems so fast.
- Ina Schneider who shared the office with me for many years. Thank you for the nice atmosphere and the discussions about TiN. We can look back to measurement times with astonishing results. I have to thank you and the other collegues

of my office for standing all the craziness due to hard times of data analysis and especially the Galitski-Larkin fits.

- My collegue Markus Brunner for the nice atmosphere in the office and for the fruitful discussions about agriculture and sheep farming.
- My collegue Lorenz Fuchs who is my successor in the topic of SIT in TiN at this workgroup. Thank you for asking many questions about the measurements and for listening to my answers, sometimes even without a preceding question.
- Ondrej Vavra for the best athmospere ever in an office and for good discussions about everything, sometimes physics.
- All members of the workgroup for the pleasant atmosphere.
- My friends for the help during the last years. Especially Rudi Kronfeldner, who always had some time at the evenings.
- My classmates Markus Härtinger and Sebastian Putz for the nice time during the studies and the PhD time.
- My Brother, Dr. Helmut Kronfeldner, who encouraged me during the hard times of my thesis. I would like to thank him for the medical help he supported and for the nice time we spent together especially on the farm of our parents and in the mountains.
- My parents who supported me during the last ten years of the physics studies and the PhD time.
- My girlfriend Tanja Ullrich for the great support of my work. She always was sympathetic when I came home late and when I reported from the university. Your craziness and your warm heart illuminate my life.